OXYGEN AND ITS CONTROL OVER STRUCTURAL AND ELECTRONIC PROPERTIES OF PB BASED 1212 SUPERCONDUCTORS

Brian James Mitchell

A Thesis Submitted for the Degree of PhD
at the
University of St Andrews

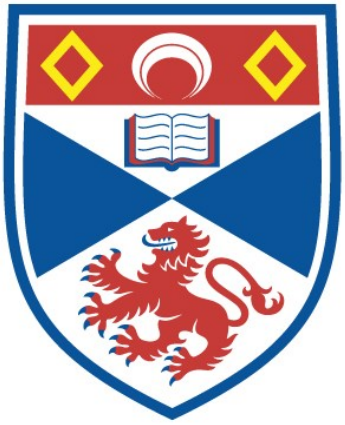

1998

University of St Andrews

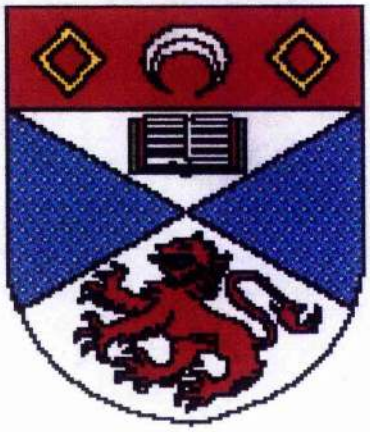

School of Chemistry
North Haugh
St Andrews. KY16 9ST

Oxygen and its control over structural and electronic properties of Pb based 1212 superconductors

Brian James Mitchell

A thesis presented for the degree of Doctor of Philosophy

DECLARATION

I, Brian J. Mitchell, hereby certify that this thesis, which is approximately 33300 words in length, has been written by me, that it is the record of work carried out by me and that it has not been submitted in any previous application for a higher degree.

Date 23/1/98 signature of candidate

I was admitted as a research student in October 1994 and as a candidate for the degree of Doctor of Philosophy in October 1995; for higher study for which this is a record was carried out in the University of St Andrews between 1994 and 1997.

Date 23/1/98 signature of candidate

I hereby certify that the candidate has fulfilled the conditions of the Resolution and Regulations appropriate for the degree of Doctor of Philosophy in the University of St. Andrews and that the candidate is qualified to submit this thesis in application for that degree.

Date 23/1/98 signature of supervisor

In submitting this thesis to the University of St. Andrews I understand that I am giving permission for it to be made available for use in accordance with the regulations of the University Library for the time being in force, subject to any copyright vested in the work not being affected thereby. I also understand that the title and abstract will be published, and that a copy of the work maybe made and supplied to any bona fide library or research worker.

Date 23/1/98 signature of candidate

ACKNOWLEDGEMENTS

On the academic side of things I would like to thank the following for their assistance with experiments and useful discussions:

ILL Grenoble France. Clemens Ritter and Alan Hewat.

ESRF Grenoble France. Andy Fitch, Eric Dooryhee, Gavin Vaughan.

ISIS Didcot. Kevin Knight.

SRS Daresbury Warrington - Andy Dent and Mark Roberts

Edinburgh University. Andrew Harrison, Gavin Whittaker and Andrew Wills

St Andrews University. Bob Cywinski, Adrian Hillier, David Tunstall, Svetlana Titova and Stephanie Lagrave.

Great thanks though to my supervisor John Irvine for his encouragement and help with this research in what has been at times extremely challenging occasionally tedious, and of course the University of St Andrews for providing my funding.

My colleague Richard Gover and St Andrews University Rifle Club deserve praise for helping me relax out of hours. Lastly, but not least, I must especially mention my fiancée Rachel Catto who has to put up with my absence for the past three years.

ABSTRACT

The phase stability, electronic properties and crystal structure of the Pb based 1212 cuprate superconductor $(Pb_{[1+x]/2}Cu_{[1-x]/2})Sr_2(Y_{1-x}Ca_x)Cu_2O_{7\pm\delta}$ were studied using a number of techniques.

Since synthetic difficulties limited study of these materials, sol-gel techniques incorporating mixed metal nitrate precursors were applied. Novel synthesis techniques improved reaction rate but did not entirely overcome synthesis difficulties. The effects of Ca content; reaction temperature, and oxygen content in controlling product phase formation and phase stability under synthesis conditions were investigated.

X-ray and neutron diffraction were used to probe structural disorder within samples as Ca levels increased and sample oxygen content was varied. The subsequent Rietveld refinements revealed that the levels of cation site disorder increase in line with increasing Ca levels.

Under oxidising conditions, annealing temperature and thus oxygen content of the sample plays a critical role in controlling superconducting properties. Optimal T_c and superconducting volume are only achieved over the oxygen content range 6.99-7.00. Low pO_2 annealing conditions were used to control sample oxygen content; however, these were not significantly better than standard techniques. Low pO_2 environments facilitate the removal of oxygen from samples and allowed the study of phase stability. It was possible to show that decomposition of the 1212 phase leads to formation of new superconducting phases that might well account for contentious literature claims.

EXAFS and NMR measurements show that on a local scale, the structure of the 1212 phase rocksalt layer is quite different to the average structure generated from diffraction measurements. The Pb atoms tend to form a PbO_{4+x} molecular type cluster, in which x can increase up to 0.5 to accommodate the inclusion of an excess 0.1 oxygens into the structure. Solid-state NMR measurements reveal in Ca containing samples that up to 20% of the Y within the structure is dimerised.

CONTENTS

Chapter 1. INTRODUCTION

1.1 Overview

Although the 1986 discovery of superconductivity in the La-Ba-Cu-O (cuprate) system by Bednorz and Müller[1], who subsequently received the Nobel prize, caused great interest and initiated one of the greatest surges of research activity of the Century, superconductivity had first been discovered in 1911 by Kamerlingh Onnes[2]. Over the next 75 years thousands of materials were studied. Properties improved, industrial uses developed e.g. high field magnets, and of course the theory from Bardeen Cooper and Schrieffer[3] that describes the phenomenon of superconductivity was developed. The limitation, until 1986, was the superconducting transition temperature of the materials. Indeed the maximum onset temperature (T_c) achieved was 22.3K in a Nb_3Ge sample by Testardi et al[4]. This meant that liquid He was required as the cooling medium. Liquid He is approximately 20 times more expensive than liquid N_2. Of course there had been claims by a number of scientists that superconductivity could be induced at temperatures far above 23K e.g. Ogg et al[5,6] in metallic solutions of sodium in ammonia, or the prediction of high transition temperatures in organic material by Little[7]. These claims, however, have either been disproved or not yet confirmed.

The discovery of High Temperature Superconductivity (HTS) in LBCO, an oxide material by Bednorz and Müller, initially raised interest because the T_c was >30K, well above the previous record which had only been achieved after decades of research. Although treated initially with scepticism, laboratories began working on these systems and the real breakthrough came at the end of 1986 when Wu[8] et al discovered a T_c >90K in a sample containing Y-Ba-Cu-O. The liquid Nitrogen barrier had been broken and the number of groups working in the field mushroomed. Onset temperatures climbed steadily above the 100K mark with the discovery of multi-elemental $Bi_2Sr_2CaCu_2O_8$and $Tl_2Ba_2Ca_2Cu_3O_{10}$. The maximum onset temperature to date was achieved in 1993 at ~135K by Schilling et al[9] (~165K under pressure) in $HgBa_2Ca_2Cu_3O_8$ samples. Since then the Hg based system has produced the highest onset temperatures, though they are still around the 135K mark.

The sheer volume of work produced by the many thousands of research groups has dropped from the high of the late 1980's as many have moved away from the

superconductivity field. There still remains a large number of multi-disciplinary groups specialising in superconductivity research. For the HTS systems, research has focused on the discovery of new novel superconducting materials and improvement of existing material properties with the view to developing industrial applications. However, most applications so far have only been small scale and more of novel value e.g. ultra sensitive magnetic detectors (SQUIDS), and the low temperature BCS type superconductors still are the most amenable to development for industrial applications. HTS materials can compete on cost, but fabrication and reliability problems are still a major drawback.

The cuprate based superconductors interested theoreticians from very early on since superconductivity occurs at temperatures far exceeding the limit imposed by BCS theory. These materials show marked differences in a number of properties e.g. coherence length, penetration depth and large spatial anisotropy from the conventional BCS low temperature superconductors. Even at the present time, there are a number of theories being put forward to describe the cuprate systems, yet no one theory is showing dominance. Interest has also been sparked in a number of new low Tc superconductors such as $Y(Ni_{1-x}Co_x)_2B_2C$, which appear not to be simply classified as BCS materials. Superconductivity may well have been studied for a long period of time, but it still leaves many unanswered questions and great scope for research.

1.2. Properties of Superconductors.

1.21. Historical review

The discovery of "zero" resistance in superconducting Hg by Kamerlingh Onnes could not be accounted for by the 'free electron' model, which described behaviour of electrons in a metal and associated resistance. Thus, a completely new theory to describe the behaviour of such materials was required.

Various elements and binary alloys were made to superconduct and Silsbee[10] in 1916 showed that superconductivity could be destroyed by applying a critical current to the sample. It was not until 1933 that Meissner and Ochsenfeld[11] showed that a superconducting material when cooled below its T_c with no external magnetic field present and then subjected to an external magnetic field, totally expels the magnetic flux from its core. This leads to a situation where there is no magnetic flux within its interior, figure 1.1(a1 and a2). If the sample temperature is above T_c in the presence of an external field flux penetrates the sample, figure 1(b1). When this superconducting material is cooled below T_c in the presence of a magnetic field, then the magnetic flux is also expelled from its interior, figure 1.1(b2).

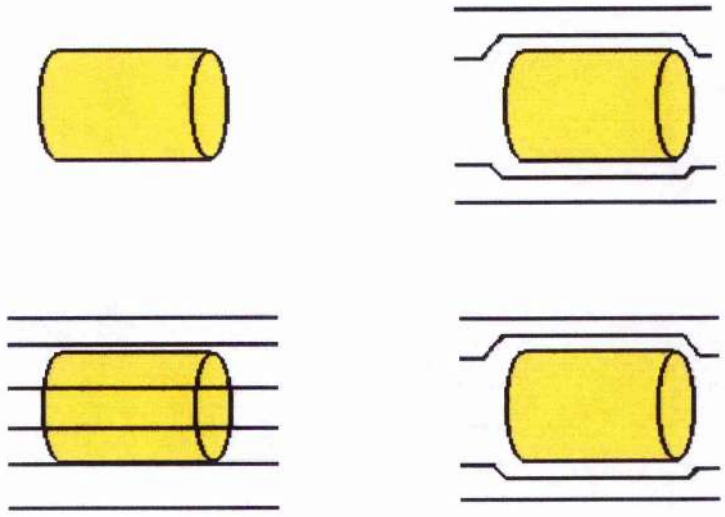

Figure 1.1. Top left to right. (a1) Cooling below T_c with zero applied field. (a2) Expulsion of flux from within sample as external field is applied. Bottom left to right. (b1) Above T_c magnetic flux enters sample. (b2) Expulsion of flux from sample below T_c with magnetic field applied.

Critically, the work by Meissner and Ochsenfeld showed that the superconducting state not only possessed the property **R**=0, but should be treated as a thermodynamic phase since the magnetic flux was expelled from its interior independent of experimental conditions.

F. and H. London[12] developed a phenomenological theory of superconductivity (London theory), which was capable of detailing a large number of observations and

indicated where a microscopic theory must start. The London equations describe the depth into which the magnetic field must penetrate into the superconductor (λ penetration depth).

For many years the evidence suggested that the lattice played no part in the superconducting mechanism; however, the development of nuclear physics allowed preparation of large amounts of the isotopes of a particular element. The work of Maxwell[13] and Reynolds et al[14] in 1950 showed that the T_c of a material was found to depend on the isotopic mass, M, such that:

$$T_c \propto 1/\sqrt{M} \qquad (1.1)$$

The frequency, ν, of vibration of a diatomic molecule is known to be given by:

$$\nu = \frac{1}{2\pi}\sqrt{k/\mu} \qquad (1.2)$$

where μ is the reduced mass of the molecule, and **k** the force constant of the bond. The force constant depends on the bonding of the atoms in the material and ought not to be altered by variation of the isotopic mass, so $\nu \propto \mu^{-1/2}$. Although the situation for a lattice is more complex it remains that the frequency of vibration of the lattice is altered by isotopic substitution.

Fröhlich[15] and Bardeen[16] in 1950 independently suggested that there was an interaction of the electrons via the lattice in superconducting materials. The vibrational modes of a lattice are quantized, as are the modes of an isolated molecule, the quanta of the lattice vibrations being called phonons.

Fröhlich made a suggestion that there could be a strong phonon-electron interaction in a superconductor leading to an attractive force between two electrons that is strong enough to overcome the Coulomb repulsion between them. As a conduction electron passes through the lattice, it can disturb some of the positively charged ions from their

equilibrium positions, pushing them together and giving a region of increased positive charge density. As these oscillate, a second electron passing this moving region of positive charge density is attracted to it. The net effect is that the two electrons have interacted with one another, using the lattice vibration as an intermediary. Furthermore, the interaction between the electrons is attractive because each of the two separate steps involved has an attractive Coulomb interaction.

High frequency techniques to determine λ gave an effective depth considerably larger than calculated from the London equations, and this was resolved by Pippard[17] who introduced a coherence length (ξ) for the wavefunctions of the superconducting carriers, such that a perturbation at one point influences every carrier within a distance ξ_o of that point.

Around the same time Ginzberg and Landau[18] (GL) proposed phenomenological equations, which were an alternative to London theory. One important parameter is:

$$k = \lambda_L / \xi \qquad (1.3)$$

The GL parameter is a dimensionless ratio, which proves important in differentiating between types of superconductor.

In 1957 Bardeen Cooper and Schrieffer published their theory of superconductivity (BCS theory) which predicts that under certain conditions, the attraction between two conduction electrons due to a succession of phonon interactions can slightly exceed the repulsion that they exert directly on one another due to the Coulomb interaction of their like charges. The two electrons are thus weakly bound together forming a so-called Cooper pair.

Assuming that electron pairs exist, then many properties[19,20,21] of a superconductor may be described. In the BCS model there is an attractive interaction between electrons close to the Fermi surface in which the formation of some 'bound pairs' leads to the formation of further bound pairs. This is a co-operative effect which results in the

presence of a ground state that is separated by an energy gap immediately above the Fermi edge, figure 1.2(a), from the allowed excited states of the system. In the normal metallic state there is no discontinuity in the density of states at the Fermi edge. However, on cooling a gap arises at the superconducting transition, which increases on further cooling, figure 1.2(b)

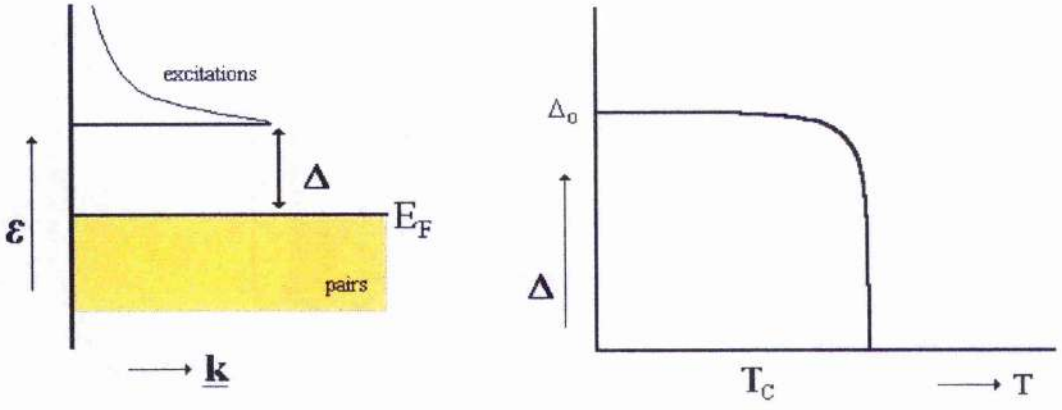

Figure 1.2. From left. 1.2(a). Schematic density of states near the Fermi edge of a superconductor. 1.2(b) Variation of the superconducting energy gap with temperature.

In the superconducting state, carriers immediately below the Fermi edge are paired, those above the superconducting gap are electron-like or hole like excitations, figure 1.2(b). The lowest energy for a Cooper pair is achieved by binding together an electron with wave vector **+k** and an electron with **-k**, and with their spins anti parallel, so that the net spin is zero. The net linear momentum of such a pair is zero. Particles with odd half-integral spins e.g. electrons are subject to Fermi statistics and as a result can only occupy a state defined by all the quantum numbers once. Here, we are dealing with a situation where a state is occupied by very many particles and these are composed of electrons. The reason, simply put, is that Cooper pairs obey Bose-Einstein statistics.

1.22. Behaviour of superconductors in a magnetic field[19,20,21]

The effect of a magnetic field is not the same for all types of superconductors and by

studying this in more detail we can expand on a number of important parameters, which categorise superconductors.

Neglecting demagnetisation effects, if a superconductor is placed in a magnetic field up to a critical value H_c, figure 1.3, it generates a screening current and associated magnetic field that completely counters the external applied magnetic field. The magnetic flux, B, is thus zero inside a superconductor and the material is a perfect diamagnet.

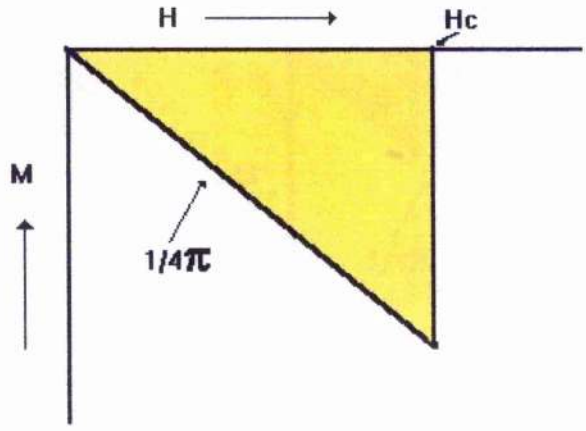

Figure 1.3. Magnetisation curve for a superconductor up to H_c.

However, if the magnetic field were to drop discontinuously to zero at the surface of the superconductor then the surface current would have to rise to an infinite value, which is impractical. Thus, the magnetic field must penetrate somewhat into the surface of the material. F. and H. London developed equations which relate the penetration depth to pair density:

$$\lambda = \sqrt{m_e / 2\mu_0 c^2 n_p} \qquad (1.5)$$

Where m_e is the mass of the electron, μ_0 is the permeability of free space and n_p is the superconducting pair density. The pair density is a function of temperature, increasing from zero at the superconducting transition temperature to ideally, encompass all the electrons at 0K.

For the type of superconductor shown in figure 1.3 increasing the field above the critical field H_c leads to the destruction of superconductivity, re-entry of magnetic flux into the sample and a return to the normal state. This transition is reversible and lowering the field below H_c leads to a return of superconductivity. Superconductors, that display this type of behaviour are described as Type 1 or soft superconductors. They usually are single elements e.g. Pb, and are not suited for industrial applications.
In type 1 superconductors, λ is small compared to ξ (the range within which electrons can interact to form Cooper pairs), thus $\mathbf{k \ll 1}$.

If, however, λ is large compared to ξ, then different sort behaviour in a magnetic field occurs, figure 1.4. This type of superconductor is known as a Type II or hard superconductor.

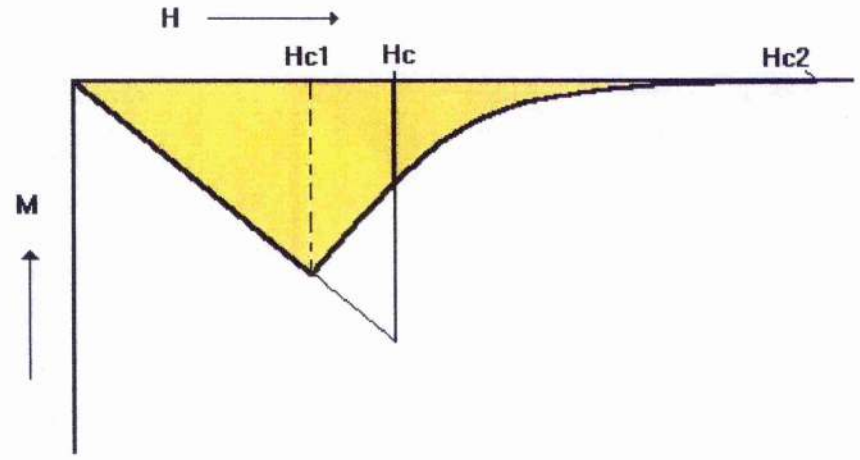

Figure 1.4. Magnetisation curve for a Type II superconductor.

Up to the point H_{c1} the superconductor is a perfect diamagnet, just as for type I materials. However, above H_{c1} magnetic flux penetrates the sample and the magnetisation of the sample decreases until all superconductivity has been abolished at the point H_{c2}. Known as the mixed or 'vortex' state, the region between H_{c1} and H_{c2} is described ideally in figure 1.5.

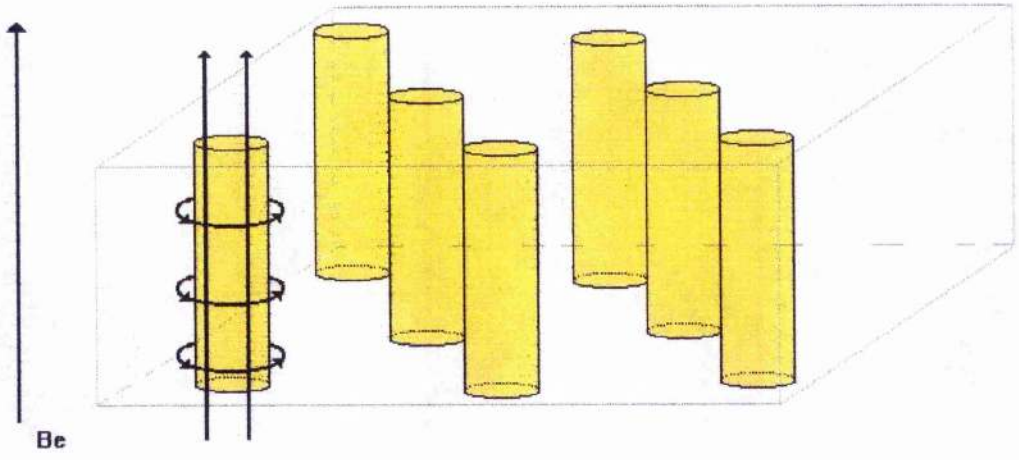

Figure 1.5. Representation of the mixed phase. Magnetic field and supercurrent shown for one tube.

It consists of tiny vortices, typically in a hexagonal lattice, of supercurrent in the form of Cooper pairs, circulating around regions of magnetic flux. The current density and the number of Cooper pairs decreases towards the centre of each vortex, where the material is in the normal state. The ideal pattern is disrupted by lattice imperfections and grain boundaries.

Type II superconductors e.g. Nb_3Ge, are used in many industrial applications. However, not all type II superconductors are suitable for industrial use, and it is only by careful manufacturing conditions or chemical modification of material that the required properties may be developed. For example, in figure 1.5, the supercurrent and magnetic field interaction in a flux tube leads to the generation of the Lorentz force, which acts perpendicular to B_e and the current. This leads to the movement of the tube and a dissipation of energy. The flux tubes may be fixed (pinned) to alleviate this problem.

1.3. High T_c superconductivity[22,23,24,25].

The discovery of HTS superconductivity in doped lanthanum cuprate certainly created a large number of problems for experimentalists and theorists alike. Before 1987 it was believed that superconductivity was the select domain of low-temperature physics.

These cuprates contain layers of copper oxide sandwiched between insulating oxide layers that donate the charged carriers into the conducting planes. Even in their normal metallic state these materials are unusual. Usually their resistances are almost linear functions of temperature up to 600K; they are exceptionally anisotropic conductors; and a small reduction in the density of carriers in the copper oxide layers converts them to magnetically ordered insulators. Even after ten years, there is no consensus on the mechanism of cuprate superconductivity. Indeed, there is heated debate on whether or not electron pairs with s-wave or d-wave symmetry are favoured. It is beyond the scope of this review to discuss proposed theories; however, it is clear that this is a particularly 'grey area' where experimental results are not convincing and indeed are open to very loose interpretation. On the other hand, the cuprate systems have generated challenging problems to condensed matter scientists that may well lead to a reappraisal of the way we approach the behaviour of systems on the microscopic and macroscopic level.

1.31. Properties of HTS materials.

Such large onset temperatures immediately cast doubt on the applicability of the conventional superconductor BCS theory to these cuprate materials. In table 1-1 some of the properties which these materials share with standard BCS superconductors and following that, table 1-2, some observations which are not seen for BCS materials. This list should not be taken by any means as complete.

In the superconducting state, the electrons are paired. Several different experiments showed that in the superconducting state, the fundamental charge is 2e.
Photoemmision spectroscopy, electron tunneling and other experiments indicate an energy gap in the superconducting state. The energy gap is probably anisotropic and lies in the range $3.5k_BT_c$-$8\ k_BT_c$, larger than the isotropic BCS value of $3.54k_BT_c$.
Several experiments suggest pairing into a singlet-spin state and a s-wave orbital angular momentum state, as predicted by BCS.
HTS materials display many familiar superconducting properties, such as Josephson tunneling and vortex structure found in any type II superconductor

Table 1-1. Properties of HTS superconductors shared with conventional BCS superconductors.

Extremely high value of T_c.
Linear dc resistivity in the normal state.
Unusual behaviour of the nuclear relaxation rate below T_c.
Close proximity of antiferromagnetic phases.
Extremely small coherence lengths.
Large penetration depths.
Large spatial anisotropy.
Zero isotope effect, not reduced as seen in some BCS superconductors.

Table 1-2. Properties of HTS superconductors not seen for conventional superconductors.

1.32. Control of superconducting properties.

The properties of high temperature superconductors tend to be highly dependent on carrier concentration, which may be controlled by chemical doping. There are two principal methods of doping high temperature superconductors, oxygen non-stoichiometry and aliovalent substitution. Note these two methods can operate in tandem. Good examples of these mechanisms are in $YBa_2Cu_3O_{7-x}$ and La_2CuO_4 respectively.

In $YBa_2Cu_3O_{7-x}$ (YBCO) carrier concentration is predominantly controlled by oxygen non-stoichiometry. The doping mechanism is a redox process involving uptake of

atmospheric oxygen into the lattice with removal of electrons from the electron energy bands creating holes (1.6 and 1.7):

$$2Cu^{2+} + \tfrac{1}{2}O_2 \rightarrow 2Cu^{3+} + O^{2-} \qquad (1.6)$$

$$Cu^{3+} \rightarrow Cu^{2+} + h^{+} \qquad (1.7)$$

It is usual to consider doping in terms of nominal Cu valence; however, no assumption that hole carriers reside on Cu is implied. In YBCO the critical temperature is found to decrease smoothly as the oxygen content is decreased for stoichiometries prepared at high temperatures and quenched. In samples prepared at lower temperatures or slow cooled, plateaux behaviour is observed, figure 1.6. This behaviour which is commonly encountered is associated with oxygen ordering on the basal YBCO plane, and shows clearly how important it is to control oxygen stoichiometry in some samples.

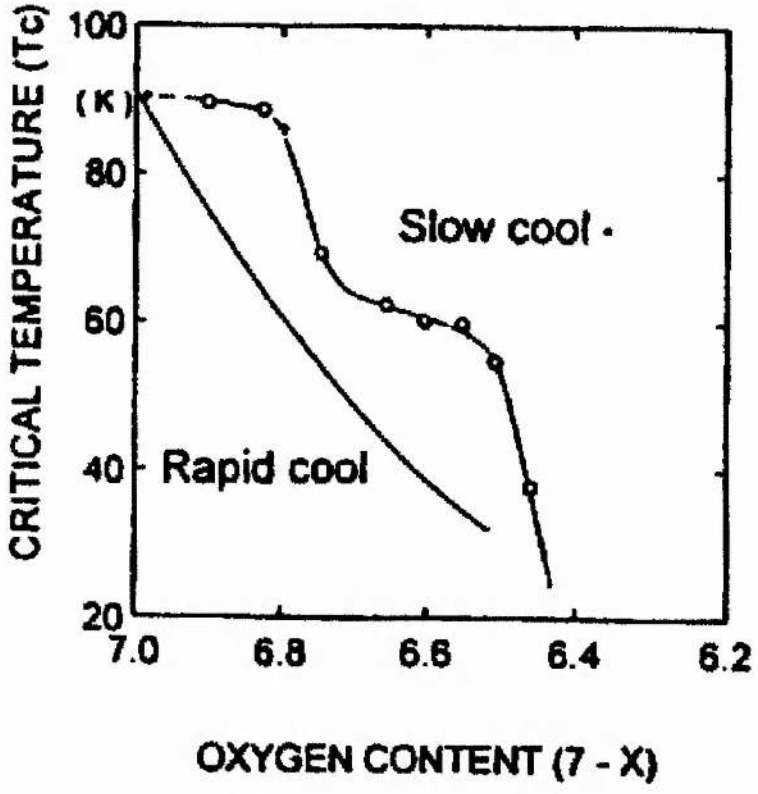

Figure 1.6. Relationship between T_c and oxygen stoichiometry in $YBa_2Cu_3O_{7-x}$.
(Taken from Thomspson[25])

In La_2CuO_4 oxygen non-stoichiometry is generally less important than aliovalent substitution. Here doping entails the replacement of La^{3+} by Sr^{2+} with the creation of an

electron hole. In this system the oxygen stoichiometry remains, more or less, constant, thus the number of holes is proportional to the extent of substitution. Figure 1.7 shows the effect of doping La_2CuO_4 with Sr. On increasing hole concentration, La_2CuO_4 transforms from an antiferromagnetic insulator to a metal at high temperatures. At lower temperatures the transition is from an antiferromagnetic insulator to a spin glass to a superconductor to a metal.

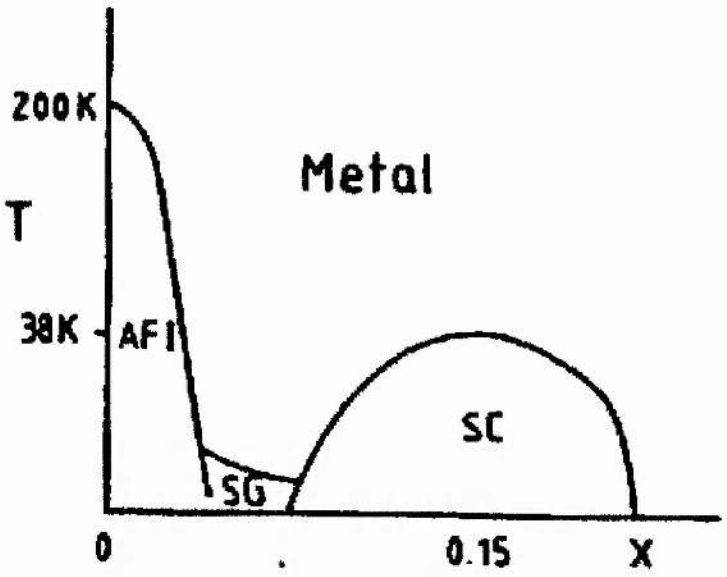

Figure 1.7. Phase diagram of $La_{2-x}Sr_xCuO_4$ (AFI = Antiferromagnetic insulator, SG = spin glass and SC = superconductor). (From Thomspson[25])

Aliovalent substitution with a cation of lower charge does not always lead to increased carrier concentration since sometimes charge neutrality is maintained by loss of oxygen. In Nd_2CuO_4, n-type doping is achieved by replacement of Nd^{3+} with an ion of higher charge. Since no significant additional oxygen is taken into the structure, the charge is neutralised by electron creation. In all systems, the superconducting onset temperature almost invariably shows a maximum at a particular level of doping.

1.4 Structural properties of cuprate superconductors[25,26,27,28].

The ideal perovskite structure upon which the cuprates are based has the general formula ABX_3. The perovskite structure has a cubic cell in which the A cations (larger and in blue in figure 1.8) lie at the centre of each cube. The structure therefore comprises a three dimensional network in which the A cations have AX_{12} dodecahedral co-ordination and the B cations (not shown but in the centre of the octahedra) have a BX_6 octahedral co-ordination.

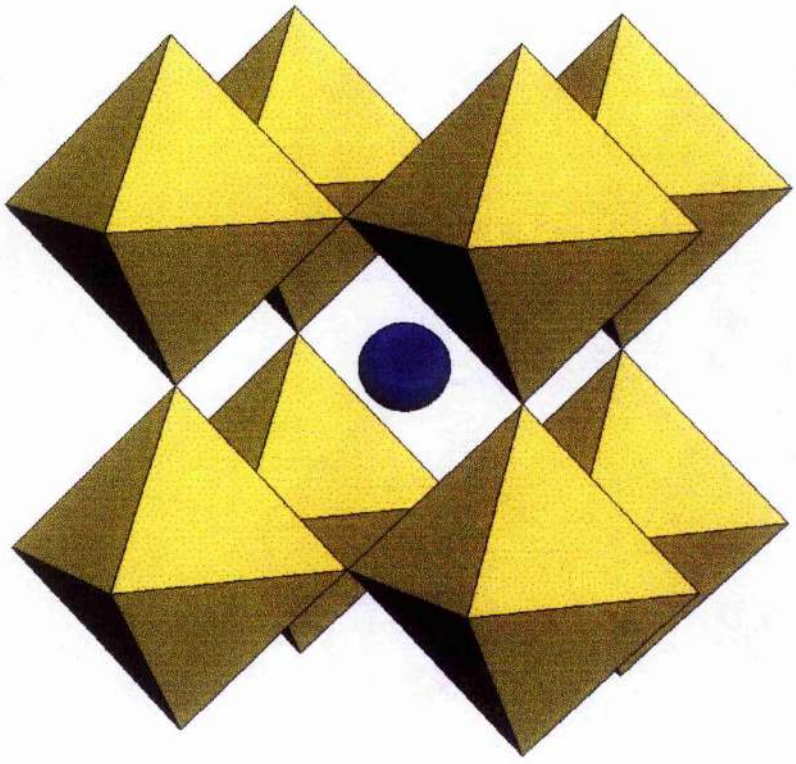

Figure 1.8. Ideal perovskite structure ABX_3.

A variety of perovskites or perovskite related structures are produced when the atoms at the A, B and X sites are changed. A or B sites can be filled with two or more different cations e.g. Ca_2CaUO_6 ($A_2BB'O_6$) or $CaCu_3Mn_4O_{12}$ ($AA'_3B_4O_{12}$). The octahedral centres can be filled not only by two different elements but also by differently charged ions of the same element, e.g. $Ba_2Bi^{3+}Bi^{5+}O_6$. Partial substitution at the A/B sites leads to mixed valence perovskites e.g. $BaPb_xBi_{1-x}O_3$ ($BA_xA'_{1-x}O_3$). Variation in oxygen stoichiometry is one of the most important parameters in determining the

physical properties of perovskite type metal oxides e.g. $YBa_2Cu_3O_{7-x}$. Ideal perovskite structures are isotropic in their electrical properties. However, many are somewhat distorted with tilted octahedra, which lower the symmetry, potentially altering the electrical and other physical properties. Thus, the electrical properties vary from insulating ($SrTiO_3$) to semiconducting ($BaBiO_3$).

In cuprate systems the phenomenon is only seen in structures which can be described as oxygen deficient perovskites or perovskite intergrowths. The key structural feature in all these systems is the presence of a CuO_2 plane or a series of CuO_2 planes. The co-ordination environment of Cu in these planes can be octahedral, square pyramidal or square. $YBa_2Cu_2O_{7-x}$, often described as an oxygen deficient perovskite. The structure of $YBa_2Cu_2O_{7-x}$ can simply be simply derived from that of a triple perovskite unit, $3ABX_3$, by removing all of the oxygens from the yttrium plane and all of the O(5) oxygens from the basal CuO_2 plane. See figure 1.9.

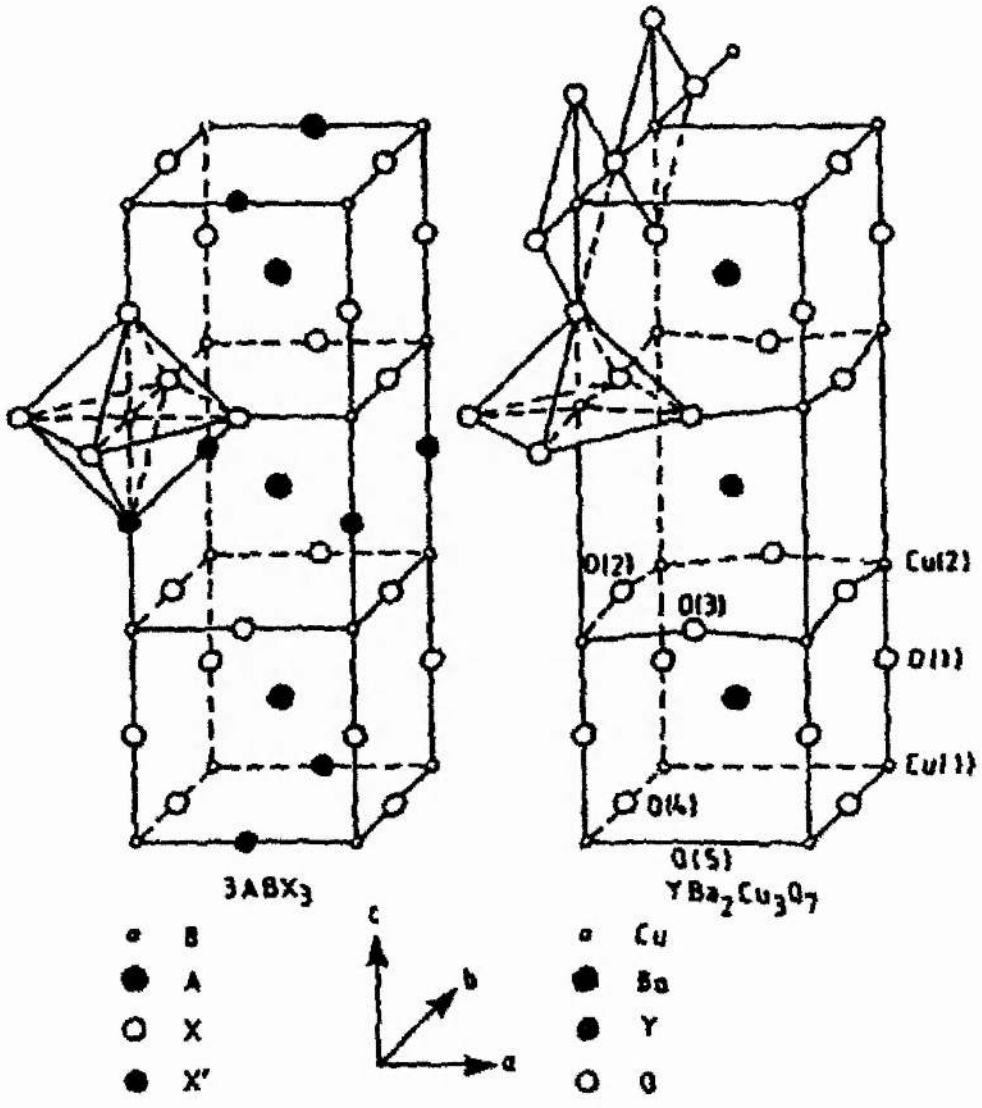

Figure 1.9. Relationships between the $YBa_2Cu_3O_7$ and triple perovskite (ABX_3) unit cells.
(From Thomspson[25])

The vast majority of HTS cuprates may be regarded as intergrowth phases between perovskite and rocksalt/fluorite blocks. The most important of these are the Ruddlesden-Popper phases of formula $(AO)_m[ABO_3]_n$, which are rocksalt perovskite intergrowths. La_2CuO_4, $(Nd,Ce)_2CuO_4$ and $(Nd,Ce,Sr)_2CuO_4$ are good examples shown in figures 1.10 and 1.11(a,b) respectively.

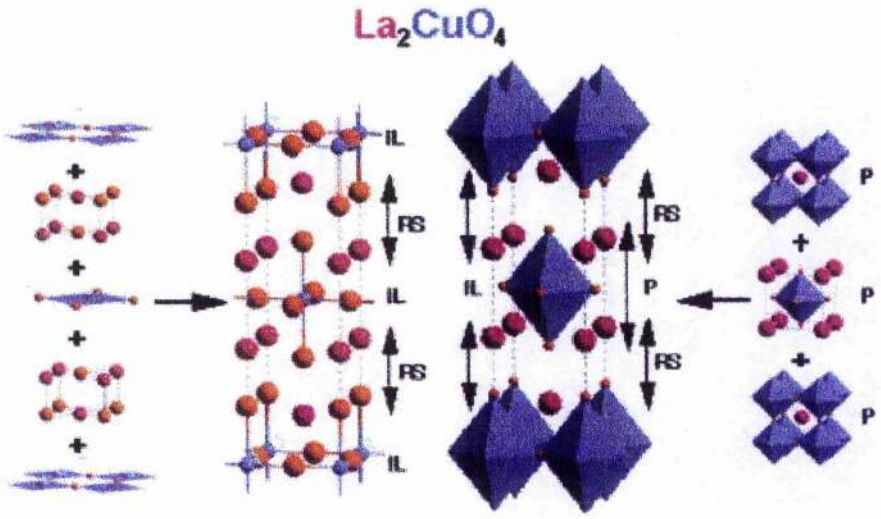

Figure 1.10. La_2CuO_4 structure. (From Park[29])

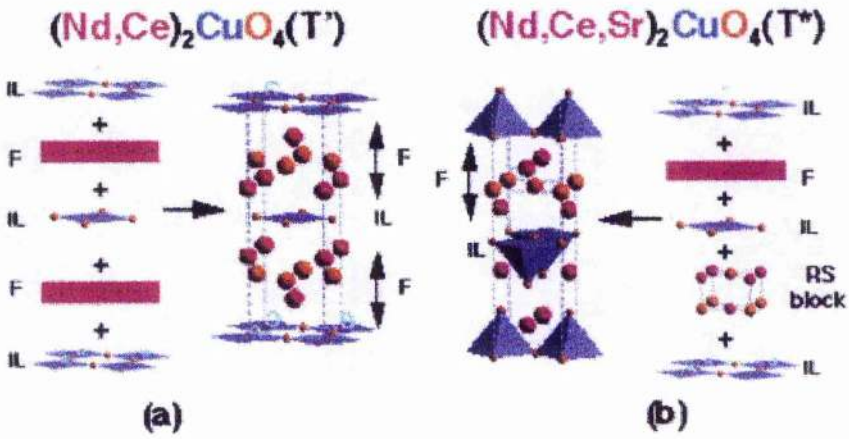

Figure 1.11(a,b). $(Nd,Ce)_2CuO_4$ and $(Nd,Ce,Sr)_2CuO_4$. (From Park[29])

The most important of the Ruddlesden-Popper phases are those based on single or double TlO, PbO, BiO and HgO rocksalt layers. These belong to two ideal structural families: 12[n-1][n] e.g. $TlBa_2CaCu_2O_{7.0}$ is 1212 where n = 2 and 22[n-1][n] e.g. $Bi_2Sr_2CaCu_2O_8$ is 2212 where n = 2. These series contain the highest T_c's discovered to date including $Bi_2Sr_2Ca_2Cu_3O_{10}$ (T_c=110K); $Tl_2Ba_2Ca_2Cu_3O_{10}$ (T_c=128K); and $HgBa_2Ca_2Cu_3O_8$ (T_c=135K).

Of course these compositions are represented with ideal stoichiometries, but in reality this is never the case in such systems. There is cation intersite substitution and oxygen non-stoichiometry and additional structural deviations arise from supercell modulations, particularly in Bi based systems where the Bi has a lone pair.

1.5 Commercial Applications of High T_c materials[30,31,32,33].

When high-temperature superconductivity reached temperatures above that of liquid nitrogen more than ten years ago, many very enthusiastic people talked of magnetically levitated trains, computers and motors all soon to be operating above 77K. However, when reality set in the field settled into a large active one, but with only the simplest of products being proposed for the following few years.

Now after many years of hard work, outstanding progress is being reported in thin film technology and electronics using HTS superconductors. Some products are already on the market and others imminent. The first HTS products to be sold in quantity were sensors for magnetometers. Now work is going well on sensors for NMR spectrometry, cellular-phone base stations and military systems.

These small beginnings should not be seen as some fad, since some predict that HTS materials could reach a market of $75-$100 billion by 2020, hardly an insignificant amount. Apart from commercial funding, governments have been active with research investment, the US government funding is geared towards smaller commercial uses while Japan is more geared towards bulk applications and power related products. For instance the US ARPA program has spent more than $250 million on developing several promising applications: RF and microwave passive components and subsystems for radar, electronic warfare, wireless communications and medical instrumentation, a conductor for power applications and interconnects for multichip modules. The following two sections deal with small scale commercial and larger scale power application of HTS superconductors, and should not be considered as being comprehensive, instead the most important applications for development and the HTS materials seen as having the best properties for use are discussed.

1.51. Small scale commercial applications.

YBCO is the workhorse material used in the fabrication of thin films. Using a bicrystal technique it is possible to control the production of grain boundaries, which of course act as weak links and reduce the supercurrent. Other materials successfully used for thin films are Tl-Ba-Ca-Cu-O and Tl-Pb-Sr-Ca-Cu-O. SQUIDs are ideal for making sensitive magnetic field measurements, and the HTS versions are showing promise for geophysics, magnetocardiology and non-destructive testing. Certainly research in this area has advanced particularly in overcoming "noise" which was a major problem. In terms of military applications SQUIDS were only really used for submarine detection; however, now they are being used in many areas including seeking of unexploded ordnance or mines. HTS SQUIDs can also be used for non-destructive testing e.g. to detect and quantify hidden cracks and corrosion in ageing commercial or military aircraft, or to test nuclear reactor vessels.

Because every large geographic region has two cellular phone providers, with interleaving frequency allocations, a filter must ensure that signals from one provider do not leak into the other's band. HTS filters have been shown to be less noisy than copper, even when copper is run at 77K. The main materials being used are YBCO and Tl-Ba-Ca-Cu-O (TBCCO) thin films. It is not just the superconductors that are complex; the existing cryogenic commercial cryogenic refrigeration systems were too unreliable and expensive. These new HTS filter units are currently 10 times smaller than existing units and this certainly is advantageous. In the future the hope is to design HTS filters for transmitting as well as receiving. With the growth of cellular communications, this market has great potential.

Magnetic resonance systems can be improved by replacing the copper RF detection coil with a HTS coil when the sample size is small or the magnetic field is low. The HTS coil offers a great increase in signal-noise ratio. Already two companies have developed low-noise receivers to replace the copper antennae in low field magnetic resonance imaging (MRI) devices. In most standard MRI devices, which have relatively high fields, the noise from the body limits the resolution. If one works in a low field or uses a

small MRI device to examine elbows, knees and fingers, the noise is limited by the sensor itself.

Many people have asked, "when will HTS materials be used for high-speed communications or computers?" A key requirement for these technologies is the ability to fabricate multilayer thin films to interconnect individual devices. It is more difficult, but such devices have been made using YBCO. Before the discovery of HTS superconductors some firms had R&D efforts to build a Josephson junction computer. Projects were cancelled because silicon technology was advancing at such a rapid rate. There is some research using HTS devices, but it would seem that considerable R&D is necessary to make reproducible, reliable Josephson devices especially as the number of junctions is increased beyond the pair needed say for a SQUID.

1.52. Power applications.

Japan is putting much more money into bulk applications than the US and its annual budget for bulk material on power related projects is estimated to be about $100 million. In addition Japan is using HTS materials in its R&D on magnetically levitated trains and flywheels.

Presently HTS materials research is concentrating on optimising materials for applications through processing. Currently, bulk applications primarily use Bi-Sr-Ca-Cu-O (BSCCO) as 2223 and 2212. The other leading HTS material is YBCO. Two major factors influence the amount of current density, J_c, which can be transported. The most important is that if the material is polycrystalline it tends to subdivide into regions of strong superconductivity separated by weak superconducting interfaces, known as weak links. The principal way of avoiding weak links is to align the grains so that grain boundaries are at low angle with respect to the Cu-O planes. One can improve the J_c characteristics of individual grain boundaries or align the "texture" of the grains to improve the links in the current path. The J_c for both BSCCO and YBCO is strongly correlated with the distribution of grain boundary misorientations. The second major factor influencing the current density is the need to develop strong flux pinning so that vortices can resist the Lorentz force that dissipates energy and causes current losses.

YBCO has better intrinsic flux pinning than BSCCO, but it has poor intergranular current flow because of weak links. Despite its inadequate flux pinning, BSCCO has been preferred for making wire because the grains align and form good grain boundaries for conduction when they are drawn, rolled into a tape shape and then fired. Tl-Ba-Ca-Cu-O TBCCO in 2223 and 1223 varieties have also shown promise for wire applications. Its properties fall between that of YBCO and BSCCO. It has links that are stronger than YBCO but its flux pinning is poorer.

For almost all of the important electric power applications, a J_c of at least 10^4 $A.cm^{-2}$ is needed. The most popular materials used in wire making are the BSCCO's and it is good grain alignment that is crucial. It is now possible using BSCCO materials to manufacture cables and coils with lengths of 100-1000 metres with a J_c above 10^4 $A.cm^{-2}$ at 77K. Much of the work involves Bi2223, although Bi2212 is easier to fabricate and has a better J_c in high magnetic fields and low temperature (<20K) it cannot be used at 77K. At 4K though 2212 is superior because it is less prone to weak links. For operation at liquid nitrogen temperature, YBCO is preferable because it retains J_c under strong magnetic fields either as an epitaxial film or a single crystal. YBCO retains high critical currents in strong fields because there is stronger coupling between its Cu-O planes than in BSCCO. YBCO lacks the micaceous layer of BSCCO, which has prevented attempts to use the powder-in-tube processing to make wire.

Projects to build prototype power transmission cables are under way. Because of the excellent performance of BSCCO conductors, electricity companies in the US, Japan and Europe are evaluating their capability to retrofit existing underground cable. At present, high performance underground cable consists of copper conductor cooled by oil. It would be replaced by BSCCO cooled by liquid nitrogen. Certainly there has been interest in fabricating coils, motors and generators with HTS components. It would appear so far that exchanging conventional low Tc materials with HTS materials basically modifies most devices. In the field of transformers and magnets in some ways the research work with HTS materials is not nearly ready to compete with the low T_c materials such as Nb_3Sn, but HTS materials are being developed for a number of other applications such as magnetic bearings used on large flywheels, fault-current limiters and current leads in advanced MRI equipment.

1.6. Bibliography and references for chapter 1.

[1] J.G. Bednorz and K.A. Müller, *Z. Phys. B*, 1986, **64**, 189.

[2] H.K. Onnes, *Comm. Leiden*, 1911, **120b.**

[3] J. Bardeen, L.N. Cooper and J.R. Schrieffer, *Phys. Rev.*, **108**, 1175.

[4] L.R. Testardi, J.H. Wernick and W.A. Royer, *Solid State Commun.*, 1974, **15**, 1.

[5] R.A. Ogg, *Phys. Rev.*, 1946, **69**, 243.

[6] R.A. Ogg, *Phys. Rev.*, 1946, **70**, 93.

[7] W.A. Little, *Phys. Rev.*, 1964, **134A**, 403.

[8] M.K. Wu, J.R. Ashburn, C.J. Torng, P.H. Hor, R.L. Meng, L. Gao, Z.J. Huang, Y.Q. Wang and C.W. Chu, *Phys. Rev. Lett.*, 1987, **58**, 908.

[9] A. Schilling, M. Cantoni, J.D. Guo, H.R. Ott, *Nature*, 1993, **363**, 56.

[10] F.B. Silsbee, *J. Wash. Acad. Sci.*, 1916, **6**, 597.

[11] W. Meissner and R. Ochsenfeld, *Naturwissensch*, 1933, **21**, 787.

[12] F. London and H. London, *Z. Phys.*, 1935, **96**, 359.

[13] E. Maxwell, *Phys. Rev.*, 1950, **78, 477.**

[14] C.A. Reynolds, B. Serin, W.H. Wright and L.B. Nesbitt, *Phys. Rev.*, 1950, **78**, 487.

[15] H. Fröhlich, *Phys. Rev.*, 1950, **79**, 845.

[16] J. Bardeen, *Phys. Rev.*, 1950, **80**, 567.

[17] A.B. Pippard, *Proc. R. Soc. London*, 1953, **216**, 547.

[18] V.L. Ginzburg and L.D. Landau, *Zh. Eksperim. I. Teor. Fiz.*, 1950, **20**, 1064.

[19] W. Buckel, *Super-conductivity:fundamentals and applications*, Weinheim, VCH, 1991.

[20] B.I. Bleaney and B. Bleaney, *Electricity and magnetism*, London, Oxford University Press, 1976.

[21] L. Smart and E. Moore, *Solid state chemistry:an introduction*, London, Chapman & Hall, 1992.

[22] P. Coleman, *Physics World*, 1995, **8**, 29.

[23] G. Burns, *High-temperature superconductivity*, New York, Academic Press, 1992.

[24] B. Batlogg, Phys. Today, 1991, **44**, 44.

[25] D. Thompson (ed.), *Insights into speciality inorganic chemicals*, Cambridge, The Royal Society of Chemistry, 1995.

[26] D.P. Tunstall and W. Barford (ed.), *High temperature superconductivity*, Bristol, Institute of Physics, 1992.

[27] T.A. Vanderah (ed.), *Chemistry of high temperature superconductors*, New Jersey, Noyes Publications, 1991.

[28] A.R. West, *Solid state chemistry and its applications*, Chichester, John Wiley and Sons, 1984.

[29] C.Park and R.L. Snyder, *J. Am. Cer. Soc.*, 1995, **78**, 3171.

[30] P.P. Edwards and C.N.R. Rao, *Chemistry in Britain*, 1994, **30**, 722.

[31] G.B. Lubkin, *Physics Today*, 1995, **48**, 20.

[32] G.B. Lubkin, *Physics Today*, 1996, **59**, 48.

[33] J. Brown, *Microwaves & RF*, 1996, **35**, 33.

Chapter 2. Pb:1212 CUPRATES RESEARCH

2.1. Literature review

This literature review covers the most important research papers published concerning (Pb,M)Sr_2(Y,Ca)Cu_2O_y Pb:1212 cuprates. Section 2.11 focuses solely on the development of the PbCu:1212 system from its discovery in 1989 up to the starting point of this study. The aims are to highlight the key results that describe the phase, and also show the problems in controlling phase stability and oxygen stoichiometry during synthesis and annealing. Section 2.12 covers the same time span, but describes other Pb:1212 based systems e.g. PbTl:1212 or PbSr:1212. In some cases these phases show better phase stability and superconducting properties than PbCu:1212, however, there are also results that contradict one another in addition to problems controlling phase stability and oxygen stoichiometry during synthesis and annealing.

2.11. The PbCu:1212 system 1989-1994

Subramanian and co-workers initially reported[1] the presence of an impurity among a $Pb_2Sr_2(Y,Ca)_1Cu_3O_{8+y}$ sample composition, which could be approximated at $(Y,Ca)Sr_2(Cu,Pb)_3O_{7-y}$. Further analyses showed the material to be non-superconducting and having the formula $(Pb_{0.7}Cu_{0.3})Sr_2(Y_{0.85}Ca_{0.15})Cu_2O_{6.8}$, corresponding to a tetragonal cell ($\underline{a} \approx 3.8$Å and $\underline{c} \approx 11.8$Å) with the P 4/mmm space group. Lee et al[2] around the same time independently reported that another non-superconducting compositional variant of this material $(Pb_{0.7}Cu_{0.3})Sr_2(Y_{0.73}Ca_{0.27})Cu_2O_7$ had lattice constants which were nearly identical to those reported[3] for $(Tl,Bi)Sr_2CaCu_2O_y$ (1212). The XRD analyses on single crystals from the two groups showed that the material possessed a layered structure consisting of (Pb,Cu)O, SrO, CuO, (Y,Ca) layers and could be classified as PbCu:1212 structure with the simple structure shown in figure 2.1.

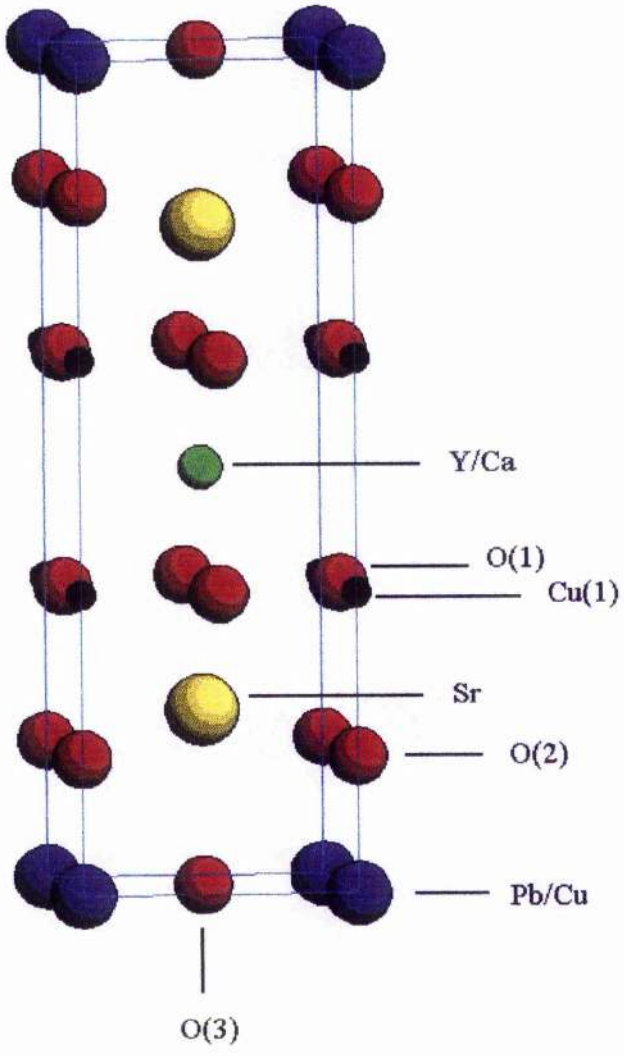

Figure 2.1. The 1212 structure represented in ideal form.

The interesting features emerging from the crystal structure analysis were that the Cu(2) was displaced from the (0,0,0) site and the O(3) atom also displaced from its ideal (½,½,0) site, seen also in $TlSr_2CuO_5$[4]. Thus, the idealised Pb-O(3) bond length of 2.7Å was shortened by these displacements. Lee also noted that there was a reversible oxygen loss when heating to and cooling from 800°C, this weight being small and corresponding to about 0.1 of an oxygen atom.

Ono and Uchida[5] provided the first major breakthrough in this system when they achieved a T_c = 17K in $(Pb_{0.65}Cu_{0.35})Sr_2(Y_{0.7}Ca_{0.3})Cu_2O_y$. This was achieved by annealing the product material at 860°C and quenching into liquid nitrogen. Another

portion of the sample annealed at 400°C showed no sign of superconductivity.

Koriyama et al[6] failed to induce superconductivity in $(Pb_{0.5}Cu_{0.5})Sr_2(Y_{1-x}Ca_x)Cu_2O_y$ samples (x = 0, 0.25) when cooling from 1000°C at 50°C.h^{-1}, although the replacement of some Sr for Ba produced superconductivity in the aforementioned samples.

Maeda et al[7] produced a series of samples in a flowing O_2 environment with composition $(Pb_{[1+x]/2}Cu_{[1-x]/2})Sr_2(Y_{1-x}Ca_x)Cu_2O_y$, where x = 0-0.4 and y ≈ 7. They found that superconductivity could be induced in quenched samples where x > 0.2 and was highest at 52K in the x = 0.4 sample, while no superconductivity could be seen in the equivalent samples which were slowly cooled. Also worth noting was the appearance of an impurity for samples where x > 0.35. Since the 1212 phase is formed in an oxidising atmosphere, the Pb and Cu atoms in the (Pb,Cu)O layers were thought to be in the 4+ and 2+ states respectively. This appeared reasonable since the ionic radii of Pb^{2+} and Pb^{4+} for the co-ordination number of 6 are 1.18Å and 0.775Å, and that of Cu^{2+} is 0.73Å. This presented a problem to the authors since they produced samples in which the increase in effective hole concentration upon increase of the Y/Ca ratio was completely offset by the removal of holes as the Pb^{4+}/Cu^{2+} ratio was increased, while the T_c increased. Therefore, they could not account for the increasing T_c when Ca^{2+} was substituting for Y^{3+} in terms of hole doping or really show that partial reduction of Pb^{4+} to Pb^{2+} was occurring. Figure 2.2 shows the effect of Ca content on the lattice parameters for superconducting (quenched) and non-superconducting (as sintered) samples.

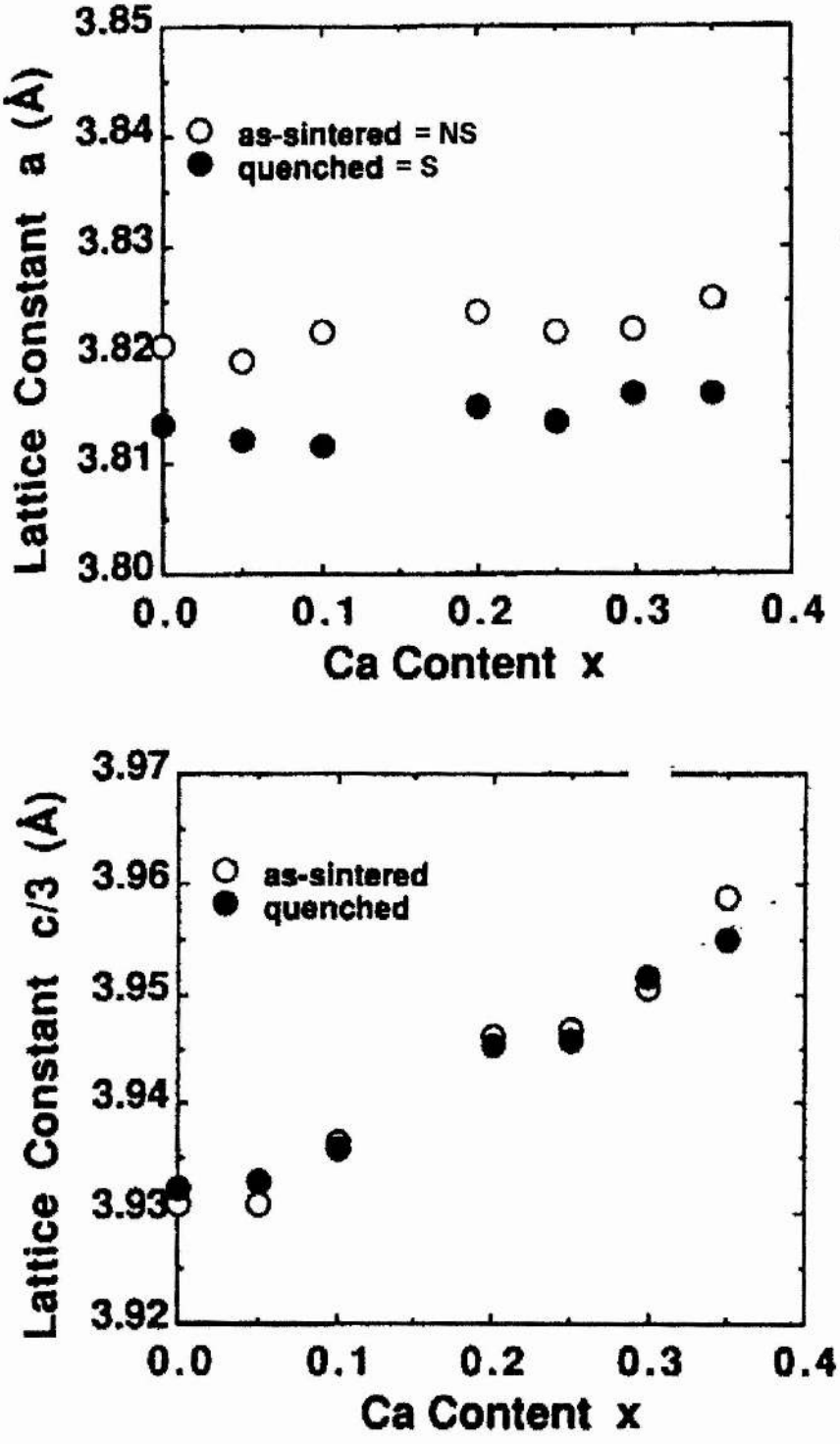

Figure 2.2. Variation in lattice parameters in superconducting (S) and non-superconducting (NS) samples. (From Maeda[7]).

The **a** lattice parameter barely changes upon increasing Ca content in either quenched or "as sintered" samples. The **c** lattice parameter increases since Ca^{2+} is larger than Y^{3+} and there is no difference between the quenched and "as sintered" samples.

Tang et al[8] then achieved superconducting onset temperature of 67K in $(Pb_{0.5}Cu_{0.5})Sr_2(Y_{0.5}Ca_{0.5})Cu_2O_y$, where the oxygen content had been adjusted by high oxygen pressure annealing (150 bar at 940°C) coupled to rapid cooling of samples. TGA analyses in samples cooled at different rates showed that there was a loss of oxygen in stages from the samples, which controlled the appearance of superconductivity, figure 2.3.

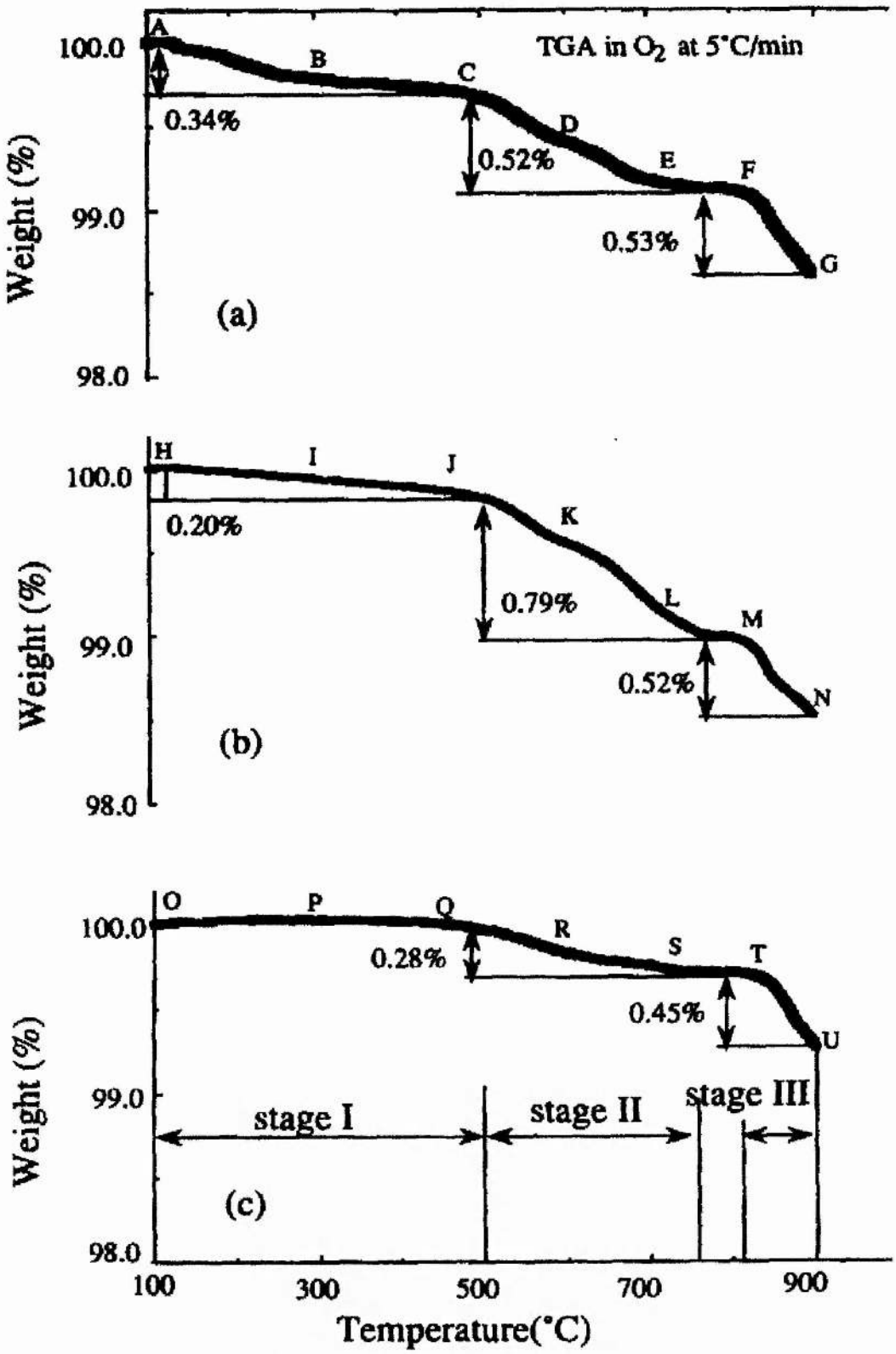

Figures 2.3(a-c). TGA plots in samples annealed at 940°C and 150 bar and subject to different cooling conditions. Figure 2.3a, cooled $1°.min^{-1}$ to 500°C $T_c < 10$ K. Figure 2.3b, cooled $10°.min^{-1}$ to 600°C $T_c = 10$ K. Figure 2.3c, cooled $50°.min^{-1}$ to 500°C $T_c = 67$ K. (From Tang[8])

The results show that the non-superconducting samples contained excess oxygen at some "unknown" site in the structure that killed superconductivity, thus it was necessary to remove this oxygen and quench to prevent its return. Worth noting is that the removal of too much oxygen, stage III, affected superconductivity. The oxidation state of the Pb in the (Pb,Cu)O layers was determined to be 4+ from Electron Spectroscopy (ESCA) measurements The authors noted impurities when the Ca content, $x \geq 0.5$ suggesting that Ca was reaching its limit of solubility.

On the subject of oxygen pressure, Maignan and co-workers[9] annealed samples of nominal composition $(Pb_{0.7}Cu_{0.3})Sr_2(Y_{0.5}Ca_{0.5})Cu_2O_y$ at 400°C for 10 hours under different oxygen pressures, figure 2.4. When annealed at this temperature at atmospheric pressure, no superconductivity existed, however, under oxygen pressures from 10-80 bar superconductivity is induced and the best signals are achieved at 30 and 50 bar before dropping off again at higher pressures.

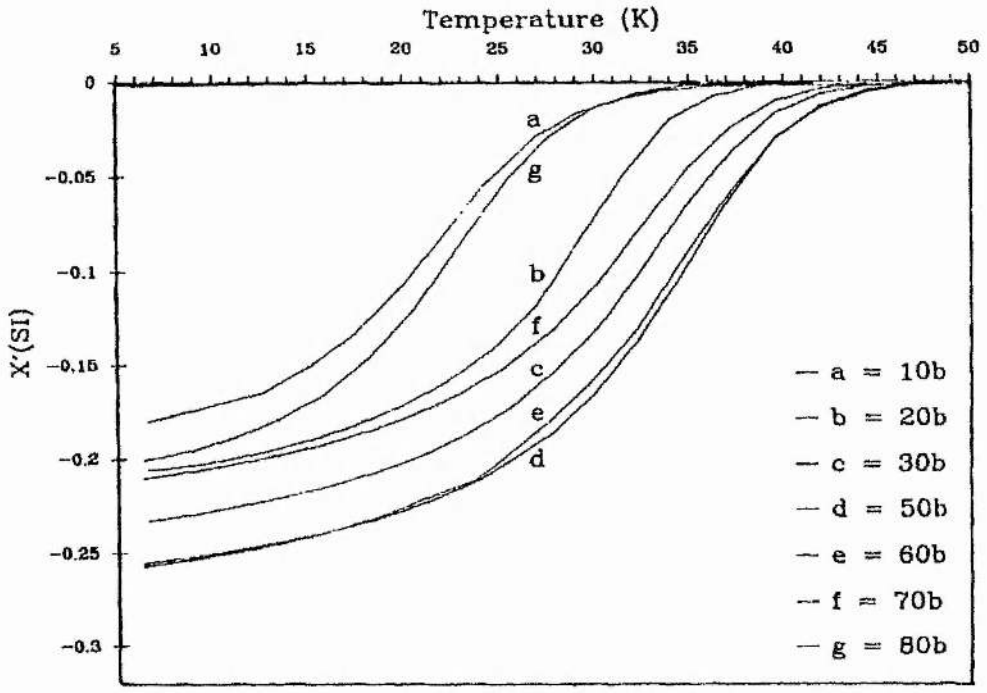

Figure 2.4. Superconductivity in $(Pb_{0.7}Cu_{0.3})Sr_2(Y_{0.5}Ca_{0.5})Cu_2O_y$.as a function of annealing pressure.
(From Maignan[9])

Adachi et al[10] investigated the effect that the annealing and quenching stage had on superconductivity and noticed that the annealing temperature is critical, figure 2.5.

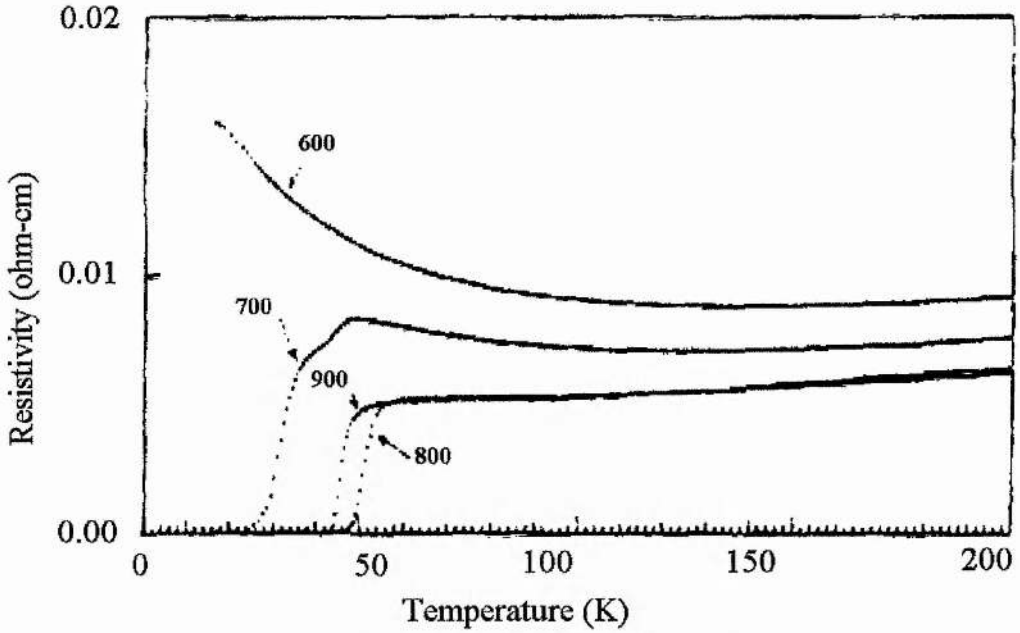

Figure 2.5. Temperature dependence of annealing stage in x = 0.5 sample. (From Adachi[10])

The above arises because the excess oxygen which destroys superconductivity is being removed to give the best results at 800°C. However, too much oxygen is being removed at 900°C which in turn affects the T_c but not as drastically as seen below 800°C. The authors tried synthesising samples of composition $(Pb_{0.75}Cu_{0.25})Sr_2(Y_{1-x}Ca_x)Cu_2O_y$, x = 0.4-0.7 and found that the samples for $x \geq 0.5$ were not single phase. Using the same annealing conditions described above, the sample with x = 0.5 gave the highest T_c but samples with $x > 0.5$ gave no superconductivity. The problem, however, may have been that the annealing temperature needed altering.

Maeda et al[11] performed a neutron powder diffraction analysis on superconducting (S) and non-superconducting (N) portions of a sample, these having the formulas $(Pb_{0.65}Cu_{0.35})Sr_2(Y_{0.7}Ca_{0.3})Cu_2O_{7.0}$ and $(Pb_{0.65}Cu_{0.35})Sr_2(Y_{0.7}Ca_{0.3})Cu_2O_{7.1}$ respectively. The key results are summarised in tables 2-1 and 2-2, and effects shown more clearly in figure 2.6.

Atom	Site	x	y	z	g-occupancy
M(Pb/Cu(1)	41	0.0605	0	0	1/4
Sr	2h	½	½	0.20842(13)	1
M'(Y/Ca)	1d	½	½	½	1
Cu(2)	2g	0	0	0.36119(13)	1
O(1)	4i	0	½	0.37462(12)	1
O(2)	2g	0	0	0.1637(2)	1
O(3)	4n	0.3315(13)	½	0	1/4
O(4)	2f	0	½	0	0.015(5)*

* B factor was fixed, probably incorrect fractional occupancy. Result, most likely 0 really.

Table 2-1. Superconducting sample (S).

Atom	Site	x	y	z	g-occupancy
M(Pb/Cu(1)	41	0.068(2)	0	0	1/4
Sr	2h	½	½	0.2081(2)	1
M'(Y/Ca)	1d	½	½	½	1
Cu(2)	2g	0	0	0.3613(2)	1
O(1)	4i	0	½	0.3750(2)	1
O(2)	8s	0.047(5)	0	0.1636(4)	1/4
O(3)	8p	0.312(2))	0.537(7)		1/8
O(4)	2f	0	½	0	0.048(5)*

* B factor fixed.

Table 2-2. Non-superconducting sample (NS).

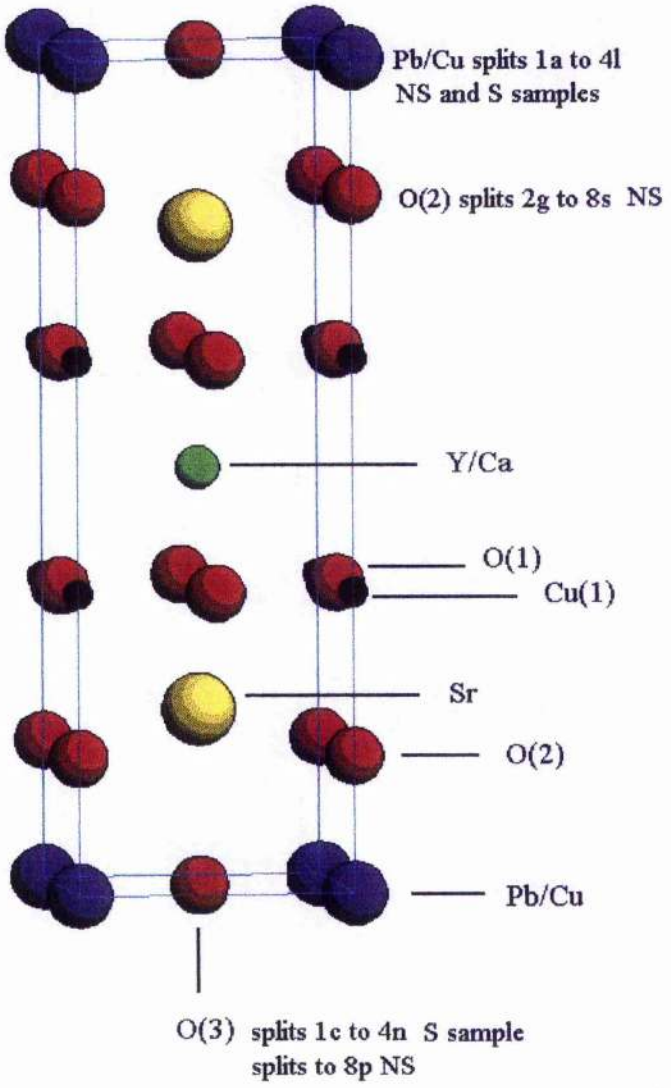

Figure 2.6. Displacements in 1212 superconducting (S) and non-superconducting samples (NS).

Both samples are similar in that the Pb and Cu(1) atoms are displaced from the ideal 1a site to a 4l site. However, the O(3) atom is displaced from an ideal 1c site to a 4n site in sample s and to an 8p site in sample N. Also in sample N the O(2) atom occupies an 8s site instead of the ideal 2g. therefore, it is clear to see that there is a greater amount of disorder in the (Pb,Cu)O and SrO planes of sample N. This is caused by the introduction of excess oxygen into the 2f site (0,½,0), and the probability of 0.05 accounts for the 0.1 oxygen content difference between the two samples. This excess oxygen affects the hole concentration and destroys superconductivity, and is confirmed by Hall coefficient measurements on these samples where sample S shows a higher concentration of mobile holes than N.

Liu et al[12] reported a compositional induced superconductor to semiconductor transition in the system $(Pb_{0.75}Cu_{0.25})Sr_2(Y_xCa_{1-x})Cu_2O_y$ with the T_c decreasing as x increases before the superconducting behaviour ceased. The multiphase nature of the samples, however, makes this difficult to realistically confirm.

Kosuge et al[13] investigated resistivity, Hall and Seebeck effect on the composition $(Pb_{[1+x]/2}Cu_{[1-x]/2})Sr_2(Y_{1-x}Ca_x)Cu_2O_y$ similar to that investigated by Maeda over the range x = 0-0.35. The authors found that as x increased, the measurements showed that the number of hole carriers increased. They believed this PbCu:1212 phase to be a self doping system. The presence of extra oxygen at the (0,½,0) site introduced a random potential which localised hole carriers in the samples.

Maeda et al[14] increased the range over which phase pure samples in the system $(Pb_{[1+x]/2}Cu_{[1-x]/2})Sr_2(Y_{1-x}Ca_x)Cu_2O_{7+\delta}$ existed by substituting some of the Sr by Ca. In $(Pb_{[1+x]/2}Cu_{[1-x]/2})(Sr_{2-y}Ca_y)(Y_{1-x}Ca_x)Cu_2O_{7+\delta}$ when y = 0.1, then multiphase samples existed when x > 0.4. More interestingly they showed that these samples exhibited superconductivity when slow cooled in addition to being quenched. The authors also noted that the samples in which the Sr sites were partially substituted by Ca were unstable in air at 800°C but not flowing O_2.

Kosuge et al[15] carried out high pressure transport studies in $(Pb_{[1+x]/2}Cu_{[1-x]/2})Sr_2(Y_{1-x}Ca_x)Cu_2O_{7+\delta}$. They found, unsurprisingly, that increasing pressure in superconducting samples caused the resistance to decrease and T_c to increase, as well as finding that the pressure coefficient $d\ln T_c/dp$ increased with ambient pressure T_c that was in good agreement with other studies. In the fully oxidised samples, they could not induce superconductivity even up to a limit of 8 GPa

Hu et al[16] found results which agreed with those of Adachi on a sample of composition $(Pb_{0.7}Cu_{0.3})Sr_2(Y_{0.5}Ca_{0.5})Cu_2O_y$. They showed that the optimal post annealing temperature, from which the samples would be quenched, was 800-900°C. TGA measurements up to 1000°C showed the sample had lost some weight on cooling also. Again the samples produced were impure.

Returning to the question of annealing conditions, Zhang et al[17] achieved an onset temperature of 77K for a sample of composition $(Pb_{0.7}Cu_{0.3})Sr_2(Y_{0.6}Ca_{0.4})Cu_2O_y$ by annealing in argon for 29 hours 800°C before quenching. Maeda[7] could only reach an onset temperature of 52K using a different annealing and quenching treatment. This shows that the post annealing treatment is essential to remove excess oxygen.

Naqvi and Boyd[18] showed that annealing in a nitrogen flow for 2 hours at 820°C before quenching gave excellent results. With nominal composition $(Pb_{0.75}Cu_{0.25})Sr_2(Y_{1-x}Ca_x)Cu_2O_y$, x = 0.4-0.7, superconductivity could be induced in these impure samples. Indeed in the x = 0.7 sample the highest T_c was 82K, unlike the samples produced by Adachi[10] mentioned previously.

Ono and Horiuchi[19] attempted 2 GPa synthesis of the PbCu:1212 cuprates, and although no exceptional onset temperatures were achieved, they did manage to produce these samples in orthorhombic form by varying the $KClO_3$/sample ratio.

2.12. The PbM:1212 system 1989-1994

Rouillon et al[20,21] reported an onset of superconductivity in samples of nominal composition $Pb_{0.5}Sr_{2.5}Y_{0.5}Ca_{0.5}Cu_2O_{7-\delta}$ at 100K. This was at about the same time as Subramanian an co-workers[1] discovery of the PbCu:1212 phase and bulk superconductivity in the Tl-Pb-Sr-Cu-O system[22,23]. In Rouillon's system superconductivity was achieved in untreated samples. Untreated is used in the sense that the prepared sample was not post-treated to induce superconductivity, although the authors noted that T_c could be enhanced by annealing in an oxygen atmosphere. The resistance ratio versus temperature plot suggested, however, that two superconducting phases were present.

Rouillon et al[24] also reported superconductivity in $(Pb_{0.5}Ca_{0.5})Sr_2(Y_{1-x}Ca_x)Cu_2O_{7-\delta}$ over the range x = 0.5-0.6. Their synthesis methods, also used for the PbSr:1212 system, were carried out in evacuated quartz tubes in which the sample compositions were mixed in such a way as to provide a slight oxygen over pressure during synthesis. In the study a range of oxygen over pressures were produced. Although a number of

compositions could be synthesised, only the x = 0.5-0.6 samples showed superconductivity and no post annealing treatments were used.

Liu et al[25] reported that the T_c in the $(Pb_{0.5}Tl_{0.5})Sr_2(Y_xCa_{1-x})Cu_2O_{7-\delta}$ system could reach 108K and pointed out some interesting features:

1. Monophasic samples were produced for the entire composition range ($1 \geq x \geq 0$).

2. Increasing yttrium level (Y^{3+}) causes room temperature resistivity to rise.

3. Cu^{3+} concentration decreases with increasing Y concentration figure 2.7. Adding Y^{3+} lowers the concentration of holes in the CuO_2 layers.

4. The **c** lattice parameter decreases with increasing Y concentration, figure 2.7. This may be explained simply by the fact that the Y^{3+} ion is smaller in eight-fold co-ordination than Ca^{2+}.

5. The **a** lattice parameter increases with decreasing Ca^{2+} concentration, figure 2.7. In this case[26] we are seeing a decrease in the number of holes in the CuO_2 layers. This causes the population of the antibonding Cu $3d_{x^2-y^2}$ orbitals to increase, thereby weakening the Cu-O bonds.

6. For x = 0 the material is a 78K superconductor with a metallic normal state. On increasing x the T_c then increases to 108K at x = 0.2, and then decreases to 44K at x = 0.5. For $x \geq 0.6$ the material exhibits semiconducting behaviour, and is an antiferromagnetic insulator for x = 1. The effect seen for x = 0-0.2 is consistent with the parent $(Pb_{0.5}Tl_{0.5})Sr_2CaCu_2O_{7-\delta}$ being "overcompensated" and reduction of excess Cu^{3+} increases the T_c. the decrease from 0.2 onwards is explained by further removal of holes.

7. The Pb:Tl ratio of 1:1 gives the optimal T_c for the $(Pb_{1-z}Tl_z)Sr_2(Y_xCa_{1-x})Cu_2O_y$ system the reason is not totally clear.

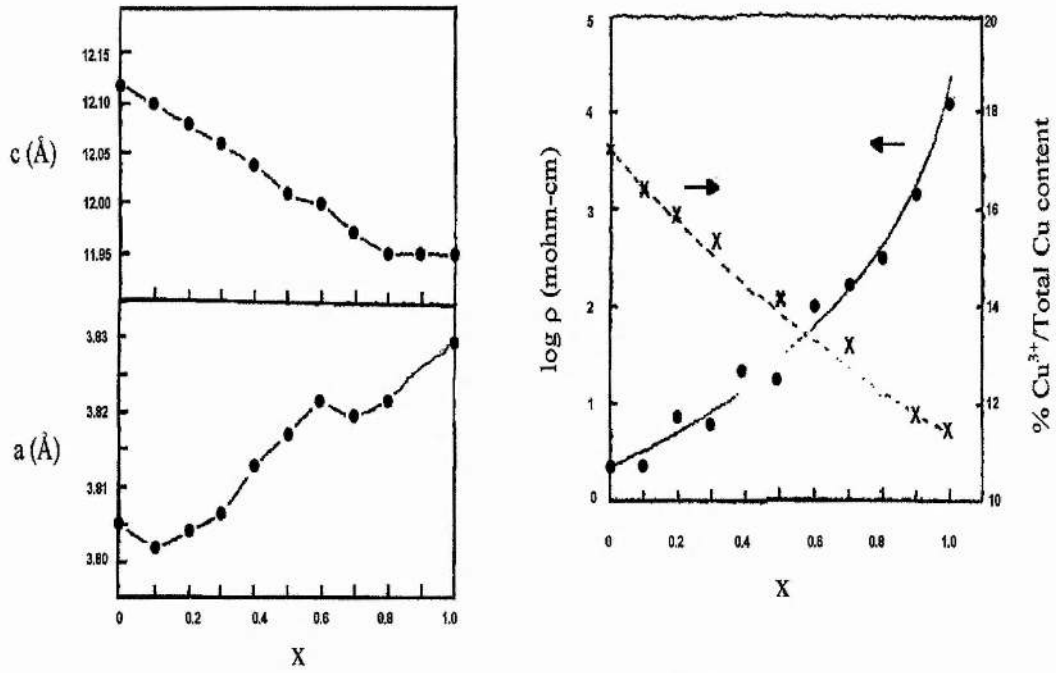

Figure 2.7. Variation of lattice parameters as a function of x in $(Pb_{0.5}Tl_{0.5})Sr_2(Y_xCa_{1-x})Cu_2O_7$. Variation of Cu^{3+} concentration as a function of x in $(Pb_{0.5}Tl_{0.5})Sr_2(Y_xCa_{1-x})Cu_2O_7$. (From Liu[25])

Substituting the rocksalt layer Cu with Cd was first shown by Liu et al[27] to give quite reasonable onset temperatures, 70 K in $(Pb_{0.5}Cd_{0.5})Sr_2(Y_{0.5}Ca_{0.5})Cu_2O_{7-\delta}$. However, Beales et al[28] really demonstrated the potential of PbCd:1212 by achieving a 92K onset temperature in partially melted samples of nominal composition $(Pb_{0.5}Cd_{0.5})Sr_2(Y_{0.7}Ca_{0.3})Cu_2O_{7-\delta}$.

In addition to Tl, Sr, Ca and Cu atoms in the rocksalt layer, the great flexibility of these layers was demonstrated by Maignan et al[29]. The authors in addition to those above synthesised samples containing Mg, Sc, Zn, Fe and Ni and were able to induce superconductivity in the first three. For Fe and Ni inducing superconductivity by any means was impossible, most likely due to the fact that iron and nickel can adopt a pyramidal co-ordination and will also tend to substitute for copper in the CuO_5 pyramids.

Hechtl and co-workers[30] studied PbSr:1212 and PbCa:1212 in the series $(Pb_{0.5}M_{0.5})Sr_2(Y_{1-x}Ca_x)Cu_2O_y$ and although were able to induce superconductivity in

samples up to x = 0.8 they could not produce single-phase samples over the entire compositional range. Nor could they synthesise any of the 1212 phase for the $(Pb_{0.5}M_{0.5})Sr_2Ca_1Cu_2O_y$ end members. The authors also found that post annealing treatment at 800°C coupled to quenching were necessary to induce superconductivity in some samples.

2.13. Conclusions

From the very simple viewpoint of superconductivity onset temperature, then PbTl:1212 and PbCd:1212 are much more promising. Neglecting toxicity for a moment, then it is only the PbTl:1212 system that has proved itself. The clear advantage of $(Pb_{0.5}Tl_{0.5})Sr_2(Y_xCa_{1-x})Cu_2O_{7-\delta}$ is the ease of synthesis of monophasic samples for the entire composition range ($1 \geq x \geq 0$) under non-extreme conditions. It has allowed a comprehensive study of the electronic and structural properties of the material to be completed. Toxicity and volatility of Tl based oxides has realistically limited their potential for industrial uses and Cd is an extremely toxic element also. Of course the question arises as to the suitability of Pb in any material, it certainly is not the least toxic element in the periodic table. But it is certainly less volatile than Tl or say Hg and definitely less toxic than Tl, Hg or Cd and is not noted in research for its unsuitability due to toxicity.

For the rest of the Pb based 1212 systems, then none have been synthesised as a single 1212 product phase when the doping of 100% Ca^{2+} in place of Y^{3+} is attempted. If the level of interest is gauged, then the PbCu:1212, PbSr:1212 and PbCa:1212 systems certainly are the most important.

The PbCu:1212 system seemed to the greatest potential for further research in a number of aspects i.e. synthesis, post synthetic annealing, oxygen content control, cation disorder and average/local structure. Section 2.2. covers these aspects more fully in terms of the research aims for this thesis.

2.2. Research aims

From the literature it was clear that the PbCu:1212 system had not fulfilled the potential, which had originally been expected, and a number of areas were identified as warranting further attention. The aim of this research was to study the PbCu:1212 system develop its potential. In addition to the routine electronic and structural measurements, it was clear that some areas in particular were key to the research as outlined in the following sections.

2.21. Synthesis

In the cases above the synthesis route is the standard solid state method and has not been successful, so the approach must tend towards novel synthesis methods. Sol-gel methods certainly have been applied successfully in a wide range of areas[31] and the aim was to attempt synthesis of the PbCu:1212 using this technique.

Previous research never really touched upon the formation route of the 1212 phase from precursors to product. Impurity formation and determination had been covered, but not necessarily correctly and there had been no attention paid to the role of oxygen during synthesis. The aim here was to study all areas of the synthesis procedure and understand the system and attempt to produce ideal synthesis conditions, which could eliminate impurity formation.

2.22. Post annealing.

The aims from post annealing treatments were two-fold. The first was to optimise the electronic properties of samples in high pO_2 environments and study the full effect oxygen content has on these properties. The second involved investigating low pO_2 post-annealing to determine whether or not this route was more efficient and could reproduce the high onset temperatures previously reported[17,18].

2.23. Structural determination.

To examine general structural details, the aim was to use diffraction techniques to study structural changes occurring in 1212 samples as the composition varied, and also to determine levels of disorder. Diffraction techniques only reveal structures on a general level and there had been no studies investigating short-range order. The actual structure was unknown on a local level and the influence of variation in oxygen content was not well known.

2.3. Bibliography and references for chapter 2

[1] M.A. Subramanian, J. Gopalakrishnan, C.C. Torardi, P.L. Gai, E.D. Boyes, T.R. Askew, R.B. Flippen, W.E. Farneth and A.W. Sleight, *Physica C*, 1989, **157**, 124.

[2] J.Y. Lee, J.S. Swinnea and H. Steinfink, *J. Mat. Res.*, 1989, **4**, 763.

[3] P. Haldar, S. Sridhar, A. Roig-Janicki, W. Kennedy, D.H. Wu, C. Zahopoulos and B. Giessen, *J. of Superconductivity*, 1988, **1**, 211.

[4] S.A. Sunshine, T. Siegrist, L.F. Schneemeyer, D.W. murphy, R.J. Cava, B. Batlogg, R.B. van Dover, R.M. Fleming, S.H. Glarum, S. Nakahara, R. Farrow, J.J. Krajewski, S.M. Zahurak, J.V. Waszczak, J.H. Marshall, P. Marsh, L.W. Rupp and W.F. Peck, *Phys. Rev. B*, 1988, **38**, 893.

[5] A. Ono and Y. Uchida, *Jpn. J. Appl. Phys.*, 1990, **29**, L586.

[6] S. Koriyama, K. Sakuyama, F. Izumi, H. Yamauchi and S. Tanaka, *Physica C*, 1990, **166**, 413.

[7] T. Maeda, K. Sakuyama, F. Izumi, H. Yamauchi, H. Asano and S. Tanaka, *Physica C*, 1991, **175**, 393.

[8] X.X. Tang, D.E. Sinha and A.P.B. Sinha, *Phys. Rev. B*, 1991, **43**, 7936.

[9] A. Maignan, T. Rouillon, D. Groult, J. Provost, M. Hervieu, C. Michel and B. Raveau, *Physica C*, 1991, **177**, 461.

[10] S. Adachi, H. Adachi, K. Setsune and K. Wasa, *Jpn. J. Appl. Phys.*, 1991, **30**, L690.

[11] T. Maeda, K. Sakuyama, S. Koriyama, H. Yamauchi and S. Tanaka, *Phys. Rev. B*, 1991, **43**, 7866.

[12] R.S. Liu, S.F. Hu, I. Gameson and P.P. Edwards, *J. Solid State Chem.*, 1991, **93**, 276.

[13] M. Kosuge, T. Maeda, K. Sakuyama, H. Yamauchi, N. Koshizuka and S. Tanaka, *Physica C*, 1991, **182**, 157.

[14] T. Maeda, K. Sakuyama, K. Isawa, H. Yamauchi and S. Tanaka, *Physica C*, 1991, **185-189**, 687.

[15] M. Kosuge, T. Maeda, K. Sakuyama, T. Miyatake, N. Koshizuka and H. Yamauchi, *Phys. Rev. B*, 1992, **45**, 10713.

[16] S.F. Hu, D.A. Jefferson, R.S. Liu and P.P. Edwards, *J. Solid State Chem.*, 1992, **96**, 455.

[17] H. Zhang, G.S. Chen, S.Q. Feng, X. Zhu and Q.R. Feng, *Solid State Comm.*, 1992, **83**, 601.

[18] S.H.H. Naqvi and I.W. Boyd, *Physica C*, 1993, **213**, 161.

[19] A. Ono and S. Horiuchi, *Jpn. J. Appl. Phys.*, 1994, **33**, 1839.

[20] T. Rouillon, J. Provost, M. Hervieu, D. Groult, C. Michel and B. Raveau, *Physica C*, 1989, **159**, 201.

[21] T. Rouillon, J. Provost, M. Hervieu, D. Groult, C. Michel and B. Raveau, *J. Solid State Chem.*, 1990, **84**, 375.

[22] M.A. Subramanian, C.C. Torardi, J. Gopalakrishnan, P.L. Gai, J.C. Calabrese, T.R. Askew, R.B. Flippen and A.W. Sleight, *Science*, 1988, **242**, 249.

[23] J.B. Parise, P.L. Gai, M.A. Subramanian, J. Gopalakrishnan and A.W. Sleight, *Physica C*, 1989, **159**, 245.

[24] T. Rouillon, A. Maignan, M. Hervieu, C. Michel, D. Groult and B. Raveau, *Physica C*, 1990, **171**, 7.

[25] R.S. Liu, P.P. Edwards, Y.T. Huang, S.F. Wu and P.T. Wu, *J. Solid State Chem.*, 1990, **86**, 334.

[26] A.R. Armstrong and W.I.F. David, *Chemistry in Britain*, 1994, **30**, 727.

[27] R.S. Liu, D. Groult, A. Maignan, S.F. Hu, D.A. Jefferson, B. Raveau, C. Michel, M. Hervieu and B. Raveau, *Physica C*, 1992, **195**, 35.

[28] T.P. Beales, C. Dineen, W.G. Freeman, S.R. Hall, M.R. Harrison, D.M. Jacobson and S.J. Zammattio, *Supercond. Sci. Technol.*, 1992, **5**, 47.

[29] A. Maignan, D. Groult, R.S. Liu, T. Rouillon, P. Daniel, C. Michel, M. Hervieu and B. Raveau, *J. Solid State Chem.*, 1993, **102**, 31.

[30] M. Hechtl, J. Bernhard and K.F. Renk, *Supercond. Sci. Technol.*, 1994, **7**, 407.

[31] C.J. Brinker, *Sol-gel science: the chemistry and physics of sol-gel processing*, San Diego: Academic Press, 1990.

Chapter 3. EXPERIMENTAL

3.1. Chemicals

The chemicals used for all synthetic work are shown in table 3-1.

Formula	Name and Grade	Supplier
CuO	Copper(II) oxide, 99+%	Aldrich
$SrCO_3$	Strontium carbonate, 99+%	Fisher
Y_2O_3	Yttrium oxide, 99+%	Aldrich
PbO	Lead(II) oxide, 99+%	Aldrich
$CaCO_3$	Calcium carbonate, 99+%	Fisher
$Y(NO_3)_3.5H_2O$	Yttrium nitrate pentahydrate, 99+%	Aldrich
$Sr(NO_3)$	Strontium nitrate, 99+%	Aldrich
$Pb(NO_3)$	Lead nitrate, 99+%	Aldrich
$Cu(NO_3).3H_2O$	Copper nitrate trihydrate (Analar), 99+%	BDH
$Ca(NO_3).4H_2O$	Calcium nitrate tetrahydrate, 99+%	Aldrich
Poly(acrylic acid)	25 wt.% soln. in H_2O, 240 000 mwt.	Aldrich
Ethane Diol	Ethane Diol, 99%	Aldrich

Table 3-1. Listing of chemicals used in sample synthesis.

3.2. Sample Preparation

Samples were synthesised by two routes, either sol-gel or by the conventional solid-state routes. These routes are described below.

3.11. Sol-gel synthesis

A ***sol***[1] is a dispersion of solid particles or polymers in a liquid. It is possible to precipitate particles that are amorphous or crystalline, or to make amorphous particles that become crystalline through dissolution and reprecipitation.

A ***gel***[1] consists of a continuous solid network surrounding and supporting a continuous liquid phase. The network can result from the destabilisation of a particulate sol by reduction of a repulsive double layer or removal of a steric barrier, or it can be built by crosslinking of polymer clusters. In either case, the free energy of the gel is similar to that of the sol, because relatively few bonds have to be formed to produce a spanning cluster.

Sol-gel enables materials to be mixed on a molecular level and then brought out of solution either as a colloidal gel or polymerised macromolecular network, advantageous over the solid-state route. The gel can be evaporated off leaving a solid with a fine porosity. The sol-gel method in principal also allows the material to be sintered and densified at much lower temperatures than would be expected for more conventional methods, since the fine porosity creates a large amount of free energy in the gel whilst pyrolising to drive the reaction along. The great advantage of sol-gel is that many of the problems of coprecipitation are avoided.

A number of sol-gel materials may be used when synthesising superconductors e.g. citrate, oxalate and alkoxide, but many still suffer from strict pH control, carbonate formation and cost. From a previous study[2], Polyacrylic acid seemed to avoid many of these problems while still being reasonably inexpensive and safe to handle and control its conditions. These reasons seemed to make this material suitable for syntheses required in this work.

Polyacrylic acid has a long chain structure made up from repeat units of the acrylic acid unit. In solution these long chains tangle to give a viscous liquid which has a pH ranging from 2-3. The metals are introduced in the form of their nitrates, which are usually readily soluble. This means that all of the metals can enter into solution and mix freely on the atomic scale to give an even distribution of each ionic species. Another advantage of the nitrate is that it can be totally removed as NO_x at reasonably low temperatures.

When the metal ion (M^{z+}) enters the reaction mixture it should co-ordinate with H_2O as well as some of the COO^- chains of the acid. As the water is removed the metal ion

co-ordinates with more of the acid groups, and thus begins to cause cross-linking of the acid strands which leads to production of a gel. More polar cations can immediately cause this cross-linking to produce a gel.

Ethane diol is another cross-linking agent, which is added to affect cross-linking by condensation reaction; however, the pH would seem to affect whether or not the condensation and thus cross-linking will occur.

For the $(Pb,Cu)Sr_2(Y,Ca)Cu_2O_y$ materials, appropriate amounts of the metal nitrates were accurately weighed out (±0.1 mg), to provide ~5g of the product, which was then dissolved in boiling distilled H_2O. This solution was slowly added while stirring to a solution containing 30 ml distilled H_2O, 2-5 ml of 10% NH_3OH[A], 10 ml ethane diol and 10 g polyacrylic acid. The clear blue solution was then transferred to an oven at 80-120°C to remove the water and produce a dried gel. The carbon matrix of the gel was removed by slowly heating the gel to 400°C in either an air or flowing O_2 for 1 hour before increasing the temperature to 750°C and then 850°C to ensure total removal of the carbon matrix.

The resulting black powder was then ground in acetone for 10-30 minutes and the acetone allowed to evaporate at room temperature before pressing into pellets in a 13 mm diameter stainless steel die at a pressure of 2 tonnes. The pellets were placed on Au foil to prevent reaction with the alumina boat, before being fired in air (muffle furnace) or flowing O_2 (tube furnace) for 24-48 hours at 850-950°C. Regrinding and refiring stages were repeated, until the reaction could be deemed complete from X-ray powder diffraction analysis. At this point the powder was ready to undergo various heat treatments, section 3.3.

Samples of nominal composition $(Pb_{[1+x]/2}Cu_{[1-x]/2})Sr_2(Y_{[1-x]}Ca_{[x]})Cu_2O_{7\pm\delta}$ were synthesised over the range x=0-1. In addition, samples of nominal composition $(Pb_{0.5}Cu_{0.5})Sr_2(Y_{[1-x]}Ca_{[x]})Cu_2O_y$ and $(Pb_{0.7}Cu_{0.3})Sr_2(Y_{[1-x]}Ca_{[x]})Cu_2O_y$ were synthesised over the range x=0-1.

[A] Non addition of the 10% NH_3OH leads to a clear solid, which is glass like and difficult to grind.

3.22. Solid-state synthesis

The starting materials of $SrCO_3$, $CaCO_3$ and Y_2O_3 were dried at 440°C for 6 hours before use, while CuO was dried at 750°C for 6 hours and the PbO dried at 275°C. Appropriate quantities of the precursors were accurately weighed out (±0.1 mg) and then ground in acetone for 10-30 minutes. The acetone was allowed to evaporate at room temperature, before pressing the powder into pellets in a 13 mm diameter stainless steel die at a pressure of 2 tonnes. These pellets were placed on Au foil to prevent reaction with the alumina boat before being fired in air (muffle furnace) or flowing O_2 (tube furnace) for 24-48 hours at 850-950°C. Regrinding and refiring stages were repeated until the reaction could be deemed complete from X-ray powder diffraction analysis. At this point the powder was ready to undergo various heat treatments, section 3.3. Samples of nominal composition $(Pb_{[1+x]/2}Cu_{[1-x]/2})Sr_2(Y_{1-x}Ca_x)Cu_2O_{7\pm\delta}$ were produced over the range x=0-1. Also produced were samples of composition $(Pb_{0.5}Cu_{0.5})Sr_2(Y_{1-x}Ca_x)Cu_2O_y$ and $(Pb_{0.7}Cu_{0.3})Sr_2(Y_{1-x}Ca_x)Cu_2O_y$ over the range x=0-1.

In addition the solid-state route was used to make products of nominal composition $Pb_3Sr_4Y_2Cu_5O_x$, $Pb_3Sr_4Y_1Ca_1Cu_5O_x$, $Pb_1Sr_2Y_1Cu_3O_x$. These powders were weighed accurately (±0.1 mg) and ground in acetone for 10-30 minutes, before being fired at 880°C in air to undergo decarbonation. These materials were then subject to various heat treatments, section 3.3.

3.3. Heat Treatments

Although there is a set method of synthesis, it is the specialised heat treatments in the materials, which lead to the desired characteristics. In the cuprate materials oxygen content is highly critical not only in the generation of superconducting samples, but also to maintain the structural stability of the desired phase. Heat treatments can be described in two ways for this work. The first is "high pO_2" in which an air or pure O_2

environment is used, while the second "low pO_2" involves the use of Ar or N_2 medium where the typical oxygen content is lowered to values much lower than 1%. Vacuum methods are included as low pO_2 in this work.

3.31. High pO_2

For the production of fully oxygenated samples, the material is heated typically to 925°C in air or flowing O_2 before the furnace is cooled slowly (5°C.min^{-1}.) or the furnace is left to cool to room temperature at its own rate. The sample may also be allowed to isotherm at 400°C in air or flowing O_2 for 12 hours to achieve the same results.

To produce samples which are not oxygenated fully, the sample is typically heated to temperatures ranging from 650-950°C in air and held at the set temperature for 4 hours, before it is removed from the furnace and immediately dropped into 500 ml of liquid nitrogen. The nitrogen around the pellet forms a layer of gas, which prevents O_2 entering the sample while the material is cooling. The sample is then removed from the liquid nitrogen and placed in an oven at 120°C for 20 minutes.

Another means of producing oxygen deficient samples is to mount them in a vertical tube furnace as shown in figure 3.1 and quench by rapidly removing heat from the sample to prevent oxygen uptake into the sample. The sample is suspended from a Pt wire and the steel nut is held in place by a magnet. The sample (pellet) is placed in a Au envelope directly in the centre of the hot zone of the furnace before the O_2 is set flowing. Temperatures ranging from 650-950°C are typically used with an annealing time of 4-12 hours. The sample is released by removing the magnet and this results in the sample rapidly dropping from the hot zone into the Cu turnings, whereby the heat is very rapidly dissipated and the sample temperature drops below that required for O_2 to re-enter the structure and cause oxygenation.

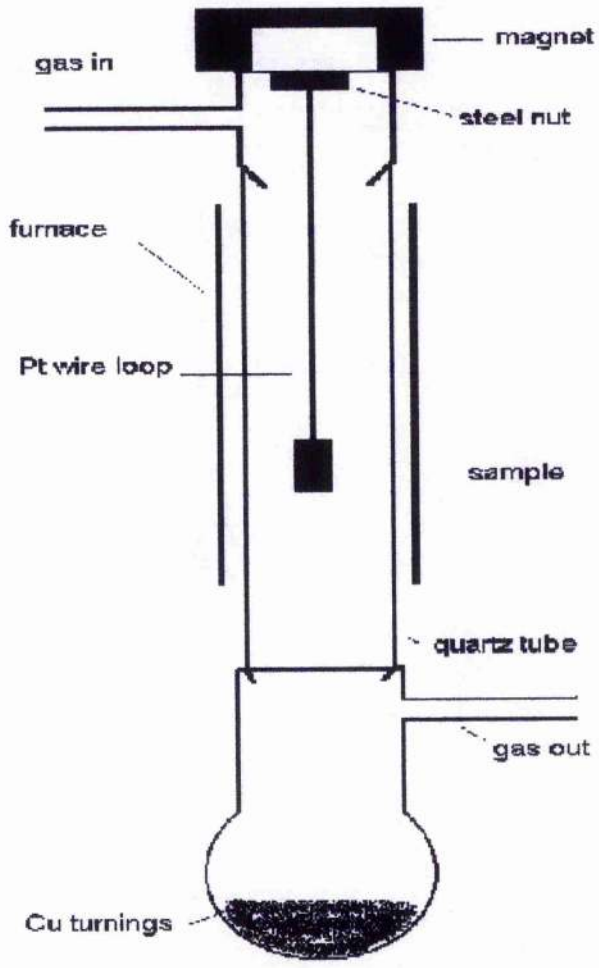

Figure 3.1. Simplified design for vertical quench furnace.

3.32. Low pO_2

Work for low pO_2 studies is carried out in a tube furnace with the tube being protected from the normal atmosphere by the end piece fittings shown in figure 3.2. The circular collar fits around the inside and outside of the tube and flush with the tube end. Epoxy resin is placed into the spaces between tube and collar to prevent air entry at these parts.

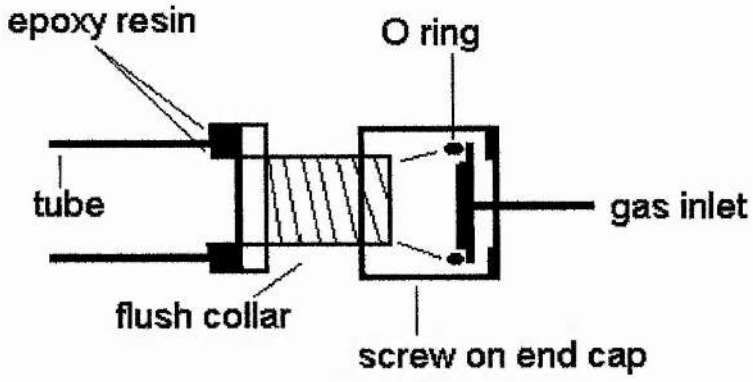

Figure 3.2. End piece construction for tube furnace

Zero Grade Argon (BOC) and oxygen free nitrogen (BOC) are used for the low pO_2 studies. Typically the sample is placed on Au foil in a reduced alumina boat[B] and heated to temperatures ranging from 600-950°C for times ranging from 5-120 minutes before being cooled at 10°C.min^{-1} to 150°C. See section 3.5 for vacuum experimental method and conditions.

3.4. Diffraction Studies[3,4]

To determine the locations and spacing of atoms which typically have a spacing of ~1 Å (10^{-10} m), three types of radiation are used. These are the X-ray, neutron and electron and all three, although having different yet overlapping uses in structural studies within the solid, interact with the periodic lattice subject to the same general laws and conditions. Since the electron is a charged particle it interacts strongly with matter and can penetrate only a few hundred Angstrom units into a crystal before it must suffer an elastic or inelastic encounter. This realistically rules its use out for bulk structural arrangements, but it proves extremely useful in studies using a Transmission Electron Microscope (TEM).

[B] Reduced Alumina boat is fired at 1000°C in 5%H_2/Ar to remove extra O_2 from the alumina. This prevents the boat releasing O_2 when heated and affecting the sample.

Laue first suggested in 1912 that a crystal could be regarded as a 3-dimensional diffraction grating for energetic electromagnetic waves of a wavelength comparable to the atomic spacing. Neglecting effects from the interactions between the electromagnetic radiation and the atoms themselves, there are minimum conditions for the efficient diffraction by a crystal using collimated monochromatic radiation. Although the Laue equations are the more rigorous way to describe diffraction from crystals, Bragg's Law, although based on the laws of physical reflection for the diffracted wave to experience constructive interference, gives an identical result. The Bragg equation is written:

$$n\lambda = 2d \sin\theta \qquad (3.1)$$

where **d** is the d-spacing (distance between adjacent parallel layers), θ is the Bragg angle, λ is the wavelength of the radiation. Normally we can set n=1 i.e. first order. Since there are many planes in real crystals, then Bragg's Law imposes stringent conditions on the angles at which reflection occurs.

As stated previously the above is only a minimum condition for efficient diffraction from a crystal. We also find that the reflections on the diffraction pattern may be reduced in intensity or actually totally absent due to the symmetry type of the crystal or the scattering intensity from individual atoms within the crystal.

The symmetry of the crystal plays a very important part in the scattering of electromagnetic radiation and this may be due to the lattice type if it is non-primitive or if elements of space symmetry are present e.g. a screw axis. To show the effect of the lattice type, it is useful to look at cubic α-Fe (figure 3.3) which has a body centred lattice type (I). Reflections in the 100 planes are systematically absent, while reflections in the 200 plane are allowed. Simply, at the Bragg angle for the 100 planes the body centred atom lies midway between these planes and diffracts X-rays 180° out of phase relative to the corner atoms. Note that the number of body atoms and corner atoms averaged over the crystal is equal, therefore there is complete cancellation and the 100

peak is absent from the diffraction pattern. The 200 planes are present because all the atoms lie in the 200 planes.

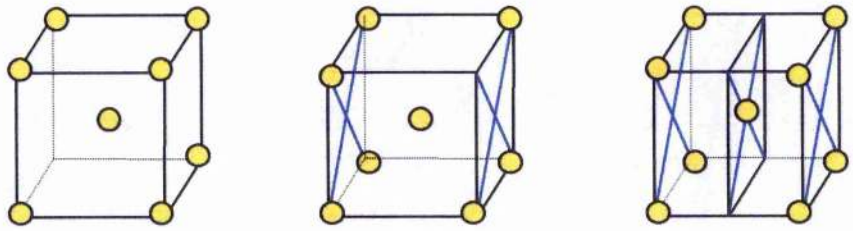

100 planes 200 planes

Figure 3.3 Systematic absences in α-Fe.

Diffraction of X-rays from an atom results from the interaction (Thomson Scattering) of X-ray photons of wavelength λ with the charge field of all the extranuclear electrons in a solid. Essentially the X-ray photon interacts with the electron to set it vibrating and shall emit radiation which is coherent (in phase) with the incoming radiation. The classical theory for coherent scattering predicts a modest decrease of scattering efficiency as the angle 2θ between incoming and outgoing wavefronts increases. However, the efficiency of coherent X-ray scattering by the electrons of a solid falls off much more rapidly as 2θ increases. This occurs because the bound electrons of each atom are distributed over a volume with diameter comparable to the X-ray wavelength.

An atom of atomic number **Z** acts as a Thomson scattering point source of charge **Ze** for X-rays of long wavelength (small scattering angle). For smaller wavelength (larger scattering angle), the atom scatters as a Thomson source of effective charge **fe.** The number **f** is the atomic scattering factor (or form factor) and decreases from **Z** as the quantity $[\sin\theta/\lambda]$ increases. Increasing the atomic number of the element in question increases the numbers of electrons present, consequently of this means that the diffracted radiation of light elements is weak. Another problem is the presence of the lighter elements e.g. oxygen and heavier elements e.g. Tl or Pb in the crystal. The heavy elements dominate the overall scattering from the crystal so that accurate quantitative determination of the number of the lighter atoms verges on impossible and other techniques must be used. The dependence of $\sin\theta/\lambda$ causes problems when using X-ray

radiation and the powder pattern contains weak lines above 70° 2θ. This puts a limit on the range of 2θ over which useful data may be collected.

Although systematic absences have already been covered, resultant diffraction intensity at a particular angle may also be less than expected from what has been discussed previously or in some cases totally absent. How much intensity (if any) is actually reflected depends on the structure factor $\mathbf{F_{hkl}}$. The structure factor takes into account the form factors of the various types of atoms present in the crystal and the places at which such atoms are located in the unit cell. To describe this, it is best to consider a solid with **N** atoms in the basis, of which $\mathbf{f_j}$ is the form factor of the **jth** atom. If all **N** atoms lie exactly on the hkl planes then every plane would return a reflected wave which is lagging exactly 2π radians compared to the plane above. The reflected amplitude would be proportional to the summation of all $\mathbf{f_j}$ over the **N** atoms of each basis. In actual samples some atoms of the basis shall return a wave advanced in phase by an angle (in radians):

$$\phi_j = (2\pi\Delta d_j / d_{hkl}) \qquad (3.2)$$

The resulting amplitude is the vector sum of the wavelets scattered from each atom per basis, and is proportional to the structure factor:

$$F_{hkl} = \sum_{j=1}^{N} f_j \exp(i\phi_j) \qquad (3.3)$$

When neutrons are used instead of X-rays, systematic absences are of course still present, however the actual mechanism of scattering is quite different. Neutrons with wavelengths comparable to interatomic spacing are scattered subject to the same laws as X-rays. The real difference lies in the fact that the neutron only interacts with the nuclei of atoms. There is no simple relationship between atomic number and scattering power. For example hydrogen scatters neutrons strongly and the isotopes of an element can have totally different scattering factors. It should also be noted that neutrons can scatter inelastically, and since the neutron has a magnetic moment, they can interact

with unpaired electrons in magnetic materials and give rise to extra "magnetic peaks" in the diffraction spectrum.

3.41. X-ray diffraction

The laboratory instrument used for both room temperature and high temperature work was a STOE STADI P Automatic Powder Diffractometer with the radiation type being monochromatic Cu $K_{\alpha 1}$. The diffractometer was configured to run in a transmission mode. For room temperature analysis, the sample was held between Mylar sheets in a flat rotating disc with measurements steps of 0.5° 2θ and a measurement time of 10/15 seconds per step, although the collection time per step could be increased when superior counting statistics were required for structural analysis. For high temperature measurements, the diffractometer furnace attachment was used. Samples were mounted in Quartz capillaries of 0.2 or 0.5 mm diameter

3.42 Neutron diffraction

Two very different ways exist for the production of neutrons for experimental diffraction work. The first source relies on the production of neutrons from a nuclear reactor, while the second source for neutrons is from a pulsed spallation source. In the pulsed technique the diffraction experiment is carried out with θ fixed at a selected value and the diffracted radiation is separated according to its time of flight (wavelength).

In situ neutron diffraction experiments on PbCu:1212 samples were performed at the 57 MW High Flux Reactor (ILL Grenoble France) on instrument D1B[Appendix]. The sample was mounted in a vanadium furnace under a vacuum, and heated at a rate of 10°C.min^{-1} while each set of data was collected over a 10 minute period. A wavelength of 2.52 Å was selected for the experiment while the furnace was heated over the range 25-800°C.

Room temperature high resolution neutron diffraction was performed at ILL on instrument D1A[Appendix]. Samples were placed in a vanadium can and mounted on the instrument, with typical counting times of 6 hours employed.

Lattice studies were performed at the RAL 200 μA ISIS[Appendix] pulsed spallation source on the HRPD[Appendix] station. For room temperature measurements the PbCu:1212 samples were placed in a vanadium can and held under vacuum. The low temperature measurements were performed using an Orange cryostat and the sample was cooled from room temperature in 2-5 K steps.

3.43. Electron diffraction

The transmission electron microscope (TEM) used for the electron diffraction experiments was the Jeol JEM 200CX microscope operating at 200 keV and equipped with a LaB_6 filament. The microscope was equipped with a tilting goniometer stage (±10°). Electron diffraction patterns and micrographs were recorded on Agfa photographic plates. Samples were prepared by gently crushing the material under n-butanol, before transferring the n-butanol droplets onto 2.05 mm Cu grids (Agar, 200 mesh) which had been coated with a holey 'Triafol' polymer carbon coated film. The grids were then dried under an infra red lamp before transferral to the electron microscope.

Thanks to Professor Richard Tilley and Denis Pasero, University of Wales College of Cardiff for assistance in performing the measurements and helpful discussion on their interpretation.

3.44. Resonant diffraction[5,6]

The ability to tune synchrotron radiation to any desired wavelength allows the modification of the scattering factor (*f*) of a particular element by selecting an X-ray wavelength in close proximity to its absorption edge. The resultant resonance effects lead to a modification of the scattering factor:

$$f = f^o + f' + if'' \qquad (3.4)$$

where f' is the real part of the correction and f'' is the imaginary part. The main point about f' and f'' is that they have essentially no dependence on $(\sin\theta/\lambda)$ which means that they have no deleterious effects on peak intensities as 2θ angle is increased. Such resonant scattering effects can influence the X-ray patterns drastically and allow the study of elemental contrast, site disorder and valence studies as examples. Powder diffraction, however, shows poor sensitivity to f'' [7] and as a consequence most experiments rely upon the influence of f'.

The Kramers-Kronig integral relates f' and f'':

$$f'(\omega_i) = (2/\pi)\int_0^\infty \omega f''(\omega)/(\omega^2 - \omega_i^2)d\omega \qquad (3.5)$$

where ω_i is the angular frequency of the radiation.

In many materials there may be more than two distinct species located on a single crystallographic site it is not possible to determine uniquely the distribution of the cations on the site from a single diffraction data set[8]. The answer to this is to use anomalous scattering to alter the scattering power of an element.

Experiments were performed on station BM16[Appendix] at the ESRF Synchrotron Source[Appendix] in Grenoble France. The sample was mounted on the diffractometer in 0.5 mm borosilicate glass capillaries and measurements were performed at four separate energies, table 3-2.

Resonant Edge	Energy (keV)	Wavelength (λ)	Scan Range (2θ)	Count Time (hr.)
None	25	0.50020	0-58	6
Cu	8.98	1.38068	12-128	12
Pb	13.04	0.95080	10-78	8
Sr	16.105	0.76965	5-68	8

Table 3-2. Wavelengths chosen for resonant diffraction experiments.

The wavelength was accurately determined using a Si standard at each selected energy. Fluorescence measurements were also used to determine edge positions correctly. The 25 keV energy was chosen because there were no resonance effects at this energy. The diffractometer detectors moved continuously over the 2θ range and a bank of 9 detectors each separated by 2 degrees of 2θ collected the data. The data sets from each detector were summed and integrated to produce the final pattern. The values of f' and f'' were selected from the Sasaki[9] tabulation of the anomalous scattering factors based on the Cromer and Liberman[10] method.

3.45. Powder pattern analysis[11]

The growth of single crystals for structure refinement has always been desirable; however, it is clear that in many cases single crystals cannot be grown at all or be grown in a form which matches the requirements for structural analysis. Thus, the determination of the structure of a material must be made from the diffraction data obtained from a powder sample. Until the early 1960's and the advent of reasonable computing power, simple crystal structures were determined which were of high symmetry and had well separated peaks and allowed simple calculation of integrated intensities for further refinement. More complex lower symmetry structures with severely overlapping peaks could not yield integrated intensities for individual peaks.

Rietveld[12,13] devised computer based analytical procedures which allowed the information from each intensity at each step in the pattern to be usefully used. i.e. to use the full information content of the powder pattern. In the Rietveld method least squares refinements are carried out until the best fit is obtained between the entire observed

powder diffraction pattern taken as a whole and the entire calculated pattern based on the simultaneously refined models for the crystal structure(s), diffraction optics effects, instrumental factors, and other specimen characteristics. The refinement provides feedback between improving knowledge of the structure and improving allocation of observed intensity to partially overlapping individual Bragg reflections. It is important to note that the Rietveld method makes no effort in advance to allocate observed intensity to particular Bragg reflections nor to resolve overlapped reflections. As a result a good starting model is required and not a random starting point.

Generalised Structural Analysis System (GSAS)[14] is a Rietveld program designed to run on a number of operating systems. The program is versatile and works with X-ray and neutron data (fixed wavelength or time of flight) as well single crystal data combinations of these. The usage of multiple data sets in refinements is particularly important when resonant diffraction data is being used. Two other common software routines using the Rietveld method are the TFLS[15] FULLPROF[16].

On the STOE STADI P powder diffractometer, the data collected and stored using RAWDAT were handled using the PEAK and LATREF software routines to determine the unit cell dimensions and instrument zero point. Indexing of unknowns was carried out using the INDEX routine.

3.46. R factors

The quality of refinement, i.e. closeness of fit between experimental and calculated patterns is expressed in terms of R factors or residual factors. These are usually quoted as percentages. The R factors are:

1 Profile R factor, R_p

2 Weighted R Factor, R_{wp}

3 Intensity or Bragg R factor, R_I

4 Expected R factor, R_E

$$R_p = \frac{\sum_i |Y_i(obs) - Y_i(calc)|}{\sum_i Y_i(obs)} \qquad (3.6)$$

$$R_{wp} = \left[\frac{\sum_i |Y_i(obs) - Y_i(calc)^2|^2}{\sum W_i Y_i^2(obs)} \right]^{1/2} \qquad (3.7)$$

Where Y is the intensity of the point on the powder diffraction profile, and W is a weighting factor.

$$R_I = \sum_k |I_k(obs) - \frac{1}{c} I_k(calc)| \sum_k I_k(obs) \qquad (3.8)$$

I is the peak intensity. The intensity R factor is helpful in determining the quality of structural fit since it relates to the peak area and not the peak shape.

$$R_E = \left[\frac{N - P + C}{\sum W_i Y_i(obs)^2} \right]^{1/2} \qquad (3.9)$$

N is the number of observations, P is the number of variables and C is the number of constraints. Another guide to the quality of a refinement is Chi^2. This is calculated using the following relationship:

$$Chi^2 = \left(\frac{R_{wp}}{R_E} \right)^2 \qquad (3.10)$$

Therefore, in an ideal refinement, the weighted and expected R factors should be identical and hence a value of 1 obtained. However, a number of things can affect the value of Chi^2, and hence the value should not be used solely on its own as a guide to the quality of a refinement. It is also of paramount importance to examine the observed and calculated profiles at each stage of refinement in order to assess the progress and future strategy of the refinement. The R factors obtained during the course of a refinement are the best guide to the quality of the fitted profile.

The value of R_{xp}/R_p may be artificially high for a number of reasons, such as short counting times. Experiments performed in specialist environments, such as a furnace or cryostat, can lead to a contribution to the background of the collected profile and hence will lead to a lower than expected R factor. These factors and others must be considered when reporting the R factors obtained from a refinement.

3.5. Thermal Analysis (TGA/DTA)

Thermal Analysis consists[17] of a group of techniques in which a property of the sample is monitored against time or temperature while the temperature of the sample, in a specified atmosphere, is programmed.

The program may well involve heating or cooling at a fixed rate of temperature change, or holding the temperature constant, or any sequence of these.

Thermogravimetry **(TGA)**[12] is a technique in which the mass of the sample is constantly monitored against time or temperature while the temperature of the sample, in a specified atmosphere, is programmed. TGA has uses in the study of decomposition, dehydration and oxidation.

Differential Thermal analysis **(DTA)**[18] is a technique in which the difference in temperature between the sample and a reference material is monitored against time or temperature while the temperature of the sample, in a specified atmosphere, is programmed. DTA is used in the study of phase changes and reactions. It is important to note that DTA does not give satisfactory signals to relate the DTA signals obtained to the heat capacity and enthalpy changes of transitions and reactions occurring during heating. For accurate quantitative analysis, Differential Scanning Calorimetry (DSC) must be used.

Measurements were performed using the TA Instruments model 2960 simultaneous TGA/DTA. The sample and reference (Al_2O_3 dried at 1500°C) materials (~50 mg) were placed in alumina pans and the runs were carried out using varied heating/cooling conditions in a number of environments, table 3-3

Environment	Equilibrate (°C)	Ramp Rate (°C.min^{-1})	Max. Temp. (°C)	Isothermal (minutes)	Cooling (°C.min^{-1})	Cycles
O_2	25-100	10	970	0-240	10	yes
Air	100	10	970	0-120	10	yes
N_2	25-100	10	900	0-120	10	yes
Ar	25-100	10	900	0-120	10	yes
Vacuum	25	10	950	0-30	10	no
5% CO_2	25	10	850	15	10	no

Table 3-3. Summary of conditions used in typical TGA runs.

The above is a summary and typical variations are usually to the maximum temperature selected and isothermal hold times. Running programmed cycles is also used and these shall be mentioned when necessary.

3.6. Magnetic Measurements

3.61. SQUID Magnetometer

The Quantum Design SQUID magnetometer is an extremely sensitive device to measure magnetic properties of materials. The main feature of the SQUID (**S**uperconducting **QU**antum **I**nterference **D**evice) is the use one or two Josephson Junction(s) within a closed superconducting loop. The quantised state of the superconducting ring and the non-linear behaviour of the Josephson junctions means that extremely small changes (in theory 10^{-15} T) in magnetic field are detectable The SQUID, although extremely sensitive, does not directly detect the magnetic field from the sample. Instead, the sample moves through a system of superconducting detection

coils, which are connected to the SQUID with superconducting wires, allowing the current from the detection coils to inductively couple to the SQUID sensor. The SQUID electronics produce an output voltage which is proportional to the current flowing in the SQUID input coil.

The measurement is made by passing the sample through the superconducting detection coils. As the sample moves through the coils, the magnetic moment of the sample induces an electric current in the detection coils. The closed system of detection coils, connecting wires and SQUID input coil mean that any change of magnetic flux in the detection coils produces a change in the persistent current in the detection circuit, which is proportional to the change in magnetic flux.

Powdered samples are weighed and placed in a gelatine capsule and wrapped in kapton tape before insertion into a straw that was then attached to the sample-handling rod. Standard runs on the instrument involved cooling of the sample to 1.8K with 0 Gauss (G) field applied, Zero Field Cooled (ZFC). A field of 100 G is then applied and the sample heated in a stepwise manner up to 300K with measurements made at each temperature. The 100 G field is left on while the sample is again cooled to 1.8K, Field Cooled (FC). Measurements are made in the same steps as before. Measurements were made at the University of Edinburgh Department of Chemistry. Thanks to Dr A. Harrison and Dr. G. Whittaker for assistance with the measurements.

3.62. Vibrating Sample Magnetometer (VSM)

If a material is placed within a uniform magnetic field, a magnetic moment, **m**, will be induced in the sample. In a Vibrating Sample Magnetometer (VSM) such a sample is placed within the pick-up coils, and is made to undergo sinusoidal motion i.e. mechanically vibrated thus resulting in magnetic flux changes which induce a voltage in the sensing coils. The induced voltage is proportional to the magnetic moment of the sample and hence the VSM can be used to measure the materials' magnetic properties. The magnetising field (**H**) may be produced by either an electromagnet or a superconducting magnet. Thus, allowing measurements of magnetic moment or

magnetisation (**M**) as a function or magnetic field. The sensitivity of the method is lower than may be obtained from a SQUID magnetometer.

Samples for the Oxford Cryosystems 12T VSM were prepared by mixing the powder with epoxy resin to form spheres, the typical amount of powder ranged from 150-200 mg. These balls were allowed to harden before being inserted in to a delrin sample holder. The samples were first cooled down to 4.2 K under ZFC conditions upon which an applied field of 60 G was set and the sample slowly heated with measurements being made every 10 seconds until the temperature had passed through the superconducting transition. The sample was then cooled using FC conditions to 4.2 K and the same measurement routine used as shown previously. A range of field sweeps could also be performed ranging from –120000 G through 0 G to +120,000 G over a number of temperatures and variable rates.

3.7. Electron Microscopy

The function of an electron microscope is in principle similar to that of the optical microscope. Both use an illuminating source and a combination of lenses to focus and magnify objects. Electrons, with their very much shorter wavelength result in a much higher degree of resolution allowing the diffraction patterns of crystals up to 2000 Å thickness to be resolved. The disadvantage of using electrons is that they must be focused by either electromagnetic or electrostatic lenses that are prone to astigmatism and chromatic and spherical aberration unlike their optical analogues.

The electron microscope can operate in diffraction or imaging mode, figure 3.4. In either mode, electrons emitted by the illumination source are first collimated and then focused through the specimen by the condenser lens whereupon they interact with the specimen and are scattered.

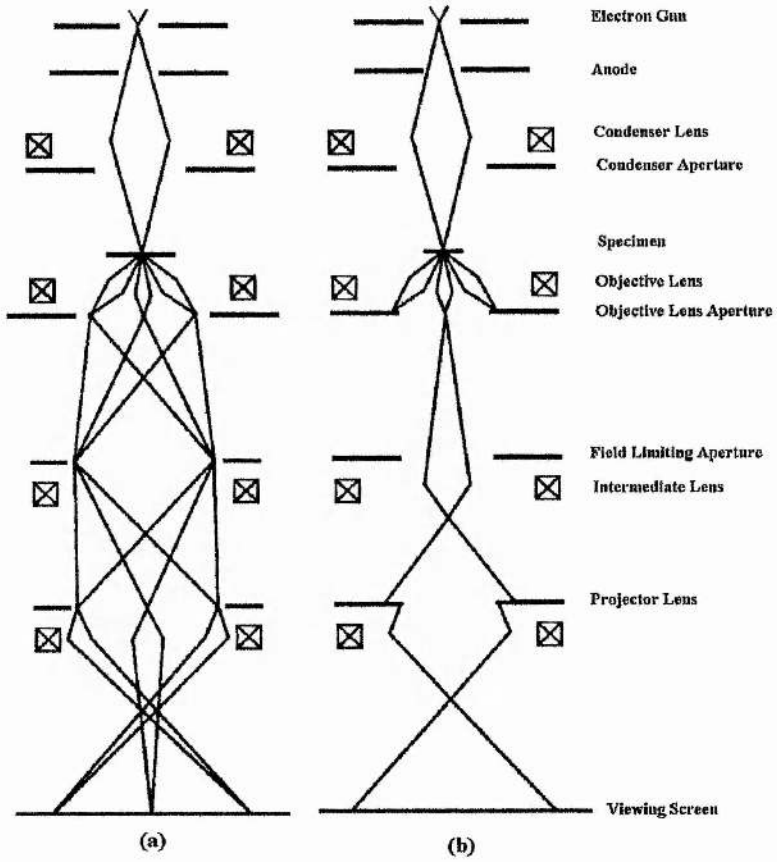

Figure 3.4. Schematic representation of TEM operating in (a) selected area diffraction mode and (b) imaging mode.

The scattered electrons are brought to focus by the objective lens and are then further magnified by a series of intermediate and projector lenses to provide an image of convenient size. With the microscope in imaging mode, the intermediate and projector lenses magnify a small portion of the image formed by the objective lens at its image plane. In diffraction mode, the intermediate and projector lens are arranged so as to enlarge the Fraunhoffer diffraction pattern formed by the objective at its back focal plane. The field-limiting aperture restricts the diffraction pattern produced by the

specimen to that generated by an area of interest. See section 3.43 for the equipment details and acknowledgements.

3.8. Extended X-ray Absorption Fine Structure (EXAFS)

X-rays can be absorbed by atoms in molecules. Generally, the proportion of X-rays absorbed (the absorption coefficient) will decrease as their energy increases, but at certain values of energy, specific to each element, a sudden increase in the amount of energy absorbed is observed. These energies are known as absorption edges. The energies correspond to the ejection of an electron from a certain orbital in the atom in question (i.e. ionisation). The ejected electron can be considered as a wave, travelling outwards from the central absorbing atom.

Simple models of X-ray absorption predict a gradual monotonic decrease in the absorption coefficient with increasing energy away from the absorption edge. Such behaviour is observed in spectra of isolated atoms, e.g. Xe, or Kr, but for atoms either in a molecule or a condensed phase, the presence of other atoms around the absorber causes oscillations in the absorption coefficient near the edge. These oscillations in the post edge region arise from the backscattering of the emitted electron wave off neighbouring atoms and so the structure of the post edge region of the X-ray absorption spectrum is related to the radial distribution of atoms in the sample. Hence, by analysing this structure (the frequency and amplitude of the oscillations), information about the local environment of the absorbing element can be derived. Figure 3.5 shows a typical EXAFS spectrum.

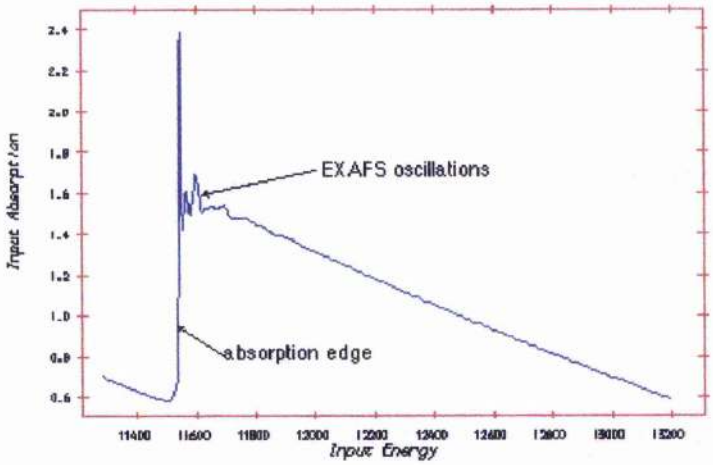

Figure 3.5. Typical EXAFS spectrum

The EXAFS effect (the oscillations in the post edge absorption coefficient) is small compared to the absorption resulting from the electron ejection (ionisation), hence a strong X-ray source is required, to produce features sufficiently intense to be analysed. Synchrotron X-ray sources meet this requirement; they produce X-ray radiation by accelerating pulses of electrons to a speed approaching that of light. The EXAFS experiment involves placing a sample of the compound under investigation in the path of the X-ray beam, selecting an absorbing element, and changing the energy of the X-rays incident on the sample so that it varies above and below the absorption edge of interest. This variation is done in a series of small steps; at each stage the amount of X-rays before and after the sample is measured, so that the amount absorbed by the sample can be determined as a function of energy.

The measurements of the amount of X-rays absorbed versus X-ray energy are corrected for certain factors such as the general background decrease in the absorption coefficient, to give the observed EXAFS spectrum. A theoretical model is then derived, to match the observed theoretical spectrum as closely as possible. The parameters of the model include the type, number and distance of atoms in the molecule, which are close to the absorbing atom under study. Hence, information about the local structure of the molecule can be obtained.

EXAFS spectroscopy differs from diffraction X-ray techniques, as it is sensitive only to short-range order and can be applied equally well to crystalline or amorphous solids, and also to liquids and even gases. The structure around different elements in the sample can be obtained simply by varying the incident X-ray energies to cause ionisation of each element in turn. As EXAFS spectroscopy is element-specific, the presence of impurities, which either do not contain the absorber, or are far from the absorber, will not cause interference.

The main deficiencies of the technique are the sensitivity only to short range order (generally to ~4 Å away from the absorbing element), the lack of three dimensional information, and the large amount of data reduction and analysis involved.

The in situ EXAFS experiments were performed at the 2GeV SRS Daresbury Laboratory (Cheshire England) Synchrotron source on station 9.3. The experiment was run in transmission mode with the sample (50 mg) being mixed with 50 mg of amorphous silica and pressed into a pellet. The sample was then mounted in the RI/DL furnace using N_2 as the purge gas. The edge under study was the Pb_{LIII} edge. The furnace was set to heat at 1°C/min with the timing being set 4 minutes for XRD and 6 minutes EXAFS. The sample was heated over the range 300-900°C with additional measurements carried out at 25 and 200°C. Data analysis was carried out using the Daresbury Laboratory Software routines, Excalib, Exback and Excurv92[19,20].

3.9. Bibliography and references for chapter 3

[1] C.J. Brinker, *Sol-gel science: the chemistry and physics of sol-gel processing*, San Diego: Academic Press, 1990.

[2] R.W. Jones, *Fundamentals of sol-gel technology*, London: The Institute of metals, 1991.

[3] A.R. West, *Solid State Chemistry and its Applications*, Chichester, John Wiley and Sons, 1984.

[4] J.S. Blakemore, *Solid State Physics - second edition*, Cambridge, Cambridge University Press, 1985.

[5] A.K. Cheetham and A.P. Wilkinson, *Angew. Chem.*, 1992, **31**, 1557.

[6] G.H. Kwei, R.B. Von Dreele, A. Williams, J.A. Goldstone, A.C. Lawson and W.K. Warbuton, *J Mol. Struct. Theoche.*, 1990, **223**, 383.

[7] A.P. Wilkinson, D.E. Cox and A.K. Cheetham, *J. Phys. Chem. Solids*, 1991, **52**, 1257.

[8] G.H. Kwei, R.B. Von Dreele, S-W. Cheong, Z. Fisk, J.D. Thompson, *Phys. Rev. Sect. B*, 1990, **41**, 1889.

[9] S. Sasaki, *KEK Report*,1989, **88-14**, 1.

[10] D.T. Cromer and D. Liberman, *Journal of Chemical Physics*, 1970, **53**, 1891.

[11] R.A. Young, *The Rietveld Method*, New York, Oxford University Press, 1995.

[12] H.M. Rietveld, *Acta Crystallogr.*, 1966, **21**, A228.

[13] H.M. Rietveld, *J. Appl. Crystallogr.*, 1969, **2**, 65.

[14] A.C. Larson and R.B. Von Dreele, *Los Alamos National Laboratory, Report*, No. LA-UR-86-748, 1987

[15] P.J. Brown and J.C. Mathewmann, *Rutherford Appleton Laboratory Report*, RAL-87-010, 1987.

[16] J. Rodriguez-Carvajal, *15th C. Int. Un. Cryst.*, 1990,127.

[17] J.O. Hill, *For Better Thermal Analysis and Calorimetry III*, ICTA, 1991.

[18] P.J. Haines, *Thermal Methods of Analysis*, Glasgow, Blackie A&P, 1995.

[19] S.J. Gurman, N. Binstead and I. Ross, *J. Phys. C.:Solid State Phys.*, 1984, **17**, 143.

[20] S.J. Gurman, , *J. Phys. C.:Solid State Phys.*, 1988, **21**, 3699.

APPENDIX

Institut Laue Langevin, Grenoble, France

Neutrons, are produced by the means of fission in a nuclear reactor, the design of which has been optimised for high intensity. They are produced continuously and, after thermalising in the surrounding moderator, beams are emitted with a broad range of wavelengths. Wavelength selection is generally achieved by Bragg scattering from a crystal monochromator or by velocity selection through a mechanical chopper

D1A[1,2] High Resolution two-axis diffractometer

D1A has a near perfect Gaussian peakshape in the 2θ range 30-150°. The instrument has a 123° take-off angle, which gives high resolution at large scattering angles. Wavelengths of 1.390-2.994 Å may be selected, while the optimum wavelength is 1.911 Å. The detection unit consists of (25 high efficiency collimators and ^{3}H counters) and is swept over the 2θ range 0-160° in 0.05° steps. The flux at sample is $1x10^6$ n.cm^{-2}.s^{-1}. The layout of D1A is shown in Figure A.1.

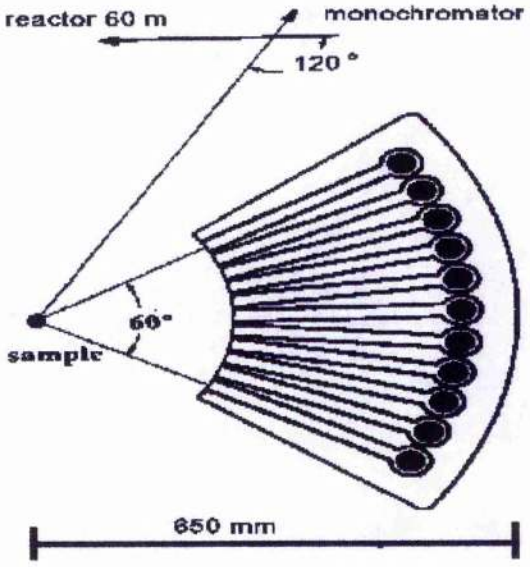

Figure A1.1. Layout of D1A.

D1B two-axis diffractometer.

The high flux of D1B at 2.52 Å ($6.5x10^6$ $n.cm^{-2}s^{-1}$) and the large multidetector makes it ideally suited for in situ experiments. The detection system on D1B consists of a ^3He detector containing 400 cells which covers a 2θ angular range of 80°, while the detector may be moved so that an angular range of -20 to 144° may be covered. Wavelengths of 1.28 and 2.52 Å may be used. The layout of D1B is shown in figure A.2.

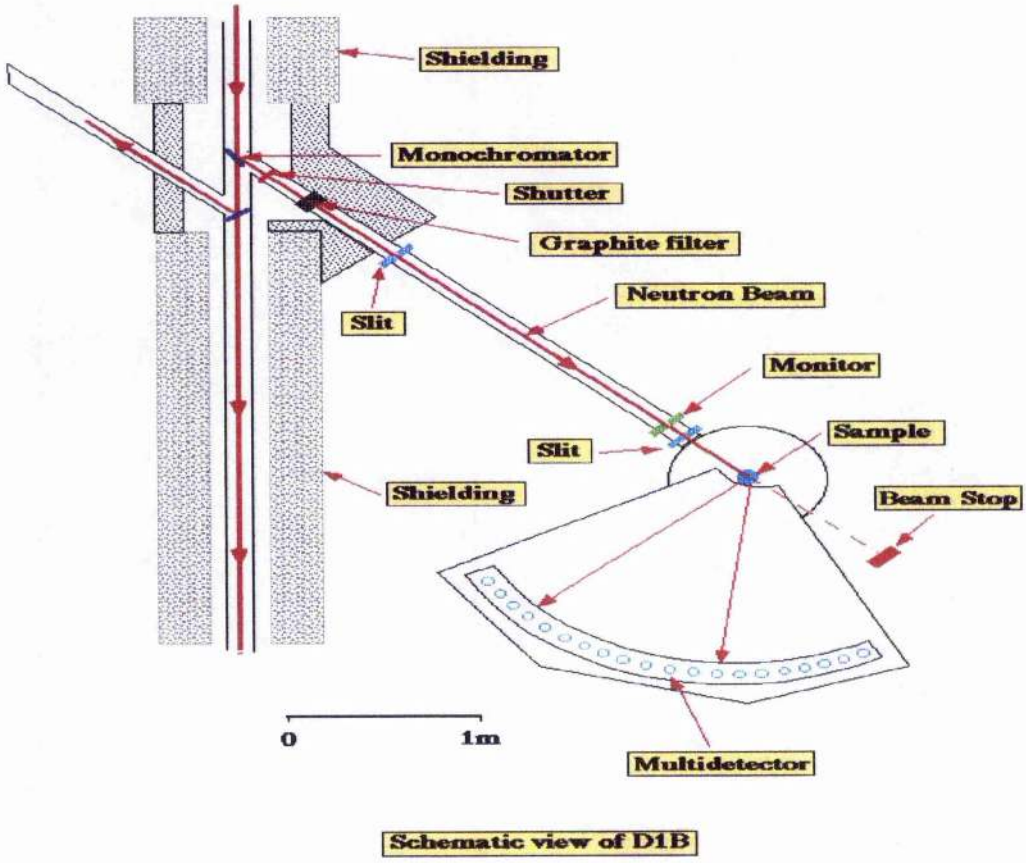

Figure A.2. Schematic of D1B

ISIS Rutherford Appleton Laboratory, Didcot, England

ISIS is a pulsed neutron source and produces neutrons by means of the spallation process, where neutrons are produced by bombarding a heavy metal target with highly energetic particles from a powerful accelerator.

The production of particles energetic enough for the production of efficient spallation involves three stages:

(i) Ion Source. H^- ions are accelerated to 665 keV in a pre injector column
(ii) LINAC. The H-ions are accelerated by rf cavities to an energy of 70 MeV.
(iii) Injection. The electrons are stripped from the H-ions by very thin Al_2O_3 foil to produce a circulating beam of protons.

The protons are then extracted (50 times per second) and collide with a depleted Uranium or Tantalum target to produce neutrons by chipping nuclear fragments from the heavy metal nucleus.

The neutrons produced have energies that are too high for diffraction studies and are slowed by hydrogenous moderators.

HRPD- High Resolution Powder diffractometer

HRPD is placed nearly 100 m from the ISIS target and is able to achieve extremely high resolution in the backscattering detector bank. It has a $\Delta d/d$ resolution of 5×10^{-4} (resolution limit set by powder particle size) which is effectively constant over a wide d-spacing range.

European Synchrotron Radiation Facility, Grenoble, France

The institute is built around a synchrotron radiation source. It consists of an 850 m long storage ring for 6 GeV electrons, a 300 m long 6 GeV booster synchrotron functioning at 10 Hz, and a LINAC pre-injector. The current may be selected to range from 5-100 mA in single or multibunch modes.

BM16 Powder diffraction

The instrument lies on beamline 15 and is built on a bending magnet and accepts 4 mrad of the hardest radiation from the available horizontal fan. The beamline is designed for powder diffraction studies with very high angular and energy resolution. Specifications of the beamline:

(i) Energy range of 5-40keV
(ii) Very high 2θ resolution with optimal instrumental contribution to the peak width of 0.002° (peak width determined by the sample)
(iii) Energy resolution of less than 1 eV at 10 keV.

The two-circle diffractometer is configured with a nine-crystal analyser stage (9xGe(111) crystals separated at 2° angles). When capillary samples are used, the sample is rotated on an independent spinner, (one-axis or two-axis Gandolfi), on the axis of the diffractometer. The general layout of the powder diffraction beamline is shown in figure A.3.

---

[1] A.W. Hewat, *Nucl. Inst. Methods*, 1975, **127**, 361.
[2] A.W. Hewat and I. Bailey, *Nucl. Inst. Methods*, 1976, **137**, 463.

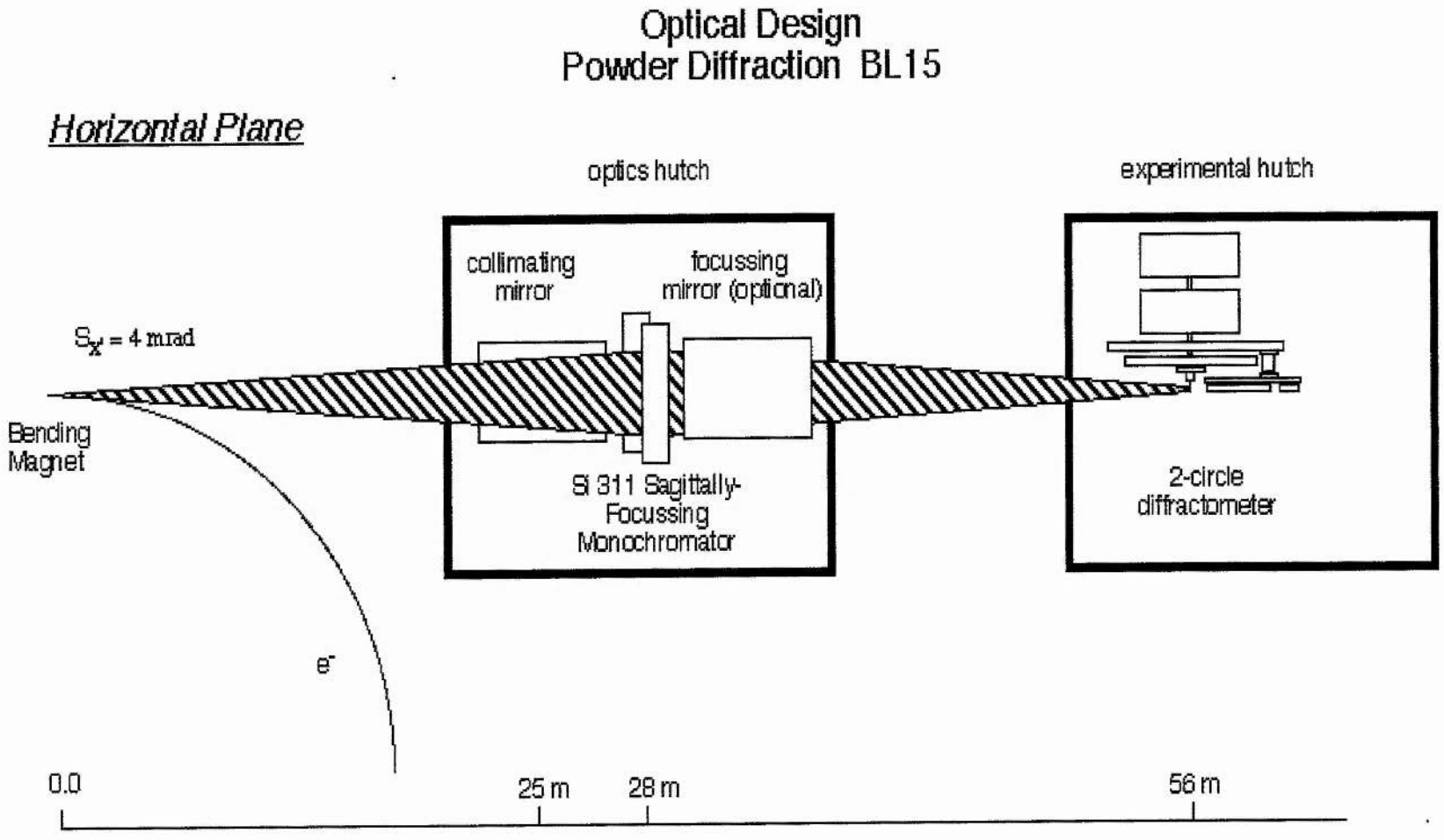

Figure A.3. Layout of BM16.

Chapter 4. SYNTHESIS AND PHASE STABILITY

4.1. Reaction Pathway

4.11. Phase evolution

To determine the reaction pathway from dried gel to the product 1212 phase, portions of sample were removed at a number of temperatures and increasing time, for XRD analysis, when the sample was being ashed or annealed in pelleted form.
Table 4-1 summarises the reaction time and conditions for figures 4.1 to 4.6.

Reaction Temp. (°C)	Reaction time (hours)	Figure
-	0	4.1
500 (closed ashing)	0.5	4.2
750 (closed ashing)	5	4.3
800 (anneal)	12	4.4
875 (anneal)	24-48	4.5
925 (anneal)	24-48	4.6

Table 4-1. Reaction conditions during formation of 1212 product.

Figure 4.1, shows the XRD pattern derived from the dried blue gel, which is typical of that seen for amorphous materials.

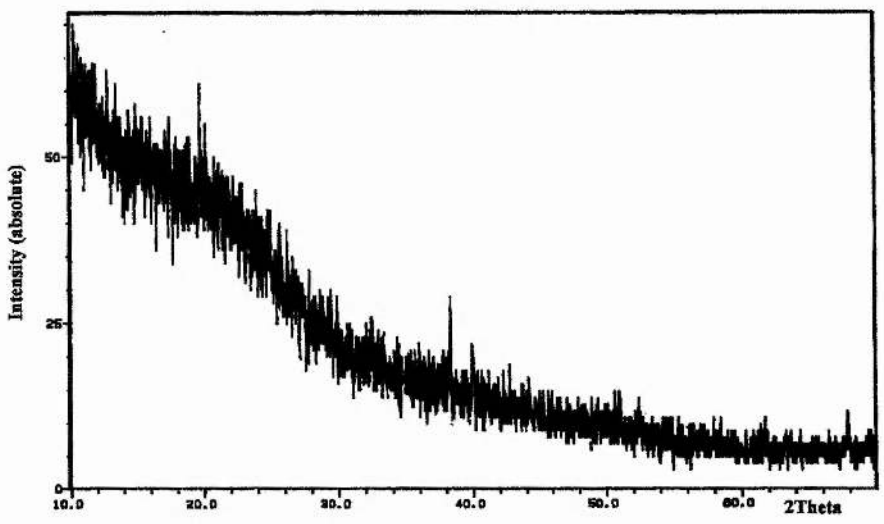

Figure 4.1. XRD from dried gel sample.

Formation of the required product 1212 phase does not proceed directly from the precursor mixture; instead there are a number of phases present as shown in figure 4.2. $SrCO_3$ (**o**) and CuO (**x**) are easily identified, although it is very difficult to ascertain what other phase(s) might be present in the sample

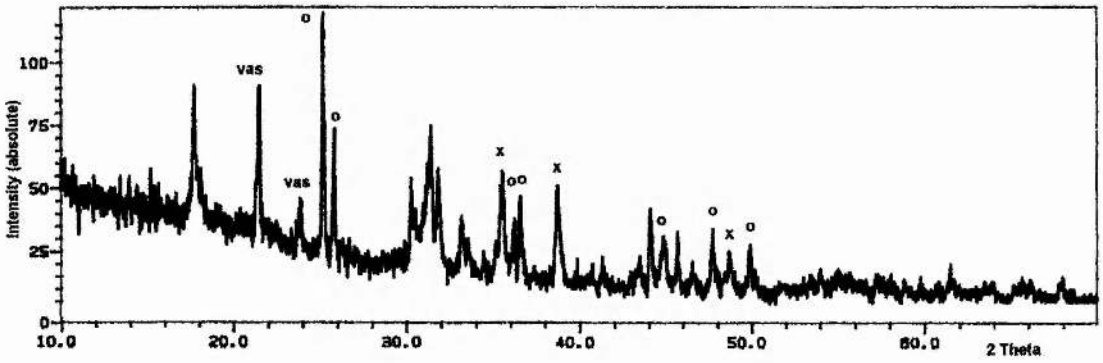

Figure 4.2. First portion removed during ashing cycle, "vas"= vaseline.

Figure 4.3, shows the presence of $SrCO_3$ and CuO with the clear evolution of a new phase (+).

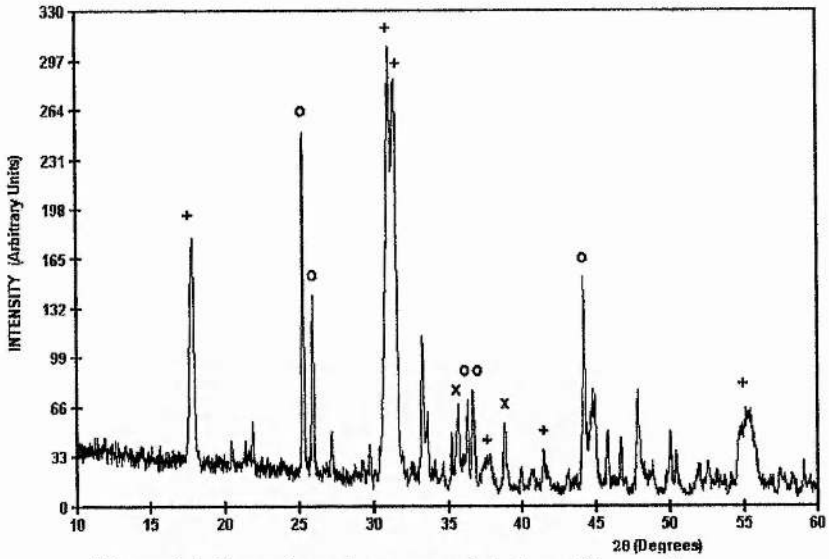

Figure 4.3. Second portion removed during ashing cycle.

Subsequent increases in temperature and time in an open system, figures 4.4 and 4.5, show the $SrCO_3$ and CuO having disappeared. The intermediate phase (+) is gradually being converted into the final required 1212 phase (**m**), shown in figure 4.6.

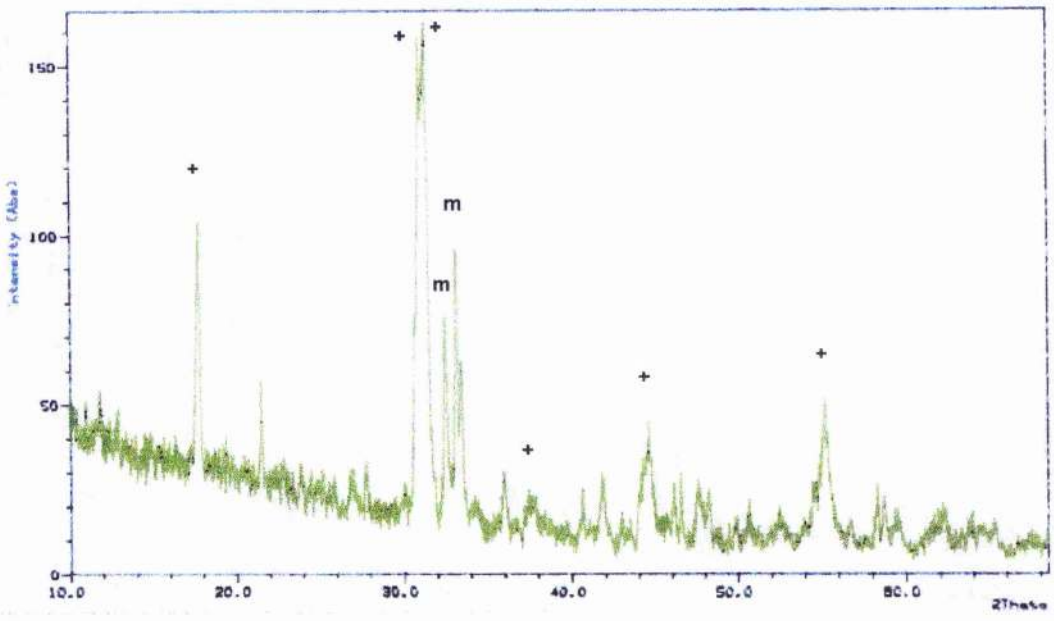

Figure 4.4. XRD showing appearance of 1212 phase.

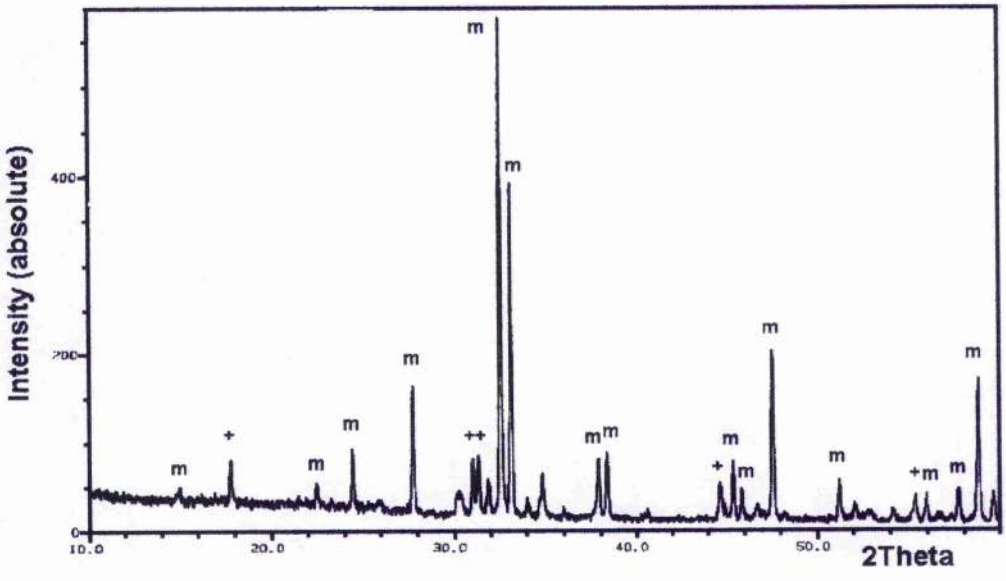

Figure 4.5. Conversion of intermediate phase into 1212 phase.

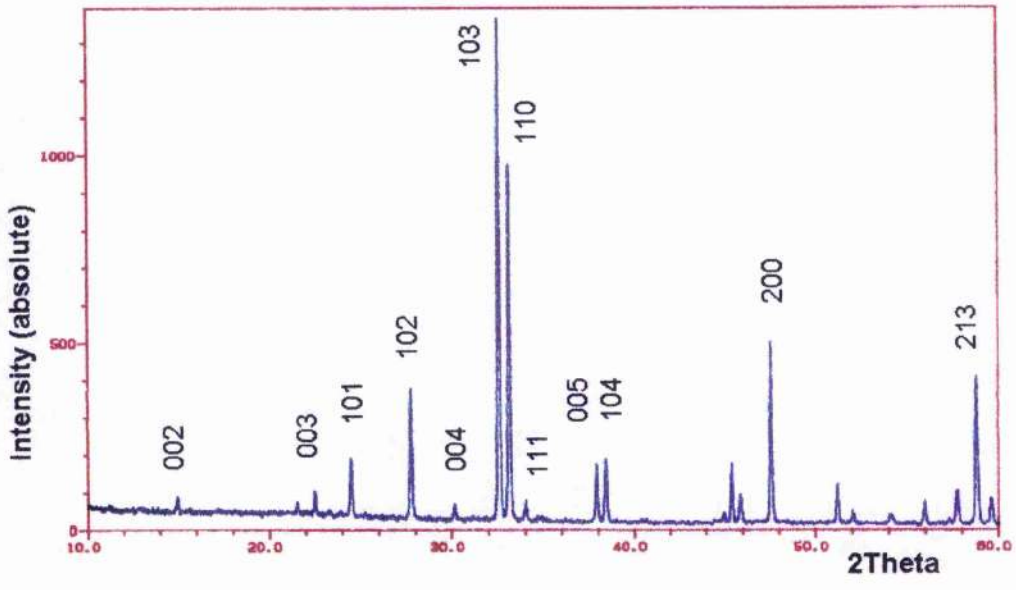

Figure 4.6. 1212 single-phase $(Pb_{0.5}Cu_{0.5})Sr_2Y_1Cu_2O_y$ sample, indexed and major peaks marked.

The 1212 phase is fitted to a tetragonal unit cell with lattice parameters **a** ≈ 3.82 Å and **c** ≈ 11.8 Å. The material is fully indexed and described by P 4/mmm (No.123) space group symmetry, in agreement with reported literature[1,2] values.

4.12. Impurity phase identification

Replacing Y^{3+} with Ca^{2+} in the $(Pb_{[1+x]/2}Cu_{[1-x]/2})Sr_2(Y_{1-x}Ca_x)Cu_2O_7$ system reveals impurity peaks (#) in the diffraction pattern in addition to the desired 1212 product phase, figure 4.7. The presence of impurity phases in such sample types had been reported previously [3,4,5].

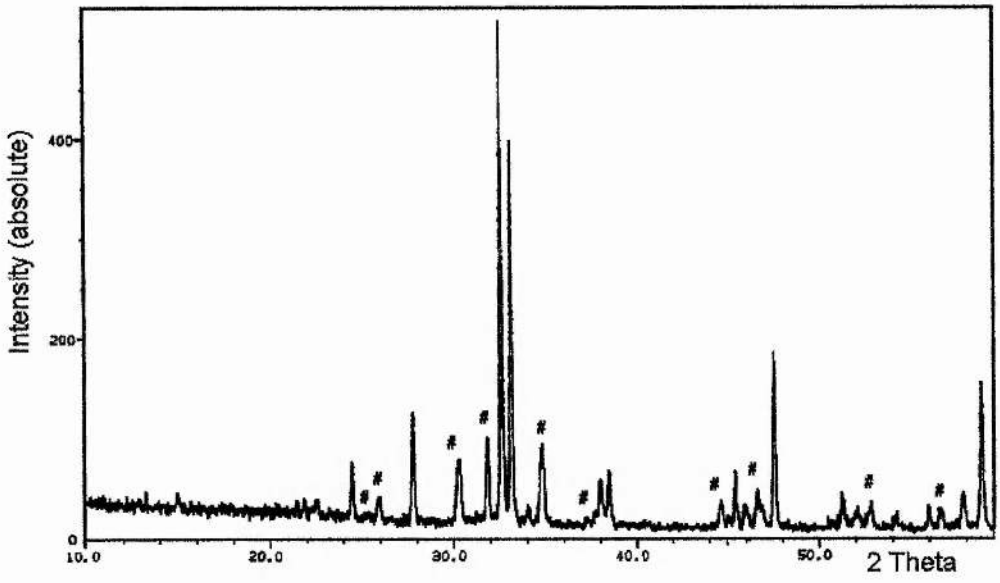

Figure 4.7. Impurity peaks (#) additional to 1212 product phase.

Since the samples contain Pb, Sr, Y, Ca and Cu, then the possibility exists for a large number of impurity phases to exist. After a lengthy elimination process, the closest match to the impurity peaks in figure 4.7 was found to be $SrCuO_2$, as shown in figure 4.8. The ideal $SrCuO_2$ peaks are displaced to higher d-spacing values i.e. to the left, indicating that the impurity phase has smaller lattice parameters. Cation substitution or deficiency in $SrCuO_2$ would appear to provide the most reasonable explanation. Replacing Sr^{2+} with Ca^{2+} i.e. $Ca_xSr_{1-x}CuO_2$ is known to reduce[6,7,8,9] the lattice parameters before a phase change occurs at $x \approx 0.4$. Since the lattice parameters vary in a reasonably linear manner in the **a**, **b** and **c** directions as Ca replaces Sr, then a possible Ca content of the impurity phase can be extracted, table 4-2.

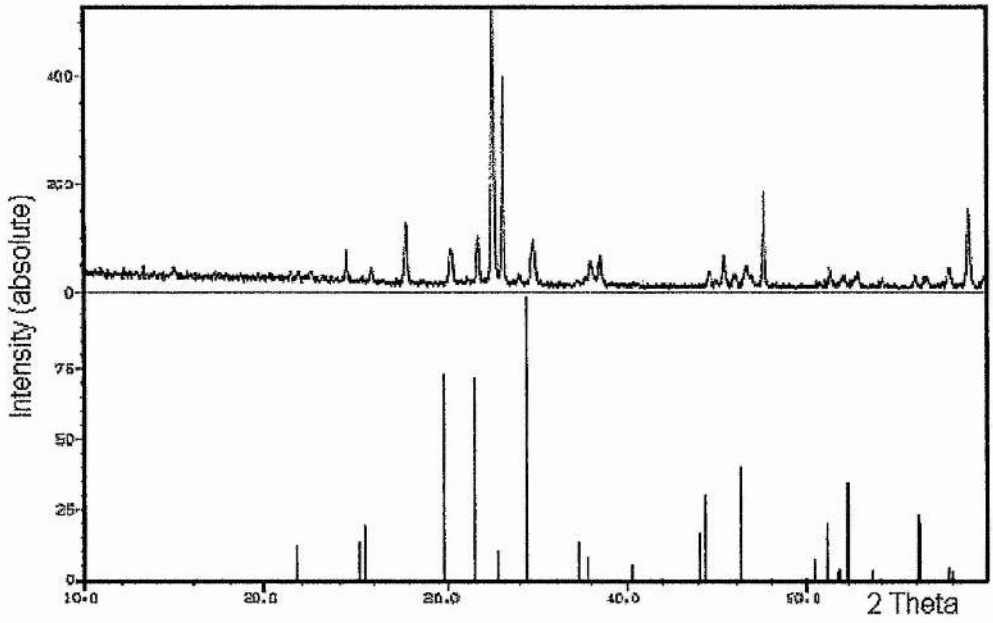

Figure 4.8. $SrCuO_2$ PDF pattern matching impurity phase XRD

Material	Cell type	Vol. (Å^3)	a (Å)	b (Å)	c (Å)
$SrCuO_2$	primitive orthorhombic	228.5	3.57	3.92	16.33
impurity	primitive orthorhombic	223.5	3.53	3.905	16.28
$Ca_{0.4}Sr_{0.6}CuO_2$	primitive orthorhombic	218.5	3.48	3.88	16.18

Table 4-2. Determination of lattice parameters for impurity phase.

After extrapolation, the Ca content of the impurity phase was estimated to lie in the region x=0.13-0.18. EDAX analysis, figure 4.9, confirms the presence of Ca, Sr and Cu in the impurity phase. No Pb based impurities were found in this examination. The lack of an acceptable standard, however, meant the impurity composition cannot be accurately determined. The impurity phase shall be described as $(Ca,Sr)CuO_y$ from this point onwards.

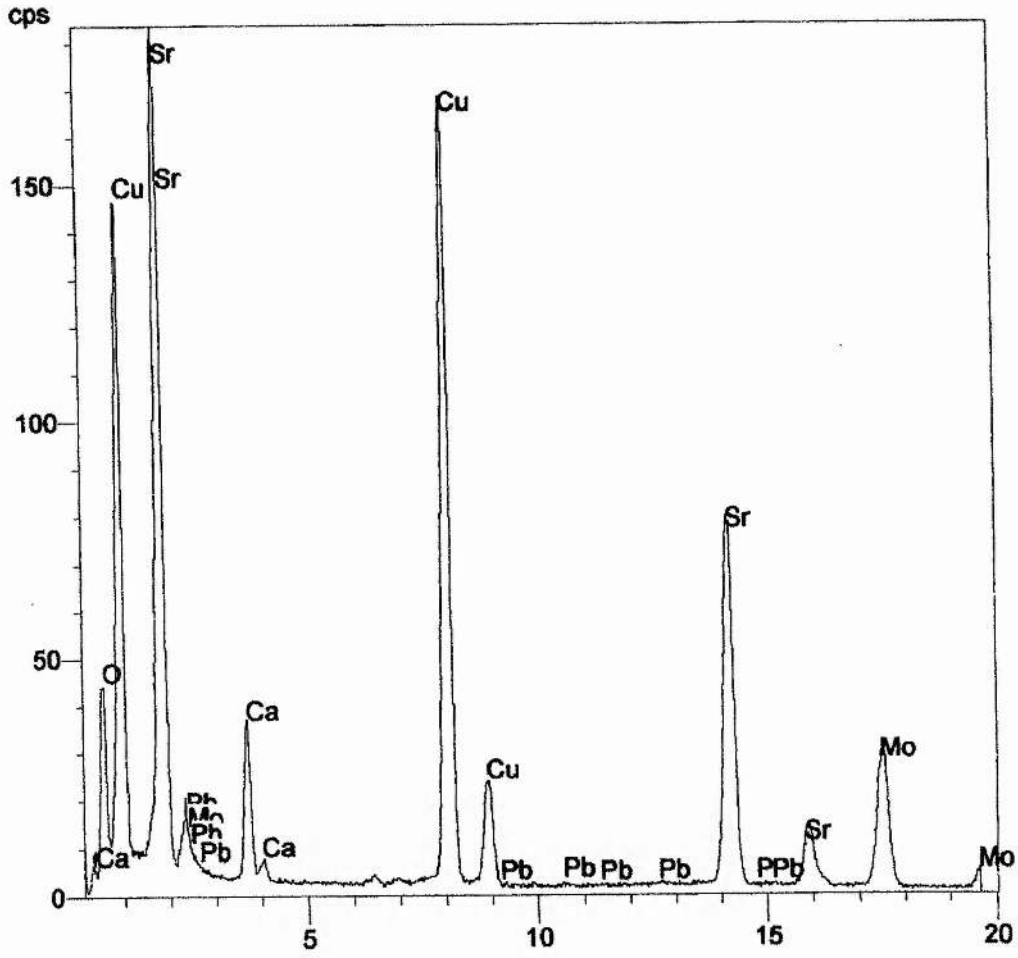

Figure 4.9. EDAX analysis of impurity phase

Using the sol-gel synthesis method, it was possible to synthesise samples in the series $(Pb_{(1+x)/2}Cu_{(1-x)/2})Sr_2(Y_{1-x}Ca_x)Cu_2O_{7\pm\delta}$ that were single-phase by XRD, up to and quite possibly beyond a Ca content of 0.3. For the x=0.4 samples, single-phase samples could only occasionally be attained despite keeping the same reaction conditions for different batches. Impurities were formed in all samples if the reaction conditions were varied too far off ideal values. Work on the same system by Maeda et al[4] showed that single-phase samples could not be formed when $x \geq 0.4$. Over the range x=0.5-0.7, the reaction requires a number of temperature increases to drive to completion. The amount of the $(Ca,Sr)CuO_y$ phase increases and quite probably the exsolution of other phases begins to occur. Figure 4.10(a-d) shows the impurity level varying over the compositional range $(Pb_{0.7}Cu_{0.3})Sr_2(Y_{0.6}Ca_{0.4})Cu_2O_y$

to $(Pb_{0.85}Cu_{0.15})Sr_2(Y_{0.3}Ca_{0.7})Cu_2O_y$. Of course judging by the level of impurities for these samples, then it is questionable that samples actually belong to this series at all. A similar effect to that in figure 4.10 is seen for samples with fixed Pb/Cu ratio e.g. $(Pb_{0.5}Cu_{0.5})Sr_2(Y_{1-x}Ca_x)Cu_2O_y$ as the Ca content rises.

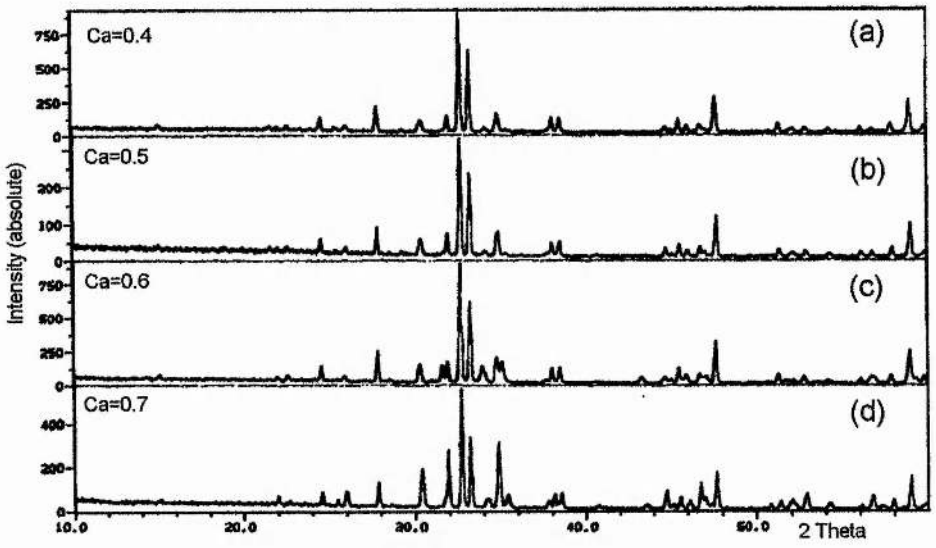

Figure 4.10. Impurity phase formation relative to Ca content.

Above x=0.7 the intermediate phase becomes more stable and dominant, and indeed upon reaching the Ca end member with nominal composition ($Pb_1Sr_2Ca_1Cu_2O_y$) no 1212 phase is formed, figure 4.11. Further raising the reaction temperature only leads to exsolution of the "SrCuO" type impurity phases, figure 4.12.

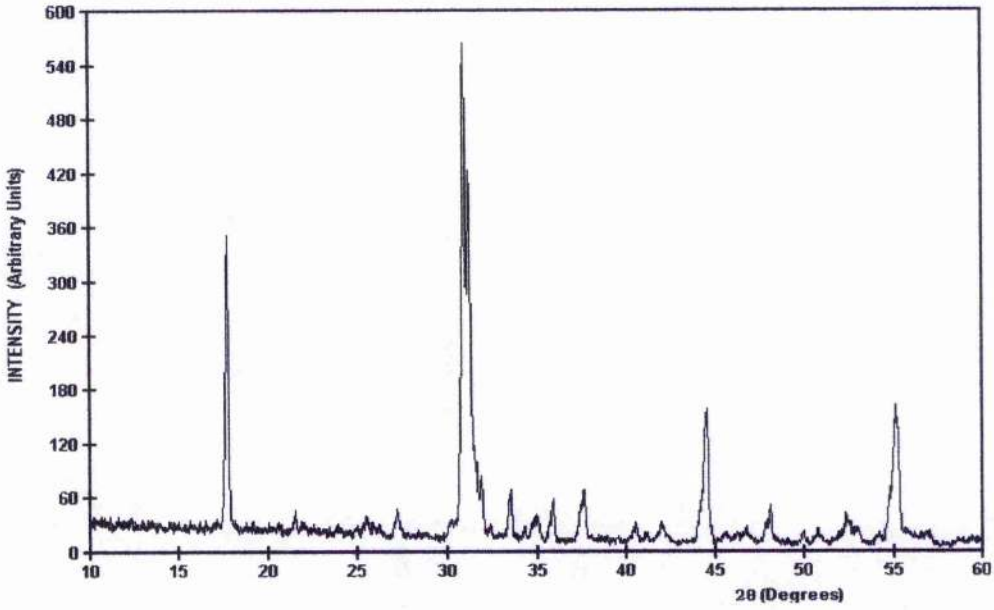

Figure 4.11. Intermediate phase dominating at high Ca levels.

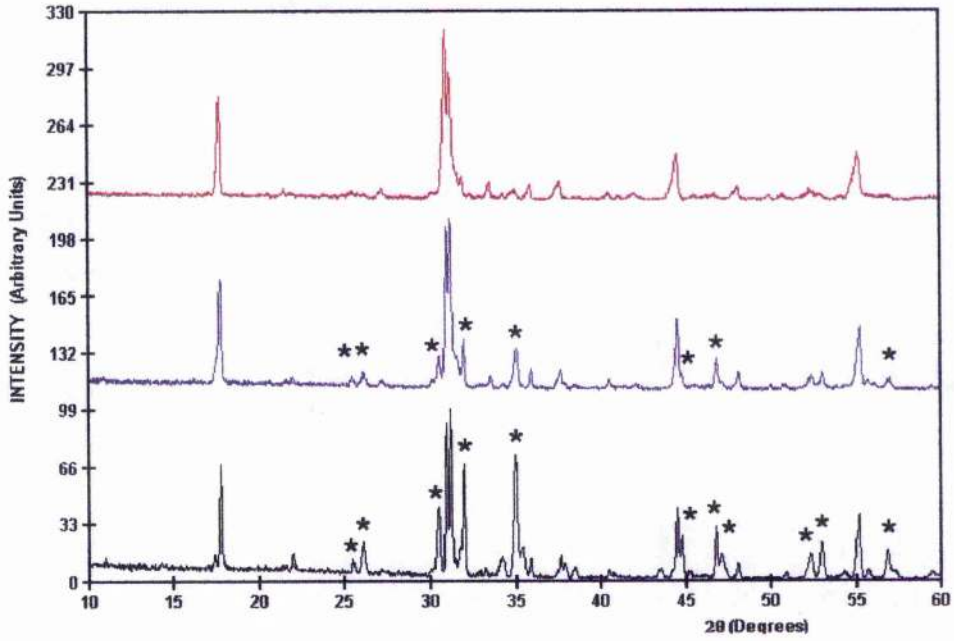

Figure 4.12. Emergence of the "SrCuO" impurity phases.

On first inspection, the intermediate appears similar to the hexagonal phases reported by Kim et al[10] or $Pb_{2.07}Sr_3Cu_{0.73}O_{7.70}$ reported by Ketaguchi et al[11]. This phase can be indexed as a hexagonal cell with lattice parameters **a** ≈9.94Å and **c** ≈6.94Å, smaller than reported previously[10,11]. However, these reported phases do not show the split

peaks that are evident in the intermediate phase. It would appear that this phase is probably hexagonal, but clear differences exist in both composition and space group.

4.2. 1212 phase stability

When the reaction temperature is too low, then the conversion of hexagonal phase to 1212 product essentially stops. Increasing the temperature drives the reaction forward but may lead to exsolution of impurities. Whether O_2 or air is used during synthesis the results are the same. To study the behaviour of the 1212 phase under synthetic conditions, thermogravimetry in a flowing O_2 environment and subsequent XRD analysis have been used.

4.21. Thermogravimetric behaviour under reaction conditions

The Thermogravimetric behaviour for a single-phase sample of composition $(Pb_{0.65}Cu_{0.35})Sr_2(Y_{0.7}Ca_{0.3})Cu_2O_y$, which had been previously annealed under flowing O_2 followed by slow cooling is shown in figure 4.13. The temperature profile during the run is also shown in this figure. In cycles 1 and 2 (maximum temperature 900°C), the sample loses weight on heating and regains it upon cooling. There is no apparent weight loss in the sample at the end of these two cycles, the sample is merely losing and regaining oxygen from a rocksalt layer site and this is not important with respect to decomposition discussed in section 4.22. In cycles 3 and 4 (maximum temperature 950°C) the same weight loss and gain can be seen; however, there is a more pronounced weight loss stage above 920°C. The final weight at the end of each stage is less than at its beginning, section 4.23.

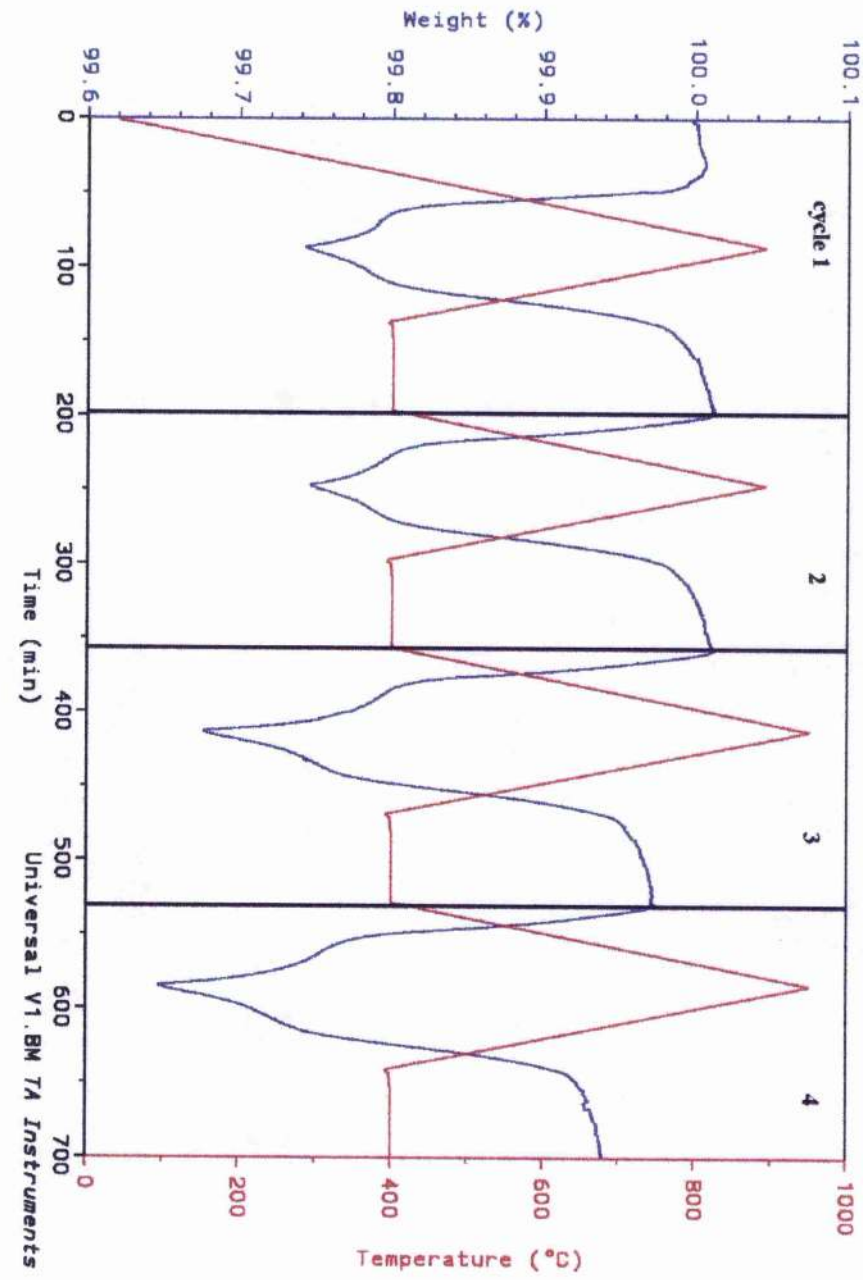

Figure 4.13. TGA plot for $(Pb_{0.65}Cu_{0.35})Sr_2(Y_{0.6}Ca_{0.4})Cu_2O_y$ heated/cooled in O_2 environment.

4.22. Cycles 1 and 2

The TGA behaviour in cycles 1 and 2 can be presented in a much clearer fashion, figure 4.14. The plot may be divided into five sections numbered I-V. Sections I and V where oxygen is lost from the rocksalt layer and regained on cooling has been described previously. Within section II the rate of weight loss is small and minimal weight loss occurs, while the sample is showing some weight loss in section III. On cooling, the section III loss is reversed in section IV. XRD analysis on samples that were subject to cycles 1 and 2 remained single-phase, as they were at the beginning of the experiment.

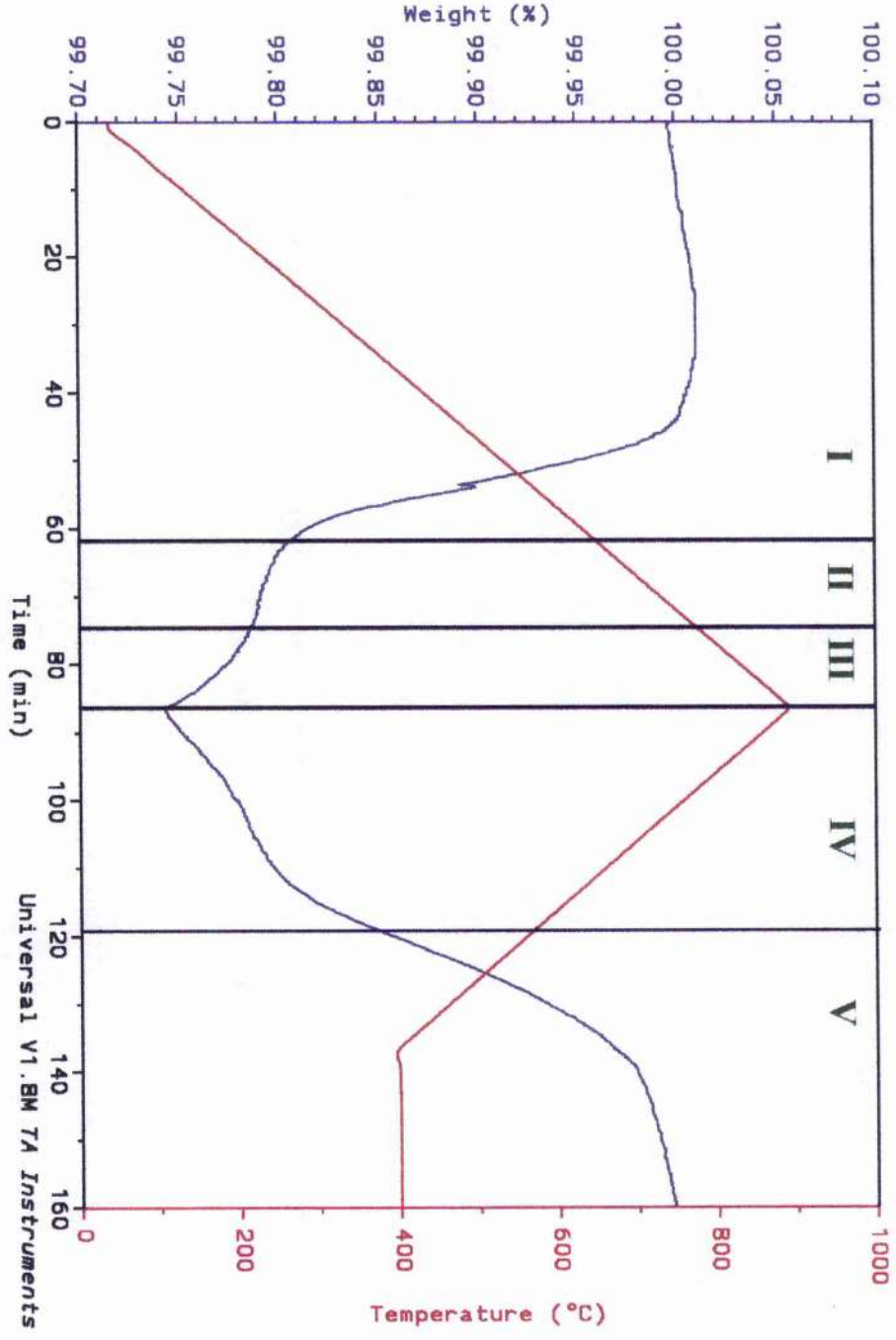

Figure 4.14. Events occurring within cycle 1 for $(Pb_{0.65}Cu_{0.35})Sr_2(Y_{0.6}Ca_{0.4})Cu_2O_y$ heated/cooled in O_2 environment.

In section II the oxygen content is 7.0 where the Pb and Cu are expected to be in 4+ and 2+ states respectively. Since all of the Pb is present as Pb^{4+}, as discussed in chapter 2 and from the EXAFS experiment discussed fully in chapter 5, then in section I some of the Cu must be present as Cu^{3+}. Section III corresponds to oxygen contents below 7.0 and it may be assumed that $Cu^{2+} \rightarrow Cu^{+}$ or possibly $Pb^{4+} \rightarrow Pb^{2+}$. In section IV any Cu^{+} or Pb^{2+} revert back to Cu^{2+} and Pb^{4+}, and within section V $Cu^{2+} \rightarrow Cu^{3+}$. Taking figure 4.14 and presenting differently in figure 4.15, the possible events occurring within the sample as the oxygen content varies are shown.

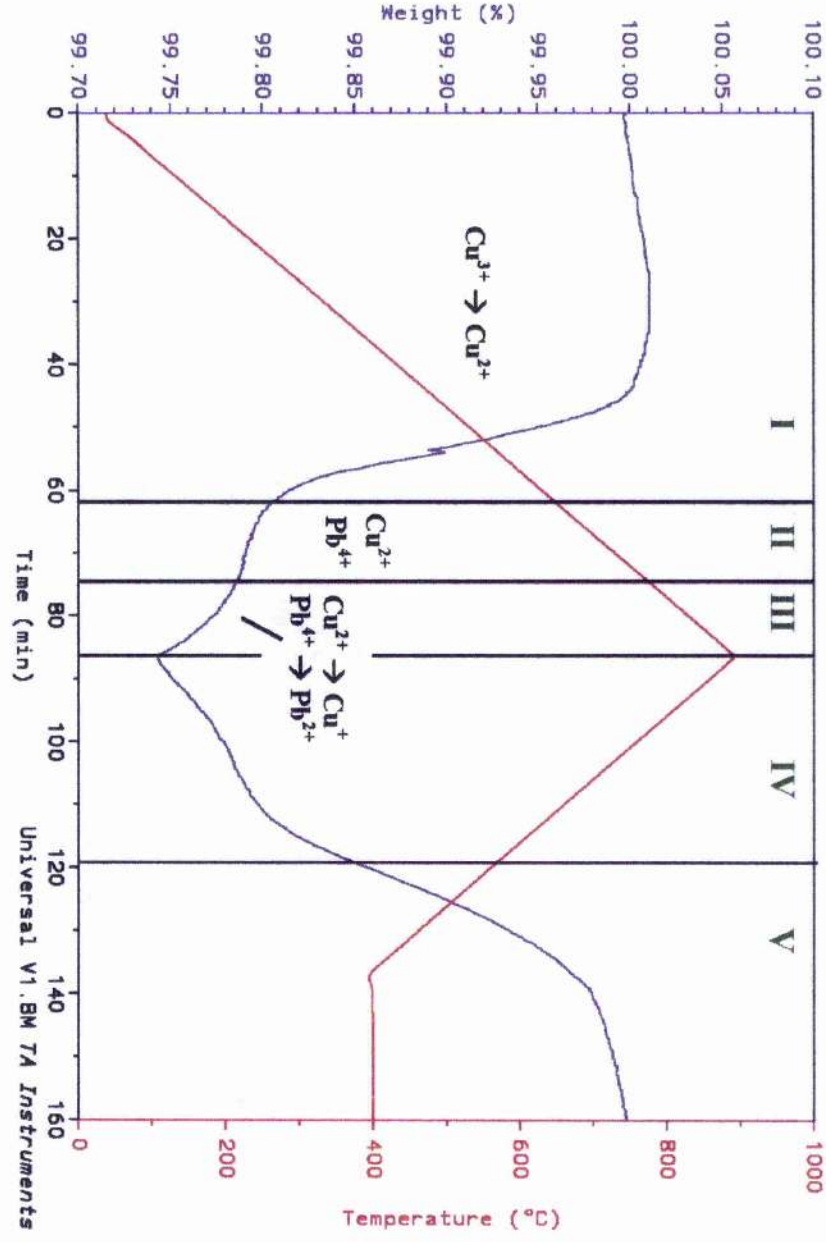

Figure 4.15. Variation in Pb and Cu oxidation states as a function of temperature within cycle 1 for $(Pb_{0.65}Cu_{0.35})Sr_2(Y_{0.6}Ca_{0.4})Cu_2O_y$.

4.23. Cycles 3 and 4

In figure 4.16, sections I and II are exactly the same as discussed in 4.22. The section III weight loss though is clearly larger when the maximum temperature is greater. Upon cooling the re-entry of oxygen into the rocksalt layer, section V, is the same size as in section I. However, there is a clear discrepancy in the section IV weight gain, which results in the sample weight being less at the end of a cycle than it was at the beginning. In section 4.22 it was possible to show that the oxygen content of the sample can fall below the 7.0 value and reveal no changes in the XRD pattern upon cooling. The results above show that the sample only remains stable up to a critical oxygen content and confirms the results seen when sample preparation conditions vary too far from ideal values. The XRD plots in figure 4.17 below show the appearance of an impurity phase after being through cycles 1-4.

Repeating the TGA experiment for samples that have a greater Ca content e.g. $(Pb_{0.7}Cu_{0.3})Sr_2(Y_{0.6}Ca_{0.4})Cu_2O_y$, the result is the same as that discussed previously. The onset of stage III, however, shifts to slightly lower temperatures, as more Ca is present. Conversely, for samples which have lower Ca contents
e.g. $(Pb_{0.6}Cu_{0.4})Sr_2(Y_{0.8}Ca_{0.2})Cu_2O_y$ the temperature at which stage III starts to occur shifts to slightly higher temperatures and the loss in this stage occurs at 950°C.

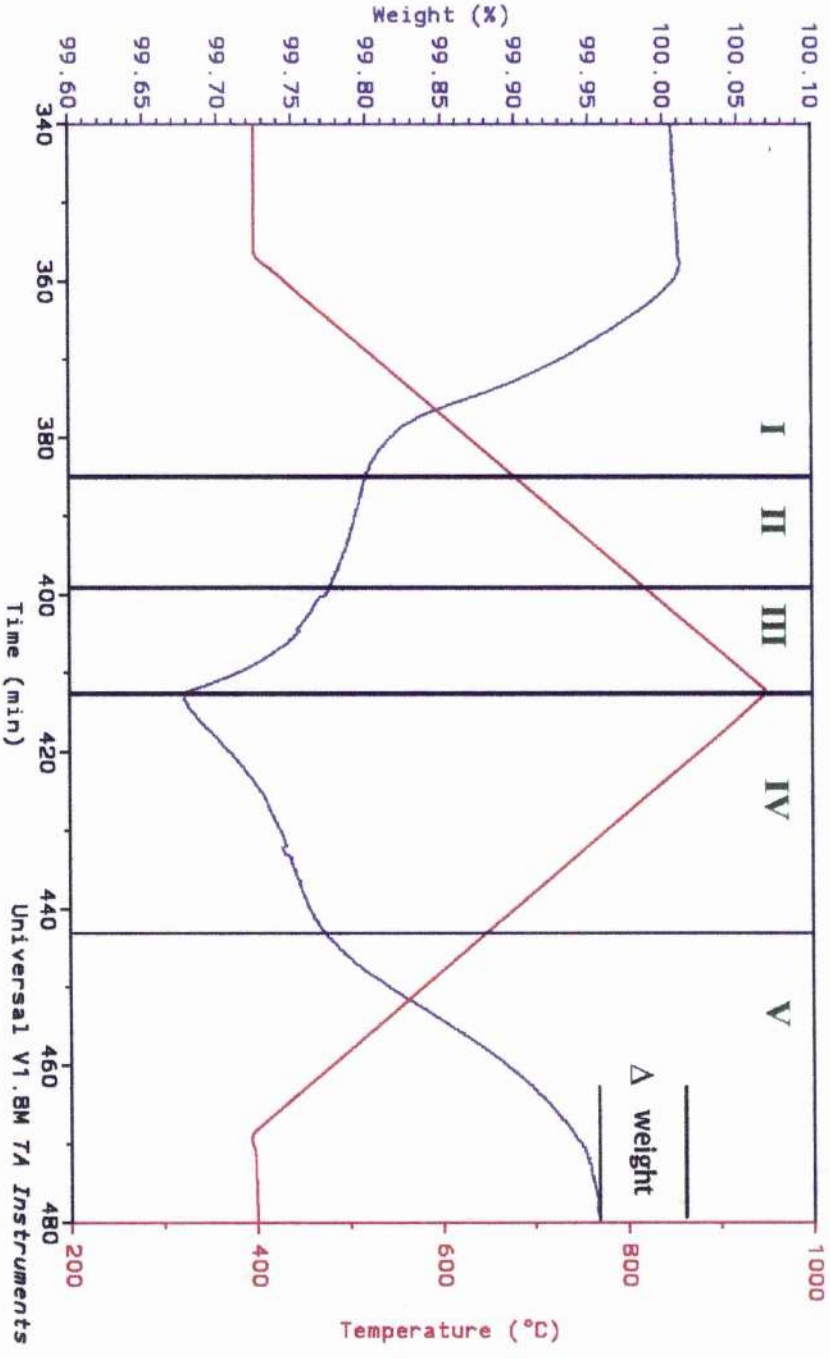

Figure 4.16. Cycle 3 from TG plot for $(Pb_{0.65}Cu_{0.35})Sr_2(Y_{0.6}Ca_{0.4})Cu_2O_y$ heated/cooled in O_2 environment.

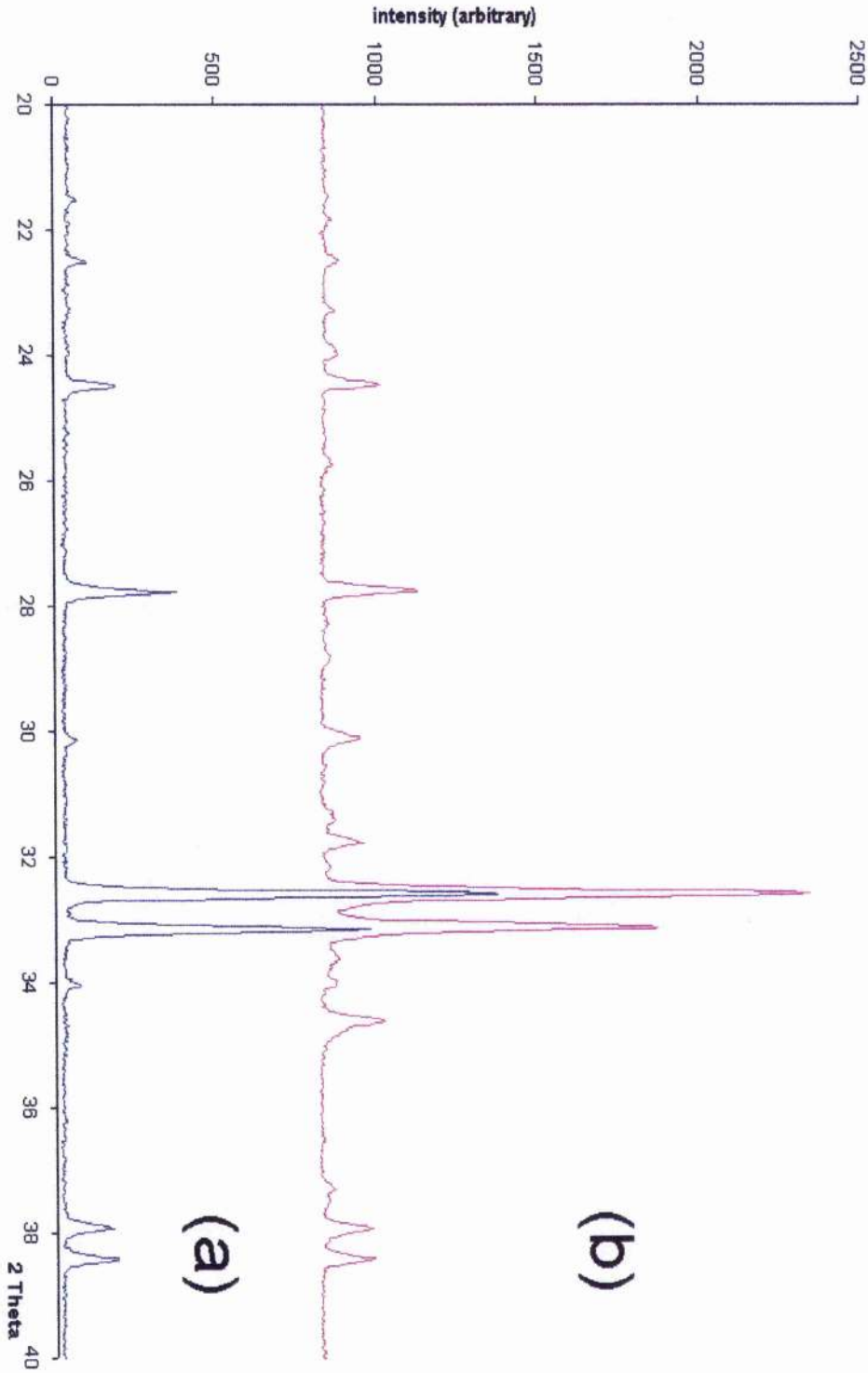

Figure 4.17(a). $(Pb_{0.65}Cu_{0.35})Sr_2(Y_{0.7}Ca_{0.3})Cu_2O_y$ before TGA experiment. 4.17(b) appearance of impurity after cycles 1-4.

4.24. Air annealed and cooled samples, thermogravimetric behaviour

Samples that have been annealed and slow cooled in air, figure 4.18, show the following behaviour when cycled as described previously. The principal difference lies in the first cycle in which there is a noticeable weight difference between the beginning and end of the cycle. The actual weight loss on heating is larger than is normally seen for samples annealed only in O_2 and the derivative of the weight loss plot shows two distinct events, figure 4.19.

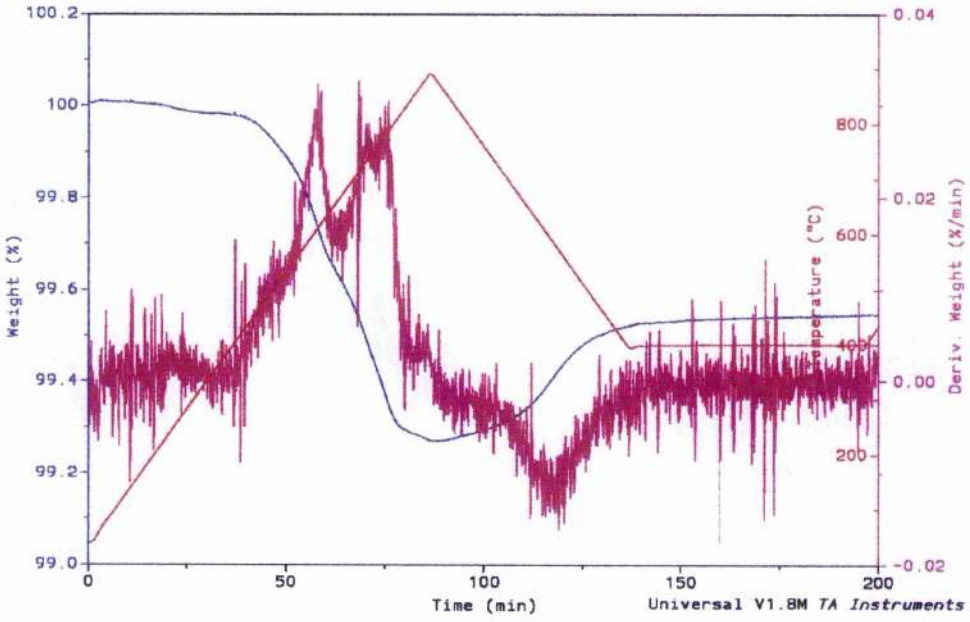

Figure 4.19. Derivative weight loss plot in cycle 1.

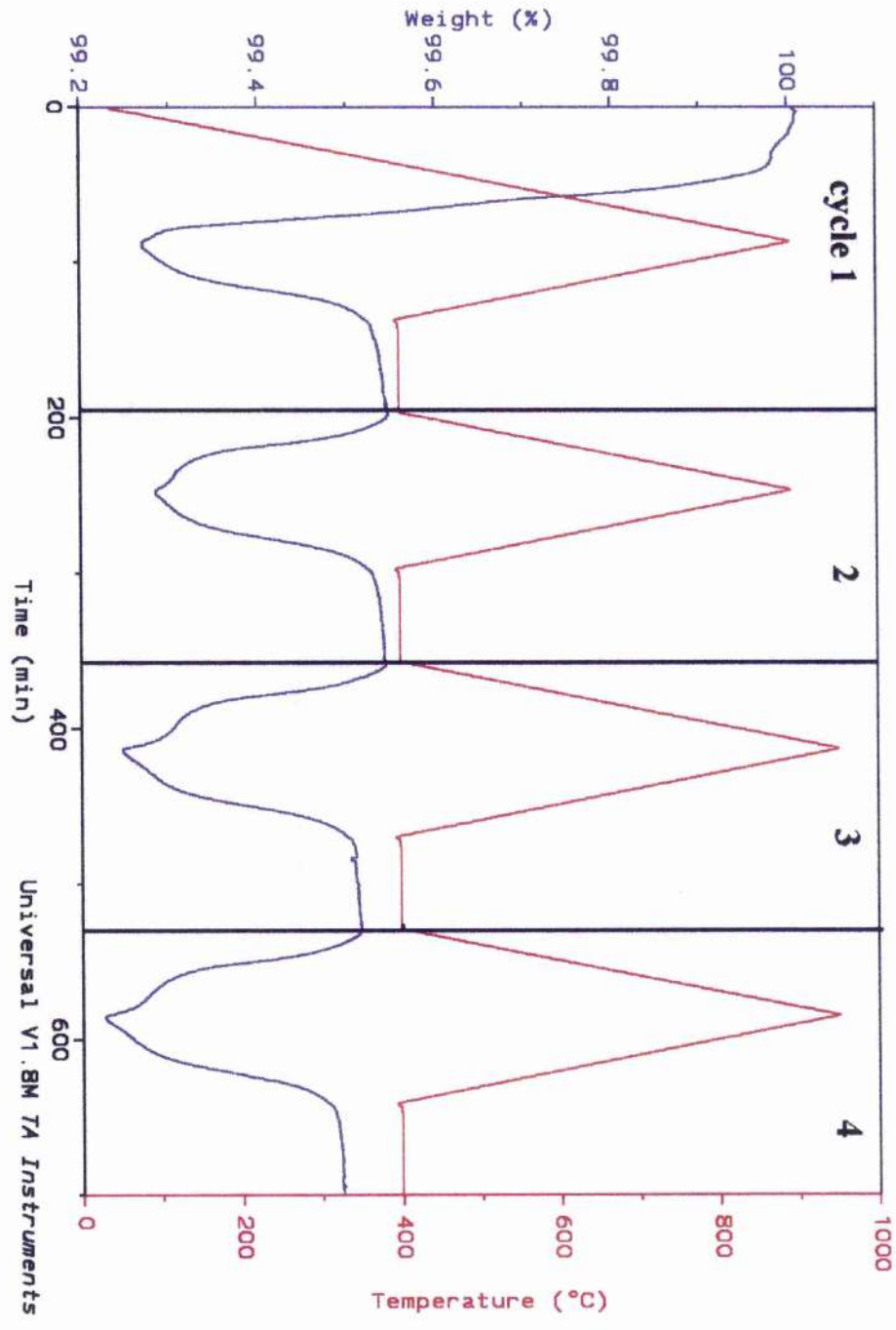

Figure 4.18. TGA plot for $(Pb_{0.65}Cu_{0.35})Sr_2(Y_{0.7}Ca_{0.3})Cu_2O_y$ sample heated/cooled in air environment.

The weight loss is most probably due to the loss of CO_2 from the material, since N_2 in air cannot be responsible. To prove that the CO_2 loss was not from carbonates still present from air annealing, an O_2 annealed sample was first checked by TGA and found to behave as seen in figure 4.13. After annealing and slow cooling in air, however, it showed the same behaviour on heating, figure 4.20, as seen in figure 4.19.

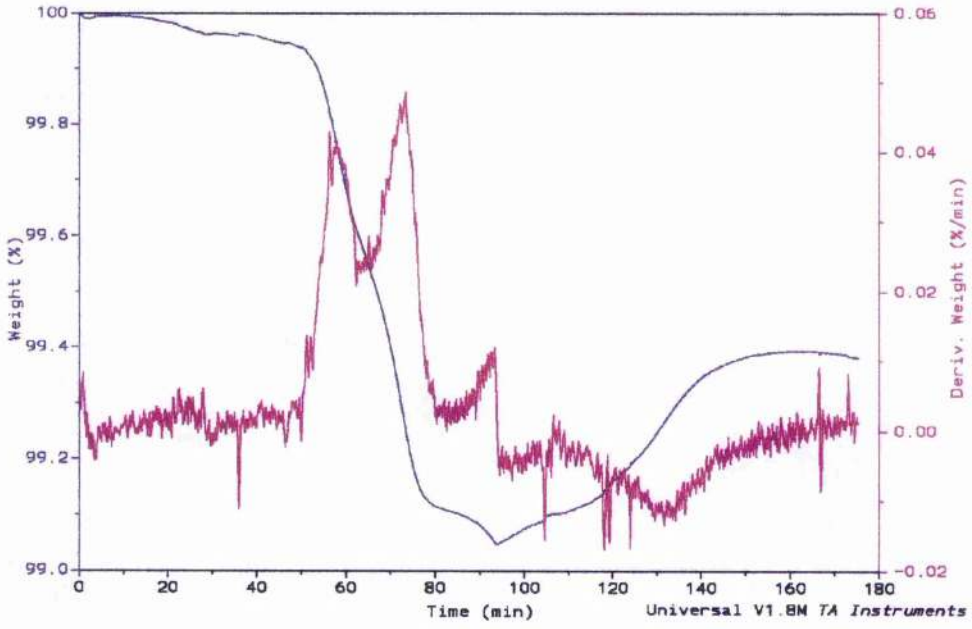

Figure 4.20. Air annealed and slow cooled sample heated in TGA.

A TGA experiment was then performed on a 1212 sample in a 5%CO_2/95%N_2 environment, figure 4.21. The sample was heated at 10°C.min^{-1} and shows no weight change until ~550°C where there is a sudden weight increase, when CO_2 must enter the 1212 structure. The weight gain levels off at ~750°C before a weight loss is seen upon further heating, but there is not a return to the original starting weight. The XRD patterns using 5% CO_2 and 100% CO_2 environments, figure 4.22(a,b) respectively, show complete destruction of the 1212 phase to a mixture of carbonates.

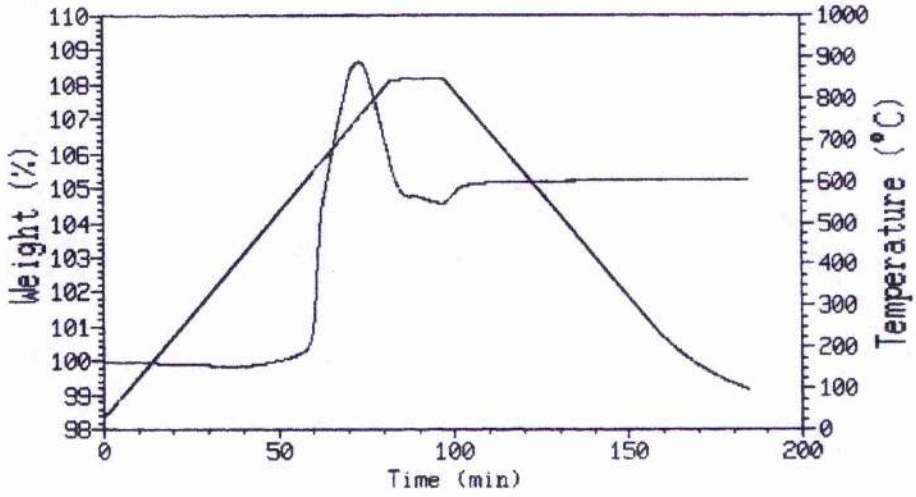

Figure 4.21. Effect of CO_2 on 1212 sample.

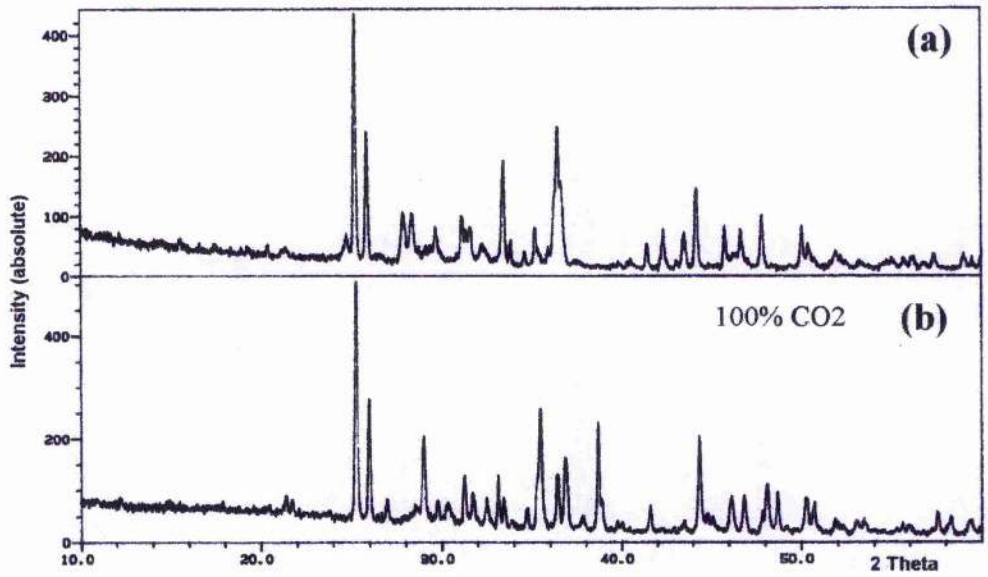

Figure 4.22. Destruction of 1212 phase after annealing in CO_2 environment.

Annealing impure 1212 samples containing (Ca,Sr)CuO_y e.g. $(Pb_{0.7}Cu_{0.3})Sr_2(Y_{0.6}Ca_{0.4})Cu_2O_y$ in air over the temperature range 500-545°C for times

greater than 240 hours results in the impurity phase disappearing, figure 4.23. $SrCO_3$ and CuO are now evident in the diffraction pattern with no apparent effects on the main 1212 phase itself. By carefully heating this sample up to 775°C in air as shown in figure 4.24 top, the $SrCO_3$ and CuO are removed, and although the impurity phase returned it was dramatically reduced in its amount.

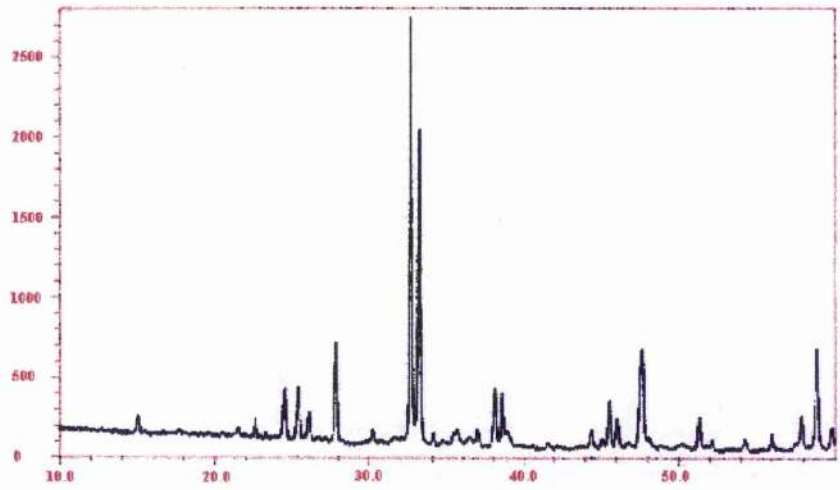

Figure 4.23. 1212 phase annealed in air at 530°C for 240 hours.

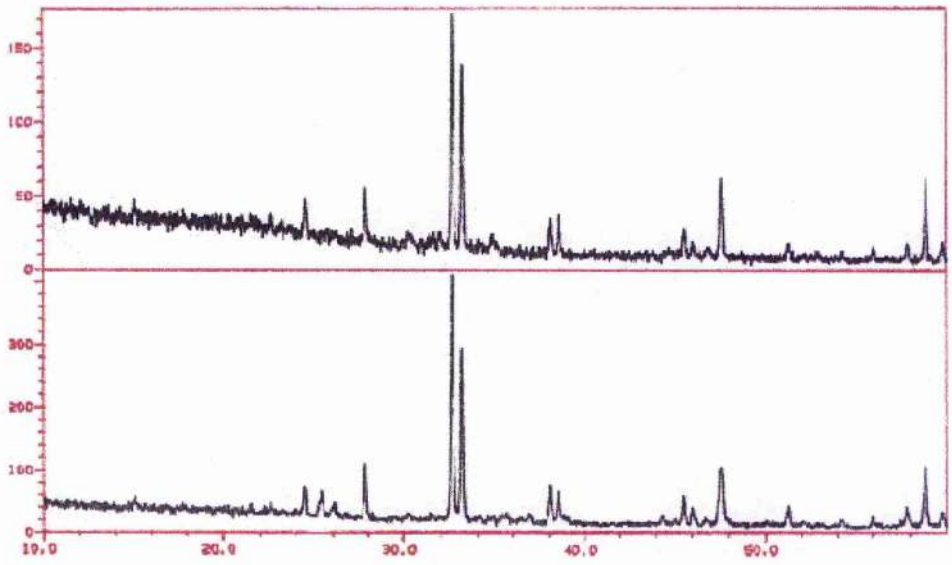

Figure 4.24. Top section of diagram shows the1212 phase heated to 775°C in air, the bottom section is that shown in figure 4.23.

4.3. Summary

Formation of the 1212 phase has been shown not to proceed directly from sample precursors to product, but instead proceeds through an intermediate phase. This hexagonal intermediate phase has previously been labelled as an impurity phase by a number of groups[3-5], however, it is quite clear that this is an intermediate through which formation of the 1212 phase proceeds. The general composition given is $Pb_{2.07}Sr_3Cu_{0.73}O_{7.70}$, but this would appear incorrect from unit cell size and the splitting of certain peaks, which was seen in the intermediate phase. It does seem clear that the intermediate phase is hexagonal, but spacegroup and composition are unknown.

In the samples of series $(Pb_{[1+x]/2}Cu_{[1-x]/2})Sr_2(Y_{1-x}Ca_x)Cu_2O_{7\pm\delta}$ then the stability of the intermediate phase is such at higher Ca levels that it begins to dominate the XRD pattern and indeed at the Ca end member $Pb_1Sr_2Ca_1Cu_2O_y$ the 1212 phase cannot be formed at all. The only method of forming this type of 1212 sample is to use highly specialised high-pressure synthesis. Tamura et al[12] used 5 GPa pressure, but did not synthesise single-phase 1212 samples.

It is possible to synthesise single-phase samples in this series up to x=0.4 and above this a $(Ca,Sr)CuO_y$ impurity was found to be exsolved. This impurity phase becomes more prominent as the Ca level increases and indeed, higher temperatures were required to drive the reaction as far forward as possible. The sol-gel method produces good 1212 samples although the reaction temperatures essentially are the same as those used in a conventional solid-state synthesis. If the temperature is too low the conversion of the hexagonal intermediate to the 1212 phase stops; however, too high a reaction temperature may drive the reaction forward but impurity formation is excessive. The ideal reaction temperature is a fine balance and it varies with composition. TGA analysis of samples under normal reaction conditions revealed the 1212 phase to be unstable. Loss of the $(Ca,Sr)CuO_y$ impurity was found to occur as the oxygen content of the sample dropped below a critical value and this reaction was also irreversible. With increasing Ca content, the temperature at which the phase instability occurred lowered.

Applying high oxygen pressure during synthesis was used by Tang et al[13] and it seems that the (Ca,Sr)CuO_y impurity formation was prevented, certainly in samples of nominal composition $(Pb_{0.5}Cu_{0.5})Sr_2(Y_{0.5}Ca_{0.5})Cu_2O_y$.

The formation of all compositions in the series $(Pb_{[1+x]/2}Cu_{[1-x]/2})Sr_2(Y_{1-x}Ca_x)Cu_2O_{7\pm\delta}$ where x=0-1 is not possible using atmospheric pressure techniques and the formation of single-phase 1212 product is actually limited to a very small range. This makes the study of this complete solid solution impossible.

4.4. Bibliography and references for chapter 4

[1] M.A. Subramanian, J. Gopalakrishnan, C.C. Torardi and P.L. Gai, *Physica C*, 1989, **157**, 124.

[2] J.Y. Lee, J.S. Swinnea and H. Steinfink, *J. Mat. Res.*, 1989, **4**, 763.

[3] R.S. Liu, S.F. Hu, I. Gameson and P.P. Edwards, *J. Solid State Chem.*, 1991, **93**, 276.

[4] T. Maeda, K. Sakuyama, F. Izumi, H. Yamauchi, H. Asano and S. Tanaka, *Physica C*, 1991, **175**, 393.

[5] S. Adachi, H. Adachi, K. Setsune and K. Wasa, *Jpn. J. Appl. Phys.*, 1991, **30**, L690.

[6] A.R. Armstrong, PhD thesis, Cambridge University, 1985.

[7] H. Yamane, Y. Miyazaki, T. Hirai, *J. Ceram. Soc. Jpn. Inter Ed.*, 1989, **97**, 140.

[8] Y. Skolis et al, *Moscow University Chemistry Bulletin*, 1991, **38**, 45.

[9] R.D. Ray, E.E. Hellstrom, *Physica C*, 1991, **175**, 255.

[10] J.S. Kim, X.X. Tang, A. Manthiram, J.S. Swinnea and H. Steinfink, *J. Solid State Chem.*, 1990, **85**, 44.

[11] H. Kitaguchi, J. Takada, K. Oda and Y. Miura, *J. Mat. Res.*, 1990, **5**, 1397.

[12] T. Tamura, S. Adachi, X.J. Wu, C.Q. Jin, T. Tatsuki and H. Yamauchi, *Physica C*, 1995, **249**, 111.

[13] X.X. Tang, D.E. Sinha and A.P.B. Sinha, *Phys. Rev. B*, 1991, **43**, 7936.

Chapter 5. STRUCTURE AND DISORDER

5.1. Structural overview

5.11. Idealised structure of 1212

First discovered by Subramanian et al[1] and Lee et al[2], the so-called 1212 phase has shown some particularly exciting chemistry, especially from addition of Tl. The structure itself is quite interesting, but the simplest way to describe it is to start from the well known 123 compound $YBa_2Cu_3O_{7-\delta}$, figures 5.1 and 5.2.

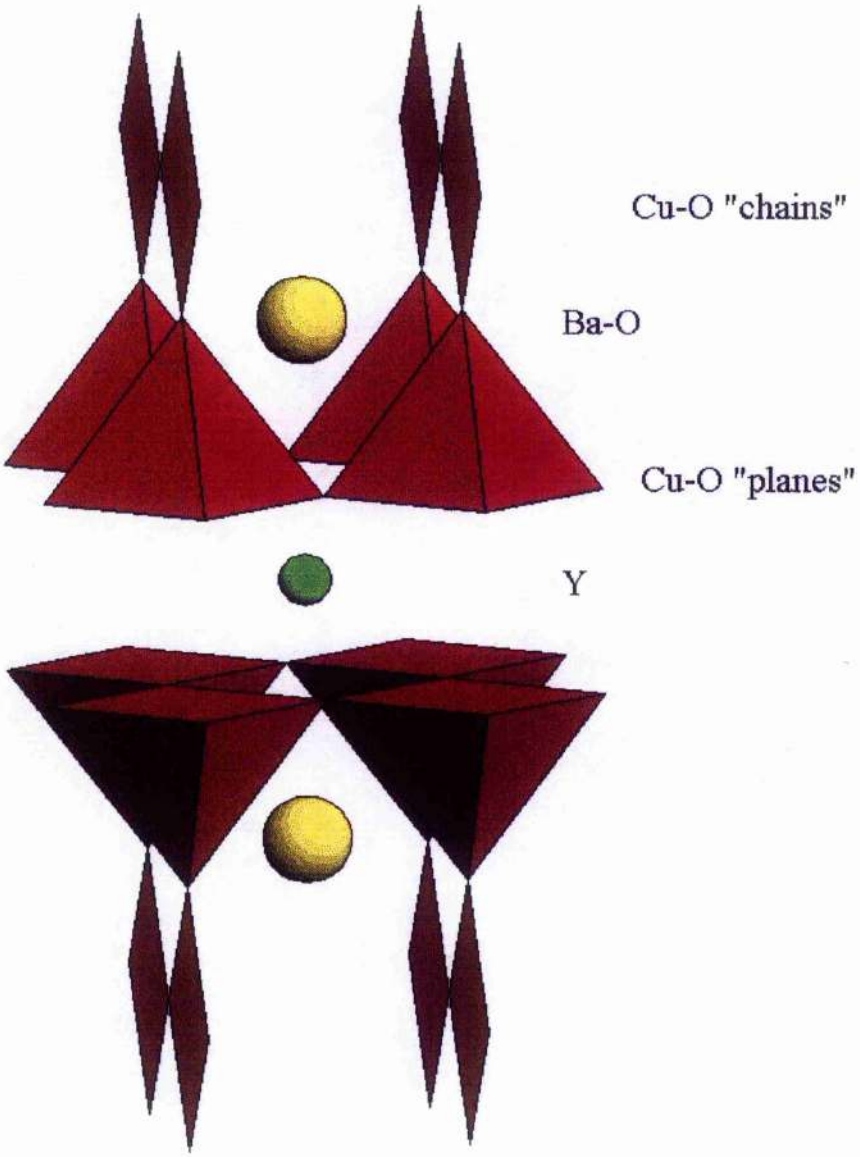

Figure 5.1. Structure of $YBa_2Cu_3O_7$ showing chain sites.

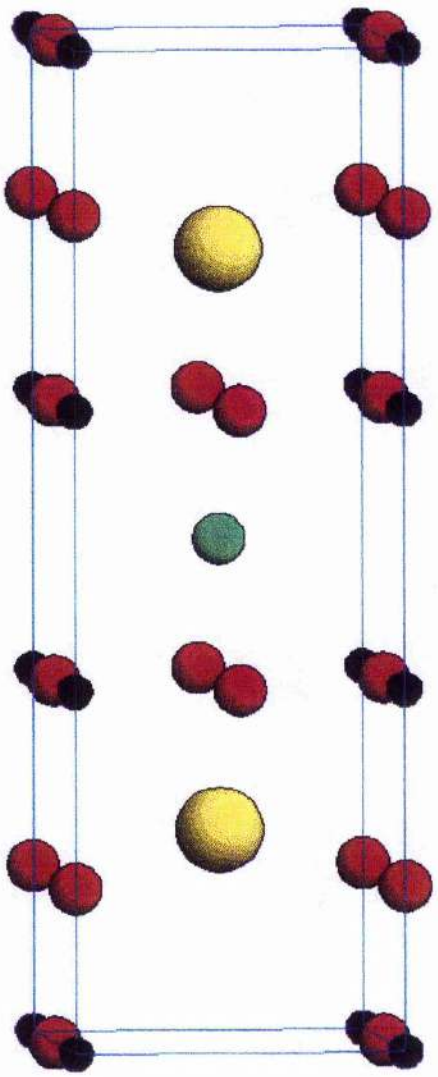

Figure 5.2. Structure of $YBa_2Cu_3O_7$.

Each Cu atom on the CuO_2 plane is co-ordinated to five oxygen atoms forming a $[CuO_5]$ pyramid. The CuO_2 plane is sandwiched between Y and BaO planes. In its fully oxygenated form, the oxygen in the charge reservoir layer preferentially occupies the (0,½,0) position and the structure is determined to be orthorhombic (space group Pmmm) with **a** ≈ 3.82Å, **b** ≈ 3.88Å and **c** ≈ 11.68Å. It is possible to remove the oxygen fully from the charge reservoir layer to leave $YBa_2Cu_3O_6$, which has a tetragonal structure (space group P4/mmm), figure 5.3.

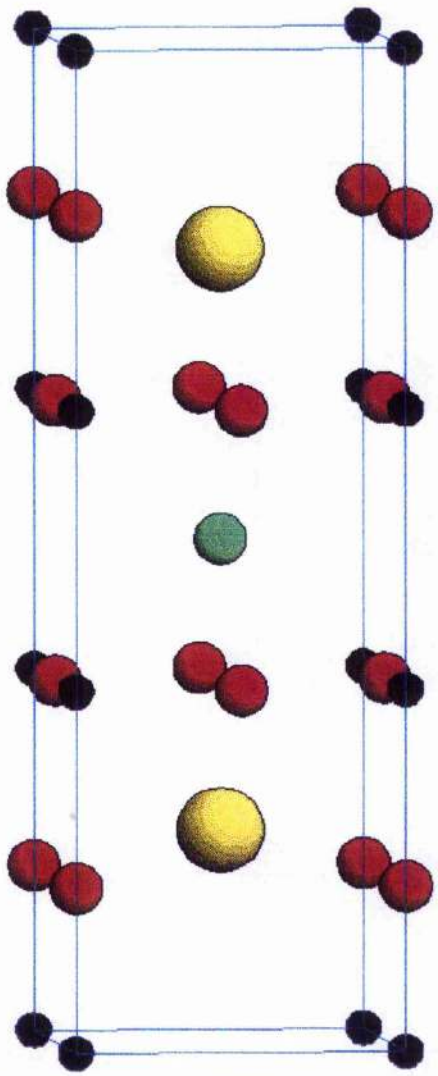

Figure 5.3. Structure of $YBa_2Cu_3O_6$.

Replacing Ba^{2+} (1.47Å at CN=10) with Sr^{2+} (1.32Å at CN=10) does not lead to the formation of $YSr_2Cu_3O_7$. This phase is not stable and may only be stabilised under high pressures[3] or by substituting elements such as W^{5+} for Cu[4]. Replacing Cu with some Pb on the charge reservoir layer does stabilise the structure; however, this layer changes structurally from perovskite type to a "rocksalt" configuration. The difference between the perovskite and rocksalt monolayers lies in the position of the oxygen. In $YBa_2Cu_3O_7$ this is (0,½,0) and in $(Pb,Cu)Sr_2YCu_2O_7$ this is (½,½,0). This latter structure is known as the 1212 structure, figure 5.4.

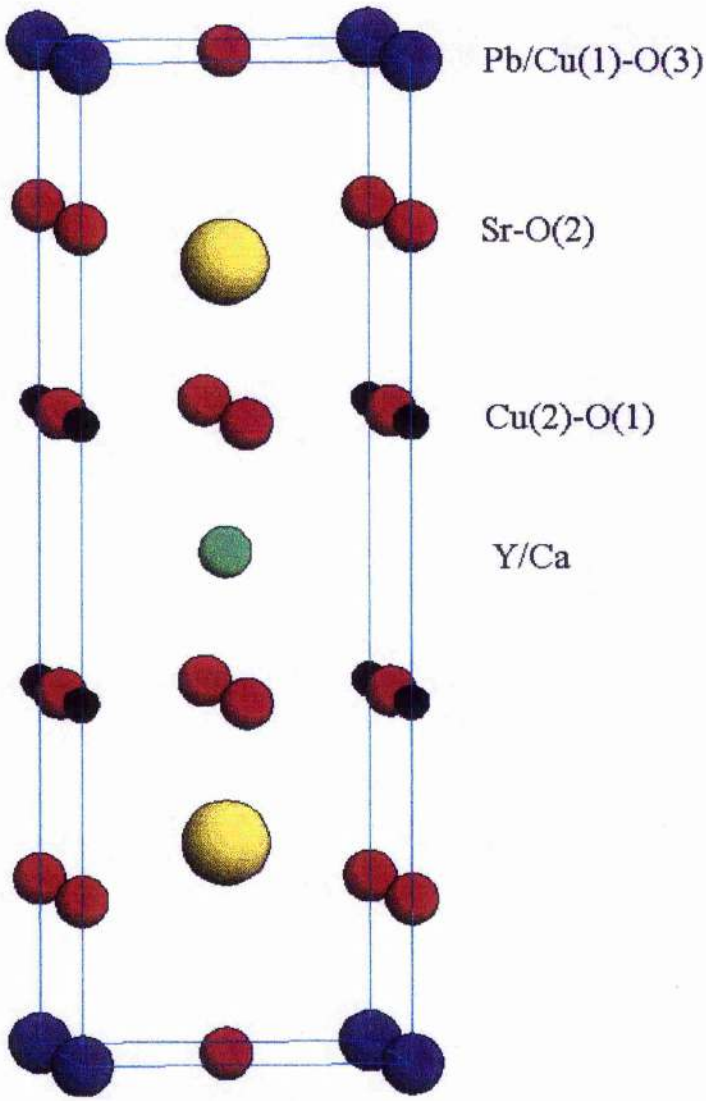

Figure 5.4. Idealised 1212 structure, atoms labelled.

The stacking sequence 1212 is essentially the same as that in $YBa_2Cu_3O_7$, but the structure belongs to a tetragonal system with space group P4/mmm. $YBa_2Cu_3O_7$ could also be described as a 1212 structure and if so is written not only as 1212 but also additionally as 1212P to show that it has a perovskite type charge reservoir layer.

The ideal structure is that shown in figure 5.4, with some important parameters summarised in table 5-1.

Atom	Site	x	y	z
Pb/Cu(1)	1a	0	0	0
Sr	2h	0.5	0.5	0.21
Y/Ca	1d	0.5	0.5	0.5
Cu(2)	2g	0	0	0.36
O(1)	4i	0	0.5	0.375
O(2)	2g	0	0	0.165
O(3)	1c	0.5	0.5	0

Table 5-1. Ideal atomic positions for a $(Pb,Cu)Sr_2(Y,Ca)Cu_2O_7$.

5.12. Rocksalt layer and cation disorder within structure

Studying the rocksalt layer more closely, figure 5.5, and assuming the standard cell edge of 3.82Å (**AB** and **BC** on diagram), then the length **AC** is 5.4Å. This leaves abnormally long bond lengths (2.7Å) between the Pb, O and/or Cu, thus the rocksalt oxygen is displaced from its (½,½,0) to a fourfold (x,½,0) site. Also, figure 5.6, there is evidence that the Pb and Cu atoms are displaced from their ideal (0,0,0) site to a (x,0,0) site, figure 5.6. In $(Pb,Cu)Sr_2(Y,Ca)Cu_2O_y$ it is possible to introduce a small excess of oxygen into the rocksalt layer. Maeda et al[5] showed this to be the 2f (0,½,0) site and estimated its amount to be approximately 0.1 oxygen's per formula unit. This excess proves to be detrimental to superconductivity.

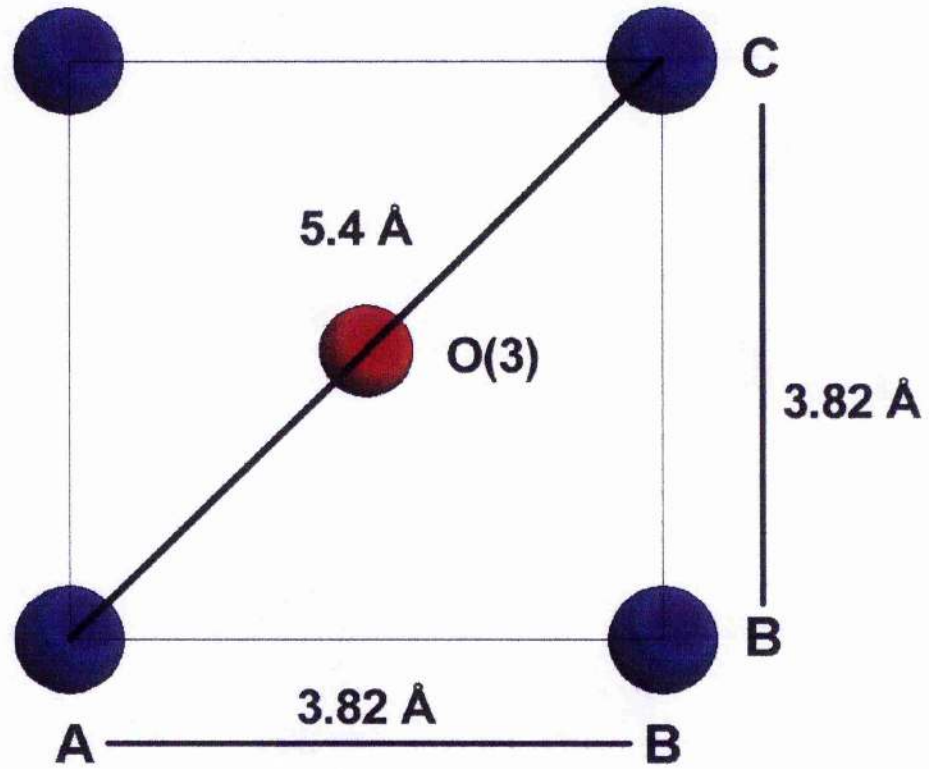

Figures 5.5. AB projection of rocksalt layer structure.

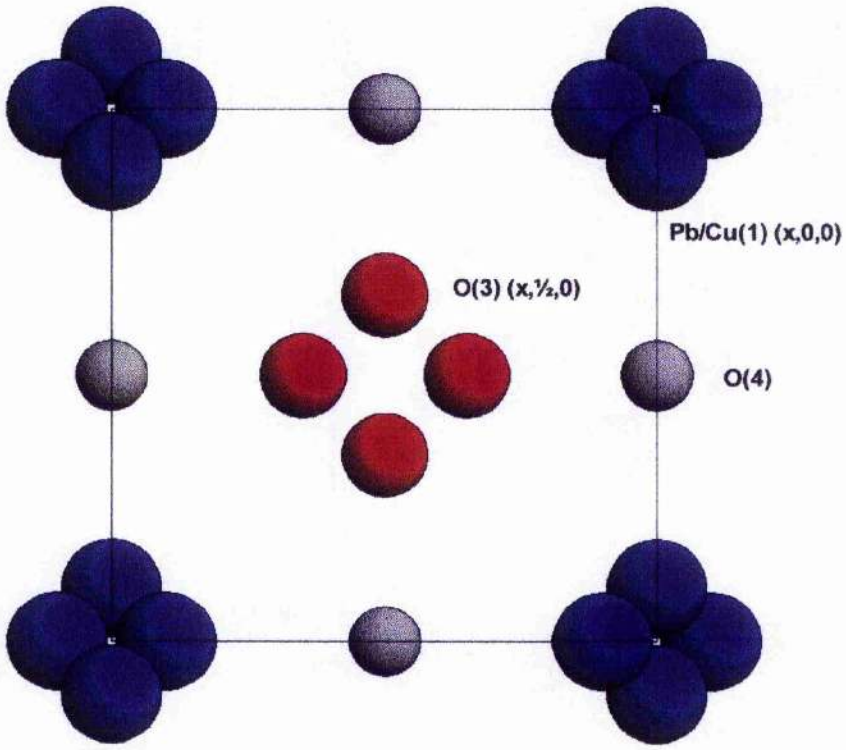

Figure 5.6. AB projection showing disorder in rocksalt layer.

Of course, it is possible to have a rocksalt configuration in which the Cu has been replaced by a number of different atoms, this was discussed in section 2.12. These elements are presented below in table 5-2.

Element	Charge	VI fold (Å)	VIII fold (Å)	X fold (Å)
Fe	3+	0.645 HS		
Ni	2+	0.70		
Mg	2+	0.720		
Cu	2+	0.73	-	
Bi	5+	0.74		
Zn	2+	0.745		
Fe	2+	0.77 HS		
Pb	4+	0.775	0.94	
Tl	3+	0.88		
Cd	2+	0.95		
Ca	2+	1.00	1.12	1.28
Bi	3+	1.02		
Hg	2+	1.02		
Sr	2+	1.16	1.25	1.32
Pb	2+	1.18		-
Y	3+	N/A	1.015	

Table 5-2. Effective ionic radii for a series of cations in different co-ordination environments. Data from Shannon[6].

With the exception of Fe and Ni that tend to occupy the Cu-O planes, it is possible to induce superconductivity with the elements above in the rocksalt layer in addition to Pb. The best onset temperatures have been found using elements which have an ionic radius larger than that of Pb^{4+} and it has never been clear whether or not Pb^{2+} is favoured in these cases. This research is not dealing with the size of rocksalt layer cation and effects on superconductivity and shall not be discussed further.

The (Y,Ca) site is an eight fold site, and column four in table 5-2 shows the ionic radius of some elements which can adopt this co-ordination. In a PbCu:1212 sample, there would appear to be the possibility for Sr and Pb to substitute onto this site. On the Sr ten-fold co-ordination site then the only possibility for substitution is Ca. For a sample of nominal composition $(Pb,Cu)Sr_2(Y,Ca)Cu_2O_y$, then the possible cation disorder may be as follows table 5-3.

Layer/Site	Disorder
Rocksalt layer	Ca, Sr and possibly Y
(Y,Ca) site	Pb and possibly Sr
SrO layer	Ca
CuO_2 planes	None of these other atoms prone to taking the pyramidal co-ordination that Cu does

Table 5-3. Possible cation disorder in $(Pb,Cu)Sr_2(Y,Ca)Cu_2O_y$.

What the above tries to show is the numerous possibilities that might exist for cation disorder in such a complex system. Whether or not this disorder enhances or degrades superconducting properties cannot be exactly determined; however samples containing several different elements would realistically be expected to have varying degrees of cation disorder. Disorder in $(Pb_{[1+x]/2}Cu_{[1-x]/2})Sr_2(Y_{1-x}Ca_x)Cu_2O_7$ is considered in sections 5.4 and 5.5.

5.2 Composition and effect on electronic properties

The system under study is $(Pb_{[1+x]/2}Cu_{[1-x]/2})Sr_2(Y_{1-x}Ca_x)Cu_2O_{7\pm\delta}$. A decrease in the positive charge induced by substitution of Ca^{2+} ions for Y^{3+} ions is completely offset by an increase in positive charge due to substitution of Pb^{4+} ions for Cu^{2+} ions. By quenching samples over the compositional range x = 0-0.6, so that the excess oxygen is removed and the nominal oxygen content of the sample is 7.0, magnetic susceptibility measurements show the following trend, table 5-4.

Ca (x)	Nominal composition	Max. onset temperature (K)
0	$(Pb_{0.5}Cu_{0.5})Sr_2YCu_2O_7$	-
0.2	$(Pb_{0.6}Cu_{0.4})Sr_2(Y_{0.8}Ca_{0.2})Cu_2O_7$	-
0.3	$(Pb_{0.65}Cu_{0.35})Sr_2(Y_{0.7}Ca_{0.3})Cu_2O_7$	35
0.4	$(Pb_{0.7}Cu_{0.3})Sr_2(Y_{0.6}Ca_{0.4})Cu_2O_7$	43
0.5	$(Pb_{0.75}Cu_{0.25})Sr_2(Y_{0.5}Ca_{0.5})Cu_2O_7$	25
0.6	$(Pb_{0.8}Cu_{0.2})Sr_2(Y_{0.4}Ca_{0.6})Cu_2O_7$	25

Table 5-4. Superconducting onset temperatures as a function of Ca content (x).

The results in some ways seem surprising considering there is no hole doping occurring; however, care must be taken with the results because the samples with an x value > 0.3 are not phase pure. In comparison to the x = 0.4 sample there is clearly a greater level of impurity in the x = 0.5 and x = 0.6 samples. Indeed it is not certain what the actual compositions of these samples are, figure 5.7. Thus, the actual superconducting onset temperatures are not necessarily representative of those which might be obtained if the sample had the exact nominal stoichiometry.

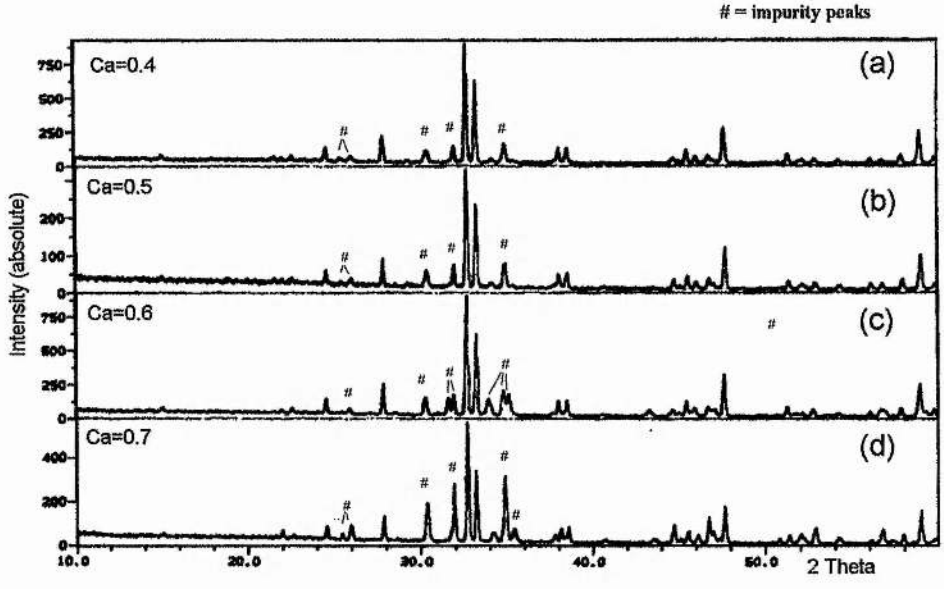

Figure 5.7(a-d). Impurity levels where Ca (x) = 0.5, 0.6 and 0.7 in comparison with Ca = 0.4.

5.3 Oxygen and its effect on electronic properties

In chapter 4, the role oxygen played in the stability of the 1212 phase was covered in depth. In this section, the role oxygen plays in controlling the electronic properties of the material shall be examined. Also the changes occurring in the oxidation states of some of the key elements shall be covered as the sample oxygen content varies.

Samples of nominal composition $(Pb_{0.7}Cu_{0.3})Sr_2(Y_{0.6}Ca_{0.4})Cu_2O_{7.1}$ were annealed in a flowing O_2 environment and quenched from a number of temperatures covering the range 400-950°C and subsequently subjected to magnetic susceptibility measurements. The results are summarised in table 5-5 and figures 5.8-5.9.

Annealing temperature (°C)	Onset temperature (K)
400	-
500	-
600	25
650	31
700	39
750	45
800	45
850	45
900	39
950	31

Table 5-5. Annealing temperature versus superconducting onset temperature

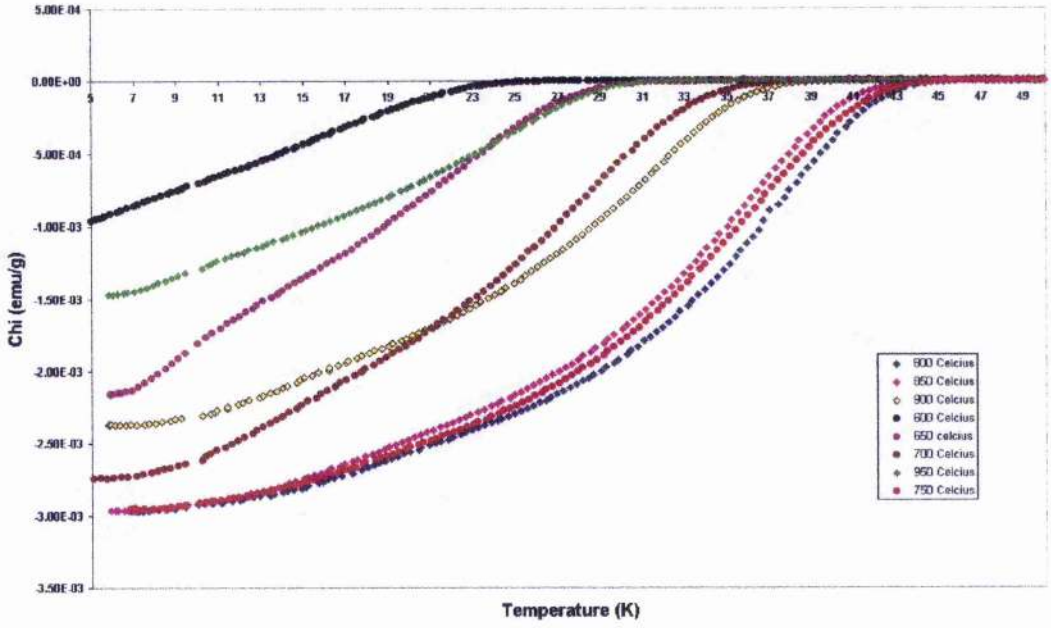

Figure 5.8 Magnetic susceptibility data as a function of annealing temperature. Legend shows the temperature from which samples have been quenched.

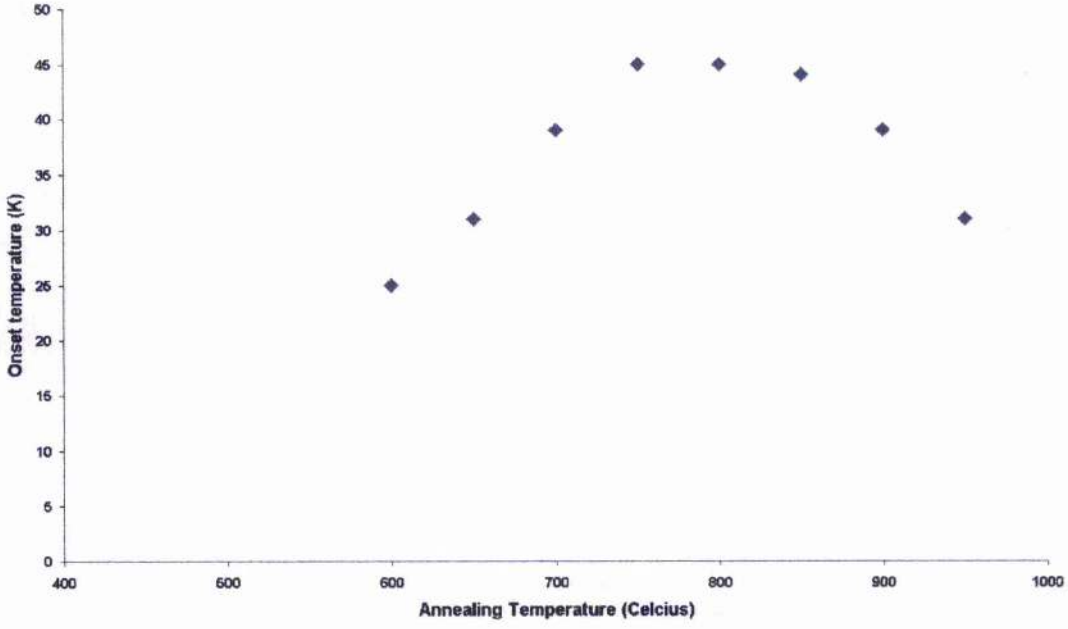

Figure 5.9. Superconducting onset as a function of annealing temperature.

The figures and tables above show quite clearly that the onset temperature and the superconducting volume fraction are affected by annealing temperature. Superconductivity is only induced when the annealing temperature is ≥ 600°C and the

onset temperature increases steadily reaching a maximum over the range 750 to 850°C before falling off above this point. The absolute magnetisation trend in samples also follows the same trend and it would appear that 800°C is the optimal safe annealing temperature for this composition. Studying the TGA plot for such a sample which has been fully oxygenated by annealing under flowing O_2 at 400°C figure 5.10, it is possible to ascribe oxygen content values in the sample as a function of annealing temperature. The FW of $(Pb_{0.7}Cu_{0.3})Sr_2(Y_{0.6}Ca_{0.4})Cu_2O_7$ is ~680 and the addition of a theoretical 0.1 excess oxygen leads to approximately 0.25% increase in weight. If it is assumed that the oxygen content of the sample is 7.00 at 800°C from titrimetry measurements, then it is possible to calculate the oxygen content at a given temperature, table 5.6. From this calculation the oxygen content as a function of annealing temperature and onset temperature as a function of oxygen content are shown in figures 5.11 and 5.12 respectively.

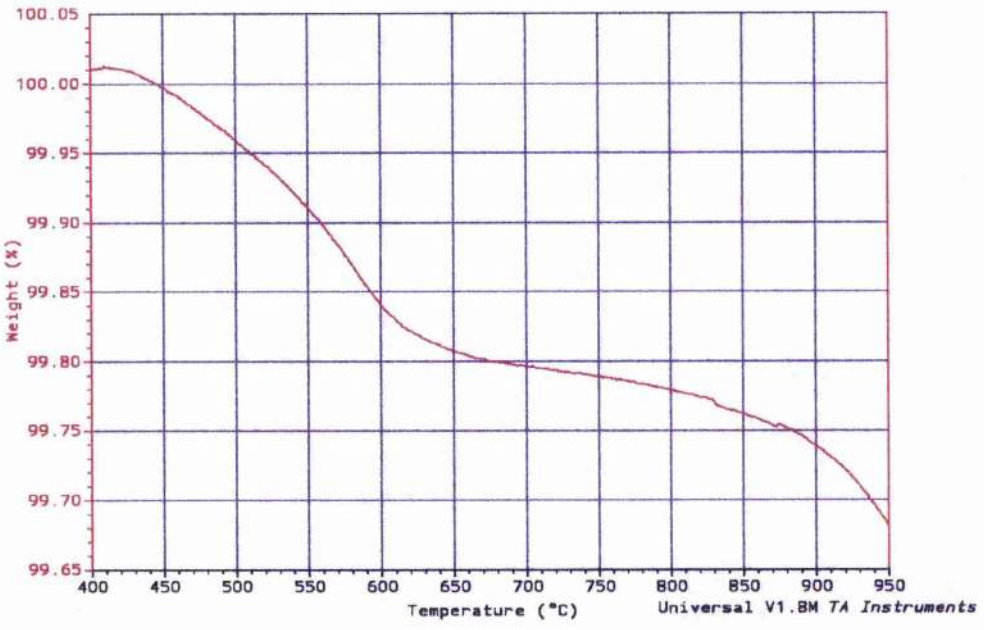

Figure 5.10. Sample oxygen content as a function of annealing temperature.

Annealing Temperature (°C)	Oxygen content calculated	Onset temperature (K)
400	7.09	
450	7.09	
500	7.07	-
550	7.05	
600	7.02	25
650	7.01	31
700	7.01	39
750	7.00	45
800	7.00	45
850	6.99	45
900	6.98	39
950	6.96	31

Table 5-6. Oxygen content calculated as function of temperature.

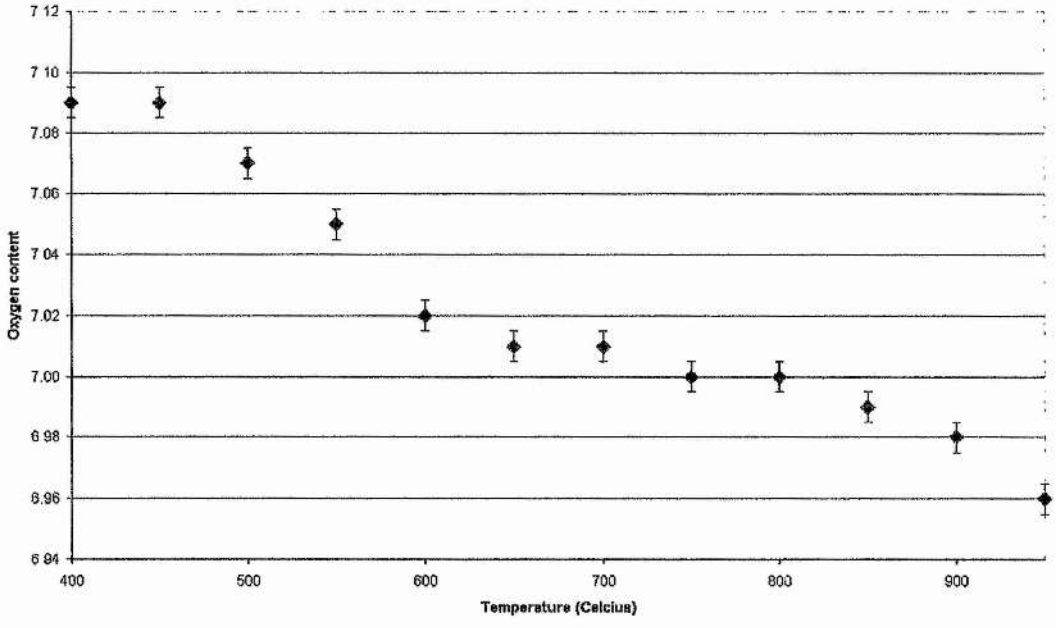

Figure 5.11. Calculated oxygen content as a function of annealing temperature.

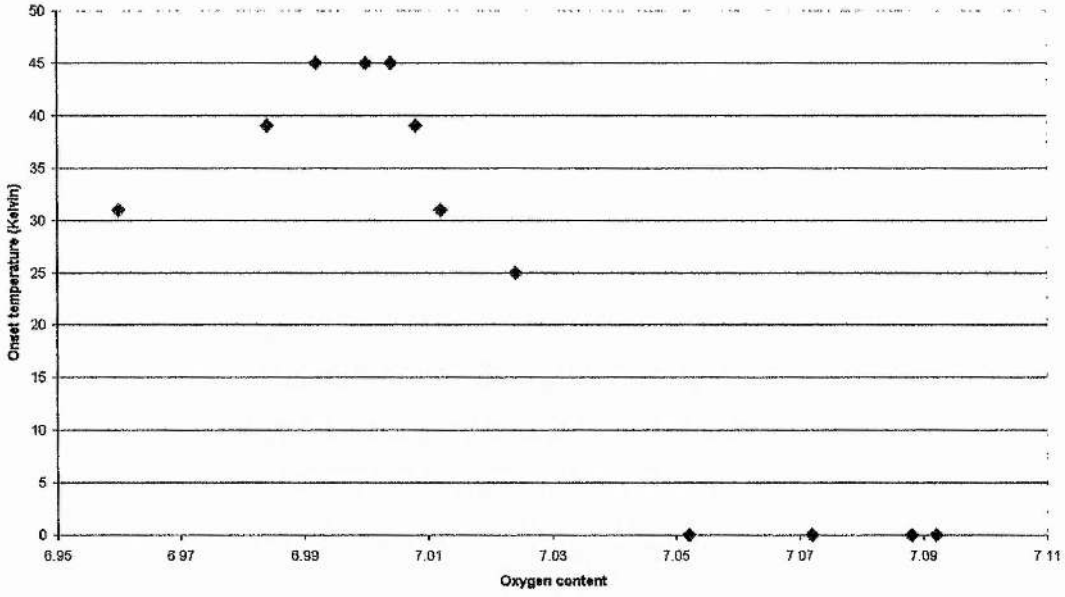

Figure 5.12. Variation in onset temperature as a function of oxygen content.

Although the change in sample oxygen content is very small 7.02-6.98 over the range 600-900°C the variation in onset temperature is very evident as the oxygen content rises above 7.00 and falls below 6.99. Most probably superconductivity is suppressed completely when the oxygen content rises above 7.03. The other means of controlling sample oxygen content requires annealing under low pO_2 conditions which is discussed in chapter 6.

5.4. Average Structural Disorder

Using X-ray and neutron diffraction techniques, the variation in atomic positions and compositional disorder has been studied.

5.41. Rocksalt layer

In samples of nominal composition $(Pb_{[1+x]/2}Cu_{[1-x]/2})Sr_2(Y_{1-x}Ca_x)Cu_2O_{7\pm\delta}$, where $x = 0\text{-}0.4$, $\delta = 0$ and $\delta \sim 0.1$, then variations in cell parameters and rocksalt layer positions are summarised in tables 5-7 and 5-8 as well as figures 5.13-5.17. XRD measurements were performed using a Stoe Stadi P diffractometer.

Ca content	a (Å)	c (Å)	vol. (Å^3)	Pb/Cu pos.	O(3) pos.
0	3.814712(20)	11.81244(7)	171.8950(17)	0.0519(8)	0.308(6)
0.2	3.815207(18)	11.82554(8)	172.1302(17)	0.0511(8)	0.341(7)
0.3	3.815656(19)	11.84479(9)	172.4516(19)	0.0505(10)	0.359(9)
0.4	3.816231(26)	11.84791(10)	172.5484(22)	0.0502(12)	0.368(10)

Table 5-7 Quenched samples, $\delta = 0$. XRD set only.

Ca content	a (Å)	c (Å)	vol. (Å^3)	Pb/Cu pos.	O(3) pos.
0	3.819381(30)	11.80678(11)	172.2334(25)	0.0559(8)	0.316(8)
0.2	3.820431(22)	11.82333(14)	172.5696(12)	0.0555(10)	0.343(7)
0.3	3.820667(20)	11.84522(12)	172.9105(8)	0.0554(10)	0.367(11)
0.4	3.821506(26)	11.84796(10)	173.0265(7)	0.0552(15)	0.396(11)

Table 5-8 Slow cooled samples, $\delta \sim 0.1$. XRD set only.

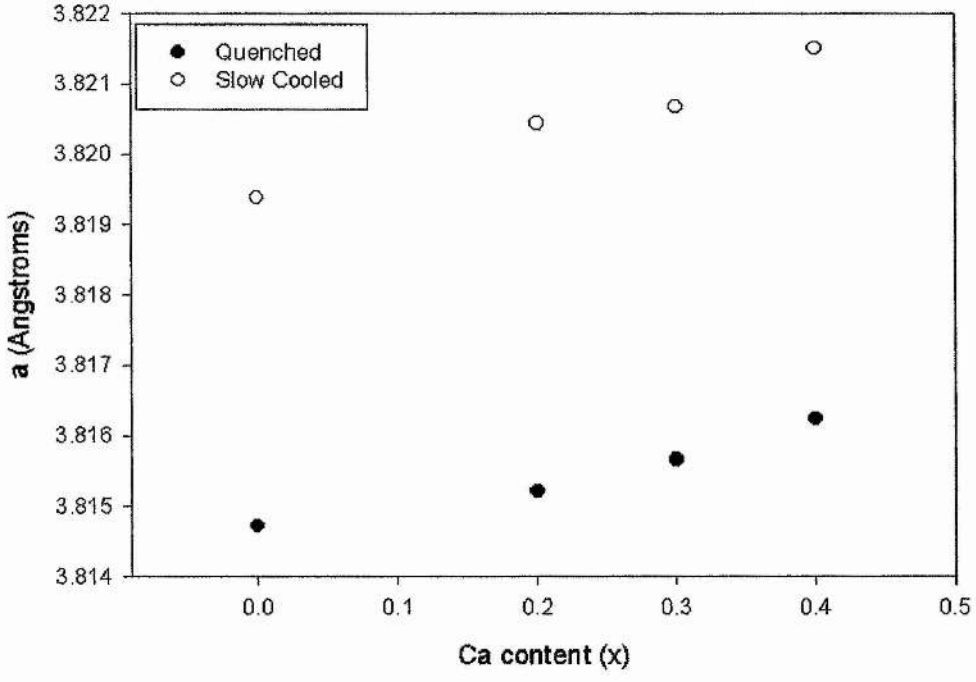

Figure 5.13. The a lattice parameter as function of Ca content in quenched and slow cooled samples.

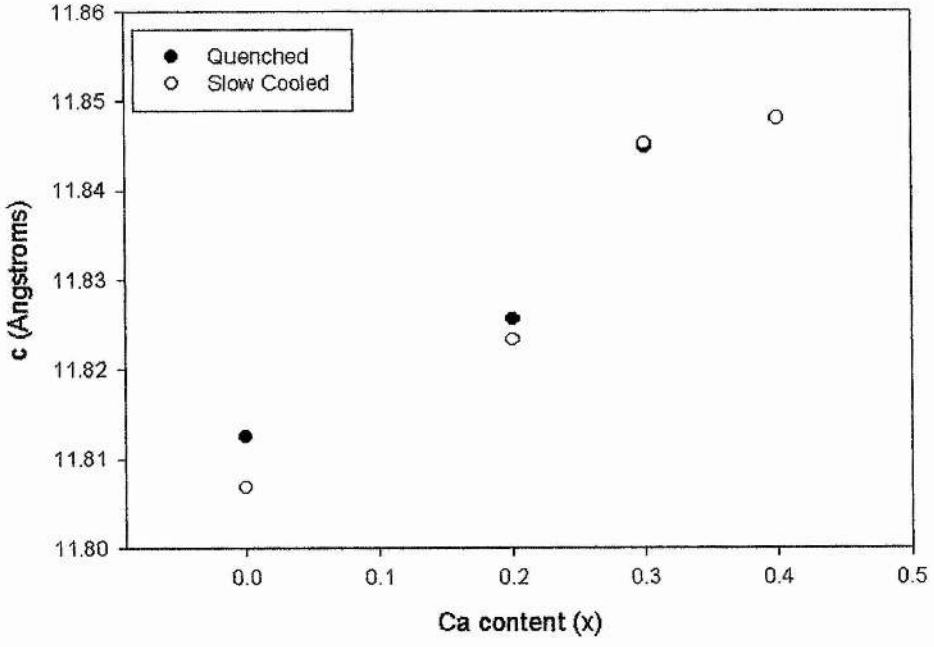

Figure 5.14. The c lattice parameter as a function of Ca content in quenched and slow cooled samples.

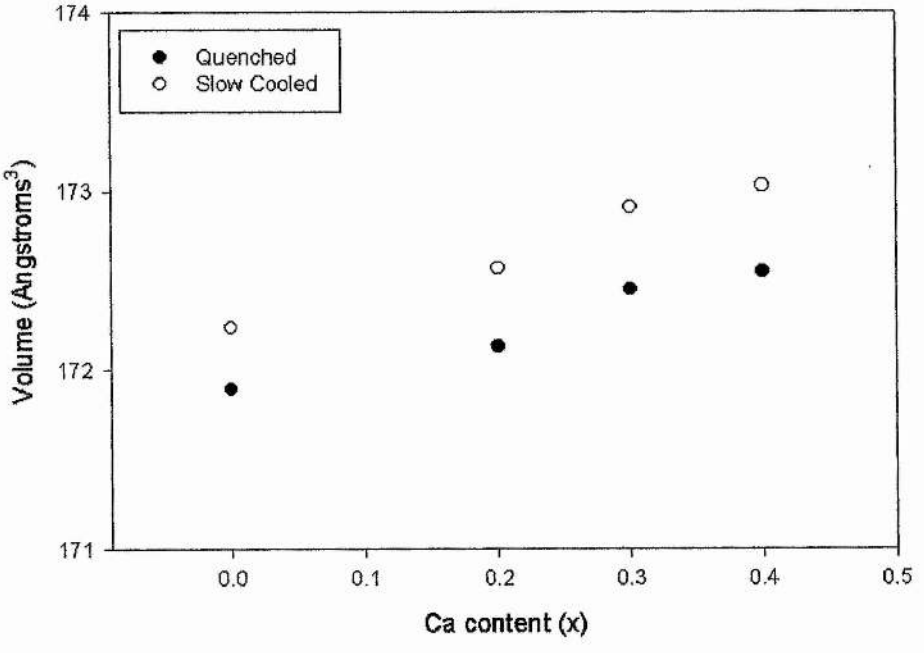

Figure 5.15. Sample volume as a function of Ca content in quenched and slow cooled samples.

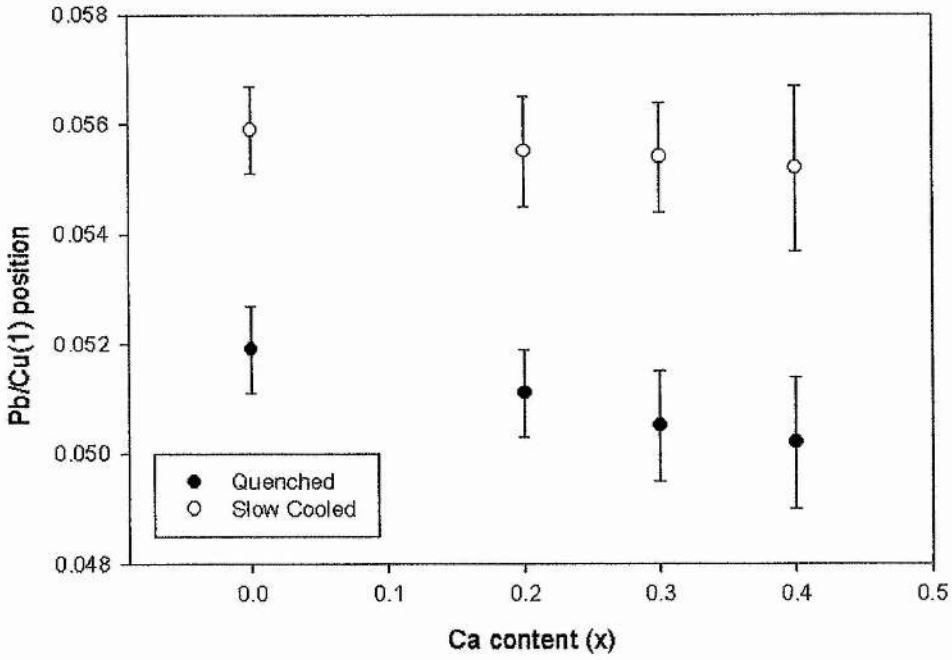

Figure 5.16. Pb/Cu position as a function of Ca content in quenched and slow cooled samples.

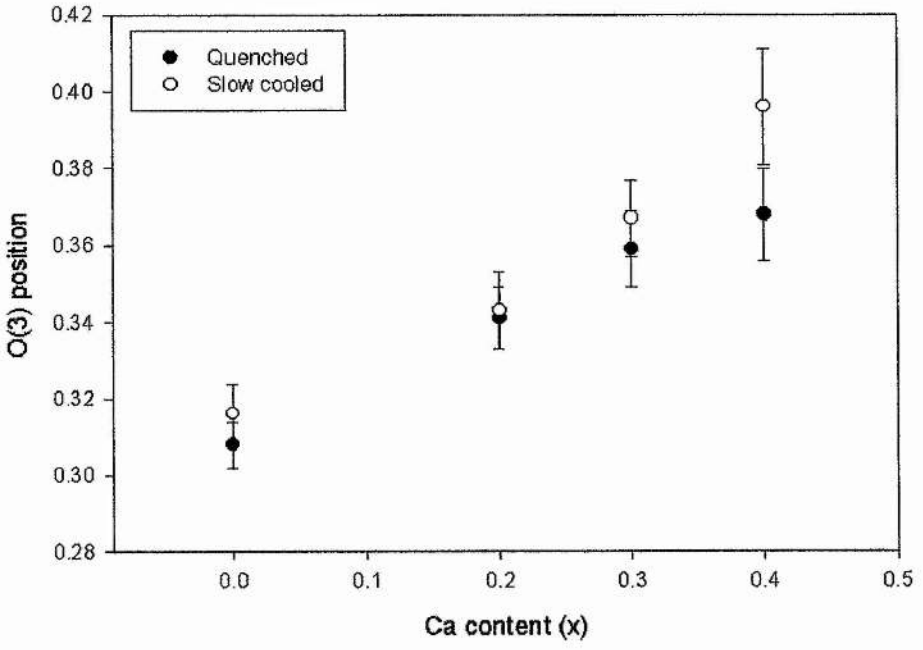

Figure 5.17. O(3) position as a function of Ca content in quenched and slow cooled samples.

The increase in the **c** axis length as Ca content is varied over the range 0-0.4 is due to the replacement of 1.015 Å Y^{3+} with larger 1.12 Å Ca^{2+}, and the excess oxygen plays no role in controlling this axis length. The **a** axis length shows a steady increase in both quenched and slow cooled samples. Liu et al[7] reported in the system $(Pb_{0.5}Tl_{0.5})Sr_2(Y_{1-x}Ca_x)Cu_2O_7$ that as x increases the **a** lattice parameter decreases due to the increasing number of holes in the CuO_2 layers. This causes[8] the population of the antibonding Cu $3d_{x^2-y^2}$ orbitals to decrease, thereby strengthening the Cu-O bonds and reducing the bond length. In this situation the CuO_2 plane controls the **a** axis length. This PbCu:1212 system of course is such that any decrease in charge and increase in holes due to Ca doping is counter-balanced by the increase in charge and removal of holes as the Pb content increases. Quite possibly the approach is to say that the **a** lattice parameter length is not determined by holes in the CuO_2 planes. Indeed the introduction of excess oxygen increases the unit cell size by a fixed amount regardless of composition. There was certainly evidence by Kosuge and co-workers[9] from Hall, Seebeck and resistivity measurements in this $(Pb_{[1+x]/2}Cu_{[1-x]/2})Sr_2(Y_{1-x}Ca_x)Cu_2O_{7\pm\delta}$ system, where x = 0.35 and 0.4, that the hole carriers were increasing in quenched samples.

Within error, there is very little shift of the Pb/Cu as the Ca content increases in quenched and slow cooled samples, but there is quite a significant offset in the position when the excess oxygen is present that is the same at all Ca levels, figure 5.16. The excess oxygen O(4) is sandwiched between the Pb/Cu sites and it is hardly surprising that the Pb/Cu are offset to accommodate its presence and minimise the energy within the system. The O(3) oxygen certainly shifts towards a more central point in the cell as the composition changes, but the presence of the excess oxygen does not appear to bring about any significant difference from quenched samples until higher Ca contents are reached, figure 5.17. The errors in the O(3) position should be reduced if neutron diffraction were used for this study and it might well show that there is a significant difference in position of the O(3) in quenched and slow cooled samples.

With the Pb split from its ideal position, there are four Pb-O(3) bond lengths generated which are less than 2.7Å, these are called bonds 1-4 and the results from the Rietveld refinements are shown in figures 5.18-5.21 respectively. In both quenched

and slow cooled samples the bond lengths show a fairly linear increase as the Ca content increases, this mirrors the increase in the unit cell **a** axis. There is actually very little difference in the Pb-O(3) bond lengths between the quenched and slow cooled samples, and it is only at the higher Ca contents that any real differences begin to appear. The same trend is also seen in figure 5.22 for the Pb-O(2) bond length. The XRD results would appear to suggest that the Pb and O(3) vary in position essentially to maintain the bond length when the excess oxygen has been removed or is present, but these movements are very small and the resulting change in the bond length is very small. Note, for the quenched Ca=0 sample the Pb-O(3) bond lengths vary from ~2.07-2.41Å and the Pb-O(2) bond length is ~1.93Å. This of course may not, as mentioned previously, describe the Pb-O environment on the local scale and the EXAFS experiments in 5.51 attempt to confirm the applicability of these results shown above on a local scale. Two Pb-Sr bond lengths are generated when the Pb/Cu is displaced from the ideal (0,0,0) position. In the quenched samples these are ~3.51Å and ~3.74Å respectively and there is a slight change in these lengths in fully oxidised samples, ~3.55Å and ~3.77Å respectively. On the whole there is very little information to be gained from the bond lengths except to say that there is no significant discrepancy between quenched and slow cooled samples except at higher Ca levels.

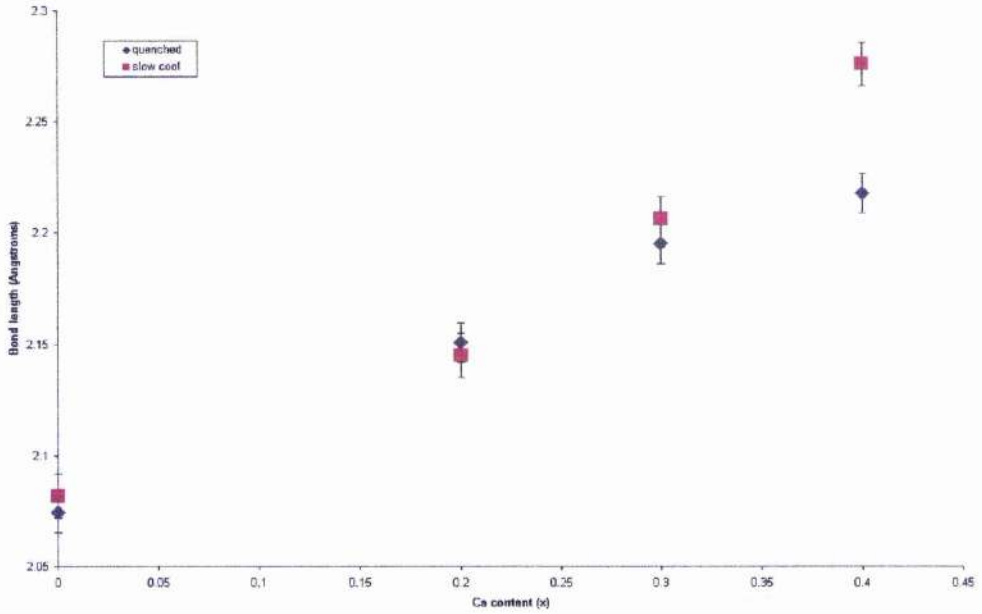

Figure 5.18. Variation in Pb-O(3) bond 1 in quenched and slow cooled samples.

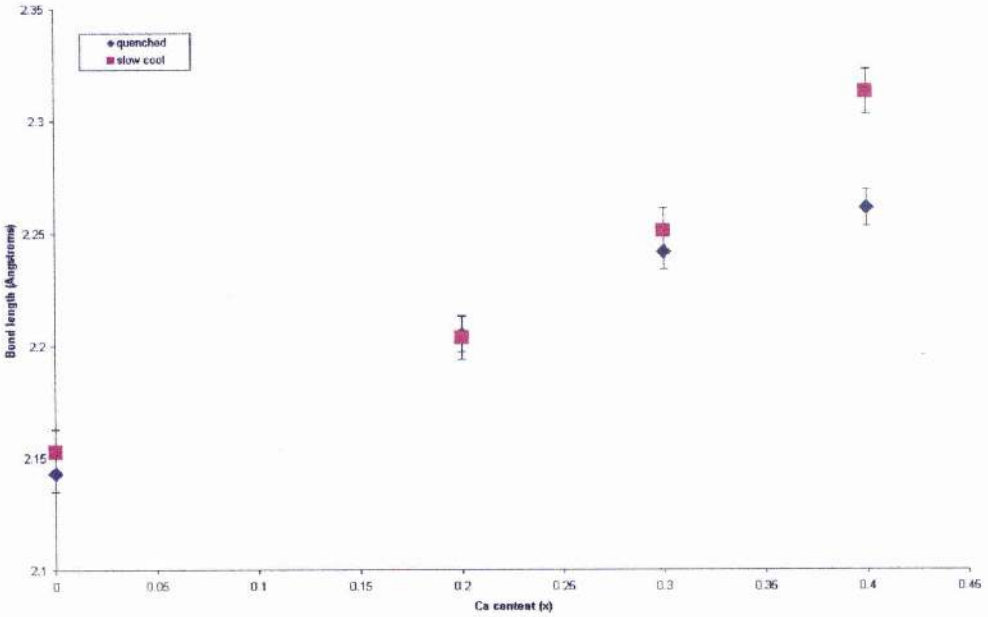

Figure 5.19. Variation in Pb-O(3) bond 2 in quenched and slow cooled samples.

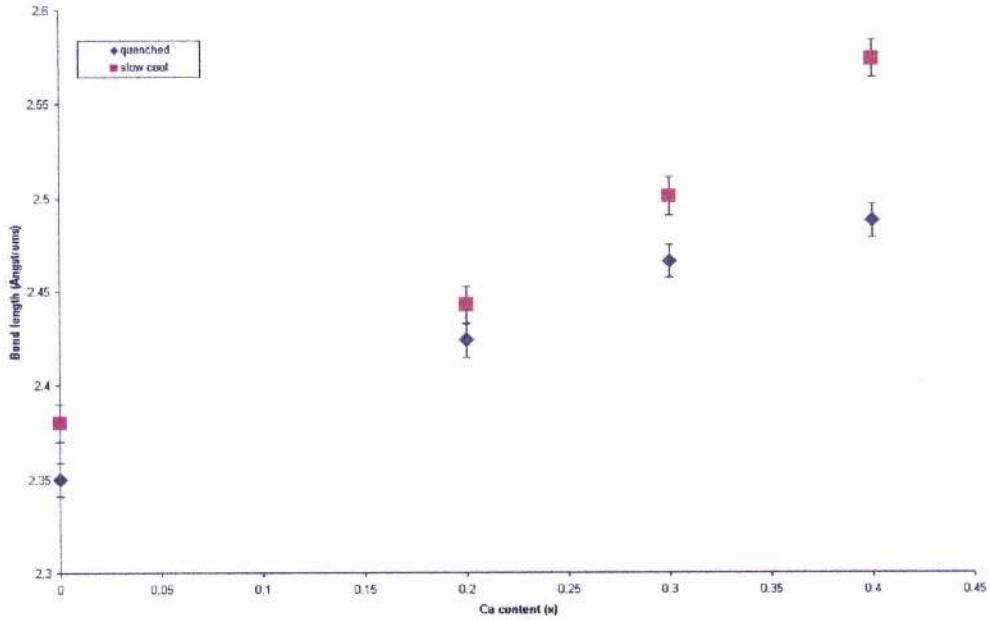

Figure 5.20. Variation in Pb-O(3) bond 3 in quenched and slow cooled samples.

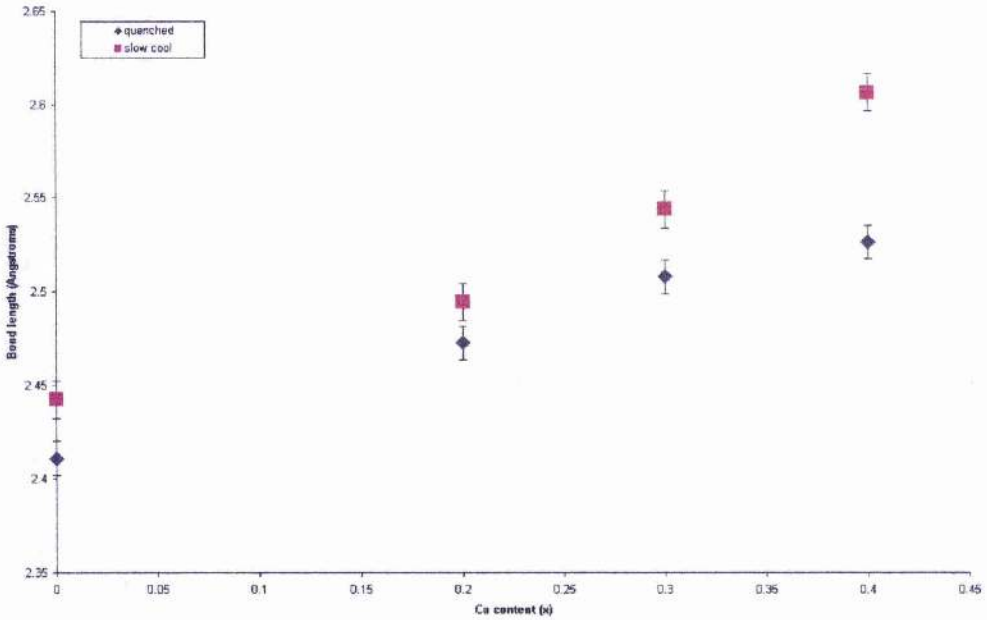

Figure 5.21. Variation in Pb-O(3) bond 4 in quenched and slow cooled samples.

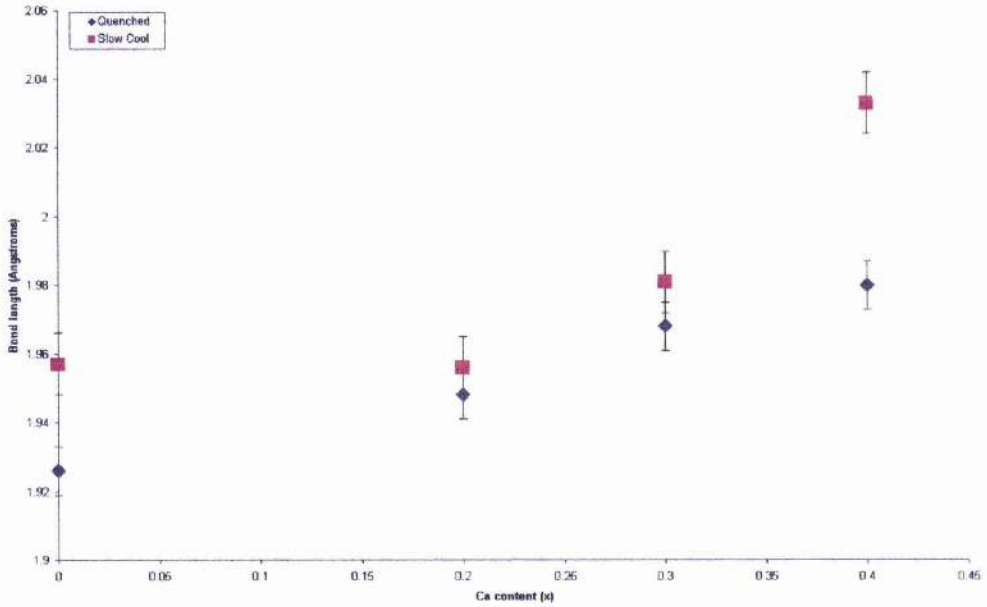

Figure 5.22. Variation in Pb-O(2) bond length in quenched and slow cooled samples.

5.42. Phase composition and oxygen content

There is evidence that changes are occurring within the structure as composition and oxygen content vary, but does evidence exist to suggest that the nominal composition relates to the actual composition? Two samples of nominal composition $(Pb_{0.7}Cu_{0.3})Sr_2(Y_{0.6}Ca_{0.4})Cu_2O_7$ and $(Pb_{0.7}Cu_{0.3})Sr_2(Y_{0.6}Ca_{0.4})Cu_2O_{7.1}$ were studied using XRD and neutron diffraction to determine cation composition and oxygen content respectively. The XRD results are summarised in tables 5-9 and 5-10 for quenched $(Pb_{0.7}Cu_{0.3})Sr_2(Y_{0.6}Ca_{0.4})Cu_2O_7$ samples, while the neutron diffraction results on quenched and slow cooled samples are summarised in tables 5-11 and 5-12.

a (Å)	c (Å)	vol. (Å^3)	R_{wp}	R_p	Chi^2
3.81688(7)	11.85962(25)	172.778(6)	10.09	7.42	6.053

Atom	x	y	z	Ui/Ue*100 (Å^2)	Frac
Pb	0.0604(20)	0	0	1.27(13)	0.175x4
Cu(1)	0.0604(20)	0	0	1.27(13)	0.075x4
Sr	0.5	0.5	0.20882(15)	0.76(8)	1
Y	0.5	0.5	0.5	-1.06(10)	0.6
Ca	0.5	0.5	0.5	-1.06(10)	0.4
Cu(2)	0	0	0.35994(21)	0.18(9)	1
O(1)	0	0.5	0.3741(7)	1.0	1
O(2)	0	0	0.1672(9)	1.0	1
O(3)	0.352(6)	0.5	0	1.0	0.25x4

ITFs for O(1), O(2) and O(3) fixed at 1.0 Å^2. Fractional occupancies fixed for all atoms.

Pb-Cu(1) site positions and ITF constrained. Y-Ca site ITF constrained.

Table 5-9. Refined parameters for XRD data on $(Pb_{0.7}Cu_{0.3})Sr_2(Y_{0.6}Ca_{0.4})Cu_2O_{7.0}$ sample.

a (Å)	c (Å)	vol. (Å^3)	R_{wp}	Rp	Chi^2
3.81686(7)	11.85956(25)	172.775(6)	9.92	7.17	5.854

Atom	x	y	z	Ui/Uc*100 (Å^2)	Frac
Pb	0.0607(20)	0	0	0.97(9)	0.170(2)x4
Cu(1)	0.0607(20)	0	0	0.97(9)	0.08(2)x4
Sr	0.5	0.5	0.20882(15)	0.62(9)	1
Y	0.5	0.5	0.5	0.42(11)	0.77*
Ca	0.5	0.5	0.5	0.42(11)	0.23*
Cu(2)	0	0	0.36042(21)	0.15(10)	1
O(1)	0	0.5	0.3732(7)	1.0	1
O(2)	0	0	0.1666(9)	1.0	1
O(3)	0.351(7)	0.5	0	1.0	0.25x4

ITF's for O(1), O(2) and O(3) fixed at 1.0 Å^2 and fractional occupancies not varied. Fractional occupancies constrained for Pb-Cu(1) site and Y-Ca site to be 1. Pb-Cu(1) site positions and ITF constrained. Y-Ca site ITF constrained. * Value shown rounded to two decimal places, Correct error is Y 0.772(2) for example.

Table 5-10. Refined parameters for XRD data on $(Pb_{0.7}Cu_{0.3})Sr_2(Y_{0.6}Ca_{0.4})Cu_2O_{7.0}$ sample, fractional occupancies varied.

In terms of the two models presented above, there is very little difference in results and certainly the atomic positions of atoms are not realistically affected. On the Pb site there would appear to be some evidence that there is less Pb on this site than the nominal composition suggests. Whether there is cation substitution is uncertain and since the occupancy on the site was fully constrained no evidence to suggest overall deficiency on the site may be put forward. The Y/Ca site, however, reveals a completely different picture. The results suggest that the Y/Ca ratio is much greater than the nominal content suggests. The results would seem to show that the sample is Y rich and Ca deficient, but the particularly low isotropic temperature factors (ITF) might even suggest that these results are incorrect and that some other atom is present on this site.

a (Å)	c (Å)	vol. (Å^3)	R_{wp}	R_p	Chi^2
3.81124(5)	11.84507(16)	172.056(4)	7.85	6.08	6.533

Atom	x	y	z	Ui/Ue*100 (Å^2)	Frac
Pb	0.0612(12)	0	0	0.88(13)	0.175x4
Cu(1)	0.0612(12)	0	0	0.88(13)	0.075x4
Sr	0.5	0.5	0.20815(14)	0.76(8)	1
Y	0.5	0.5	0.5	0.56(7)	0.666(17)
Ca	0.5	0.5	0.5	0.56(7)	0.334(17)
Cu(2)	0	0	0.36094(13)	0.80(4)	1
O(1)	0	0.5	0.37402(12)	1.11(4)	1
O(2)	0	0	0.16348(22)	2.53(7)	1
O(3)	0.3346(14)	0.5	0	2.59(20)	0.25(x4)
O(4)	0	0.5	0	1.00	0

Pb-Cu(1) occupancy fixed, site positions and ITF constrained. Y-Ca site ITF constrained. ITF for O(4) fixed at 1.0 Å^2.

Table 5-11. Refined parameters for neutron diffraction data on $(Pb_{0.7}Cu_{0.3})Sr_2(Y_{0.6}Ca_{0.4})Cu_2O_{7.0}$ sample.

a (Å)	c (Å)	vol. (Å^3)	R_{wp}	R_p	Chi^2
3.81688(7)	11.85962(25)	172.778(6)	10.09	7.42	6.053

Atom	x	y	z	Ui/Ue*100 (Å^2)	Frac
Pb	0.0693(30)	0	0	1.40(25)	0.175x4
Cu(1)	0.0693(30)	0	0	1.40(25)	0.075x4
Sr	0.5	0.5	0.20728(27)	2.19(12)	1
Y	0.5	0.5	0.5	0.28(12)	0.663(19)
Ca	0.5	0.5	0.5	0.28(12)	0.337(19)
Cu(2)	0	0	0.36071(24)	0.79(7)	1
O(1)	0	0.5	0.37426(7)	0.99(7)	1
O(2)	0	0	0.1672(9)	3.76(13)	1
O(3)	0.352(6)	0.5	0	3.46(38)	0.25x4
O(4)	0	0.5	0	1.00	0.025(8)x2

Pb-Cu(1) occupancy fixed, site positions and ITF constrained. Y-Ca site ITF constrained. ITF for O(4) fixed at 1.0 Å^2.

Table 5-12. Refined parameters for neutron diffraction data on $(Pb_{0.7}Cu_{0.3})Sr_2(Y_{0.6}Ca_{0.4})Cu_2O_{7.1}$ sample.

Going back to the Y/Ca site question, neutron diffraction reveals a different picture. In neutron diffraction Ca has a much larger scattering power than in XRD, so although Ca deficient there appears to be some element other than Y present on this site. The scattering lengths/factors using neutrons for Pb, Cu, Sr and Y are very similar and it is not possible to answer this question properly just as it is not possible to determine the Pb/Cu ratio accurately. Rietveld refinement using neutrons gives a Pb/Cu ratio in this material of 45/55, which is not correct since the large scattering power of Pb using XRD should more accurately reveal its content in the sample.

The refinements in the quenched and fully oxygenated samples show that the O(1), O(2) and O(3) sites are fully occupied by oxygen and no evidence for deficiency exists. In the quenched sample the fractional occupancy of the oxygen on the O(4) always falls to 0 and negative values which indicates this site is unoccupied in this sample. Thus, the oxygen content of this sample matches the nominal O = 7.0 value. In the slow cooled sample refinements reveal a fractional occupancy of 0.025, and since this is a two fold site indicates that the excess oxygen amounts to approximately 0.05. The excess oxygen certainly affects Pb/Cu(1), O(3), O(2) and Sr sites judging by the increased ITF values. With such a small oxygen excess it is not possible to extract accurate values for the fractional occupancy; however, the results do correctly indicate the presence of oxygen on this site.

5.43. Resonant X-ray diffraction studies

The results presented previously suggest that some cation disorder exists with these 1212 samples and resonant X-ray diffraction experiments were used to investigate this. The technique is discussed in chapter 3. Using this technique it is possible with the four data sets to refine atoms on a site without correlation to other atoms on a site and it provides contrast between atoms of similar atomic number. Two samples were investigated, those having nominal compositions $(Pb_{0.5}Cu_{0.5})Sr_2Y_1Cu_2O_{7.0}$ and $(Pb_{0.7}Cu_{0.3})Sr_2(Y_{0.6}Ca_{0.4})Cu_2O_{7.0}$. In the Ca free sample there was no evidence that any cation deficiency or disorder existed on the Pb/Cu site, Sr site, Y site and the Cu site in the CuO_2 planes, table 5-13 Thus, the nominal composition would appear within experimental errors to match the actual sample composition. In the other sample there was evidence for cation disorder. Table 5-14 shows a summary of the best results

obtained from the Rietveld refinements for uncompressed and compressed data sets, and figures 5.23-5.26 the actual fits obtained to the data from each particular data set.

a (Å)	c (Å)	vol. (Å^3)
3.814680(13)	11.81193(7)	171.81193(7)

Data sets	R_{wp} (%)	R_p (%)	R_E (%)	Chi^2
Uncompressed	17.87	13.73	9.70	3.00

Atom	x	y	z	Ui/Ue*100 (Å^2)	Frac
Pb(1)	0.0519(7)	0	0	1.12(4)	0.125x4
Cu(1)	0.0519(7)	0	0	1.12(4)	0.125x4
Sr	0.5	0.5	0.20448(8)	1.055(24)	1
Y	0.5	0.5	0.5	0.58(8)	1
Cu(2)	0	0	0.35858(10)	0.32(8)	1
O(1)	0	0.5	0.37703(16)	1.0	1
O(2)	0	0	0.16223(18)	1.0	1
O(3)	0.297(4)	0.5	0	1.0	0.25(x4)

ITF's for O(1), O(2) and O(3) fixed at 1.0 Å.

Table 5-13. Resonant XRD results obtained for sample of nominal composition $(Pb_{0.5}Cu_{0.5})Sr_2Y_1Cu_2O_{7.0}$.

a (Å)	c (Å)	vol. (Å^3)
3.816221(14)	11.84797(7)	172.5484(14)

Data sets	R_{wp} (%)	R_p (%)	R_E (%)	Chi^2
Uncompressed	22.41	19.36	13.4	2.04
Compressed	15.05	12.71	6.32	4.04

Atom	x	y	z	Ui/Ue*100 (Å^2)	Frac
Pb(1)	0.0516(11)	0	0	1.09(7)	0.163(2)x4
Cu(1)	0.0516(11)	0	0	1.09(7)	0.075(3)x4
Sr	0.5	0.5	0.20795(12)	0.881(27)	1
Y	0.5	0.5	0.5	0.62(4)	0.65*
Ca	0.5	0.5	0.5	0.62(4)	0.30*
Pb(2)	0.5	0.5	0.5	0.62(4)	0.05*
Cu(2)	0	0	0.36084(17)	0.32(8)	1
O(1)	0	0.5	0.3751(6)	1.0	1
O(2)	0	0	0.1673(8)	1.0	1
O(3)	0.335(6)	0.5	0	1.0	0.25(x4)

* Value rounded to two decimal places e.g. Y Frac. is 0.651(2). ITF's for O(1), O(2) and O(3) fixed at 1.0 Å.

Table 5-14. Resonant XRD results obtained for sample of nominal composition $(Pb_{0.7}Cu_{0.3})Sr_2(Y_{0.6}Ca_{0.4})Cu_2O_{7.0}$.

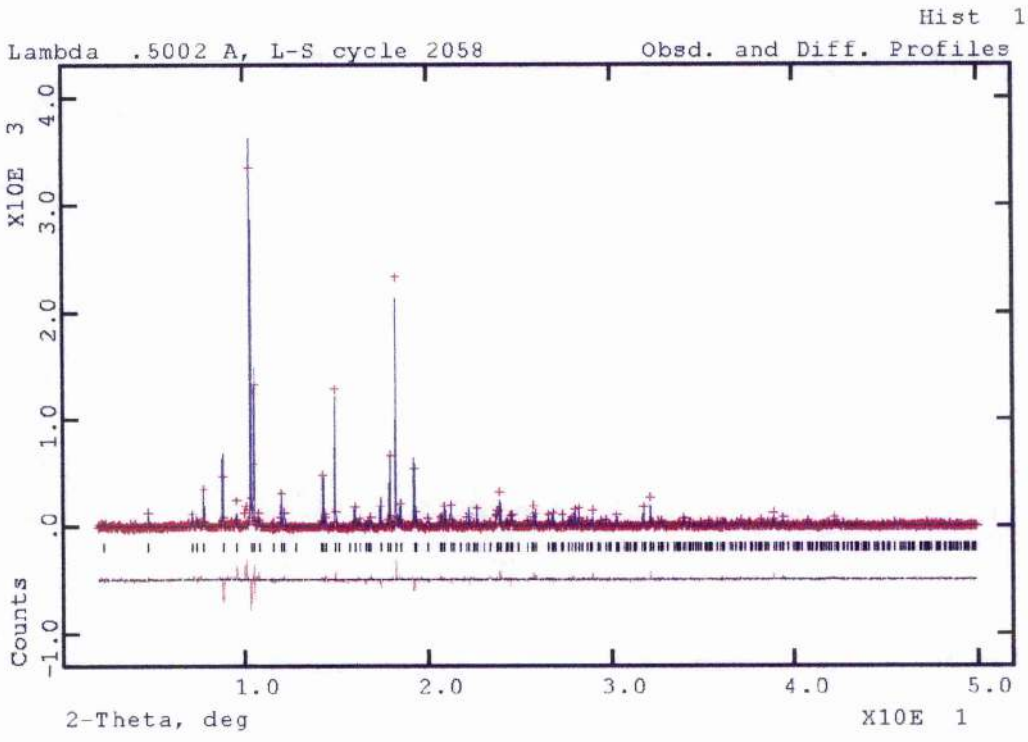

Figure 5.23. Fit obtained from 25 keV data set.

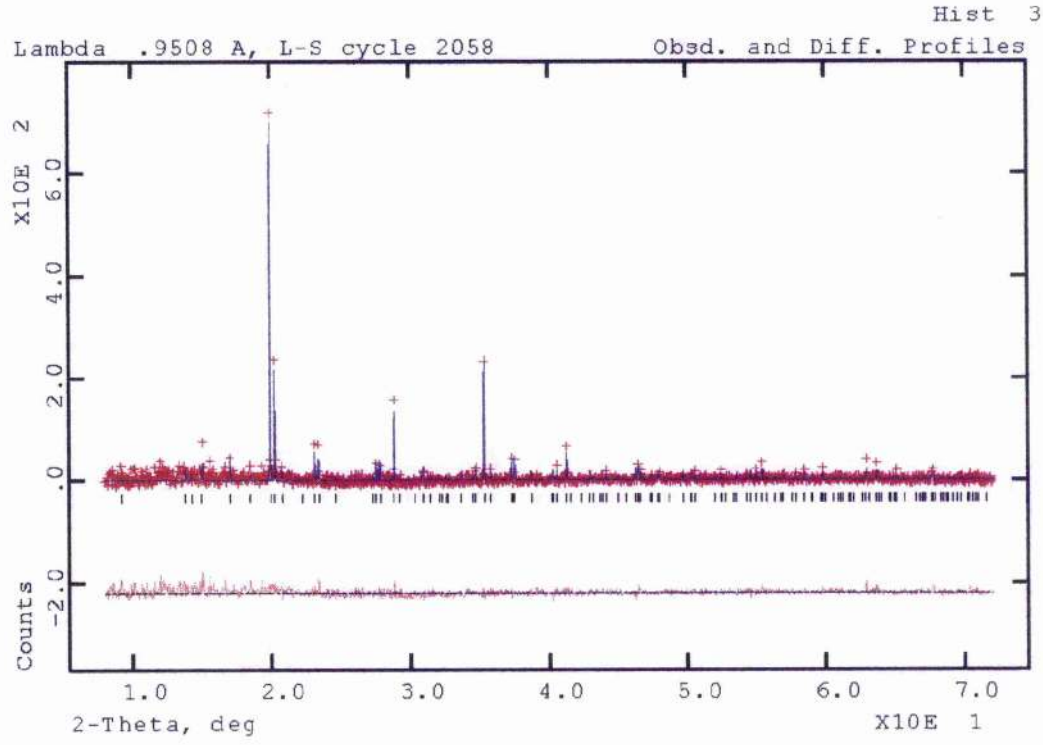

Figure 5.24. Fit obtained from Pb edge data set.

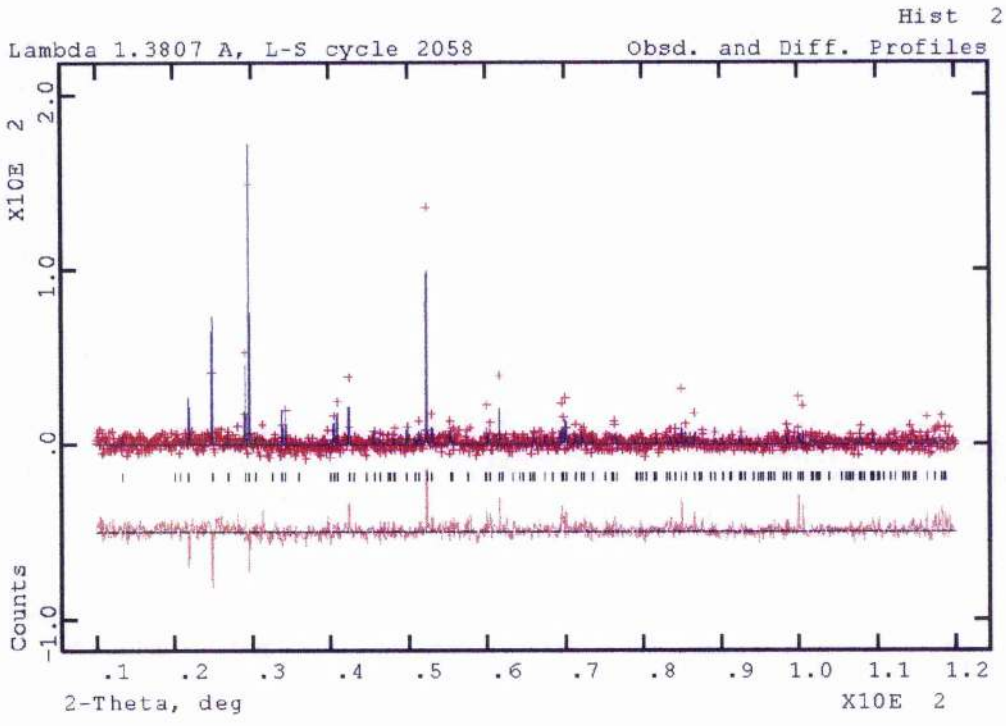

Figure 5.25. Fit obtained from Cu edge data set.

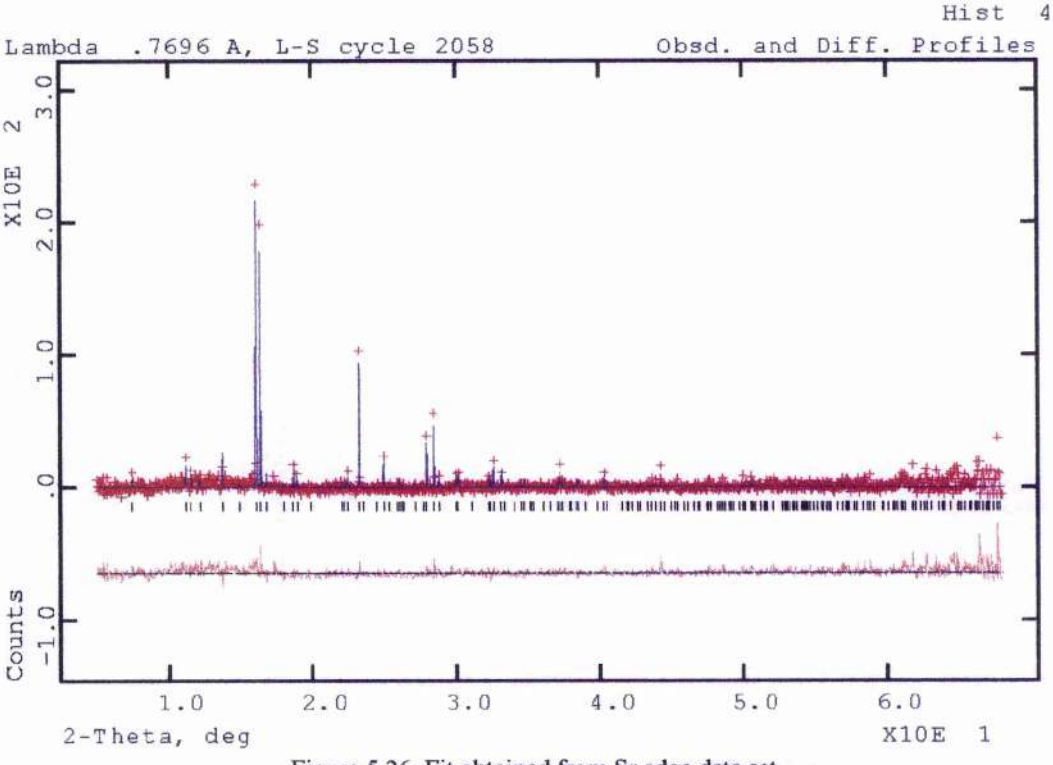

Figure 5.26. Fit obtained from Sr edge data set.

The first thing about these resonant diffraction results is the relatively poor R_{wp} and R_p values obtained for uncompressed data sets, despite what is a very respectable fit to the data itself. The large number of data points for such refinements would seem to explain the above, see table 5-15.

Edge	Uncompressed	Compressed
25 keV	15000	3750
Cu	23600	3800
Pb	12800	4300
Sr	21000	3500

Table 5-15. Number of data points in uncompressed and compressed form.

The average data set contains upwards of 15000 data points and the spacing between points is either 0.003 or 0.005 degrees. Since the f' and f'' values are basically independent of variations in $\sin\theta/\lambda$ then it is necessary to collect out to high 2θ, low $\sin\theta/\lambda$, to gain the maximum effect from the data. Compressing the data i.e. removing points, leads to more respectable values as far as R_{wp}, R_p and R_E are concerned. Since $Chi^2 = [R_{wp}/R_E]^2$, then Chi^2 will of course vary. However, the aim of the experiment was to collect as much useful data as possible to achieve the most accurate results from the refinement, so frankly the high R factors are not critical. Another problem that affects counting statistics in particular is the increasing sample absorbency occurring as the X-ray wavelength is increased (energy is decreased). Most badly affected is the Cu edge measurement. To overcome this problem, thinner capillaries are required i.e. 0.1/0.2 mm capillaries instead of 0.5 mm. In this experiment only 0.5 mm capillaries were used, unlike the resonance diffraction experiment described in chapter 6 where the optimal capillary size was selected for a particular wavelength.

On the Sr site there is absolutely no evidence for any significant degree of disorder present. Placing other atoms on this site and carrying out refinements always leads to insignificant or negative values. Repeating this exercise for the Cu(2) site there is again no evidence for any significant cation disorder.

On the Y/Ca site the only substituted atom which did not refine to insignificant

values was Pb. The fractional occupancy was constrained such that the site was always fully occupied. The result was a lowering of the Y level and the Pb content coming out about 5%, while Ca was assumed to make up the remaining amount.

At the Pb/Cu site the extra data sets allow the Pb and Cu occupancy to be refined without interfering with one another. It would seem that the site is about 5% Pb deficient and the Cu retains its nominal value. It is not clear if the Pb/Cu site is fully occupied with some other element possibly Ca. But it would be quite realistic to say that in addition to Ca on this site there may well be vacancies.

The above values suggest a sample of composition $(Pb_{0.65}Cu_{0.3})Sr_2(Y_{0.65}Pb_{0.5}Ca_{0.3})Cu_2O_y$. Assuming all the Cu say is in the Cu^{2+} state and Pb in the Pb^{4+} state then the nominal oxygen content would be 6.975, so any extra Ca in the rocksalt layer could easily increase the value to its nominal 7.00 value. It would seem clear that disorder increases in this system as the Ca levels are increased. Whether or not the system could still be described as self-doping is not totally clear since the experimental composition of $Pb_{0.7}Cu_{2.3}Sr_2Y_{0.65}Ca_{0.35}O_{6.975}$ is virtually the same as the nominal composition of $Pb_{0.7}Cu_{2.3}Sr_2Y_{0.6}Ca_{0.4}O_{7.0}$. Further studies on a greater range of samples would be required to answer this question properly.

5.5. Local structure/structural disorder

Diffraction experiments although very useful still have limitations, since their results reflect the structure on a general level and of course do not reveal the true picture of the positions of atoms on the local scale.

5.51. In situ EXAFS/XRD study of 1212 phase

The relatively high ITF of the O(3) oxygen would suggest that it tends to "move around" significantly and indeed it is of interest to determine the environment of the Pb and Cu atoms in the rocksalt layer and how their positions relate to that of the O(3) oxygen. One problem though with EXAFS experiments on PbCu:1212 cuprates is the

presence of the two different Cu environments existing within the material. This makes any EXAFS measurements involving the Cu atom very difficult to interpret, thus Cu edge analysis is effectively ruled out experimentally. Of course it would be possible to substitute some other cation onto the rocksalt layer; however, the local environment need not be the same and frankly such material would be of no benefit. So the Pb L_{III} edge was chosen for study. The experiment was designed to use the QEXAFS/XRD technique, monitor changes in the local environment and gain qualitative information on changes in the diffraction pattern as a whole. The XRD section of the experiment worked up to ~750°C whereupon the sample, upon decomposition, began to react with the amorphous silica.

The raw absorption spectra are plotted, figure 5.27, over the temperature range 250-800°C and the edge shows a shift towards lower energy at ~700-750°C whereupon the impurity formation begins to occur. In figure 5.28 the absorption edge is seen to begin shifting above 720°C. The shift in the edge would seem to indicate a change in the valence state of Pb. The position of the absorption edge at 13.04 keV matches that of the PbO_2 standard material, which would appear to indicate, that the Pb is actually present in its Pb^{4+} state. Studying the XANES and EXAFS section of the plots there is very little change in the patterns as temperature varies. However, there is not particularly much detail to be seen from this alone.

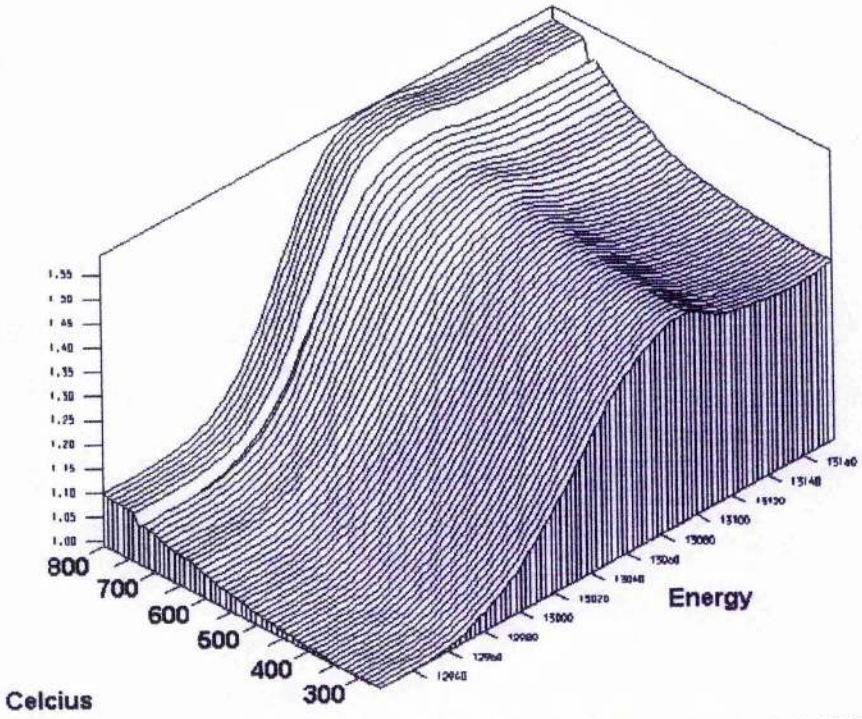

Figure 5.27. Raw absorption spectra plotted over range 250-800°C.

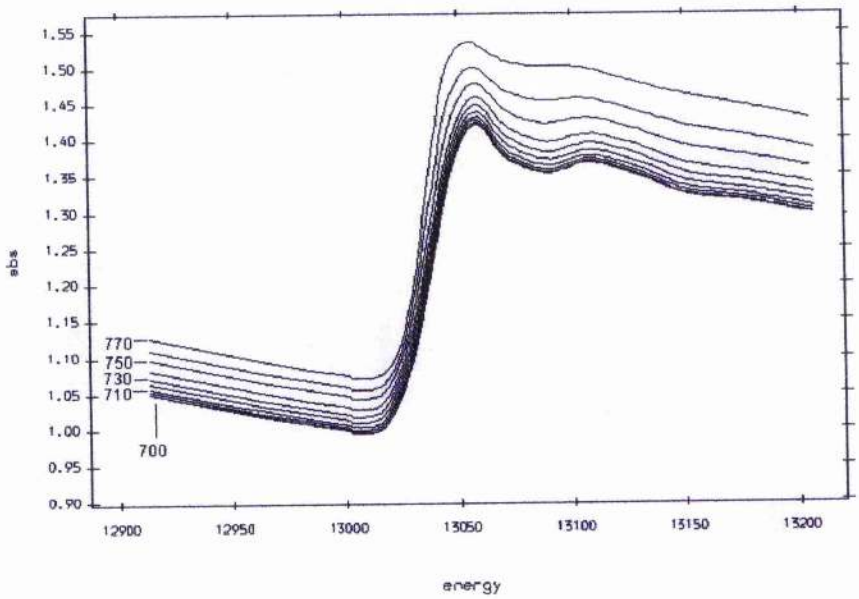

Figure 5.28. Variation in absorption edge plotted at selected temperatures, 700-770°C.

After converting the raw EXAFS data into the correct format and carrying out all necessary steps, the data was then entered into the EXCURV92 routine. EXCURV92 is a program for comparing the results of EXAFS experiments with the results of calculations based on a model of the local atomic structure. The structural model can be manipulated in various ways within the program in order to optimise the agreement between the experimental and theoretical results. A typical output from the routine is shown in figure 5.29. The top portion shows a weighted EXAFS spectrum plotted as a function of the wave vector **k**, which is rather noisy due to the particularly short data collection time of 6 minutes in comparison to the more usual 60 minutes if a normal EXAFS experiment were being undertaken. The dashed line represents the result from the simulation. In the bottom of the plot a Fourier transform results in a radial distribution function made up of pair correlation involving the absorber. The dashed line is the result of such a simulation. The basic steps in the use of EXCURV are:

1. Specification of an experimental spectrum.
2. Specification of the positions and types of atoms for a structure.
3. Calculation of a theoretical spectrum from the structural information provided.
4. Comparison of experimental and theoretical spectra and the differences between them.
5. Adjustments to the atomic positions and other parameters via least squares fitting procedure in order to optimise the agreement.

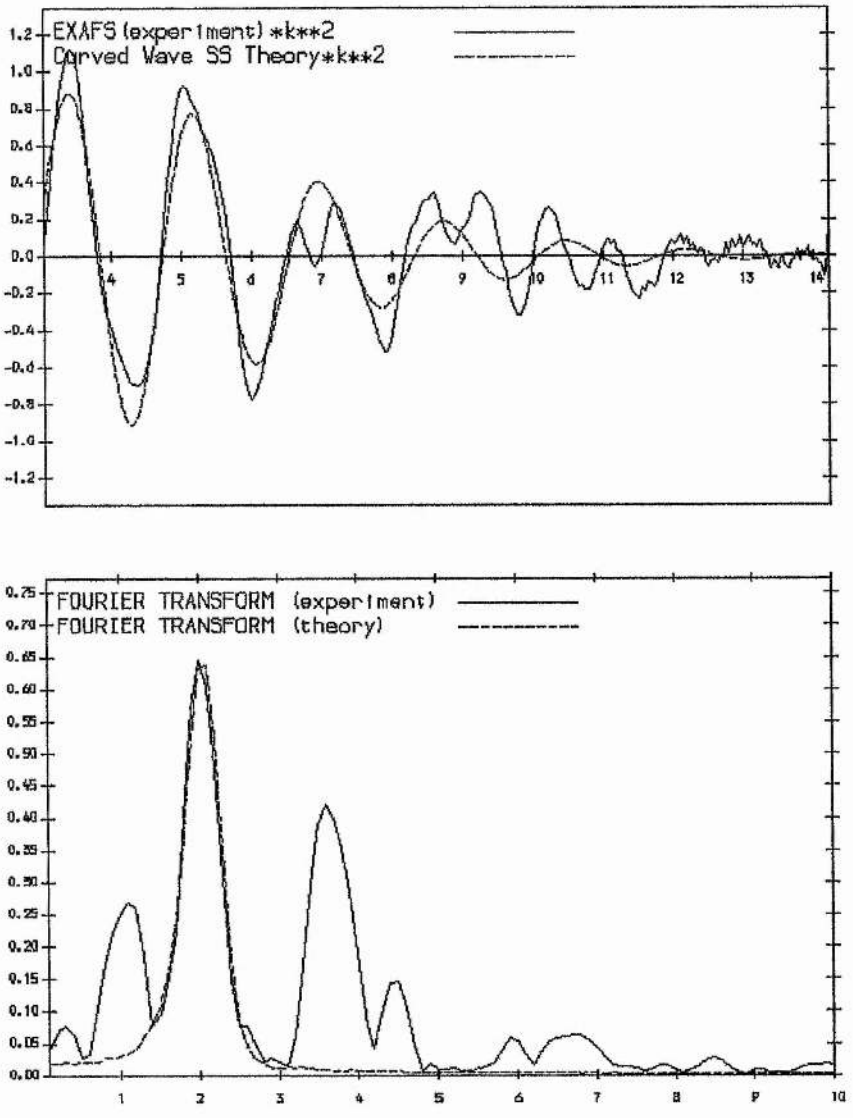

Figure 5.29. Weighted EXAFS spectrum and associated Fourier transform.

Looking more closely at the Fourier transform in figure 5.30, the region 0-1.5Å should ideally be flat, this is a generated artefact occurring during the initial data processing steps which arises from noise in the spectrum at the high **k** limit but does not affect the results. All the data processed in this experiment contained this feature. The fitting occurs by adding the atoms surrounding the absorber as shells and checking whether results obtained are sensible or indicate that the model is incorrect.

Fully oxygenated samples of nominal composition $(Pb_{0.5}Cu_{0.5})Sr_2Y_1Cu_2O_{7.1}$, $(Pb_{0.6}Cu_{0.4})Sr_2(Y_{0.8}Ca_{0.2})Cu_2O_{7.1}$, $(Pb_{0.65}Cu_{0.35})Sr_2(Y_{0.7}Ca_{0.3})Cu_2O_{7.1}$ and

$(Pb_{0.7}Cu_{0.3})Sr_2(Y_{0.6}Ca_{0.4})Cu_2O_{7.1}$ were first measured at room temperature and then heated at 10°C.min^{-1} to 900°C. The aim of the EXAFS work was to study the variation in the local environment of the Pb as temperature increased and oxygen was removed from the structure.

The starting point for shell fitting was taken from a standard model used in Rietveld refinements table 5-16, and the associated bond lengths calculated from these parameters table 5-17. Unit cell dimensions assumed as 3.82 x 11.84Å.

Atom	x	y	z
Pb/Cu(1)	0	0	0
Sr	0.5	0.5	0.21
Y/Ca	0.5	0.5	0.5
Cu(2)	0	0	0.365
O(1)	0	0.5	0.375
O(2)	0	0	0.165
O(3)	0.33	0.5	0

Table 5-16. Standard starting model for Rietveld refinement.

"Bond"	Length (Å)	Pb co-ordination number
Pb – Pb	3.82	4
Pb - Cu(1)		
Pb – Sr	3.67	8
Pb – Y	6.51	2
Pb – Ca		
Pb - Cu(2)	4.32	2
Pb - O(1)	4.83	8
Pb - O(2)	1.95	2
Pb - O(3)	2.29	4

Excess oxygen O(4) excluded from these calculations, bond length would be 1.91 Å.

Table 5-17. Data derived from table 5-16.

Beginning with the room temperature measurement on sample $(Pb_{0.5}Cu_{0.5})Sr_2Y_1Cu_2O_{7.1}$ from tables 5-16 and 5-17, the oxygen is most appropriate to fit into the first two shells that are associated with the largest peak in the plot at ~2Å. Starting values are shown in table 5-18.

Shell	**1**	**2**
Atom	oxygen	oxygen
Distance from absorber (Å)	2.0	2.3
Number of atoms	2	4

Table 5-18. Starting values for fitting of oxygen nearest neighbour.

In practice, however, this model turns out to be incorrect and instead only one shell is required, table 5-19. The fit to the experimental data is very good as seen from figure 5.30, and the errors for A (Debye-Waller factor) and N (number of atoms in the shell) are what might normally be expected when the model is fitting correctly.

Shell	**1**
Atom	oxygen
Distance from absorber-r_1 (Å)	2.121±0.005
Number of atoms in shell-N	4.53±0.14
Debye-Waller factor-A ($Å^{-2}$)	0.0199±0.0010

Table 5-19. Best fit of experimental EXAFS data to first shell.

Repeating this procedure for these data over the range 200-600°C, the following trends shown in figures 5.31 and 5.32 for the Pb-O co-ordination number and the Pb-O bond length respectively.

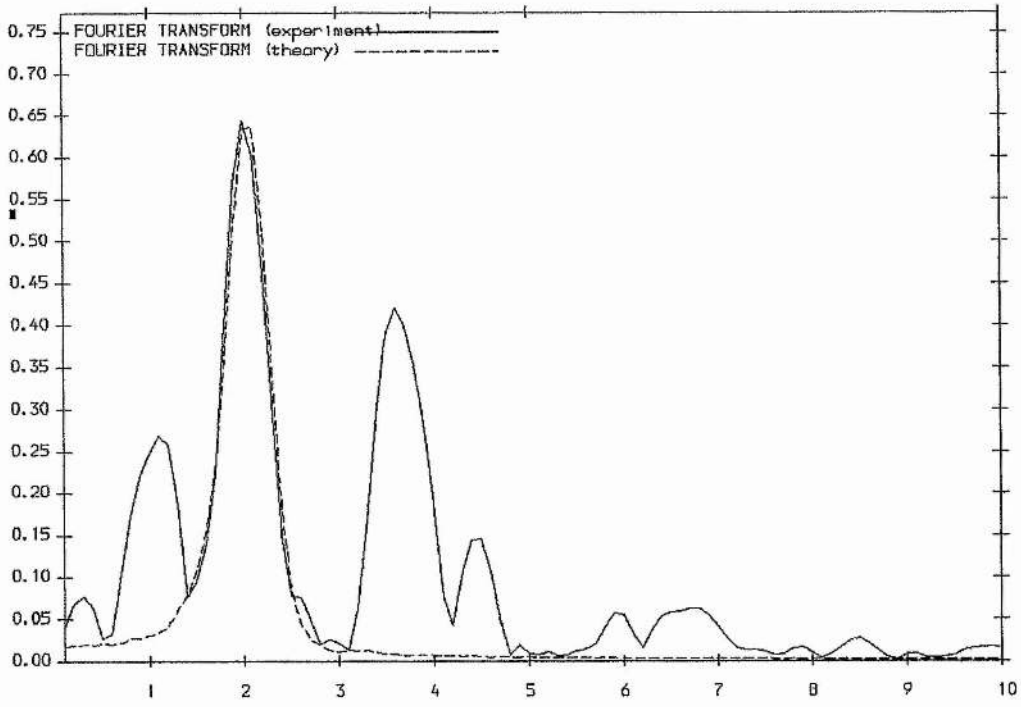

Figure 5.30. Fitted first shell to experimental data at 25°C.

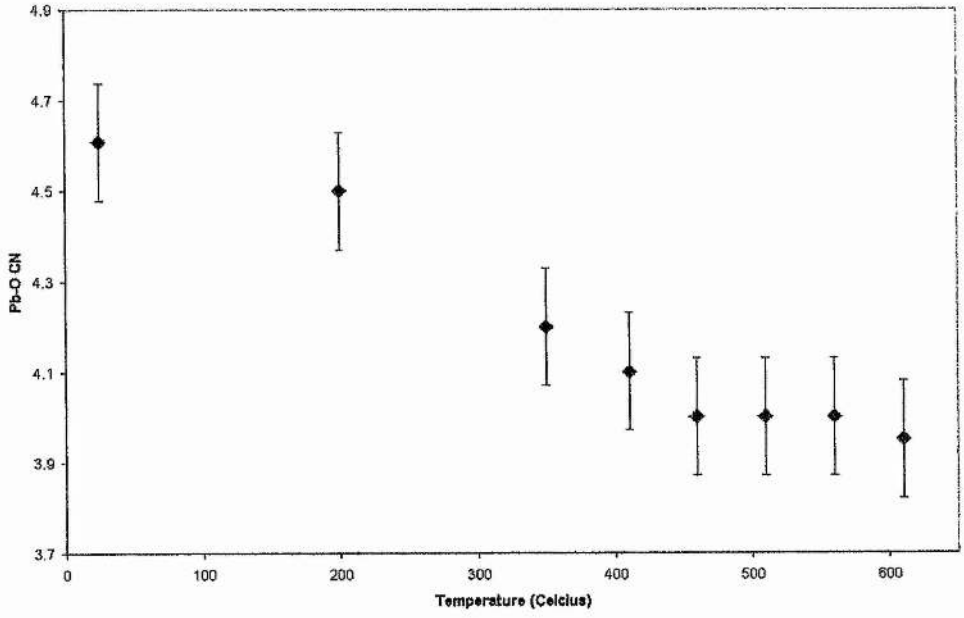

Figure 5.31. Variation in Pb-O co-ordination number over temperature range 200-600°C.

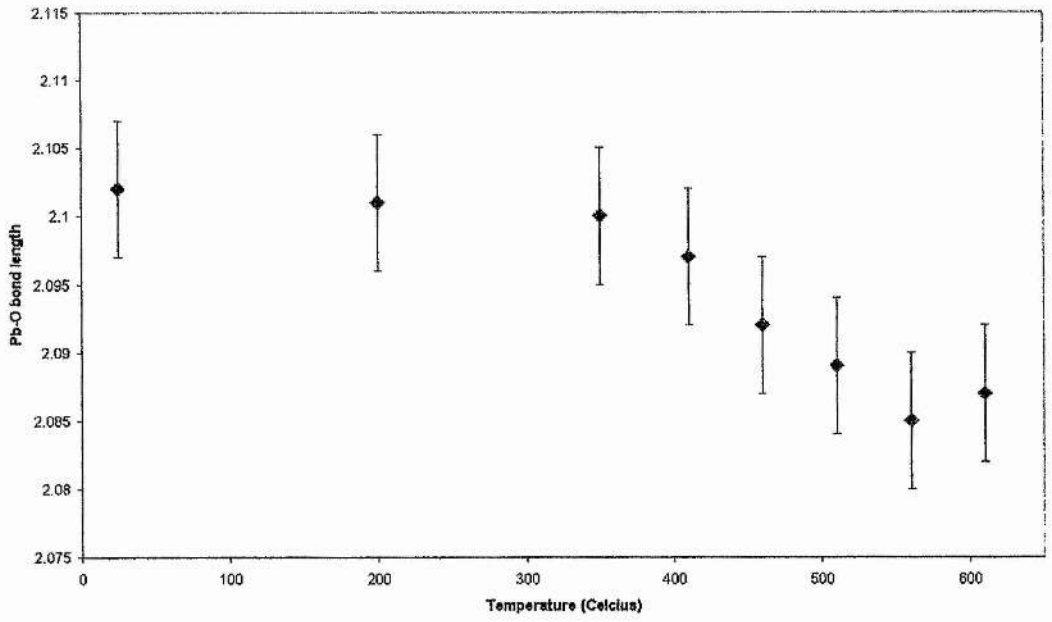

Figure 5.32. Variation in Pb-O bond length over the temperature range 200-600°C.

The Pb-O co-ordination number drops from a value of approximately 4.5 at 200°C to approximately 4.0 by 400°C and remains fairly steady from 450°C upwards. This change may be attributed to the loss of the excess oxygen present on the (0,½,0) site on the rocksalt layer that the Pb is co-ordinated to. The Pb-O bond length also follows the same trend i.e. shortens, which is sensible because the excess oxygen is sandwiched between the Pb/Cu sites and should disrupt the Pb/Cu and other oxygen neighbours. In turn these atoms would tend to move further from their ideal positions to minimise the system energy. As the excess is removed, then it again becomes more favourable for the Pb to move back towards its ideal site. If the Pb-O(3) and Pb-O(2) bond lengths derived from the Rietveld refinements were the correct model, then over the range 1.5-3Å one should expect to see a number of distinct peak maxima within this region, but the results above certainly give no evidence of any oxygen present at the 2.5Å range from the Pb atom. Since there is only one peak maxima over this range it seems fairly evident that the model derived from diffraction does not adequately describe the distribution of oxygen in the region of the Pb and Cu atoms on the rocksalt layer. Repeating the procedures for fitting the first shell described above on the other three samples

$(Pb_{0.6}Cu_{0.4})Sr_2(Y_{0.8}Ca_{0.2})Cu_2O_{7.1}$, $(Pb_{0.65}Cu_{0.35})Sr_2(Y_{0.7}Ca_{0.3})Cu_2O_{7.1}$

and $(Pb_{0.7}Cu_{0.3})Sr_2(Y_{0.7}Ca_{0.3})Cu_2O_{7.1}$ again displays the same trends as above when the temperature is increased over the range 25-600°C, shown in figures 5.33-5.35 respectively.

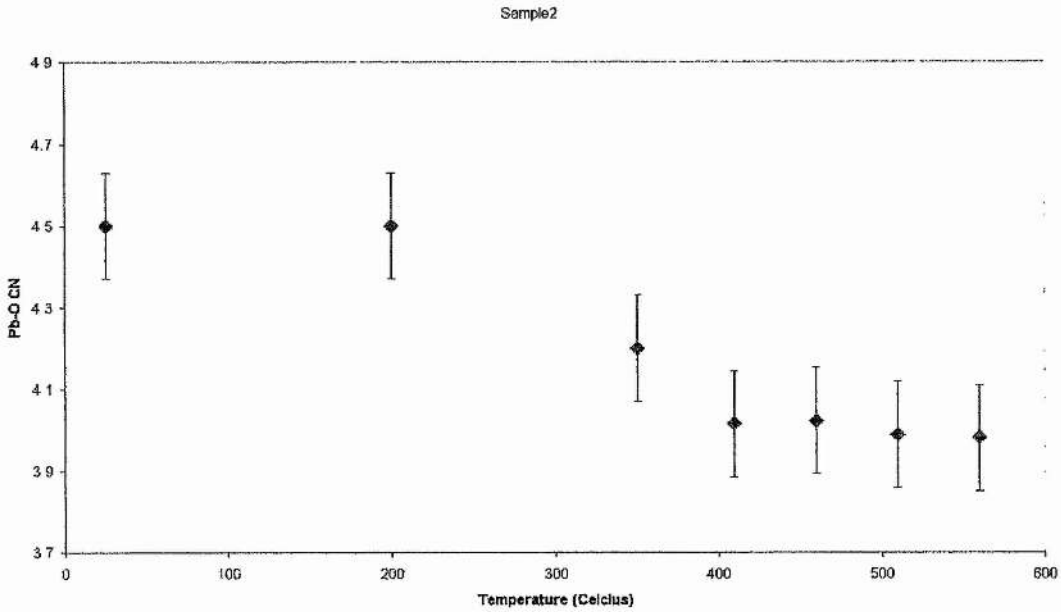

Figure 5.33. Variation in Pb-O co-ordination number over temperature range 25-600°C in sample 2, $(Pb_{0.6}Cu_{0.4})Sr_2(Y_{0.8}Ca_{0.2})Cu_2O_{7.1}$.

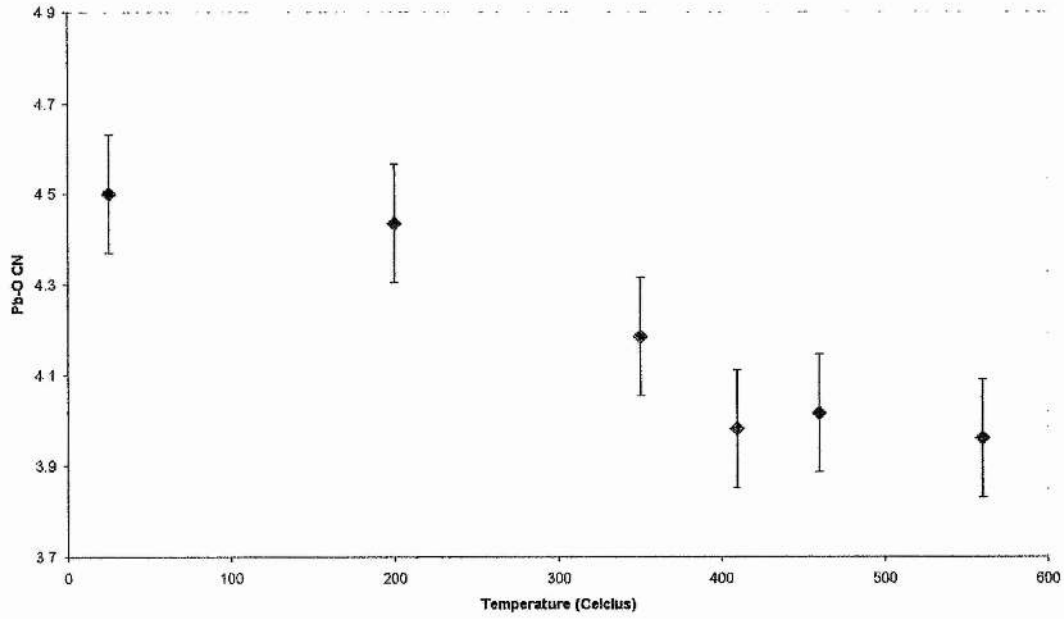

Figure 5.34. Variation in Pb-O co-ordination number over temperature range 25-600°C in sample 3, $(Pb_{0.65}Cu_{0.35})Sr_2(Y_{0.7}Ca_{0.3})Cu_2O_{7.1}$.

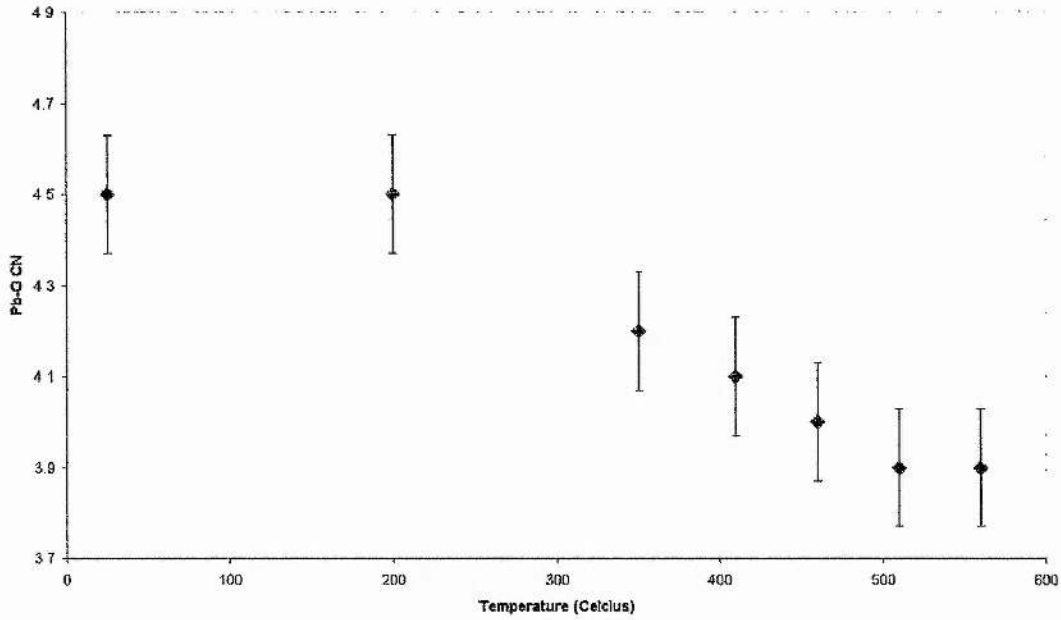

Figure 5.35. Variation in Pb-O co-ordination number over temperature range 25-600°C in sample 4, $(Pb_{0.7}Cu_{0.3})Sr_2(Y_{0.7}Ca_{0.3})Cu_2O_{7.1}$.

Returning to the $(Pb_{0.5}Cu_{0.5})Sr_2Y_1Cu_2O_{7.1}$ sample at room temperature, the next stage of the process was to fit the data over the range 3-5Å.. From table 5-17 the next nearest neighbour to the Pb is 8xSr at 3.67 Å and then from there 2xPb and 2xCu at 3.82 Å. In practice, the results are quite different and the values obtained are not satisfactory, as shown in figures 5.36-5.44. Note, the esd values are not shown on these diagrams. The number of models shown may seem extreme, but they serve to show the similar fits obtained with what are in some cases very different models. Although some of the models look better than others, particularly those with the lower Debye-Waller factors, inspection of the errors (esd) reveals a totally different picture. The errors on Debye-Waller factors (A. On the figures A1, A1, ...) and in the number of atoms in a shell (N. On the figures N1, N2, ...) tend to be large and beyond any acceptable levels. in some cases the errors are larger than the values themselves. It is not reasonable to say any one particular model is best and draw conclusions. Quite possibly it is the fact that the outer shells of Pb, Sr and Cu are so close together that their contributions to the EXAFS scattering in some way interfere with one another.

The Pb-Sr co-ordination number falls well below the expected value of 8and also it is not possible to separate the distances of Pb-Sr, Pb-Pb and Pb-Cu. Although this information obtained seems useless, it actually helps answer a few questions about the local environment of the Pb atom. As the temperature increases, the second shell begins to disappear and cannot be seen at all by 550°C so nothing realistically can be extracted.

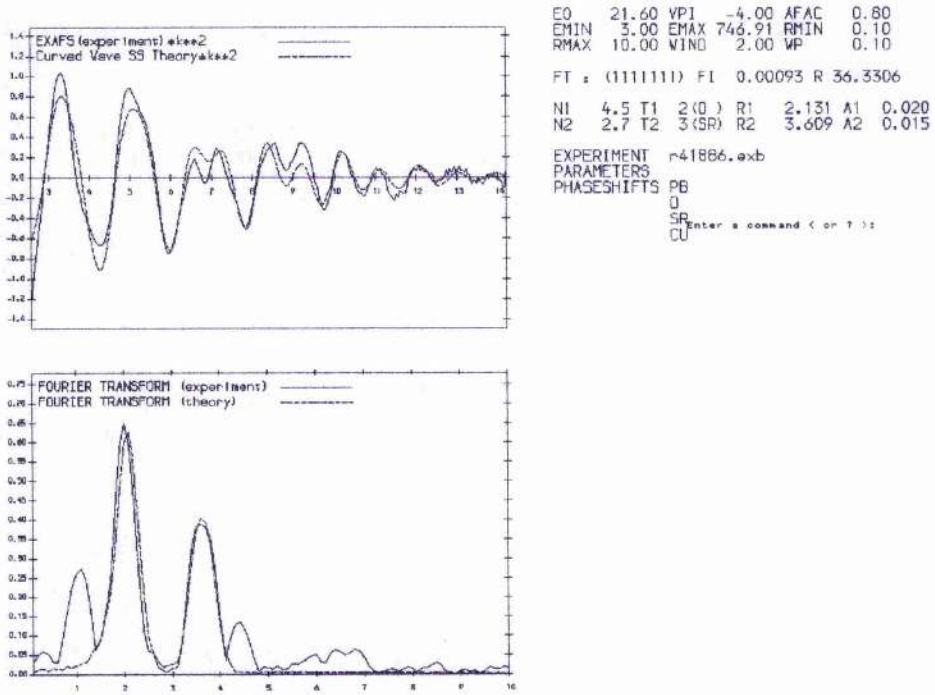

5.36. Shells 2/3 model 1.

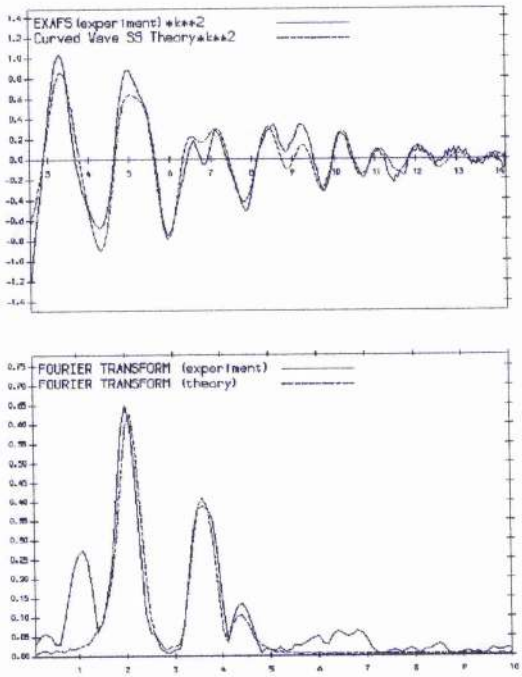


```
E0    21.58 VPI   -4.00 AFAC   0.80
EMIN   3.00 EMAX 746.91 RMIN   0.10
RMAX  10.00 WIND   2.00 WP     0.10

FT : (1111111) FI  0.00084 R 34.1317

N1   4.5 T1  2(O )  R1   2.132 A1  0.02(
N2   2.5 T2  3(SR)  R2   3.608 A2  0.01
N3   4.6 T3  3(SR)  R3   4.215 A3  0.03
```

5.37. Shells 2/3 model 2.

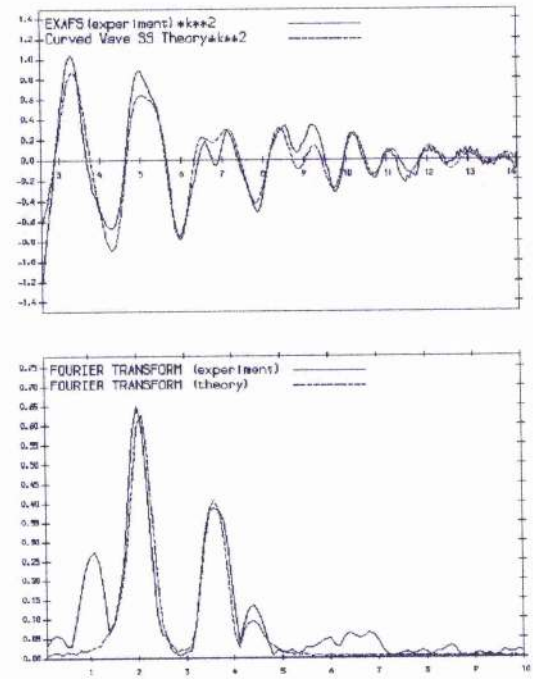


```
E0    21.63 VPI   -4.00 AFAC   0.80
EMIN   3.00 EMAX 746.91 RMIN   0.10
RMAX  10.00 WIND   2.00 WP     0.10

FT : (1111111) FI  0.00083 R 34.1084

N1   4.5 T1  2(O )  R1   2.131 A1  0.020
N2   2.4 T2  3(SR)  R2   3.607 A2  0.013
N3   6.1 T3  3(SR)  R3   4.212 A3  0.043
```

5.38. Shells 2/3 model 3.

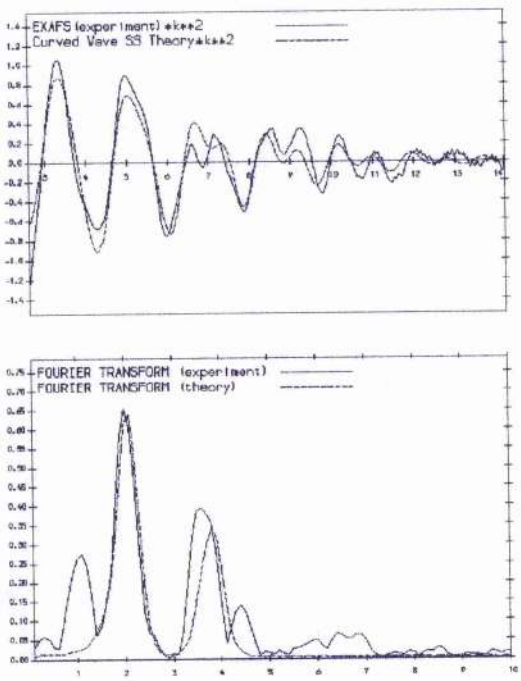


```
E0    22.52 VPI   -4.00 AFAC   0.80
EMIN   3.00 EMAX 746.91 RMIN   0.10
RMAX  10.00 WIND   2.00 WP     0.10

FT : (1111111) FI  0.00104 R 40.1770

N1   4.5 T1  2(O ) R1   2.122 A1  0.019
N2   2.6 T2  4(CU) R2   3.748 A2  0.016
```

5.39. Shells 2/3 model 4.

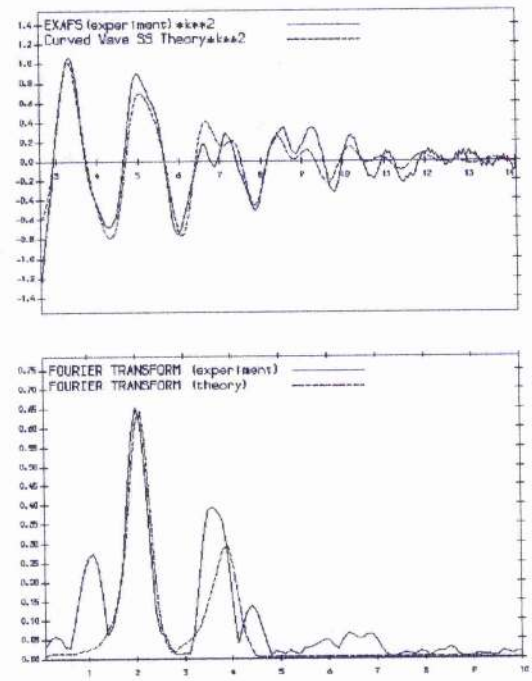


```
E0    22.55 VPI   -4.00 AFAC   0.80
EMIN   3.00 EMAX 746.91 RMIN   0.10
RMAX  10.00 WIND   2.00 WP     0.10

FT : (1111111) FI  0.00095 R 36.9649

N1   4.5 T1  2(O ) R1   2.121 A1  0.019
N2   3.3 T2  4(CU) R2   3.756 A2  0.021
N3   9.0 T3  1(PB) R3   3.290 A3  0.100
```

5.40. Shells 2/3 model 5.

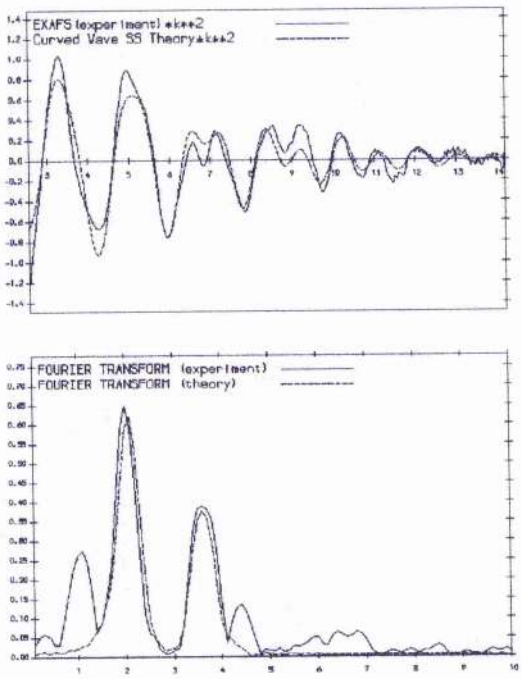

E0 21.48 VPI -4.00 AFAC 0.80
EMIN 3.00 EMAX 746.91 RMIN 0.10
RMAX 10.00 WIND 2.00 WP 0.10

FT : (1111111) FI 0.00090 R 35.8566

N1 4.5 T1 2(O) R1 2.133 A1 0.020
N2 2.4 T2 3(SR) R2 3.605 A2 0.015
N3 2.7 T3 4(CU) R3 3.882 A3 0.047

5.41. Shells 2/3 model 6.

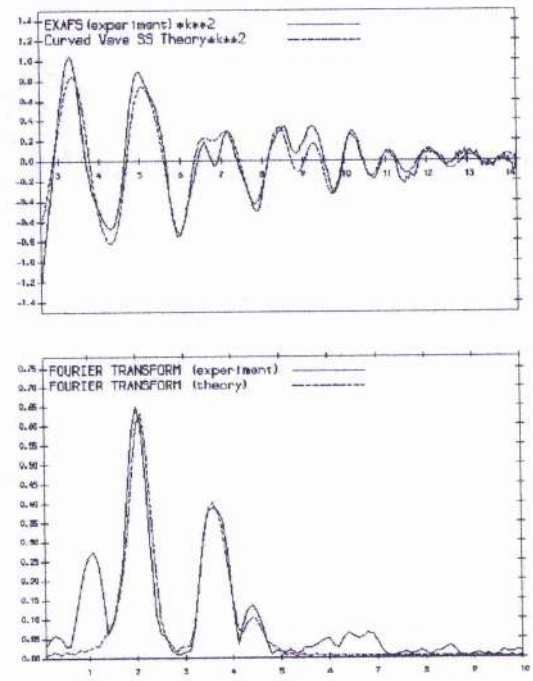

E0 21.73 VPI -4.00 AFAC 0.80
EMIN 3.00 EMAX 746.91 RMIN 0.10
RMAX 10.00 WIND 2.00 WP 0.10

FT : (1111111) FI 0.00084 R 33.5950

N1 4.5 T1 2(O) R1 2.130 A1 0.019
N2 2.5 T2 3(SR) R2 3.609 A2 0.013
N3 2.3 T3 1(PB) R3 4.049 A3 0.019

5.42. Shells 2/3 model 7.

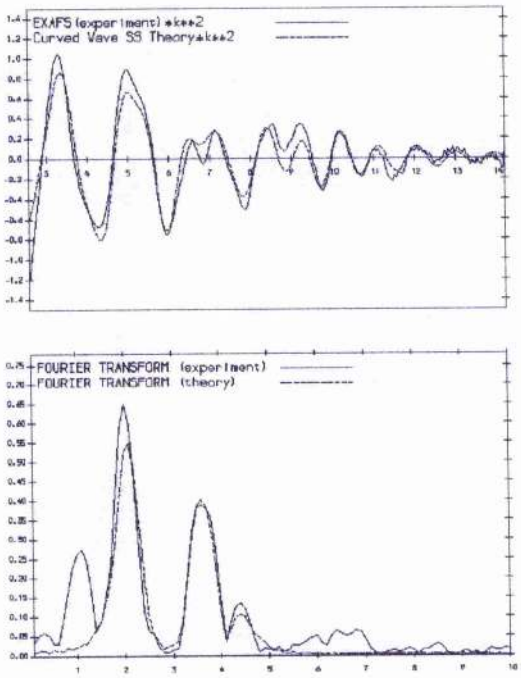


```
E0    21.74 VPI   -4.00 AFAC   0.80
EMIN   3.00 EMAX 746.91 RMIN   0.10
RMAX  10.00 WIND   2.00 WP     0.10

FT : (1111111) FI  0.00084 R 33.9296

N1   4.5 T1  2(O ) R1   2.131 A1  0.022
N2   2.7 T2  3(SR) R2   3.610 A2  0.014
N3   2.1 T3  3(SR) R3   4.197 A3  0.025
N4   3.2 T4  1(PB) R4   4.105 A4  0.034

EXPERIMENT  r41886.exb
PARAMETERS
PHASESHIFTS PB
            O
            SR
            CU
```

5.43. Shells 2/3 model 8.

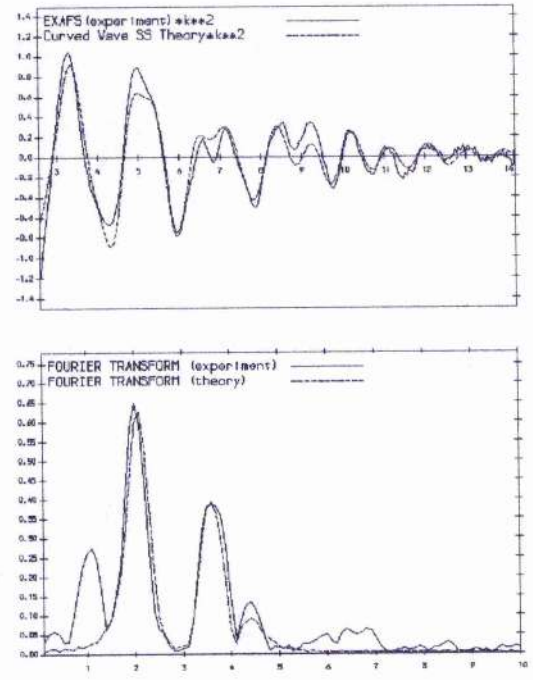


```
E0    21.71 VPI   -4.00 AFAC   0.80
EMIN   3.00 EMAX 746.91 RMIN   0.10
RMAX  10.00 WIND   2.00 WP     0.10

FT : (1111111) FI  0.00081 R 33.8654

N1   4.5 T1  2(O ) R1   2.130 A1  0.020
N2   2.3 T2  3(SR) R2   3.606 A2  0.014
N3  10.9 T3  3(SR) R3   4.208 A3  0.055
```

5.44. Shells 2/3 model 9.

The variation in the Pb-0 CN from 4.5 to 4, in figures 5.31 and-5.33-5.35 compare well to the TGA plot seen in such samples heated in such a low pO_2 environment, figure 5.45. The behaviour of a sample in the thermal analyser is different from that in the experimental furnace since the pO_2 and heating rates are not the same. But it is the trend that is important and it would seem clear that as the excess oxygen is removed then the Pb-O CN is being lowered due to this. Annealing in low pO_2 environments is discussed further in chapter 6 and the effects that small pO_2 changes have on samples are covered. If the Pb/Cu were situated on their ideal sites, then it would be expected that 8xSr should surround the Pb as mentioned previously, this was not the case. This certainly adds weight to the belief that Pb is displaced from its ideal position in this material and quite possibly the excess oxygen affects some of the Sr also.

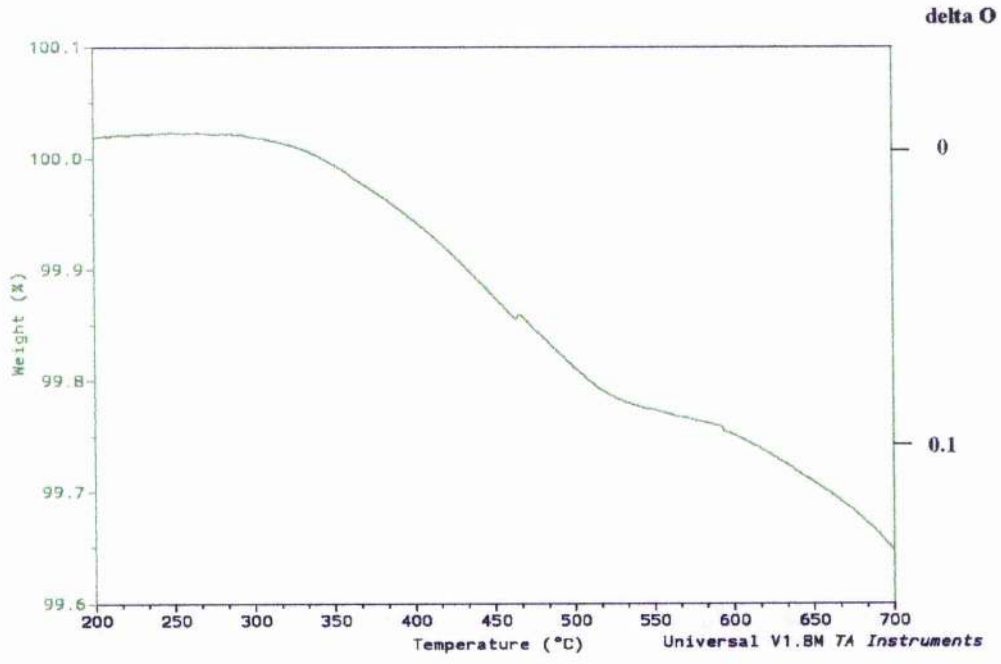

Figure 5.45. TGA plot in PbCu:1212 sample in low pO_2 environment.

5.52. Solid state NMR studies on 1212 phase

NMR measurements were performed on the yttrium and lead nuclei, measuring spin-lattice relaxation, spin-spin relaxation, linewidth and chemical/Knight shift as a function of temperature from room temperature to ~130K. A 1 Molar solution of YCl_3

was used as a secondary reference for the yttrium measurements and a $Pb(NO_3)_2$ solution as a secondary reference for the lead measurements. In general very standard pulse techniques on a MSL Brucker 500 spectrometer were used for the experiments. The Meiboom-Gill[10] multi-pulse sequence, 90_0-τ-180_{90}-2τ-180_{90}-2τ-..., was used for the measurement of the spin-spin relaxation. The ^{89}Y nucleus was chosen as a known probe of Cu-O plane behaviour, whilst the ^{207}Pb nucleus aimed to provide information about the charge reservoir away from the plane. The samples studied are listed in table 5-20 and were prepared by the standard methods discussed in chapter 3.

Sample	Composition	Calcium (x)	T_c
I2	$Pb_{0.6}Cu_{2.4}Sr_2Y_{0.8}Ca_{0.2}O_{7.0}$	0.2	0
ISIS3	$Pb_{0.65}Cu_{2.35}Sr_2Y_{0.7}Ca_{0.3}O_{7.0}$	0.3	19
ISIS4	$Pb_{0.7}Cu_{2.3}Sr_2Y_{0.6}Ca_{0.4}O_{7.0}$	0.4	37
ISIS4-07.1	$Pb_{0.7}Cu_{2.3}Sr_2Y_{0.6}Ca_{0.4}O_{7.1}$	0.4	0

Table 5-20. Sample characteristics used in NMR experiments.

In figure 5.46, with shifts referenced to a zero at +200ppm relative to the shift of a 1M solution of YCl_3, both ISIS3 and ISIS4 show the ^{89}Y shift reducing in magnitude with temperature[11]. In both samples the shift is small and negative, -165ppm at room temperature moving to around -100ppm as the temperature descends towards 100K. The ^{89}Y spin-lattice relaxation rate, figure 5.47, exhibits a weak temperature dependence in both ISIS3 and ISIS4. Discussed in the context of the decreasing magnitude of shift as T descends in figure 5.46, these temperature dependencies are surprising; in a normal metal with constant shift T_1T is also a constant, so that, if the shift gets smaller numerically, $(T_1T)^{-1}$ might be expected to get smaller as T descends. In both cases, experimentally $(T_1T)^{-1}$ becomes larger.

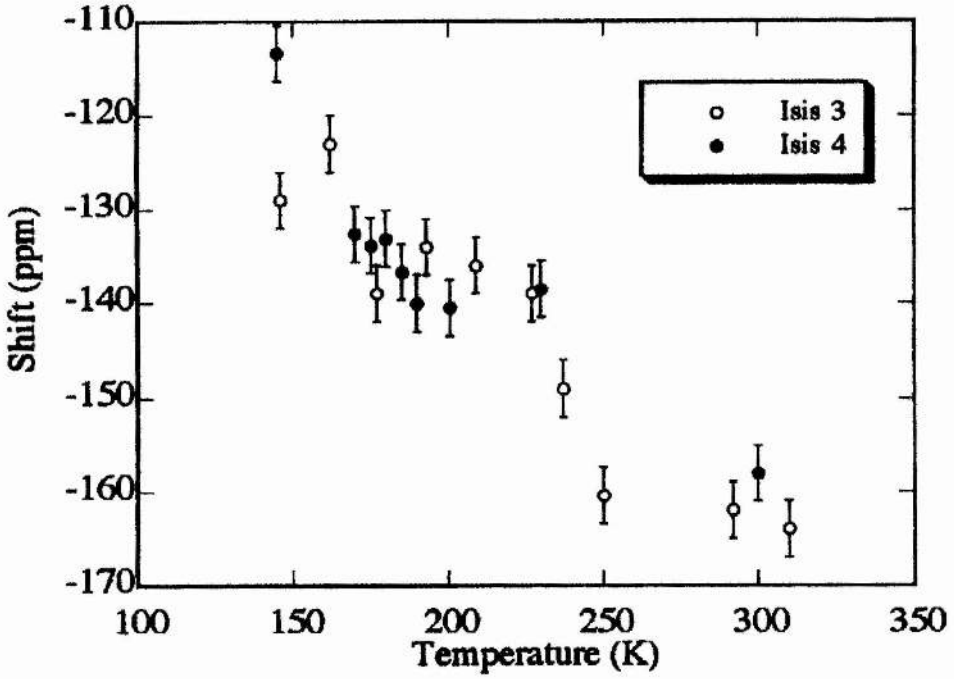

Figure 5.46. ^{89}Y NMR results for the shift in ISIS3 and ISIS4.

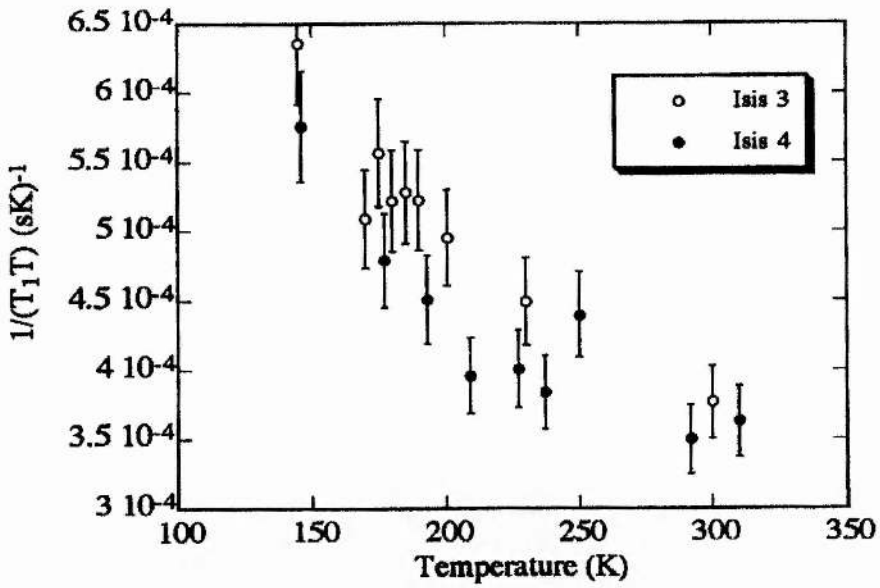

Figure 5.47. ^{89}Y NMR results for the inverse of the product of the spin-lattice relaxation time T_1 and the absolute temperature T in ISIS3 and ISIS4.

The narrowing of the linewidth as the temperature descends at higher temperatures, figure 5.48, certainly in ISIS4, may be connected with the effects shown in figures 5.49 and 5.50. In figure 5.49 the result of a Meiboom-Gill spin-echo measurement of

T_2 is shown, where the spin-echo peak maxima are plotted as a function of time from the first 90° pulse. A clear oscillation is evident, and the oscillation frequency is plotted in figure 5.50 for three samples as a function of temperature. Such behaviour is taken to be the signature of a small spin-spin interaction between two unlike ^{89}Y sites[12,13]. In ISIS4 this oscillation frequency, which measures the spin-spin splitting, is seen to decrease as the temperature is lowered, and this decrease may be the driving mechanism for the linewidth decrease observed in the high temperature range in figure 5.48 in these samples. The forms of the oscillation observed in the Meiboom-Gill spin echo decays in these samples are characteristic of a spin-spin interaction between two yttrium nuclei which need to be unlike, so some dimerisation of yttrium is necessary in the crystal structure. The data in figure 5.50 indicates that either the spin-spin coupling, observable because of the inequivalence generated by the distortion, or this distortion itself is a strong function of temperature, certainly in ISIS3 and ISIS4, but less convincingly in the non-superconductor ISIS4-07.1; 250K appears to be an onset transition temperature. The different sign of the temperature co-efficient for this oscillation frequency, figure 5.50, for ISIS3 and ISIS4 cannot be explained.

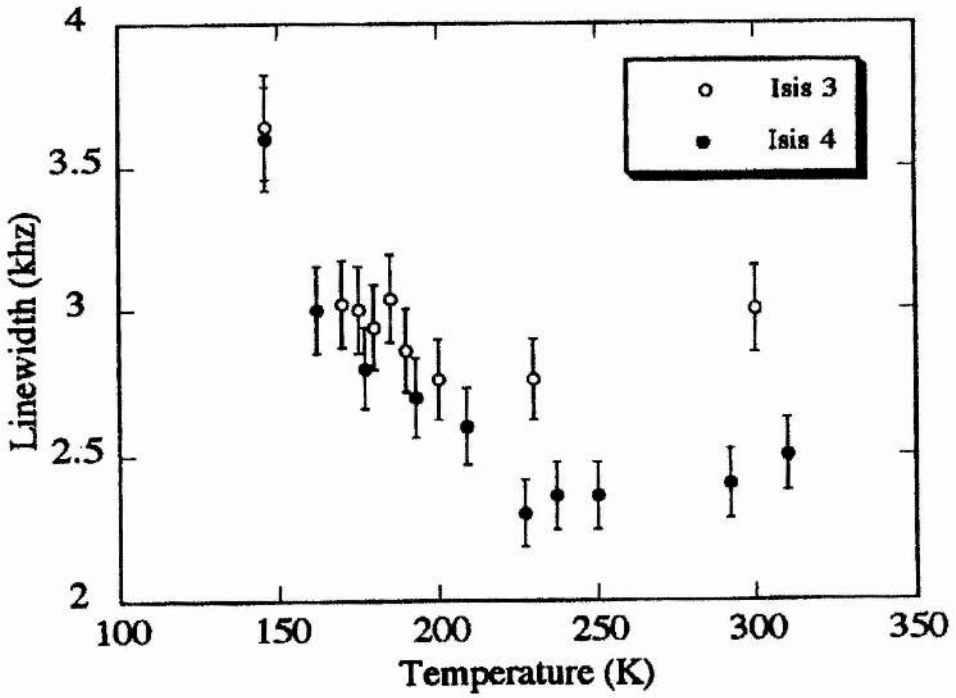

Figure 5.48. ^{89}Y NMR results for the linewidths as a function of temperature.

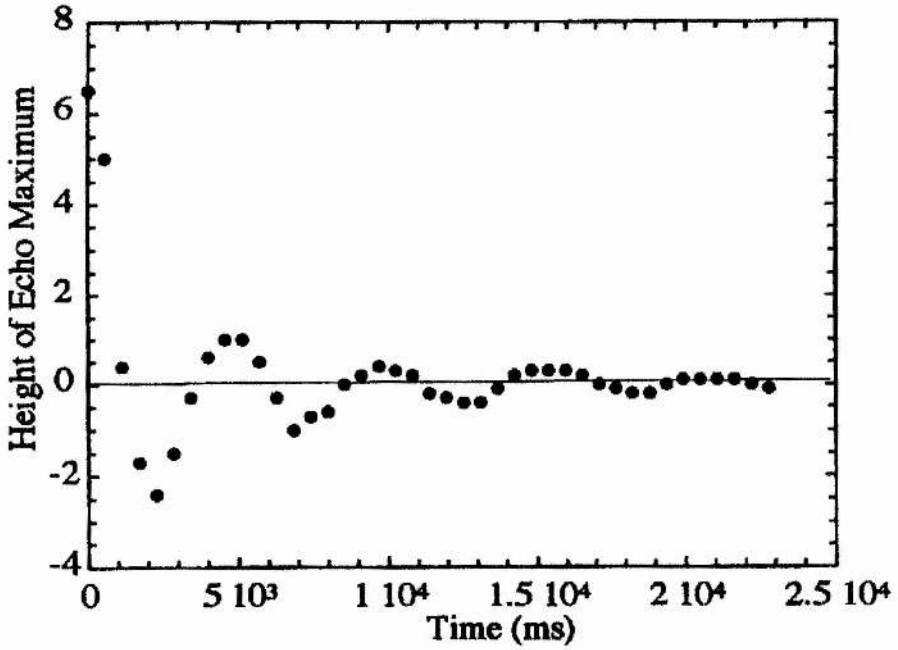

Figure 5.49. Characteristic form of the multi-pulse spin-echo decay. Plotted are the spin maxima from ISIS4 at 130K.

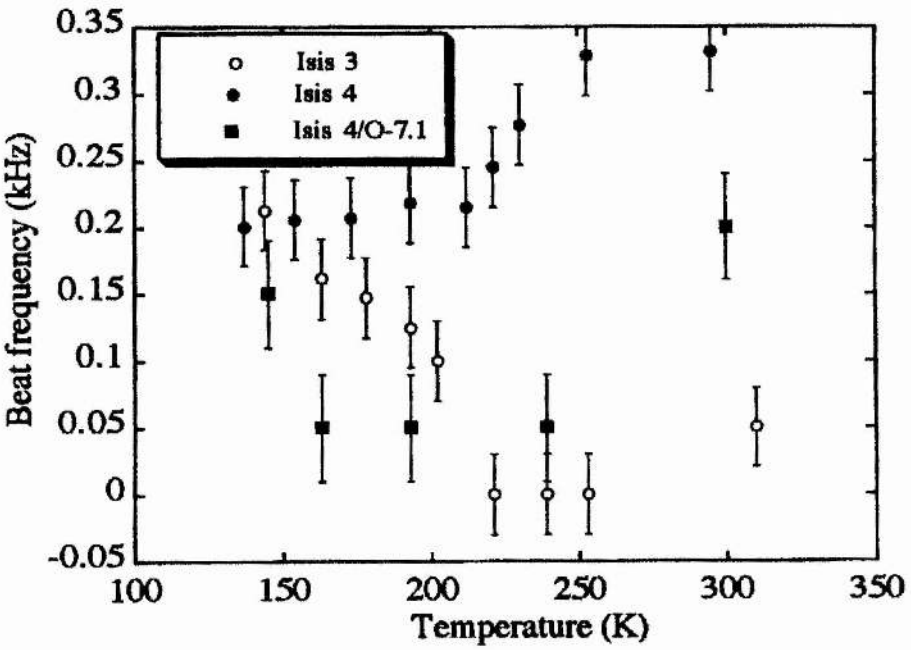

Figure 5.50. The oscillation frequency plotted as a function of temperature.

Measurement of the Pb spin-echo signal in ISIS4 at temperatures down to 160K using a step by step frequency technique, gives a broad resonance of about 160 kHz at room temperature, broadening to 250 kHz at 160K. The line maximum is independent of temperature (104.400 MHz on spectrometer). A reference sample of $Pb(NO_3)_2$ solution resonates at 104.320 MHz in the same field, and $PbCl_4$ would therefore resonate at 104.570 MHz. The absence of any temperature variation in the position of this line, in a range where the yttrium shift is changing markedly (figure 5.46) leads to the supposition that the Pb resonance is disconnected from the magnetic behaviour of the Cu-O planes. Room temperature shift data on all the Pb resonances have been added to figure 5.51 (shifts referenced with respect to $Pb(NO_3)_2$ solution), showing a pronounced variation of the shift across the sample range at room temperature.

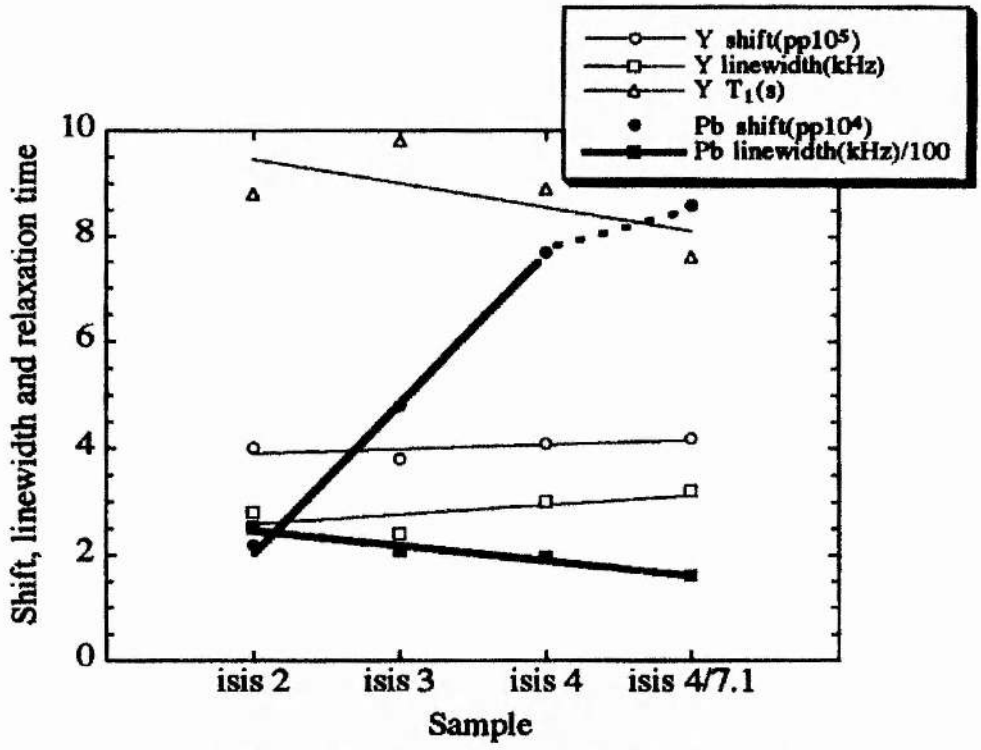

Figure 5.51. ^{89}Y shift, linewidth and T_1, as well as shift and linewidth data for ^{207}Pb, compared at room temperature in four samples. The line (bolder for Pb) are guides for the eye; for the shift case the line has been broken in going from ISIS4 to ISIS4-O7.1 since this corresponds to putting extra oxygen into the vicinity of Pb.

Comparing figures 5.46 and 5.47, the yttrium shift and relaxation rate data, the similarity in trend over the temperature range is striking. This leads to the favouring of the idea that the trend in the shift as the temperature decreases is driven by an increase

in a positive shift contribution, a well known effect in transition metal NMR and would lead, at the same time, to a decrease in the net magnitude of the shift and to a rise in the relaxation rate product $(T_1T)^{-1}$, since the shift/relaxation rates from the two contributions would add/subtract.

Figure 5.48 appears to demonstrate a strong broadening at low temperature in both samples but significantly both also show a line narrowing as T descends in the range 300-250K. The narrowing is just as significant, but the difference in width between ISIS3 and ISIS4 in this temperature range is marked. Both samples exhibit ^{89}Y NMR widths considerably broader than widths observed in stoichiometric YBCO, where 1 kHz or less is common. It may be safely assumed that the larger widths in ISIS3 and ISIS4 are associated with the distribution of Knight shifts, due to a range of local environments stemming from the random nature of the Pb/Cu and Y/Ca substitutions. The decreased width of ISIS4 in the high temperature range would therefore indicate a more ordered structure. At lower temperatures the widths in the two samples equalise, which may indicate similar numbers of paramagnetic centres in the samples.

It is quite useful to compare some of these present results with ^{89}Y NMR results in the Tl/Pb system[14,15]. In summary, the trends in shift with temperature in the Pb/Tl system are comparable to those in figure 5.47. The ^{89}Y shifts are numerically even smaller in Pb/Tl compared to Pb/Cu. In the Pb/Cu system at room temperature shifts are about -160 ppm (relative to +200 ppm in YCl_3) and are about -100 ppm relative to the same reference.

There is NMR evidence for the onset of a structural event around 250K, as shown particularly by the Meiboom-Gill splitting of figures 5.49 and 5.50. As noted previously, the appearance of this oscillation in the spin-echo decay indicates that a significant fraction, at least 20%, of yttrium nuclei form dimers. This estimate originates from an approximate fit of the spectra to the type shown in figure 5.49 into (i) decaying, and (ii) oscillating and decaying components where the dimers would correspond to component (ii).

Looking at the Pb NMR and comparing results for yttrium and lead with the TlPb:1212 system[14,15,16] then in $(Pb_{0.5}Tl_{0.5})Sr_2(Y_xCa_{1-x})Cu_2O_7$, where resonances up to 104.47 MHz were observed, the shifts varied with yttrium concentration in just the same way as did the shift of the ^{63}Cu. In this case it may be assumed that the Pb resonance senses the Cu-O planes magnetisation, which not seen in the Pb/Cu system under study here. Worth noting is the origin of the shifts[15], which in the Tl:1212 system is 104.47 MHz rather nearer Pb^{4+} (104.57) than Pb^{2+} (104.32). In the PbCu:1212 system there are indications that the Pb is nearer Pb^{2+} in character. But, other techniques such as X-ray absorption and bond valence sum calculations indicate that the Pb is present as Pb^{4+}. Further work would certainly be required to confirm these findings though.

Thanks to Drs. David P Tunstall and Svetlana G. Titova for performing and interpretation of the NMR measurements.

5.6. Summary

In the system $(Pb_{[1+x]/2}Cu_{[1-x]/2})Sr_2(Y_{1-x}Ca_x)Cu_2O_{7\pm\delta}$, superconductivity is only induced in quenched samples when the Ca content (x) is > 0.2. The onset temperature reaches a maximum of 43K in the x = 0.4 sample and drops to 25K in the x = 0.5 and 0.6 samples. However, the samples are not phase pure when x > 0.3 and the increasing level of impurity above x = 0.4 means it is not at all certain what the proper composition of the 1212 phase is. Thus, the actual superconducting onset temperatures are not necessarily representative of those that might be obtained if the sample had the exact nominal stoichiometry.

The annealing temperature proves absolutely critical and can greatly affect both the superconducting fraction and onset temperature. By annealing and quenching samples from selected temperatures, measuring superconducting properties and comparing these with TGA measurements it is possible to calculate the actual oxygen content within the sample at any particular temperature. The results show that the highest onset temperature and superconducting volume fraction are obtained over a very narrow

oxygen content range of 6.99-7.00. The excess affects superconducting properties of samples and these most probably revert to their non-superconducting form when the oxygen content reaches 7.03.

When the Ca content of samples is varied over the range x = 0-0.4, the **a** axis shows a steady increase in its length. It would appear that this axis length is not decreased by increasing number of holes in the CuO_2 planes which is seen in the PbTl:1212 system. Indeed the introduction of excess oxygen increases the unit cell size by a fixed amount regardless of composition. Kosuge[9] and co-workers showed from Hall, Seebeck and resistivity measurements that the number of hole carriers was increasing in quenched samples in the $(Pb_{[1+x]/2}Cu_{[1-x]/2})Sr_2(Y_{1-x}Ca_x)Cu_2O_{7\pm\delta}$ system, where x = 0.35-0.4.

There is no significant change in the Pb/Cu position as Ca content increases in quenched samples and indeed this trend is also seen for the slow cooled samples. However, the Pb/Cu has been offset by a fixed amount upon introduction of the excess oxygen. The rocksalt layer oxygen O(3) moves towards its ideal position as Ca content increases, but from XRD data refinements the errors on the oxygen position mean it is not absolutely clear how much O(3) shifts when the excess oxygen is present. The Pb-O(3) and Pb-O(2) bondlengths show a fairly linear increase as Ca content increases, but there is actually only a very small difference between quenched and slow cooled samples. Indeed the difference only becomes significant at the higher Ca levels.

Rietveld refinements on samples of nominal composition $(Pb_{0.7}Cu_{0.3})Sr_2(Y_{0.6}Ca_{0.4})Cu_2O_{7.0}$ and $(Pb_{0.7}Cu_{0.3})Sr_2(Y_{0.6}Ca_{0.4})Cu_2O_{7.1}$ using XRD and neutron diffraction show a number of interesting results. From XRD the results suggest that these samples are Y rich and Ca deficient as well as being Pb deficient/Cu rich on the rocksalt layer. Neutron diffraction results show that the sample does not appear to be particularly Ca deficient/Y rich and there is no indication of any oxygen deficiency in quenched samples. It is possible to detect the excess oxygen on the rocksalt layer, but an accurate value for this excess is not reliable. Low isotropic temperature factors on the Y/Ca site give some indication that some other element might be present on this site.

Resonant diffraction studies on $(Pb_{0.5}Cu_{0.5})Sr_2Y_1Cu_2O_{7.0}$ and $(Pb_{0.7}Cu_{0.3})Sr_2(Y_{0.6}Ca_{0.4})Cu_2O_{7.0}$ allow refinement of atoms on a site without correlation to other atoms on a site and it provides contrast between atoms of similar atomic number. Results show that no cation substitution is present on the Sr and CuO_2 plane Cu in any of the samples. The Ca free Y end member shows, within experimental error, no indication of any cation deficiency/substitution. The Ca containing sample shows presence of ~5% Pb on the Y/Ca site, with only a small excess of yttrium (0.65 compared to nominal 0.60). The sample is certainly Ca deficient on this site. There is evidence for a small Pb deficiency on the rocksalt layer, but the Cu content remains at its nominal level. There may well be Ca and vacancies present in the rocksalt layer. It seems fairly clear that disorder within the sample increases as Ca replaces Y in samples, but whether or not the system could still be described as self-doping is not totally clear since the experimental composition of $Pb_{0.7}Cu_{2.3}Sr_2Y_{0.65}Ca_{0.35}O_{6.975}$ is virtually the same as the nominal composition of $Pb_{0.7}Cu_{2.3}Sr_2Y_{0.6}Ca_{0.4}O_{7.0}$.

EXAFS experiments studying the local environment reveal clear differences between the local structure and the model produced from diffraction data. In fully oxygenated samples as room temperature the Pb is surrounded by ~4.5 oxygen's at ~2.12Å and this co-ordination number decreases to a stable value of ~4 upon heating. This reduction in the Pb-O co-ordination number is consistent with the loss of oxygen from a TGA experiment under similar low pO_2 conditions. The Pb is co-ordinated by 4 oxygen's, when the excess is not present, two in the plane O(3) and two out of plane i.e. O(2) above and below the plane of the Pb. It is the excess oxygen that accounts for the extra 0.5. There is no evidence for the range of Pb-O bondlengths that are produced from a diffraction model. The local environment would appear to be best described as being more PbO_4 molecular in type, rather than as PbO_6 octahedra. Although exact fitting of the next shell was unsatisfactory, the Pb-Sr co-ordination number was well below the expected value of eight which might be expected if the Pb were fixed on its ideal (0,0,0) site. This would appear to add weight to the belief that the Pb and Cu are displaced.

NMR measurements on PbCu:1212 samples generated some very interesting results, in particular the fact that the Pb resonance in this system does not sense the CuO_2 planes magnetisation unlike in the PbTl:1212 system. There is evidence of Y dimerisation in some of the PbCu:1212 samples, as shown by Meiboom-Gill spin-echo measurements. Its origin is not at all certain, perhaps the Pb which was shown to substitute on this site plays some effect.

5.7. Bibliography and references for chapter 5

[1] M.A. Subramanian, J. Gopalakrishnan, C.C. Torardi and P.L. Gai, *Physica C*, 1988, **157**, 124.

[2] J.Y. Lee, J.S. Swinnea and H. Steinfink, *J. Mat. Res.*, 1989, **4**, 763.

[3] B. Okai, *Jpn. J. Appl. Phys.*, 1990, **29**, L2091.

[4] B. Dabrowski, K. Rogacki, J.W. Koenitzer, K.R. Poepelmeier and J.D. Jorgensen, *Physica C*, 1997, **277**, 24.

[5] T. Maeda, K. Sakuyama, F. Izumi, H. Yamauchi, H. Asano and S. Tanaka, *Physica C*, 1991, **175**, 393.

[6] R.D. Shannon, *Acta Crystallogr.*,1976, **A 32**, 751.

[7] R.S. Liu, P.P. Edwards, Y.T. Huang, S.F. Wu and P.T. Wu, *J. Solid State Chem.*, 1990, **86**, 334.

[8] A.R. Armstrong and W.I.F. David, *Chemistry in Britain*, 1994, **30**, 727.

[9] M. Kosuge, T. Maeda, K. Sakuyama, H. Yamauchi, N. Koshizuka and S. Tanaka, *Physica C*, 1991, **182**, 157.

[10] S. Meiboom and D. Gill, *Rev. Sci. Instr.*, 1958, **29**, 688.

[11] H. Alloul, T. Ohno and P. Mendels, *Phys. Rev. Letters*, 1989, **63**, 1700.

[12] A. Abragam, *Principles of nuclear magnetism*, Oxford, Oxford University Press, 1961.

[13] C. Froidevaux and M. Weger, *Phys. Rev. Letters,* 1964, **12**, 123.

[14] D.P. Tunstall, G.P. Dai, W.J. Webster, H. Booth, S. Arumugam, R.S. Liu and P.P. Edwards, *Supercon. Sci. and Tech.*, 1993, **6**, 33.

[15] G. Dai, D.P. Tunstall, W.J. Webster, H. Booth, S. Arumugan, R.S. Liu and P.P. Edwards, *Proceedings of the Beijing International conference on High Tc Supercon.*, BHTSC 92, World Scientific, 1993.

[16] H. Alloul, T. Ohno and P. Mendels, *J. of Less Common Metals*, 1990, **164-165**, 1022.

Chapter 6. DECOMPOSITION OF 1212 STRUCTURE

6.1. Low pO_2 studies on 1212 materials

In the $(Pb,Cu)Sr_2(Y,Ca)Cu_2O_y$ system there have been reports[1,2] of high (>70K) onset temperatures being achieved when annealing samples in low pO_2 environments such as nitrogen or argon. Zhang et al[1] achieved superconducting onset temperatures of 77K in a sample of nominal composition $(Pb_{0.7}Cu_{0.3})Sr_2(Y_{0.6}Ca_{0.4})Cu_2O_y$ by annealing in argon, which was ~30K higher than Adachi et al[3] achieved for the same nominal composition by quenching in an oxidising atmosphere. Low pO_2 gas environments are used to remove the excess rocksalt layer oxygen more efficiently, avoiding quenching experiments and their associated problems. In figure 6.1 the TGA plot for $(Pb_{0.65}Cu_{0.35})Sr_2(Y_{0.7}Ca_{0.3})Cu_2O_{7.1}$ during a heating and cooling cycle using argon as the purge gas is shown. This is the typical behaviour seen for other compositions in this series.

Part of figure 6.1 is shown more clearly when the derivative weight ($\%.min^{-1}$) profile is plotted, figure 6.2. Effectively, figure 6.1, may be divided in to 4 sections (I-IV). Section I is attributed to the loss of the excess 0.1 oxygen from the rocksalt layer. Over the complete range of section II the weight loss is approximately 2/3 that for section I. In section III the weight loss is more rapid and larger in magnitude. On cooling, section IV, there appears to be a slight weight gain. It is very unclear whether the slope is due to some oxygen uptake since the TGA furnace is slightly porous, or is not real and arises from a baseline drift in the instrument. Note that regardless of the low pO_2 environment this part of the TGA plot still remains the same.

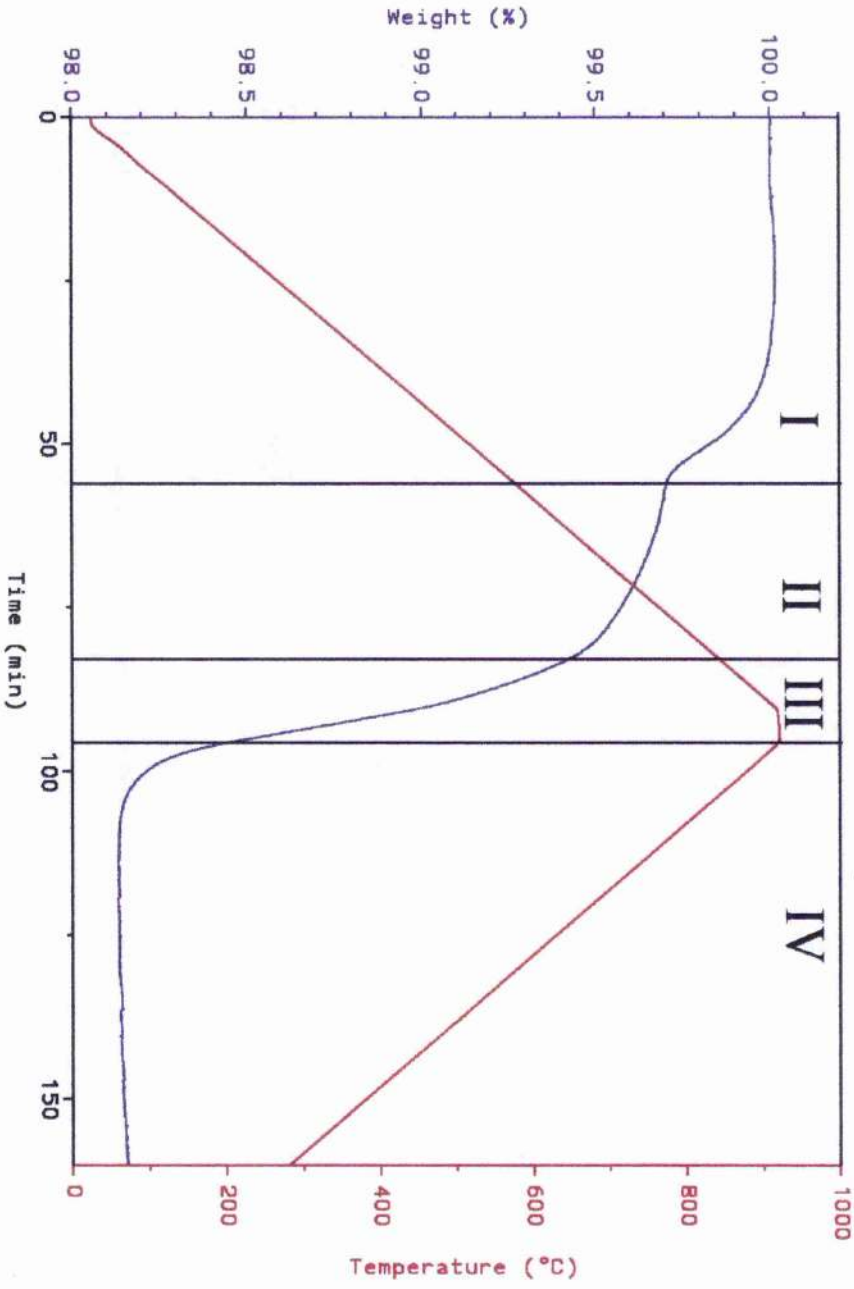

Figure 6.1. $(Pb_{0.65}C_{0.35})Sr_2(Y_{0.7}Cu_{0.3})Cu_2O_y$ sample heated/cooled in an argon environment.

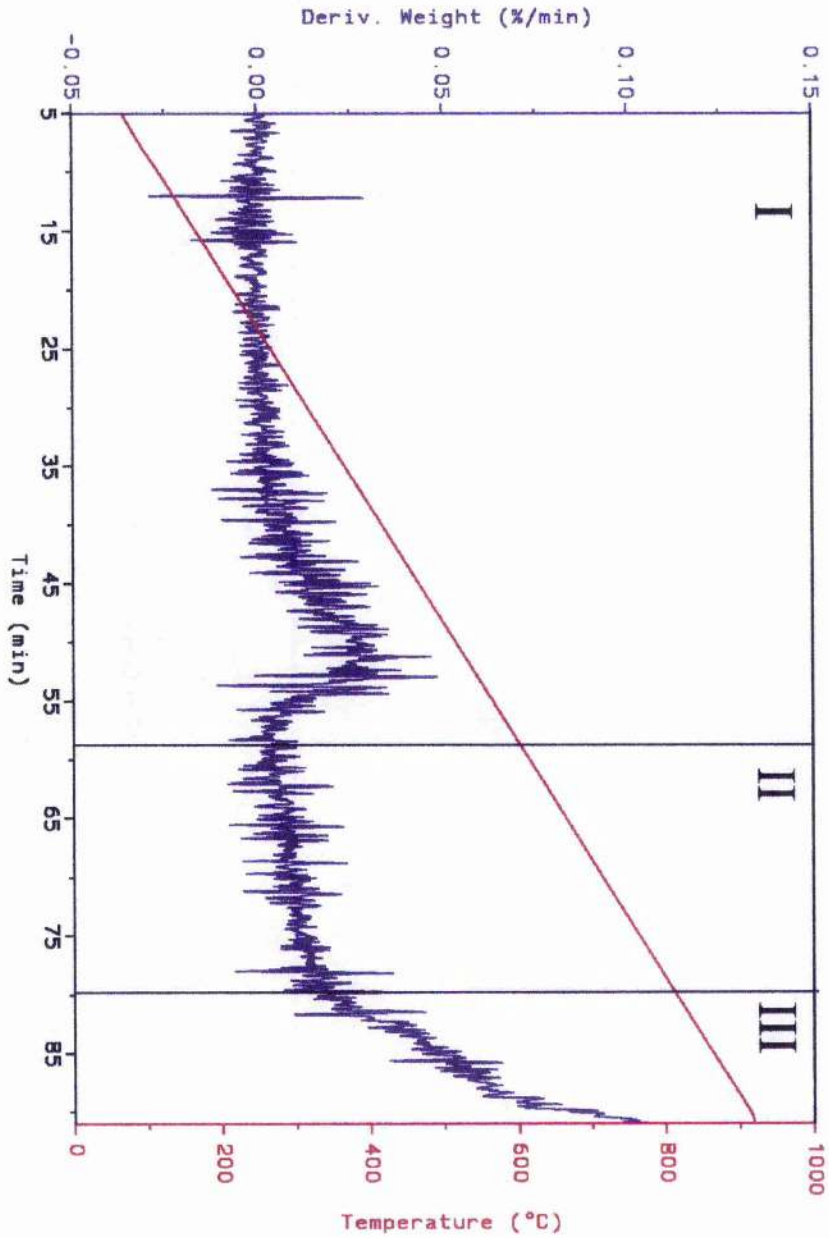

Figure 6.2. TGA derivative weight plot for $(Pb_{0.65}C_{0.35})Sr_2(Y_{0.7}Cu_{0.3})Cu_2O_y$ sample in argon environment.

6.11. Stages I and II

There is no evidence from XRD that any phase change is occurring within stage I. During stage II, figures 6.3 and 6.4, the sample is losing a small amount of oxygen and indeed the nominal oxygen content of the 1212 phase falls below 7.0. The rate of loss seems to be increasing above 700°C. Stability appears to remain until ~770°C and exsolution of the (Ca,Sr)CuO_y impurity is found to occur. In comparison to the flowing O_2 environment, stages I and II here are identical to that described in section 4.2

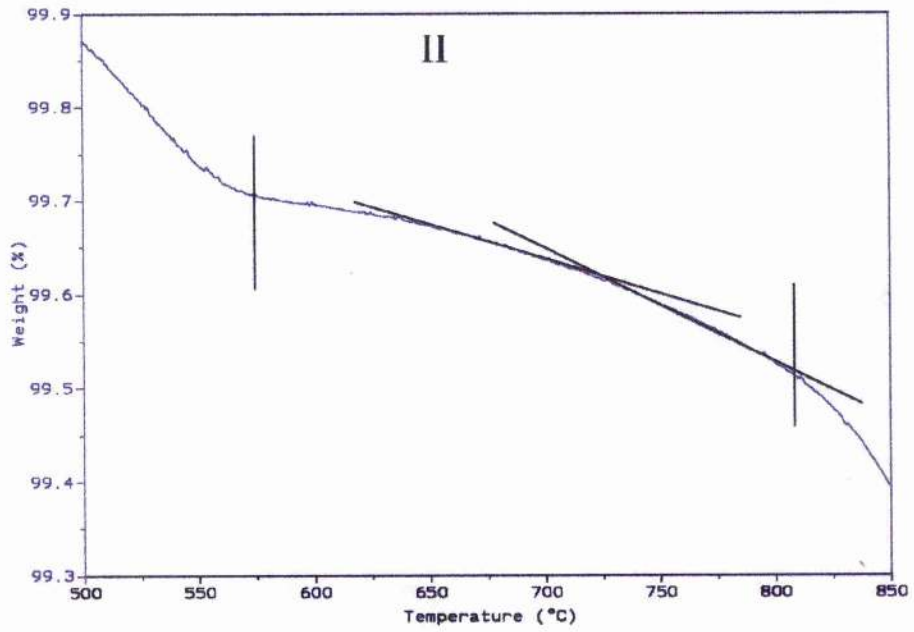

Figure 6.3. Section II weight loss in Argon environment.

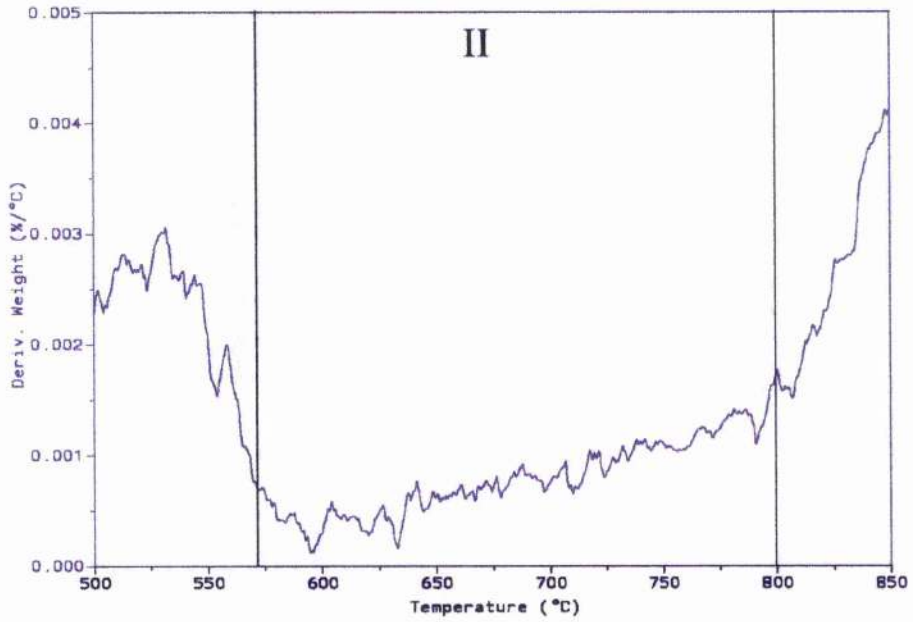

Figure 6.4. Section II derivative weight loss in Argon environment.

An in situ neutron diffraction experiment on ILL D1B was used to examine structural changes, in a sample of nominal composition $(Pb_{0.65}C_{0.35})Sr_2(Y_{0.7}Cu_{0.3})Cu_2O_{7.1}$ which was used for the TGA measurements described previously, as a function of temperature in a vacuum environment. A TGA plot for this sample carried out in a vacuum environment is shown in figures 6.5(a,b) and 6.6. Note how the whole decomposition process has been shifted to lower temperatures compared to that in figure 6.1. Heating 1212 material under vacuum to 900°C causes complete destruction of samples, the decomposed material has changed colour totally from black to grey/silver and the Al_2O_3 crucible has red marks on it. Clearly to see a 12% weight loss there has to be more than just oxygen coming from the sample. A 12% weight loss would correspond to ~5 oxygens or ~0.4 Pb so it there certainly should be Pb loss among other events occurring at these elevated temperatures in low pO_2 environments. It can be said that the sample loses oxygen only up to a certain level, after which other elements are lost in addition to oxygen. Figure 6.5b shows how the loss of 2% weight from the sample occurs at lower temperatures than it does in the Ar environment used in figure 6.1.

In figure 6.7, the variation in the ratio of **c**/**a** as a function of temperature is shown, and again this may be divided into sections. The first section shows the **c** axis expanding more rapidly compared to the **a** axis. This of course is due to the loss of oxygen from the (0,½,0) interstitial site, chapter 5, which affects the **a** axis length. Over the range 500-580°C the **c**/**a** ratio remains constant indicating that stoichiometry is constant and the phase structure is stable, and there is no evidence of any changes from the neutron diffraction patterns in figures 6.8 and 6.9. There is a change of slope over the range 580-660°C and it seems that some structural event is occurring. Neutron diffraction patterns recorded at 600°C and 650°C in figure 6.8 do not appear to be different; however, figures 6.10 and 6.11 at 600 and 650°C show subtle changes with the appearance of a shoulder on the 36° 2θ peak marked with the black arrow on the diagrams.

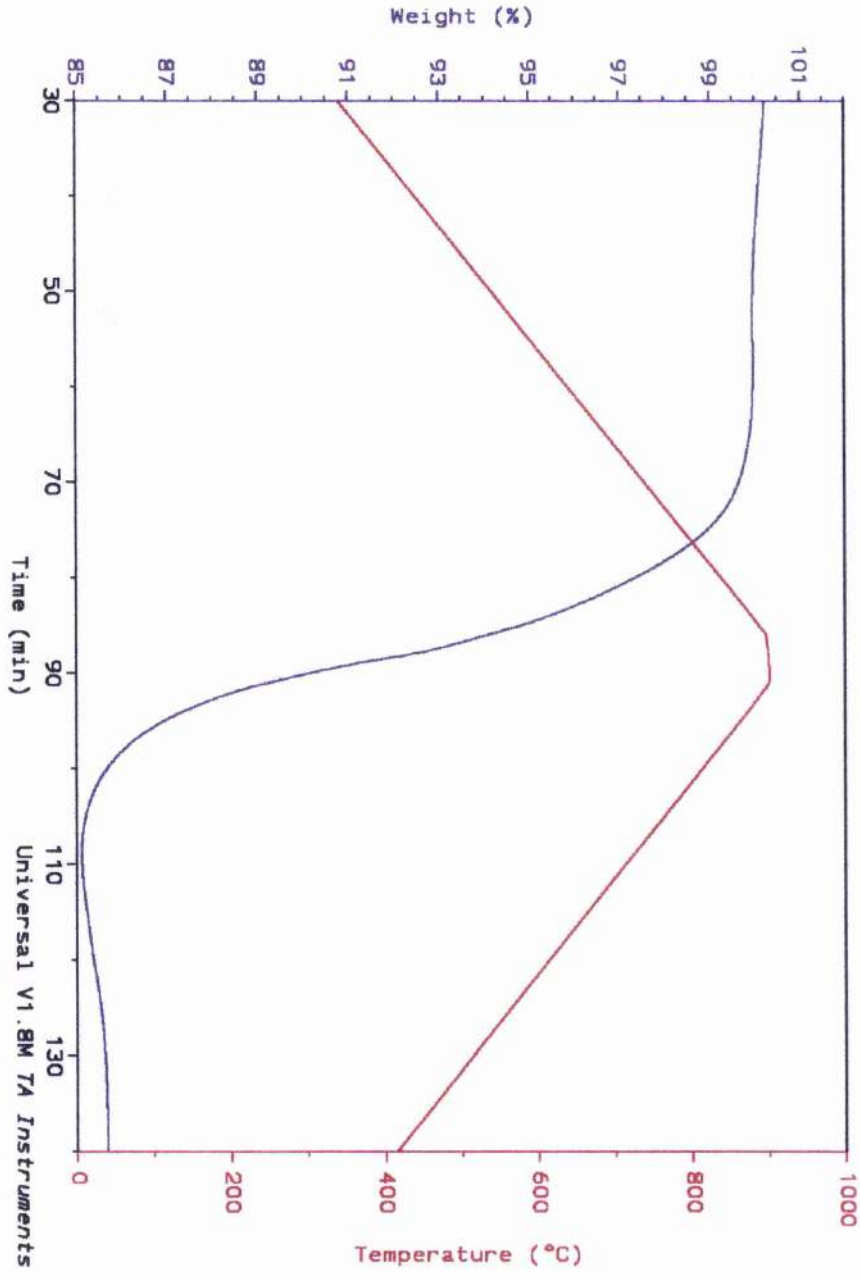

Figure 6.5. $(Pb_{0.65}C_{0.35})Sr_2(Y_{0.7}Cu_{0.3})Cu_2O_y$ sample heated/cooled in a vacuum environment.

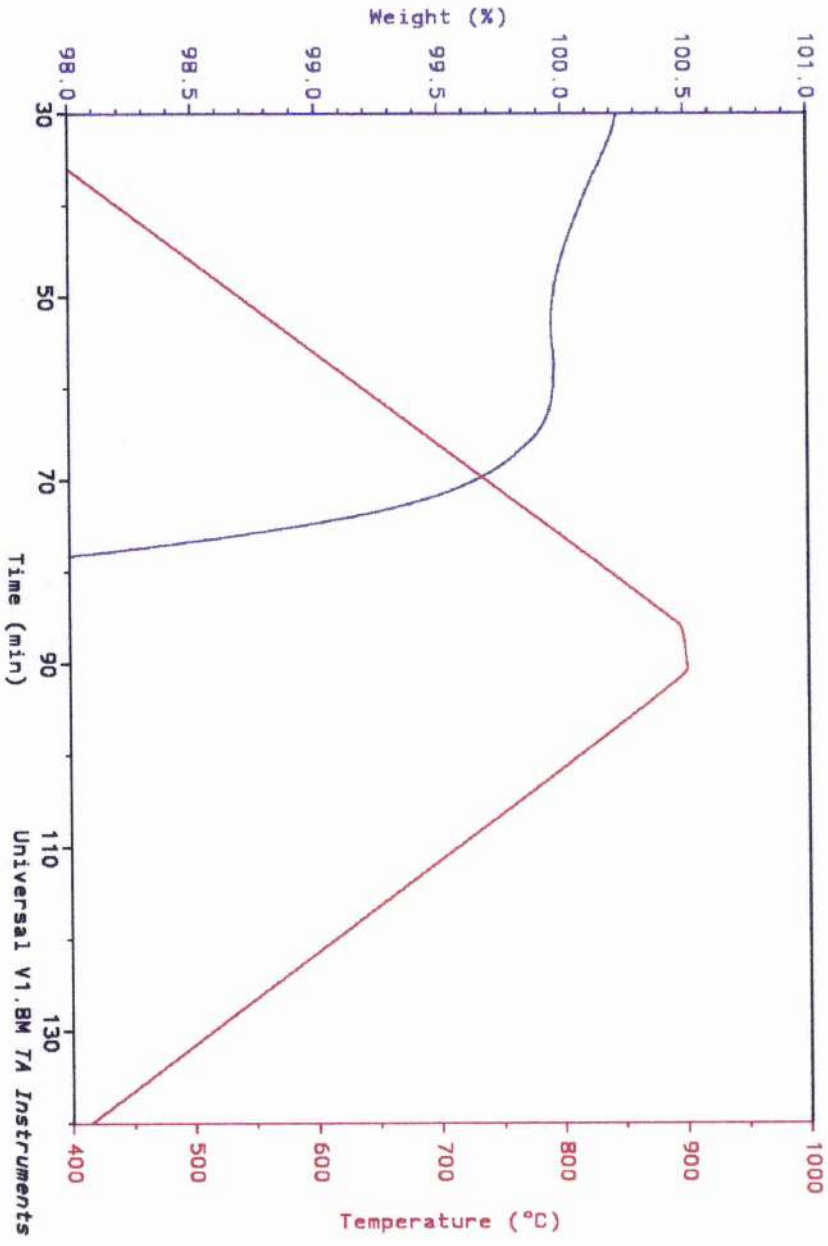

Figure 6.5b. $(Pb_{0.65}C_{0.35})Sr_2(Y_{0.7}Cu_{0.3})Cu_2O_y$ sample heated/cooled in a vacuum environment.

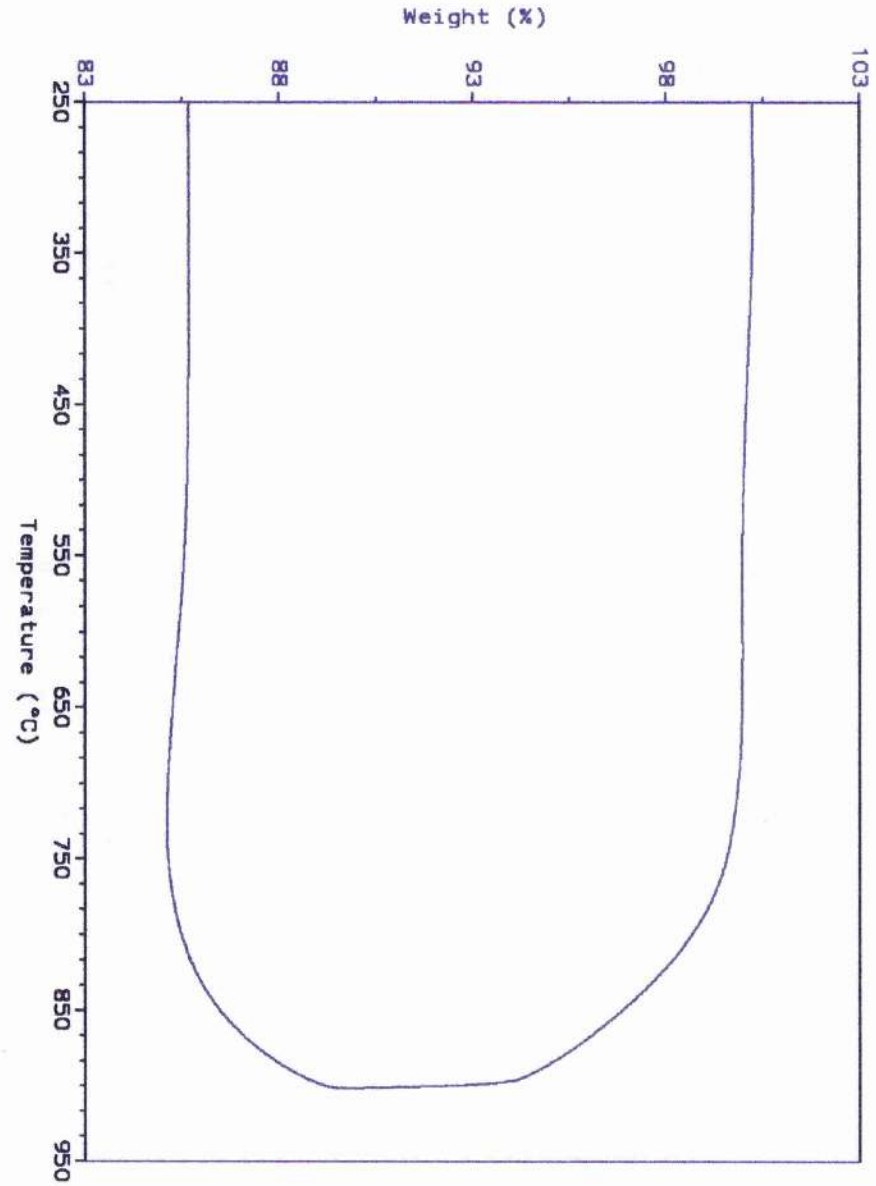

Figure 6.6. 1212 sample in a vacuum environment, weight vs. temperature.

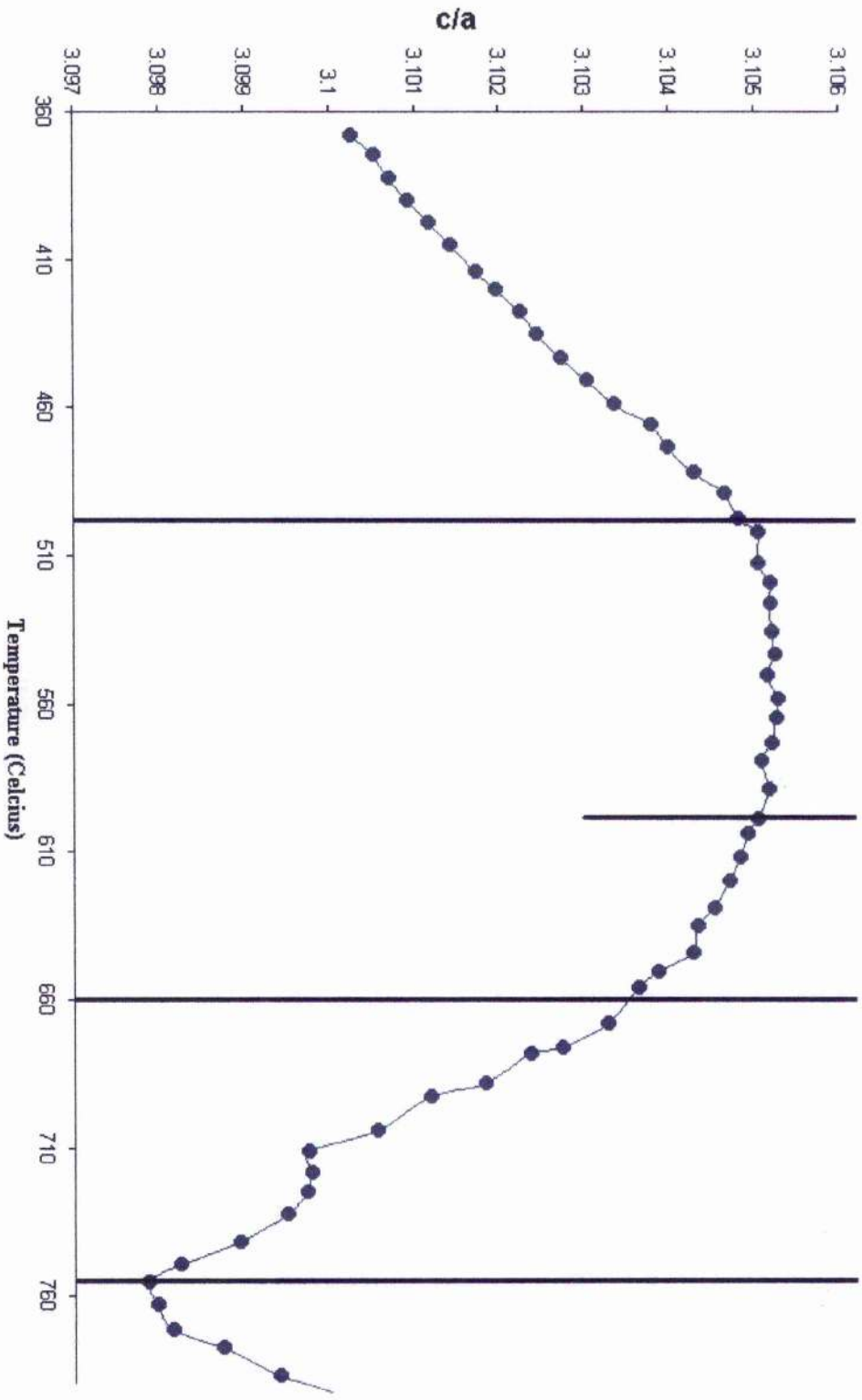

Figure 6.7. Variation in c/a axis ratio as a function of temperature.

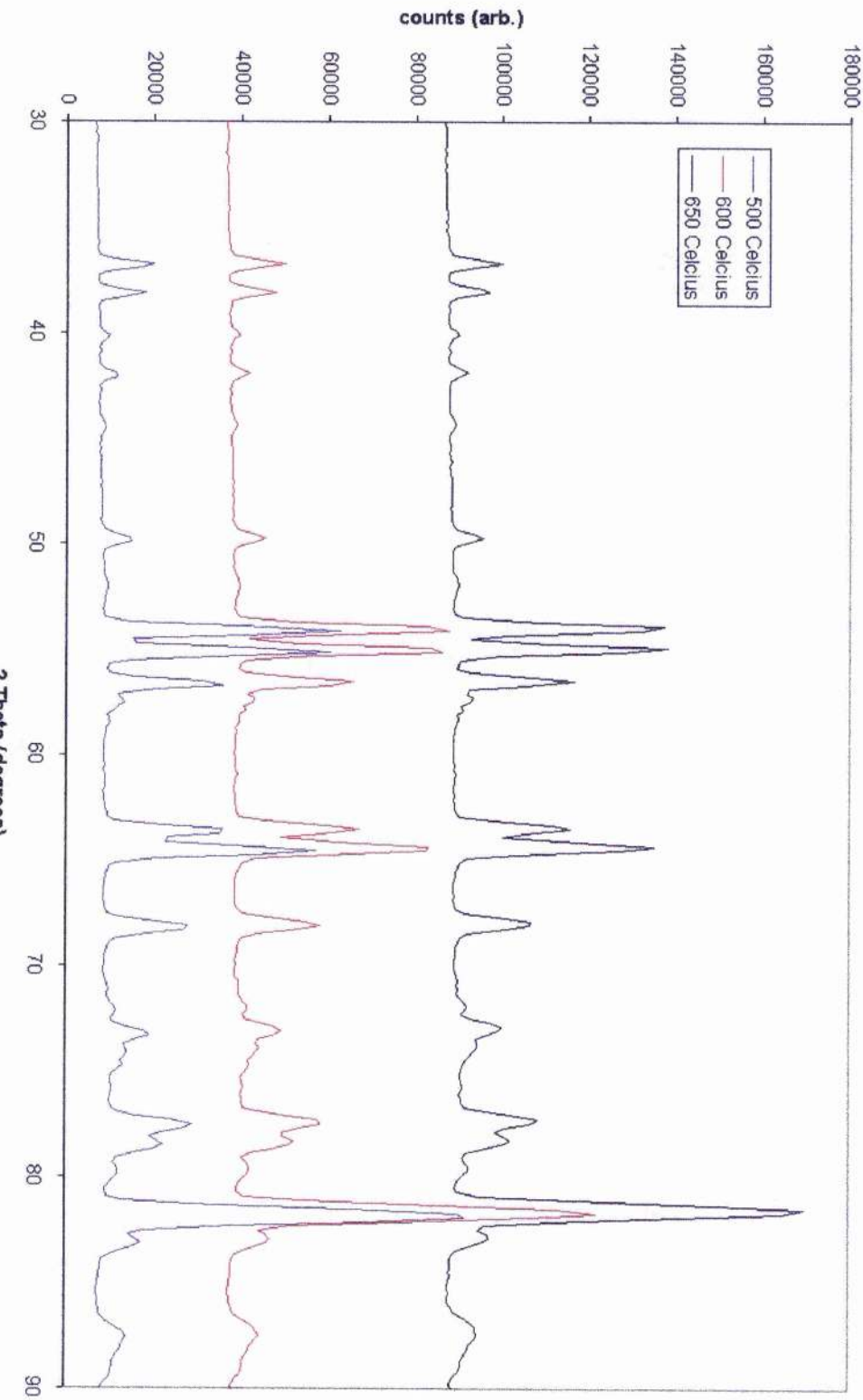

Figure 6.8. Neutron diffraction patterns collected from a sample of nominal composition $(Pb_{0.65}C_{0.35})Sr_2(Y_{0.7}Cu_{0.3})Cu_2O_{7.1}$ over the temperature range 500-650°C.

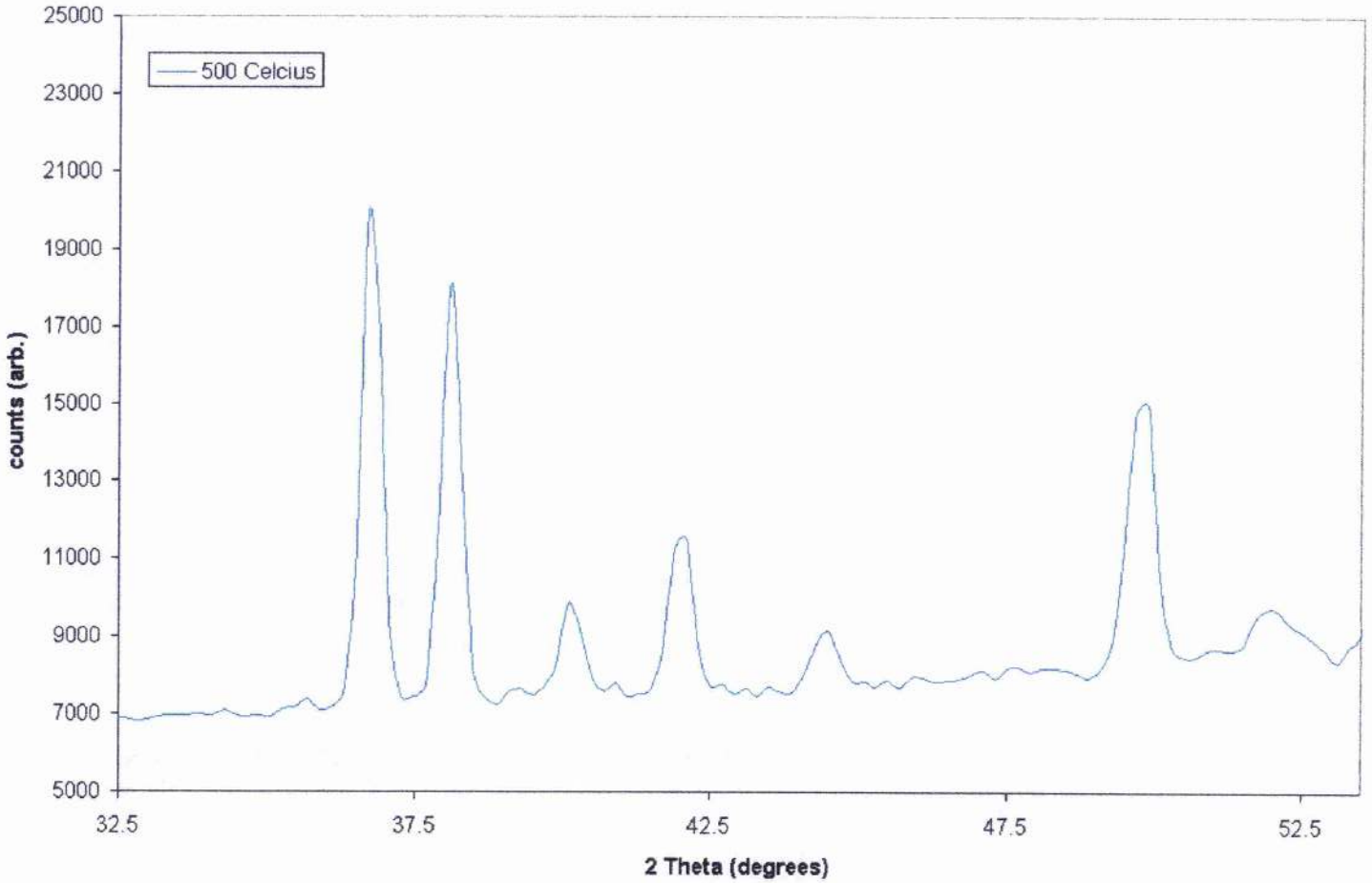

Figure 6.9. Expanded section from the neutron diffraction pattern collected in sample of nominal composition $(Pb_{0.65}C_{0.35})Sr_2(Y_{0.7}Cu_{0.3})Cu_2O_{7.1}$ at 500°C.

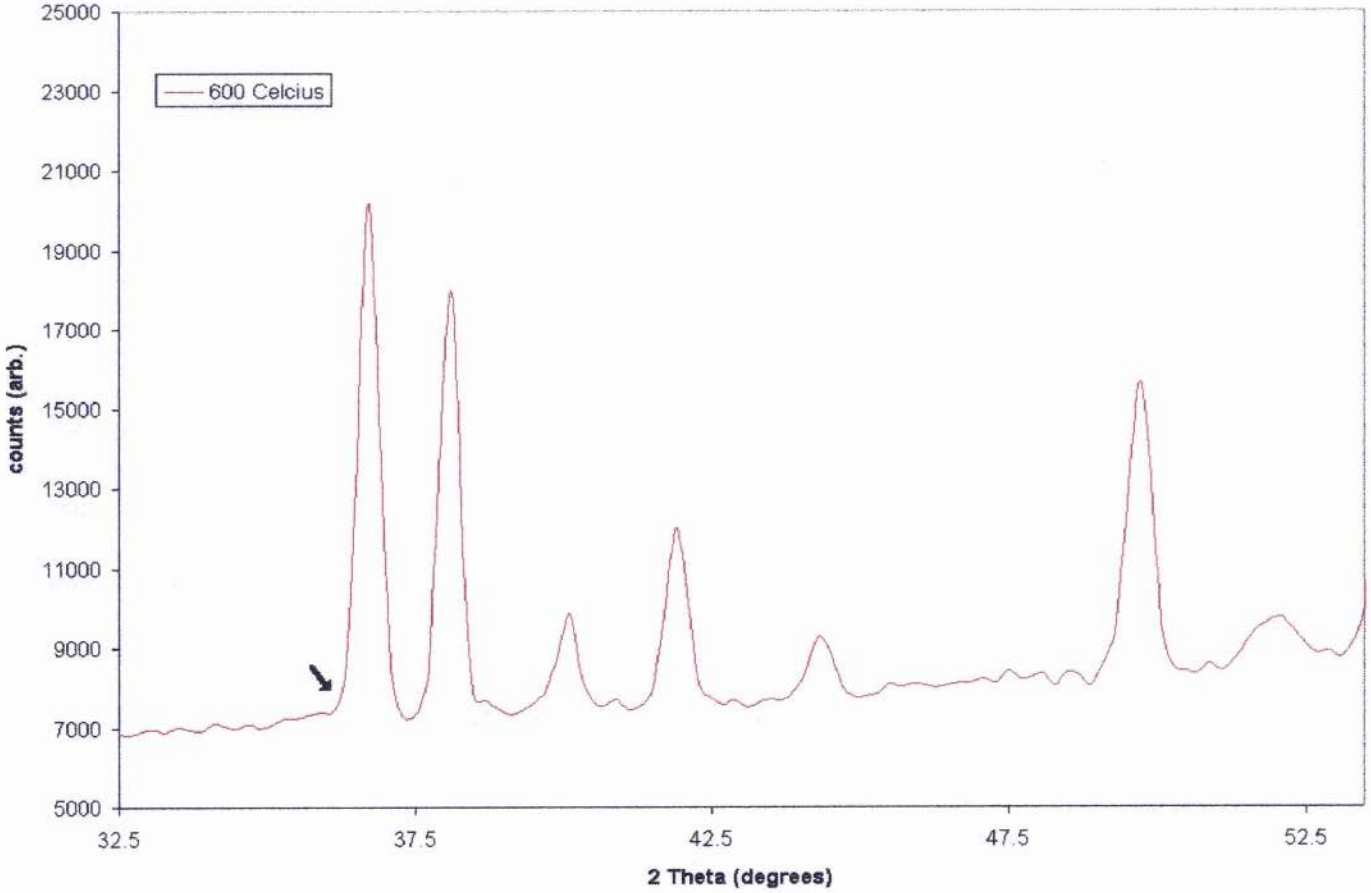

Figure 6.10. Expanded section from the neutron diffraction pattern collected in sample of nominal composition $(Pb_{0.65}C_{0.35})Sr_2(Y_{0.7}Cu_{0.3})Cu_2O_{7.1}$ at 600°C.

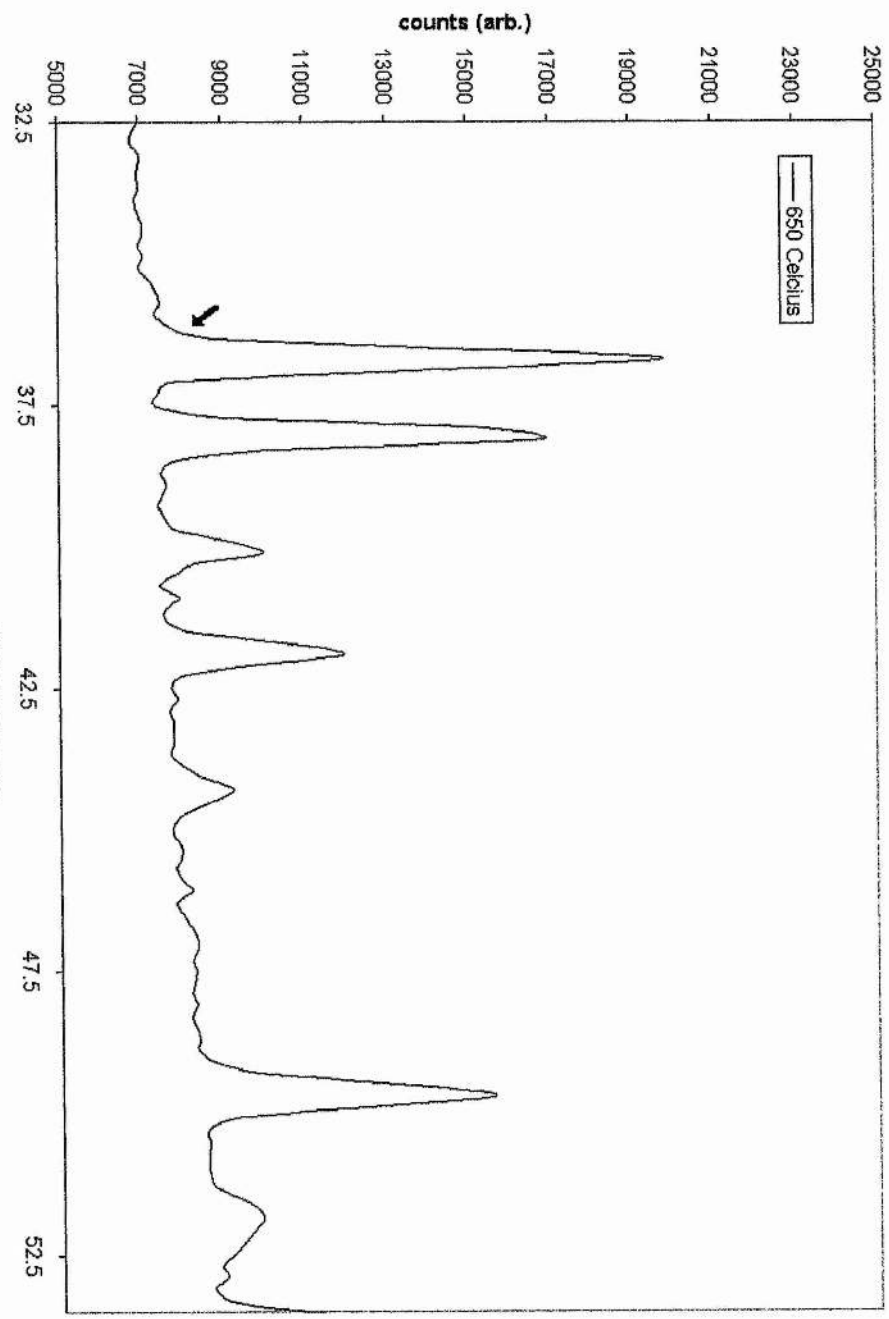

Figure 6.11. Expanded section from the neutron diffraction pattern collected in sample of nominal composition $(Pb_{0.65}C_{0.35})Sr_2(Y_{0.7}Cu_{0.3})Cu_2O_{7.1}$ at 650°C.

Studying the magnetic properties of samples which have been annealed in an argon atmosphere in the tube furnace set-up described in section 3.32 is rather interesting. It is possible to remove the excess oxygen effectively and achieve T_c's equivalent to that seen using oxidising conditions, but not significantly better. Problems occur when repeating these experiments in laboratory tube furnaces. The pO_2 is lower than the TGA instrument, is more dependent on tube condition and state of the 'O' ring seals. This means that repeating experiments at a particular temperature can give slightly different results. Small changes in furnace pO_2 alter both superconducting onset temperature and the superconducting volume fraction in samples. It is very difficult to select an exact temperature for annealing in what is a rather small ideal window. Trying to select higher temperatures again has problems since a clear window at 7.0 does not really exist and again straying too far out of this region affects onset temperature and superconducting volume fraction. This mirrors the problems seen for oxidising conditions, chapter 5. Using known pO_2 gas mixtures[4,5,6] such as 1% O_2/N_2 during annealing stages has been attempted in a number of superconducting systems. However, the same problems may exist if the system cannot be properly sealed from the external atmosphere. It is possible, though using this technique to induce superconductivity in samples of nominal composition $(Pb_{0.5}Cu_{0.5})Sr_2Y_1Cu_2O_y$. The samples exsolve some "SrCuO" during annealing and only then is the T_c of 43K observed, figure 6.12.

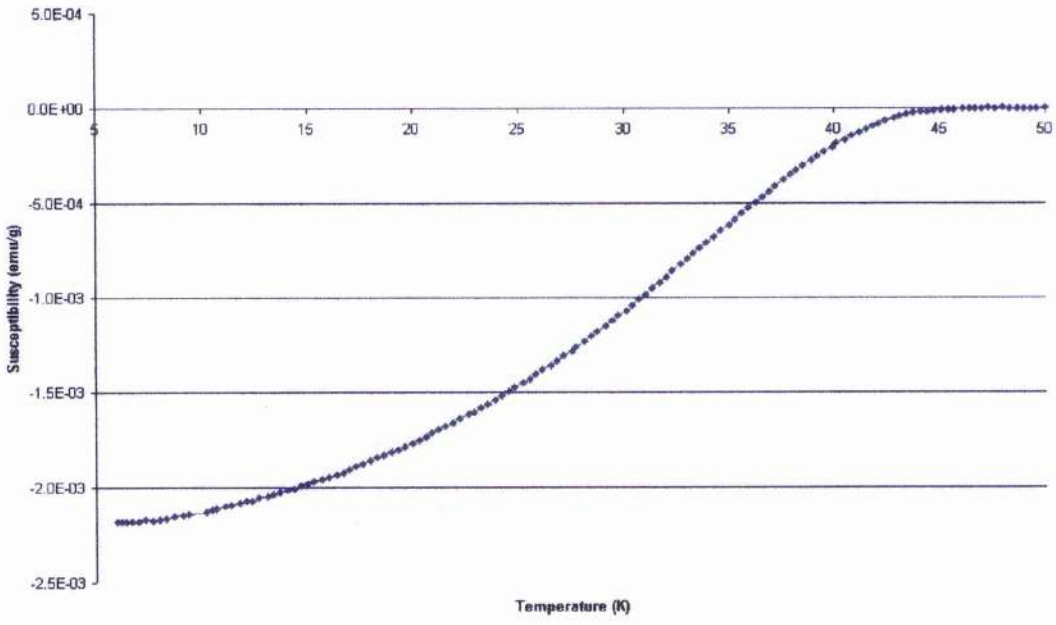

Figure 6.12. Magnetisation curve for Argon annealed $(Pb_{0.5}Cu_{0.5})Sr_2Y_1Cu_2O_y$.

What the results above suggest is that as the oxygen content initially falls below 7.0, the cation composition of the sample does not vary. Instead loss of oxygen up to a certain level has no effect then compositional variation begins to occur. The exsolution of impurities though cannot be detected by X-ray or neutron diffraction analysis until the oxygen content of the sample has dropped considerably from this point.

6.12. Section III

The satellite on the 36° 2θ peak was not very clear in figures 6.10 and 6.11, but when temperatures pass 700°C the shoulder develops into a distinct peak as shown in figures 6.13-6.16. Referring back to figures 6.1,6.2, 6.5 and 6.6, entering section III there is a rapid weight loss from the sample and the most interesting changes in the 1212 structure are occurring. The slope of the line in figure 6.7 is seen to vary once again above 660°C indicating the sample composition is changing more rapidly. More significantly the 102 reflection peak at ~44.5° 2θ disappears over the range 700-750°C, figures 6.14 and 6.15. In the vacuum case above 760°C, figure 6.7, the slope of the **c/a** plot varies once more and Rietveld refinements show instability from this point onwards. Decomposition of the 1212 phase would appear to be clearly occurring at this

stage as individual peak intensities are varying and more new peaks are clearly visible, figure 6.13. One good example is the appearance of a new peak close to the position of the former 102 reflection shown in figure 6.16. Figure 6.17 shows more clearly the disappearance of the 102 peak. In section III the weight loss also continues when the temperature has been fixed, figure 6.18. Decomposition is a rather complex process and is described more fully in section 6.2.

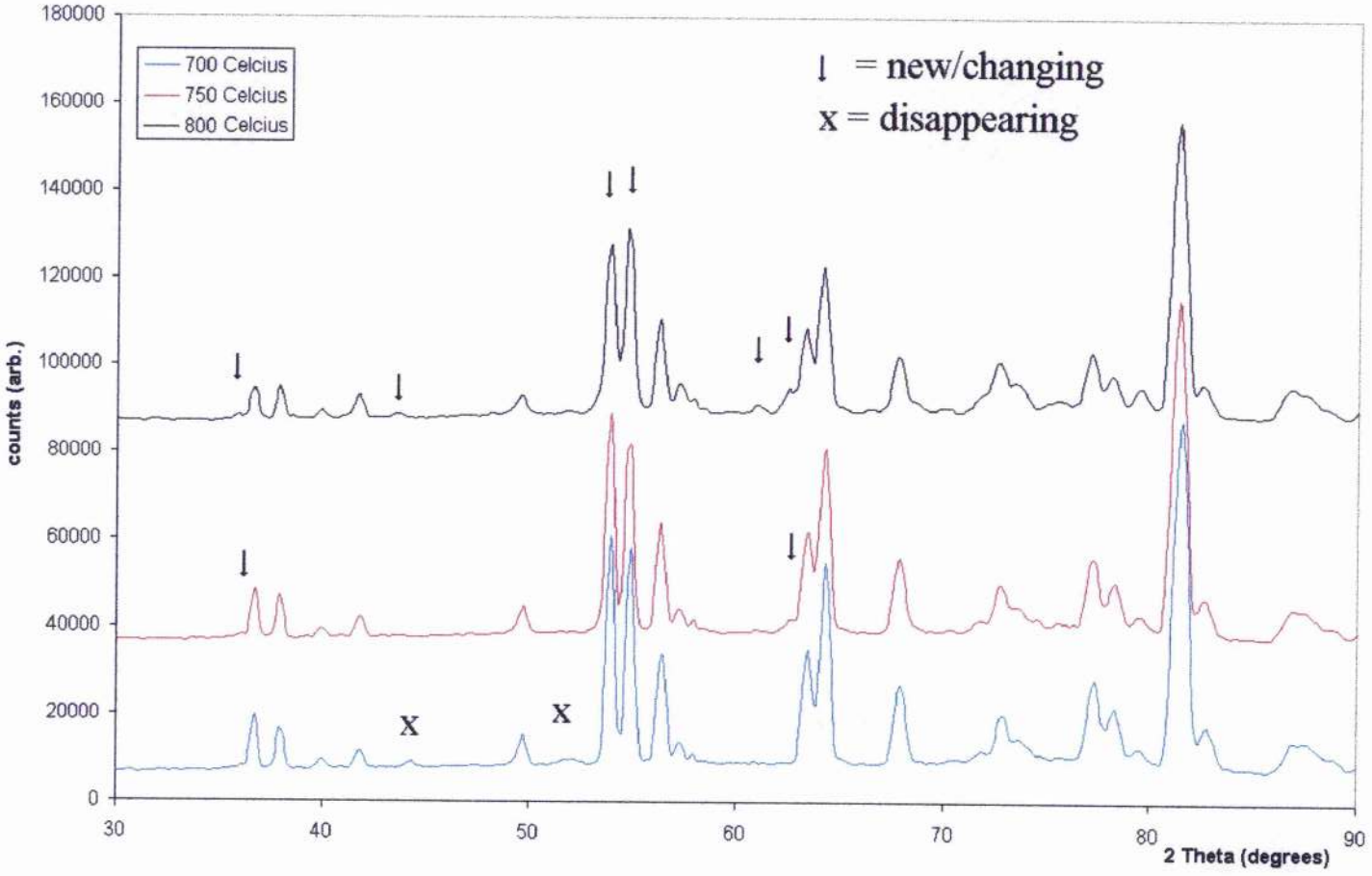

Figure 6.13. Neutron diffraction patterns collected from a sample of nominal composition $(Pb_{0.65}C_{0.35})Sr_2(Y_{0.7}Cu_{0.3})Cu_2O_{7.1}$ over the temperature range 700-800°C.

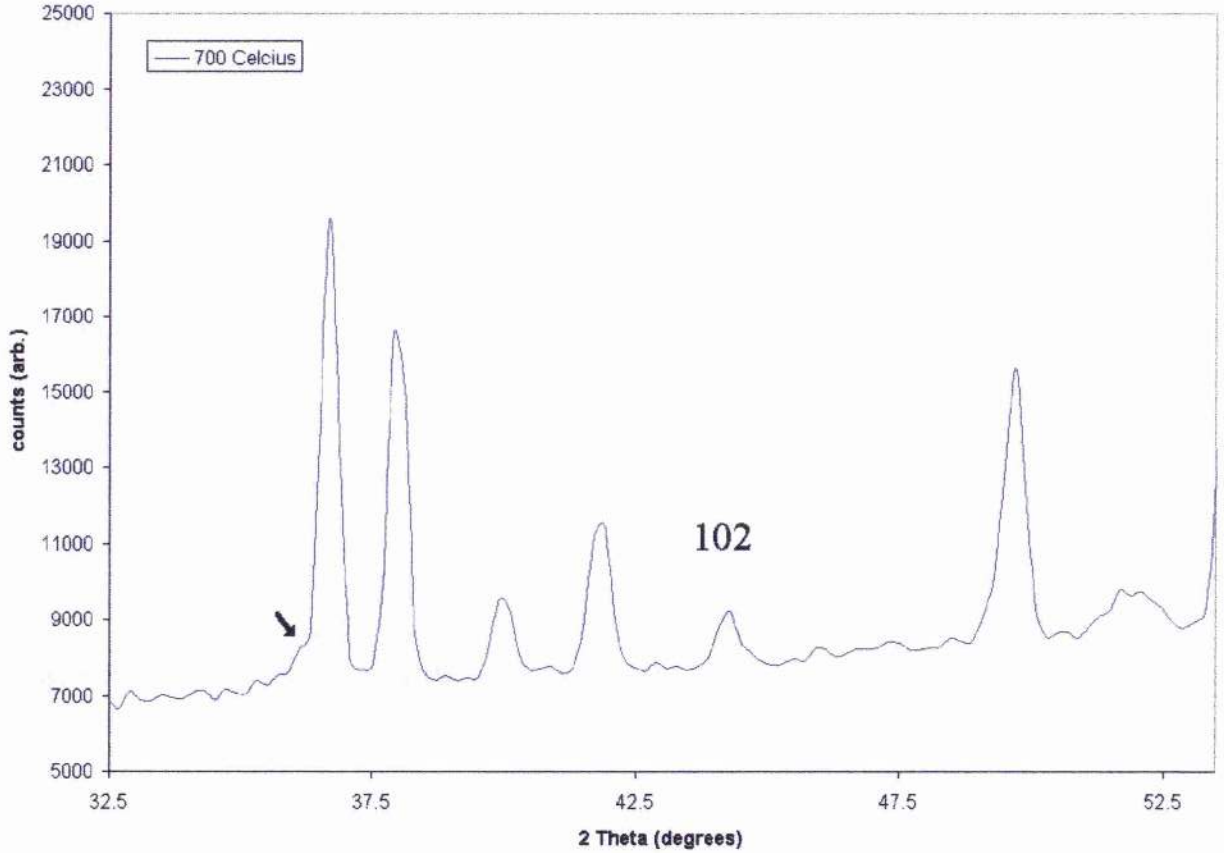

Figure 6.14. Expanded section from the neutron diffraction pattern collected in sample of nominal composition $(Pb_{0.65}C_{0.35})Sr_2(Y_{0.7}Cu_{0.3})Cu_2O_{7.1}$ at 700°C.

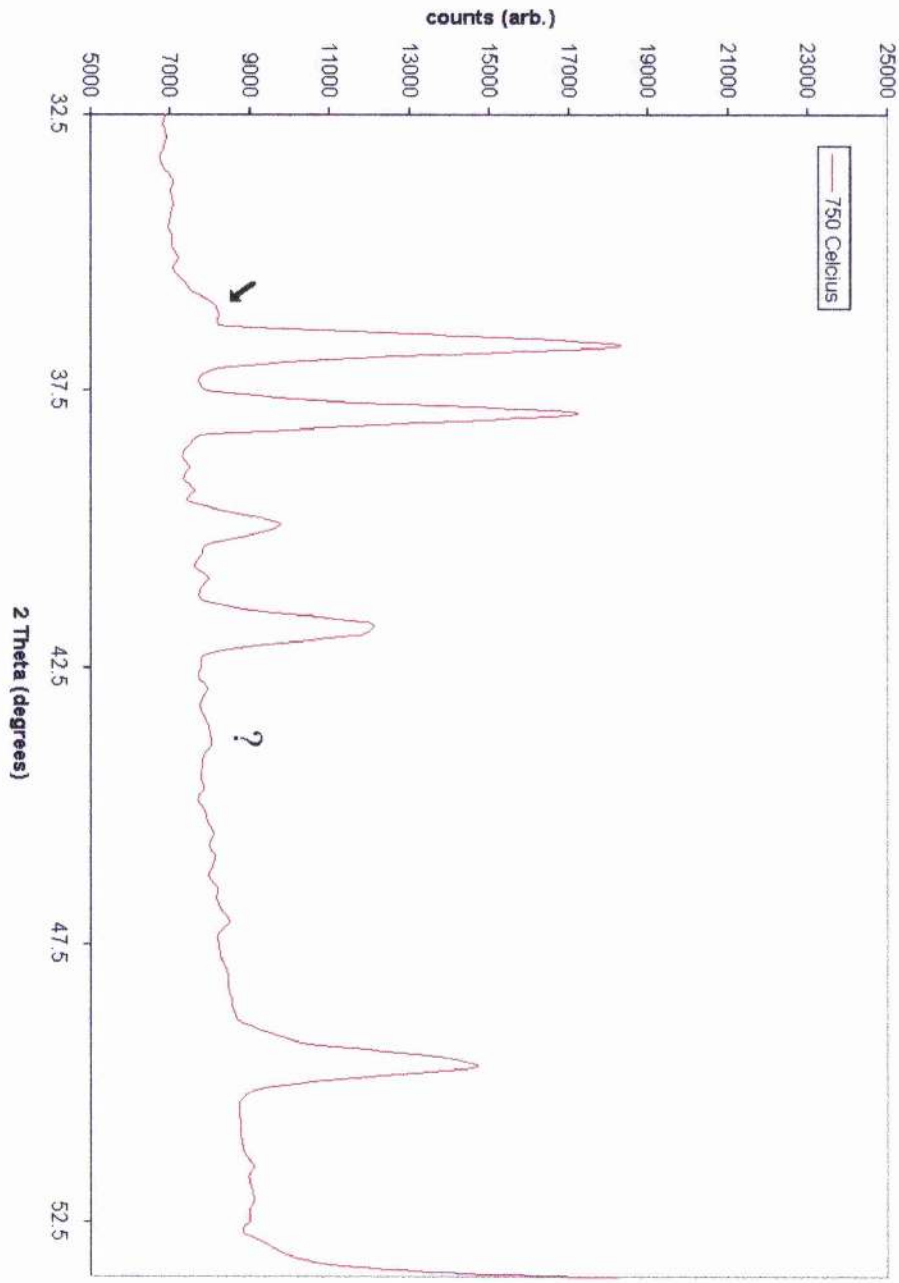

Figure 6.15. Expanded section from the neutron diffraction pattern collected in sample of nominal composition $(Pb_{0.65}C_{0.35})Sr_2(Y_{0.7}Cu_{0.3})Cu_2O_{7.1}$ at 750°C.

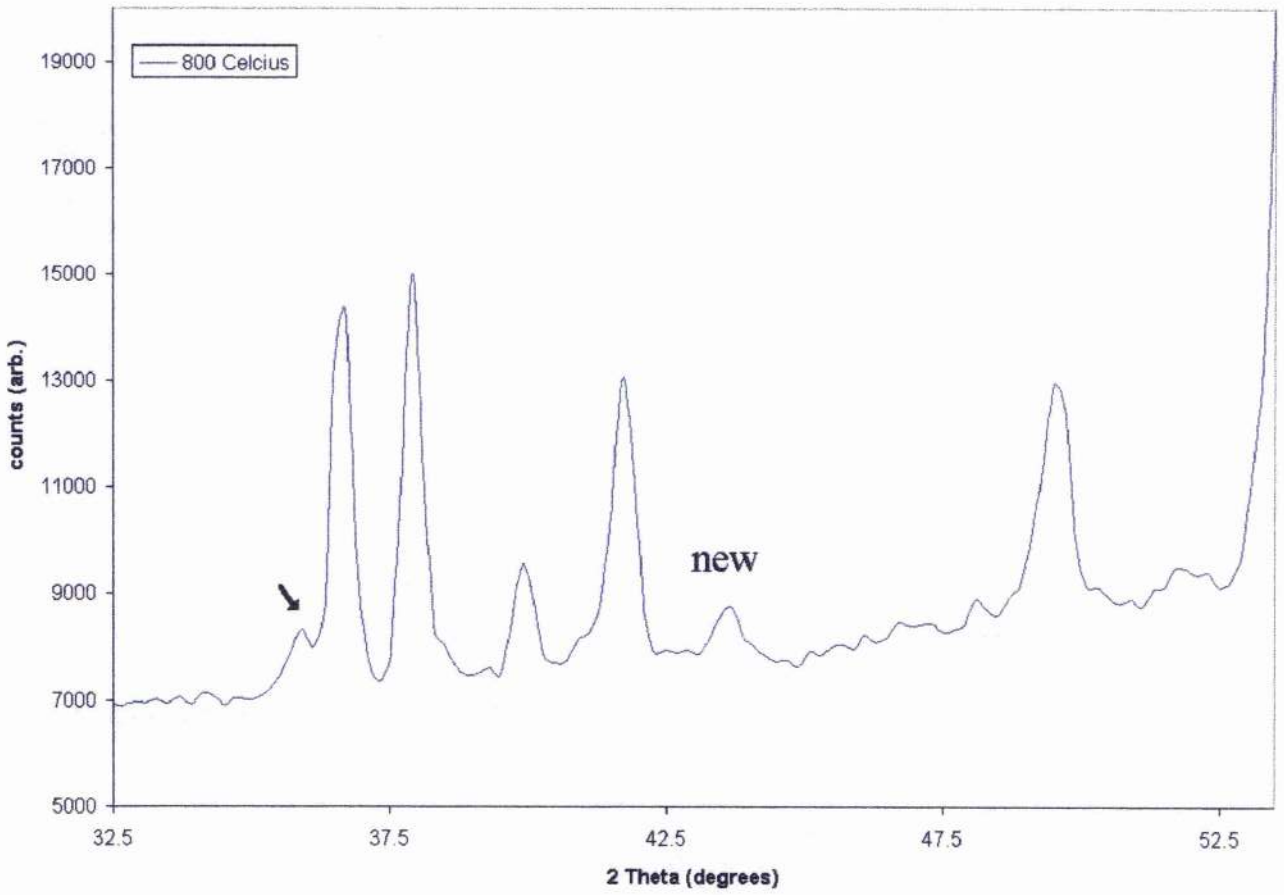

Figure 6.16. Expanded section from the neutron diffraction pattern collected in sample of nominal composition $(Pb_{0.65}C_{0.35})Sr_2(Y_{0.7}Cu_{0.3})Cu_2O_{7.1}$ at 800°C.

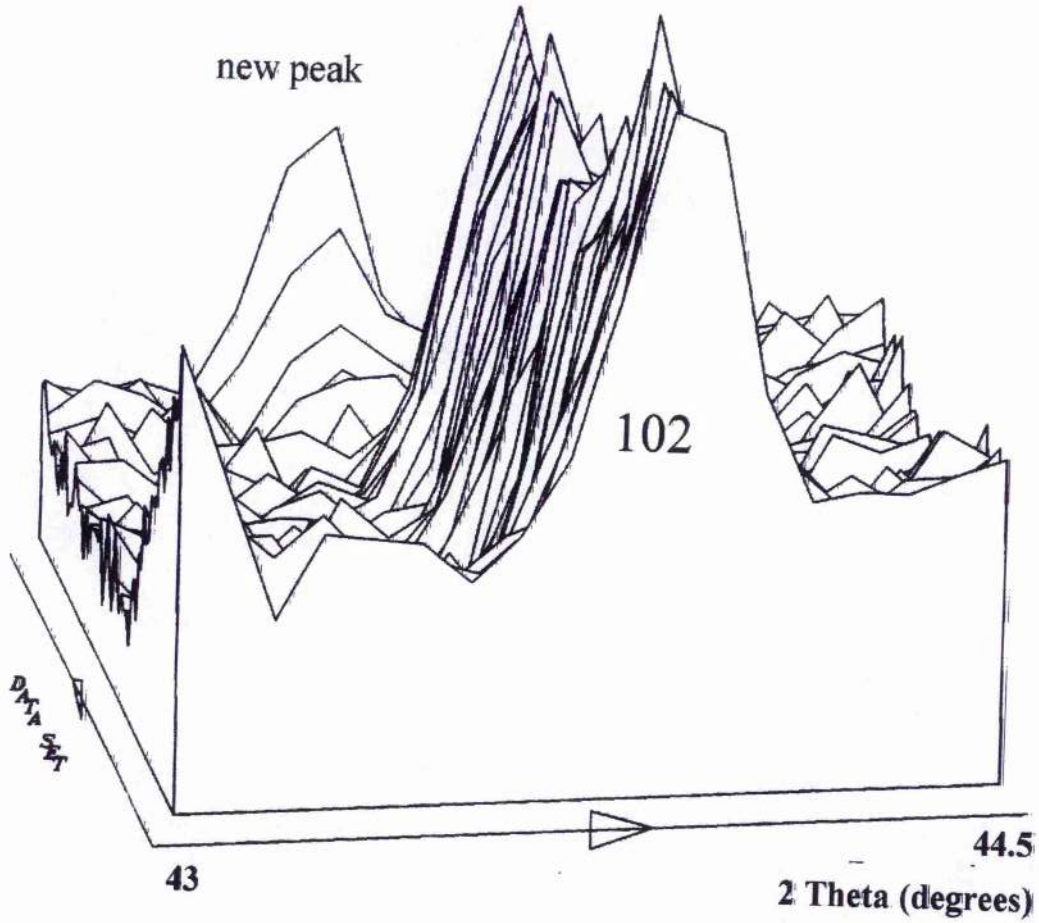

Figure 6.17. Disappearance of the 102 peak in the neutron diffraction pattern.

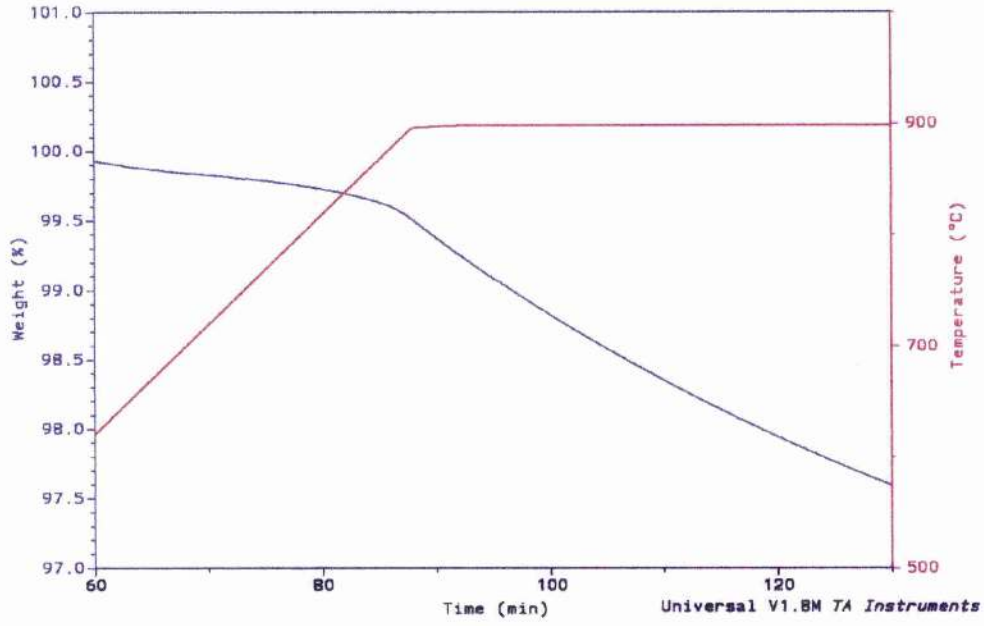

Figure 6.18. Isothermal thermogravimetric trace at 900°C.

6.2. Decomposition of the 1212 phase

In the previous section only partial decomposition of the 1212 phase was covered; however, when the temperature is high enough to drive the decomposition rapidly then a number of events are seen to occur.

6.21. Formation of new phases as a result of decomposition.

The samples in this experiment were heated to the required temperature with no annealing stages and then rapidly cooled before XRD analysis was carried out. These are not in situ measurements. Upon entering section III the sample shows some exsolution of the (Ca,Sr)CuO_y impurity and individual peak intensities vary, as described in the previous section. Figure 6.19 shows a single phase PbCu:1212 sample with the important reflections indexed. Referring to the argon environment TGA, figure 6.1, increasing the target temperature by approximately 50°C to 850°C sees

more exsolution of "SrCuO" type impurities. The appearance of some other new peaks as well as the near disappearance of the 5.9Å ~15° 2θ (002) 1212 peak is shown in figure 6.20. Instead of the (103) (110) doublet of the 1212 phase 6.10a there are clearly three peaks present, also worth noting is the appearance of a new peak at ~13° 2θ. Further increasing the temperature to 900°C, figures 6.21 and 6.22, shows the appearance of peaks at low 2θ angles, which represent d-spacings of ~15.5 and ~13.5Å. In figure 6.21, the ~13° 2θ peak intensity has increased and the triplet of peaks between 32-34° 2θ has clearly changed. What could be said about the 900°C pattern compared to that seen at 850°C is that the XRD plot looks "clearer" and less peaks appear to be present. Above 900°C there is very little change in the diffraction patterns, except for the exsolution of more "SrCuO" impurity phases. However, around the 975°C region there is evidence that Pb and a number of elements are being lost from the sample as it turns a grey colour and red marks appear on the Al_2O_3 crucible. This is what was seen when samples were heated to 900°C in a vacuum environment.

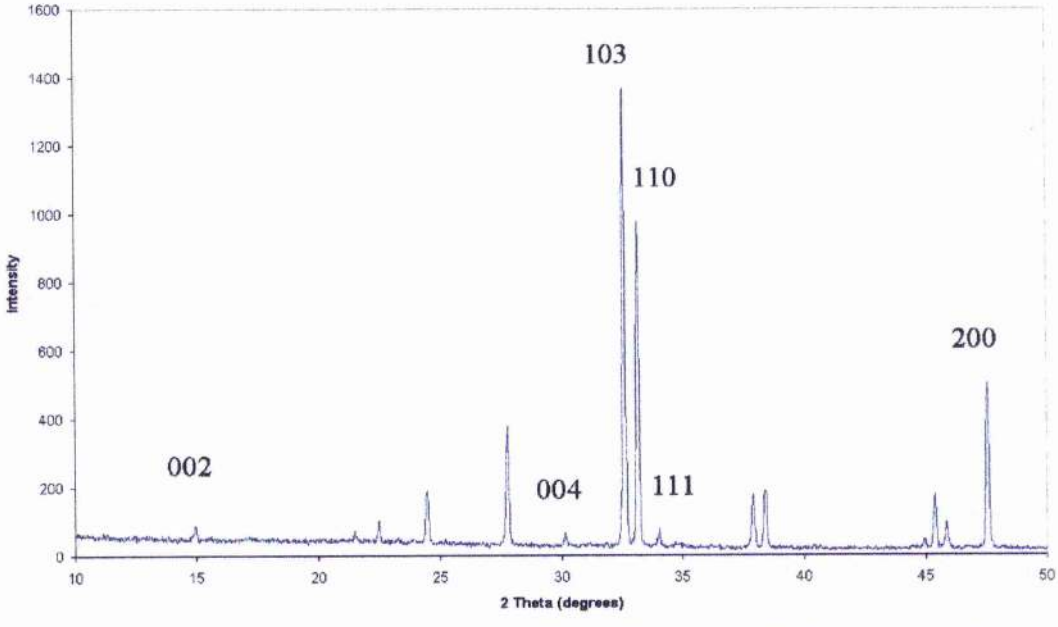

Figure 6.19. XRD pattern taken from a single phase PbCu:1212 sample with the important reflections labelled.

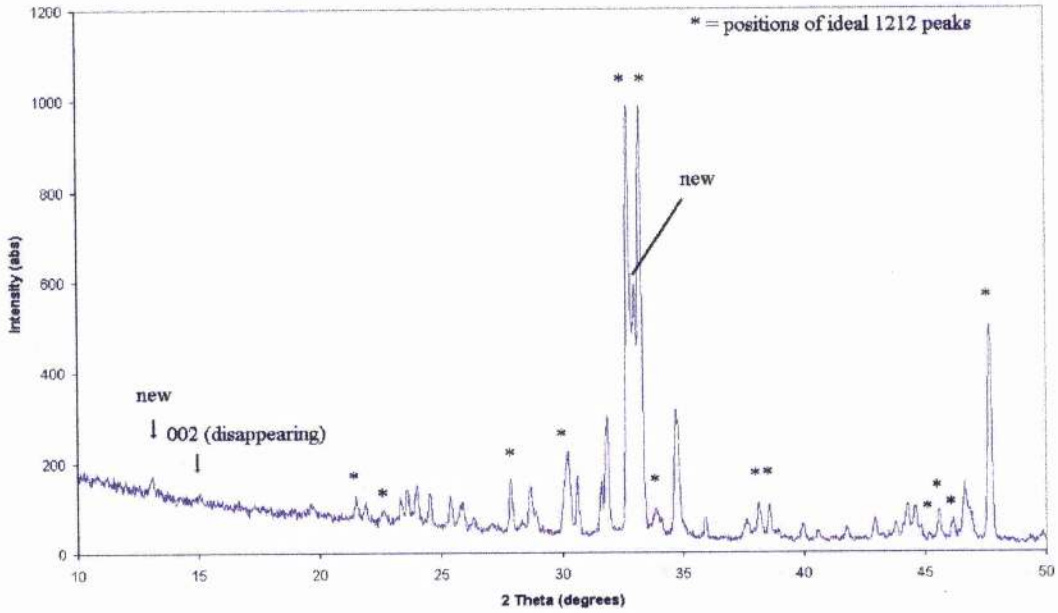

Figure 6.20. Room temperature XRD pattern collected from PbCu:1212 sample which had been heated to 850°C in low pO_2 environment.

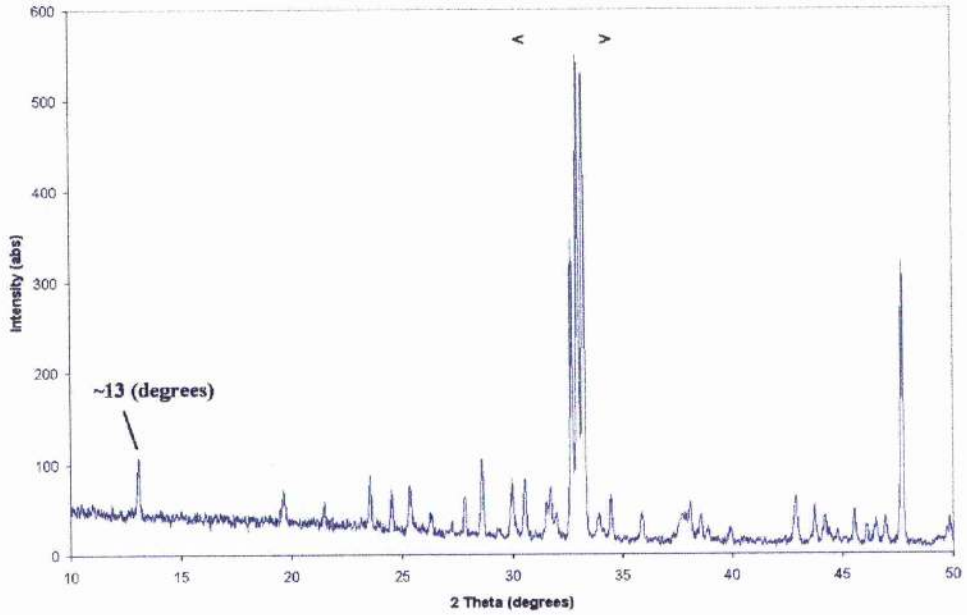

Figure 6.21. Room temperature XRD pattern collected from PbCu:1212 sample which had been heated to 900°C in low pO_2 environment. Decomposition of the 1212 phase has occurred.

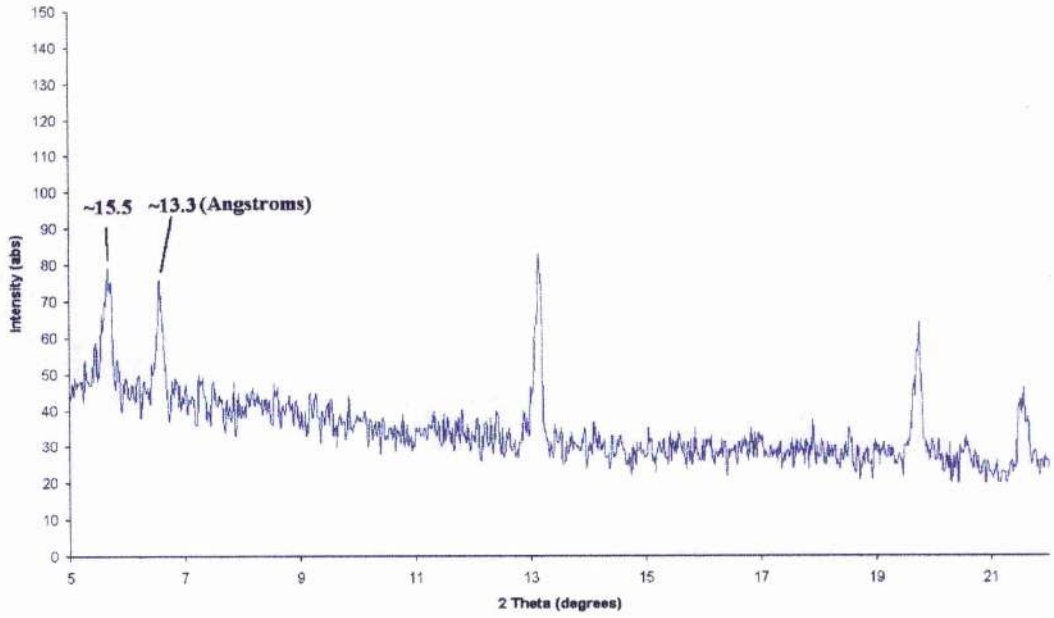

Figure 6.22. Low angle peaks present in diffraction pattern from the sample which had been heated to 900°C in a low pO_2 environment.

Examining the d-spacing values of some of the new peaks formed when the 1212 phase decomposes, indicates that possibly some sort of intergrowth phase(s) are formed. These new phases would appear to be quite dominant and there is no clear indication that the 1212 phase is present in any quantity. Looking at the largest peaks in the XRD patterns, it would seem that the 1212 phase is present at all stages, but it is more likely that the new phases show their most intense peaks around this region and give the appearance that the 1212 phase is still present. This would not be surprising for hkl peaks with l = 0 in particular, as the **a**, **b** unit cell edges are likely to be similar in the product phases, or simple multiples of these.

The decomposition of the 1212 phase may also be achieved by selecting a temperature within section III and holding the temperature (say 875°C) for varying periods of time, figure 6.23. Using a tube furnace instead of the TGA apparatus shows the same results, the only differences being in the isothermal treatment where temperature and isotherm time vary due to slight changes in pO_2. This figure also confirms that during the early stages of section III it is possible to attain equilibrium, although this process is much slower than in stage II which does not entail a phase decomposition process. Assuming that all the weight loss can be attributed to changes

in oxygen content, the final oxygen content of this $(Pb_{[1+x]/2}Cu_{[1-x]/2})Sr_2(Y_{1-x}Ca_x)Cu_2O_{7-\delta}$ (x = 0-0.4) phase assembly is 6.0. This implies that the new phases are nominally Pb^{2+} with perhaps some Cu^{+}.

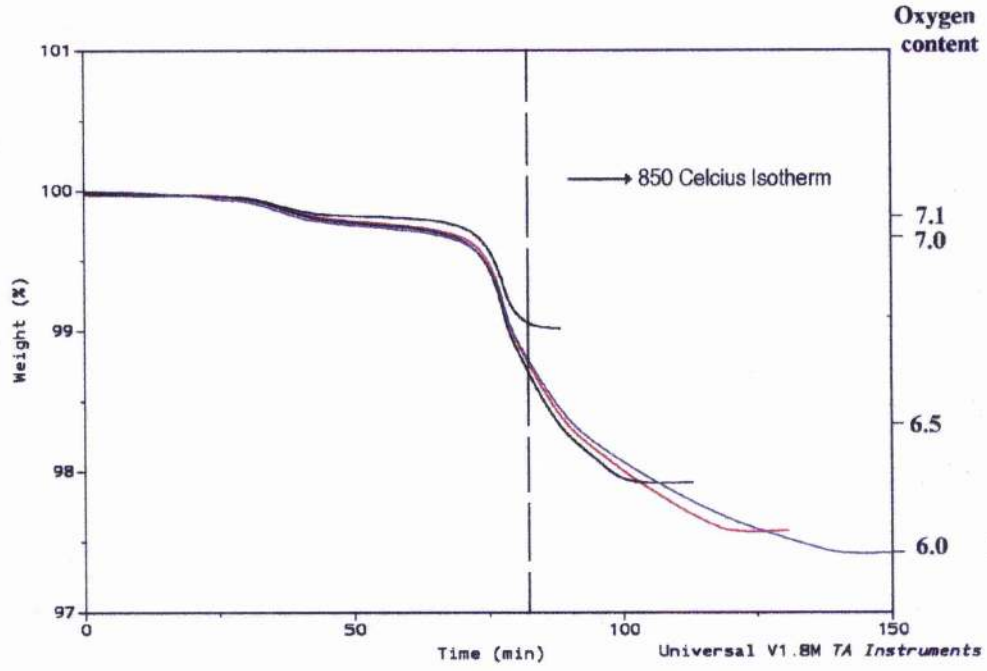

Figure 6.23. Fixed temperature variable isotherm periods in 1212 sample in a low pO_2 environment.

6.22. HREM analysis of the decomposition product

Annealing the 1212 phase at 875°C for 45 minutes in an argon environment produced the sample for electron microscopy. Initially looking at sample crystals under a light microscope showed two distinct types to be present. Under the electron microscope, one type of crystal was most probably "SrCuO" type of material and no further studies were carried out. Studying the other type, the emphasis was placed on finding crystals orientated to show the **c**-direction of the unit cell. Unsurprisingly the microscopy revealed quite a number of stacking faults to be present and the variable nature of spot intensities within layers appeared to indicate disorder also. Figure 6.24 shows the diffraction pattern from a fragment orientated in the [101] direction. The main set of spots was calculated to have a repeating length of ~13.5Å, while the weak spots represent a repeating length of ~12Å. It would seem that the 1212 phase (**c** ≈

11.8Å) was also present in the particular fragment under investigation. Of course this may well have been an isolated fragment and not a true representation of the decomposed sample. The electron micrograph in figure 6.25 shows two different blocks present. One block is what appears to be 1212 and the other is ~13.5Å. Another structure was found to be present, with a unit cell edge of ~16Å, figures 6.26-6.27. During the investigations, by far the most common structures found had cells of ~13.5Å and ~16Å. There was no sign of any regular intergrowth structures, nor was there any indication that supercells were present.

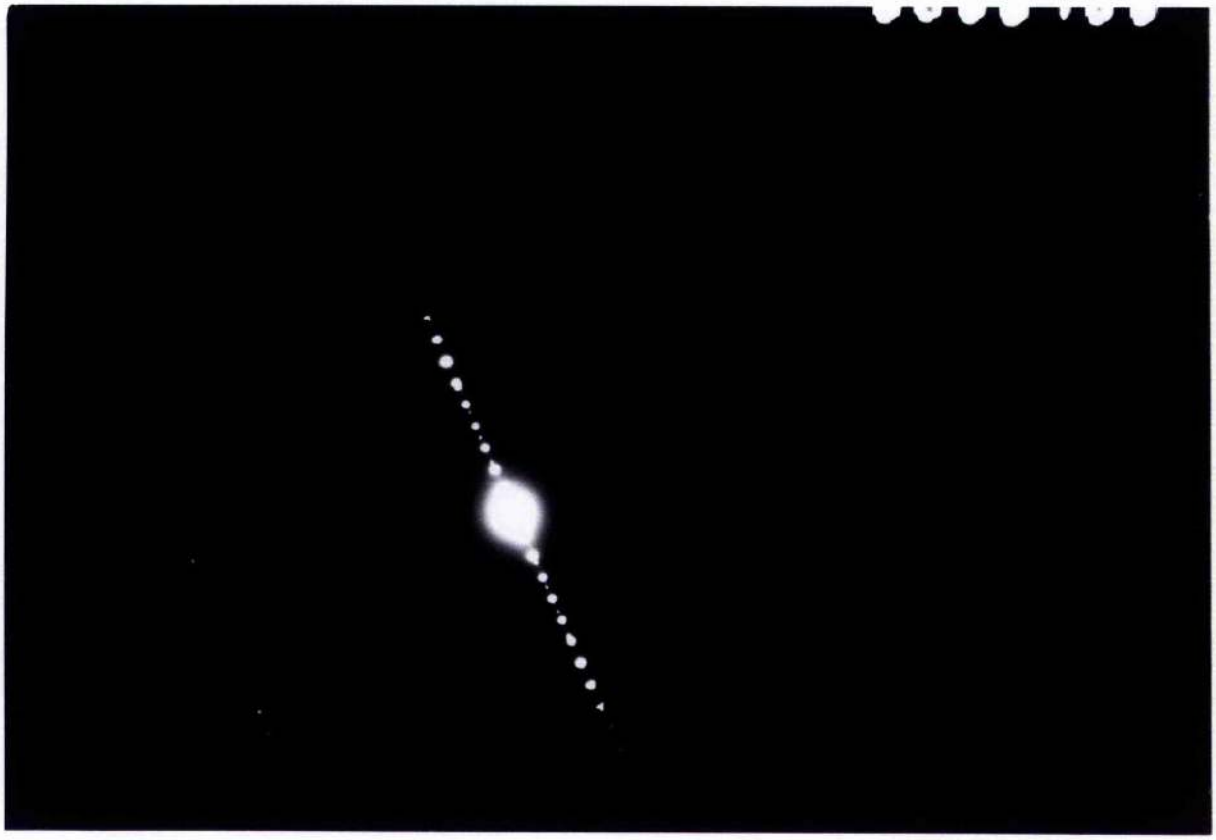

Figure 6.24. Selected area electron diffraction pattern close to [101] zone axis.

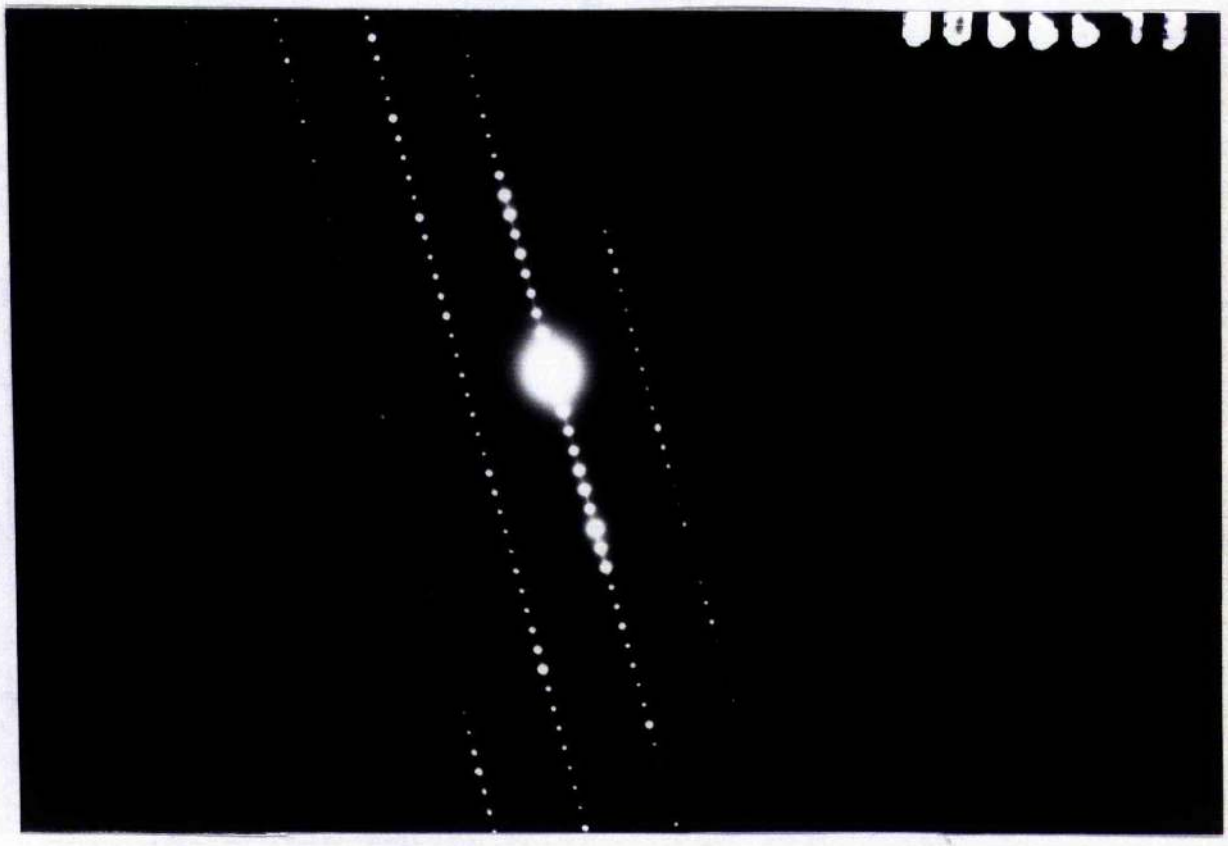

Figure 6.25. Micrograph corresponding to selected area diffraction pattern.

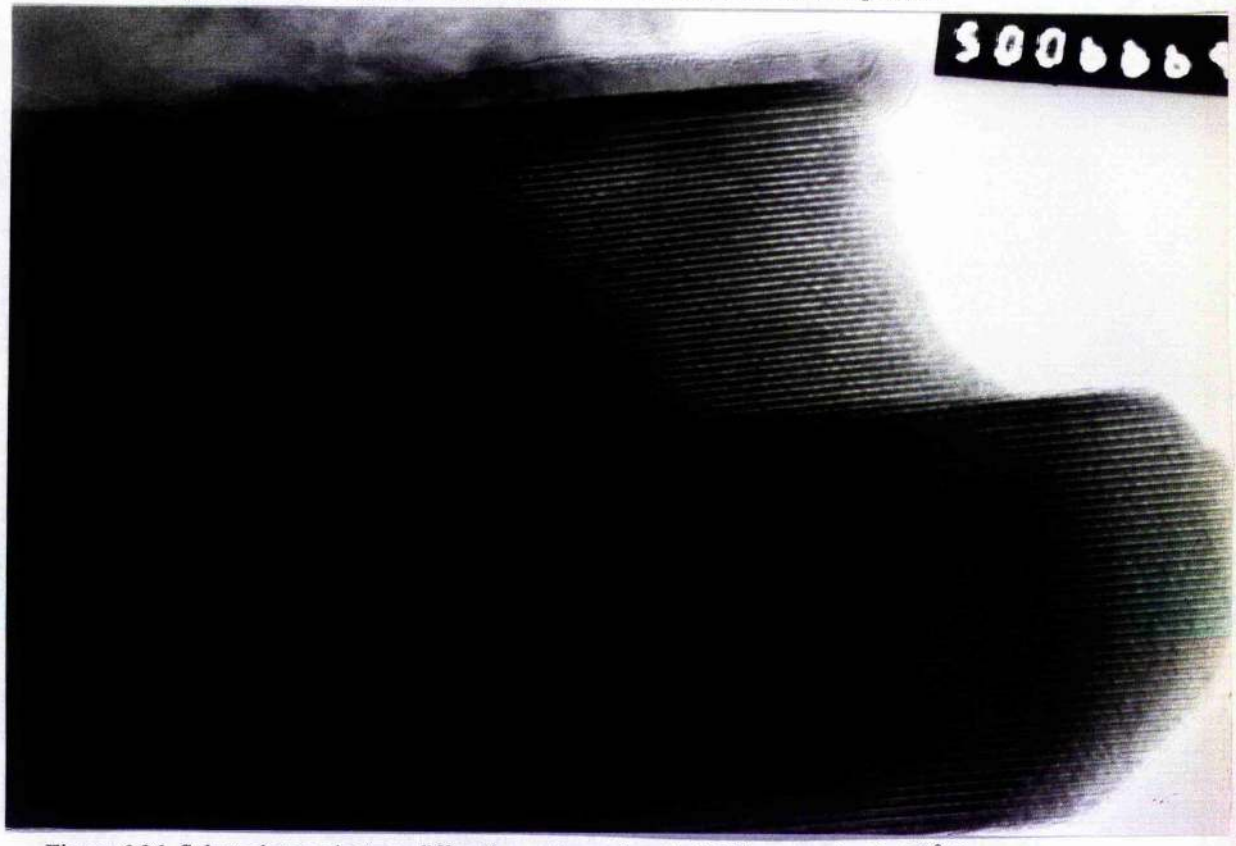

Figure 6.26. Selected area electron diffraction pattern close to [101] zone axis of ~16Å fragment.

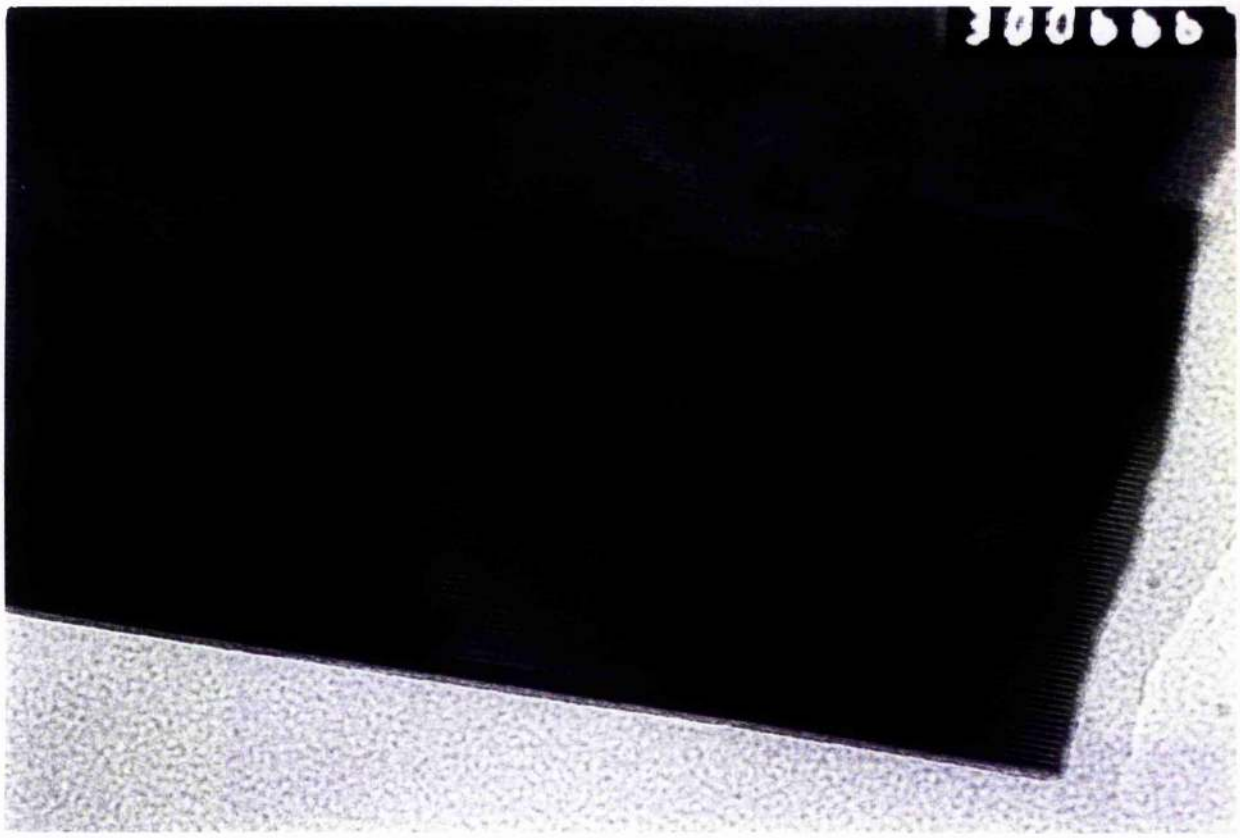

Figure 6.27. Micrograph corresponding to selected area diffraction pattern

6.23. Structures of decomposition products.

At 16Å a **c**-axis length would seem to suggest the presence of the 3212 phase in its orthorhombic Cmmm form, which is synthesised using low pO_2 conditions[4,6,7]. A simulated XRD plot for the 3212 phase, figure 6.28, may be matched as one of the phases present in a decomposed 1212 phase, figure 6.29, although the low 2θ angle data shown in figure 6.22 shows the presence of a 3212 type phase particularly clearly.

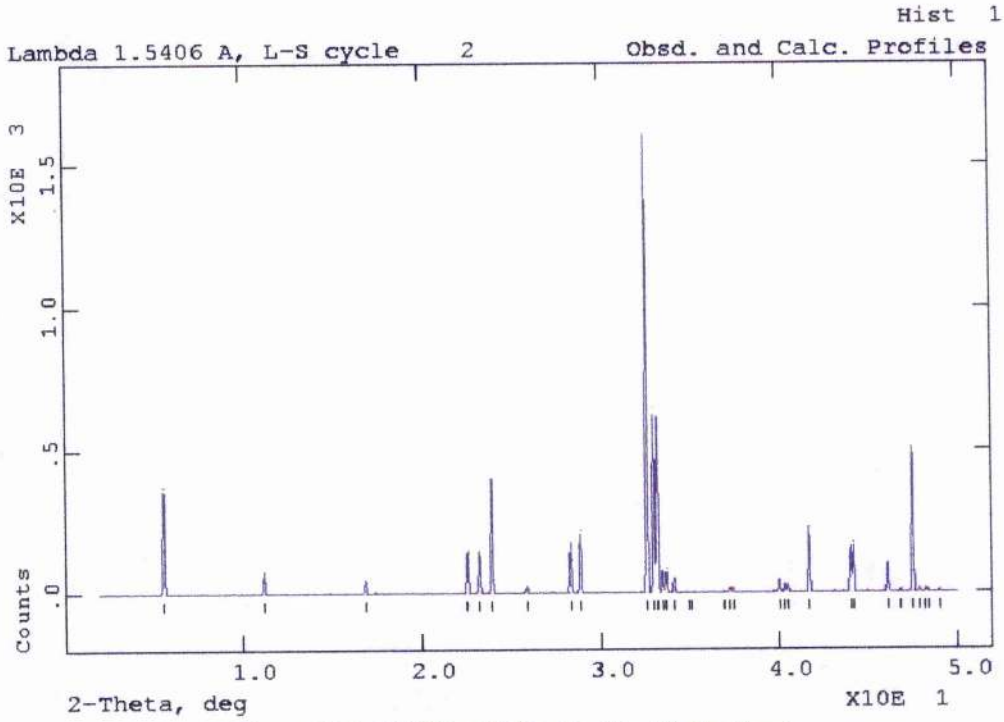

Figure 6.28. 3212 ideal XRD plot (simulated pattern).

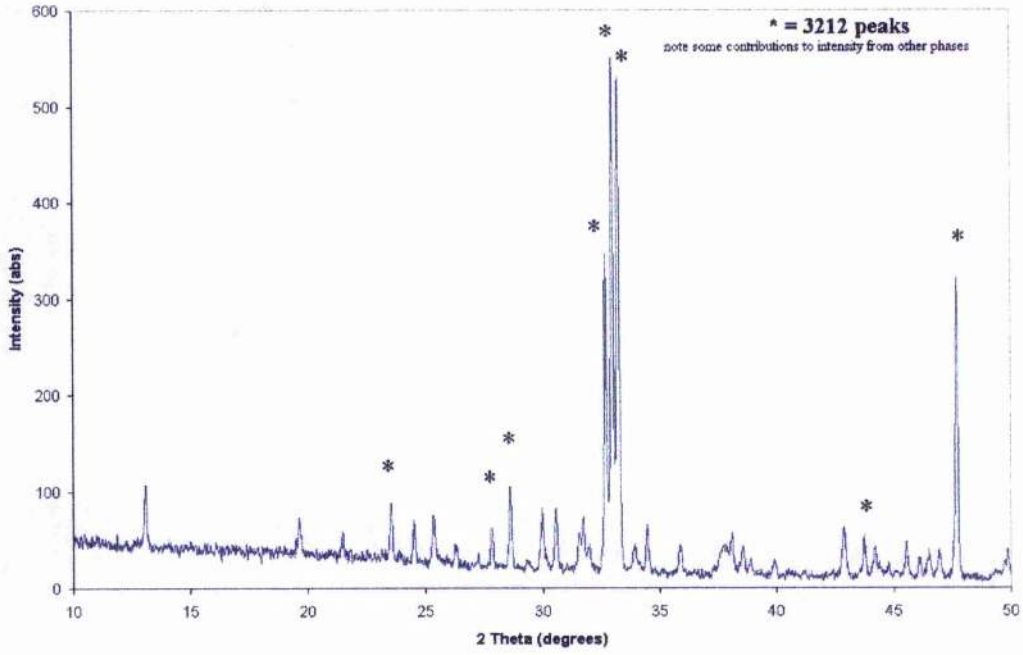

Figure 6.29. Presence of Pb based 3212 phase in decomposed 1212 sample.

Assuming that the 3212 phase is present, then a number of questions have to be asked about its actual composition. It would be quite reasonable to expect a phase which contains cation disorder, is cation deficient and has an unknown oxygen distribution. It is impossible to say what the actual composition might be without a full EDAX analysis, but the synthesis of such phases should be attempted, section 6.31.

The other material identified from electron microscopy had a structure with a c-axis of ~13.5Å that would suggest some sort of layered structure having an extra rocksalt layer relative to the 1212 phase. At these temperatures in such an environment, Pb should be in its 2+ state (1.18Å at CN=6) and Cu in a 2+ (0.73Å at CN=6), which would suggest from such a size mismatch that Pb and Cu reside in separate layers. In the 3212 phase Pb and Cu reside in separate layers and the Cu is in a 1+ oxidation state, so this is also a possibility. From literature reports[8,9,10,11,12], possible stacking sequences belong to "0223" and "2212" $PbSrBaYCu_3O_y$ based on the 3.82 x 27/28Å tetragonal unit cell. Figure 6.30 shows the powder pattern of the ideal "0223"/"2212" structure and figure 6.31 the fit of this phase to the decomposed 1212 structures.

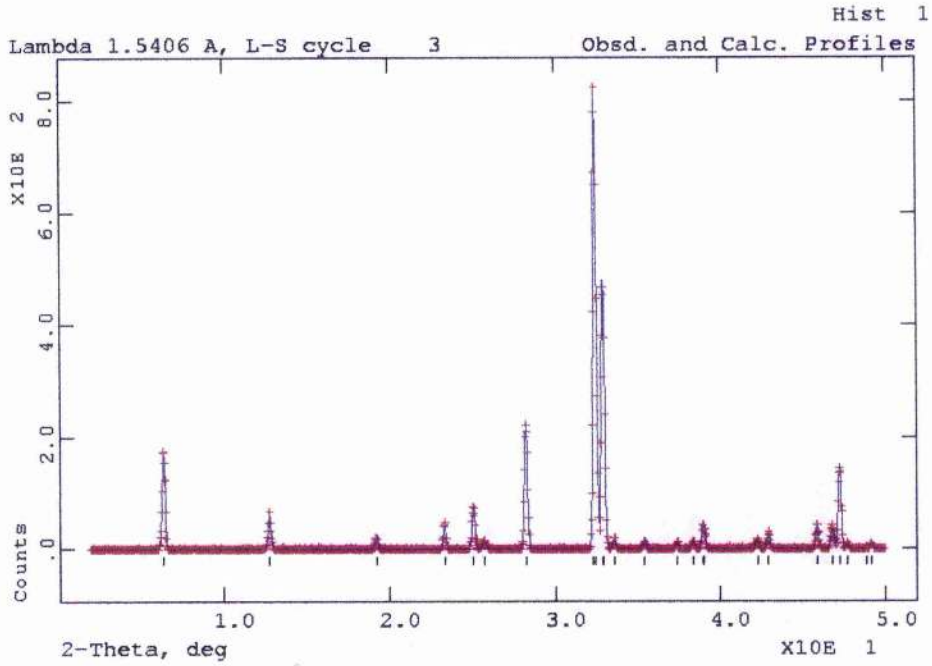

Figure 6.30. Ideal 2212 powder pattern (simulated).

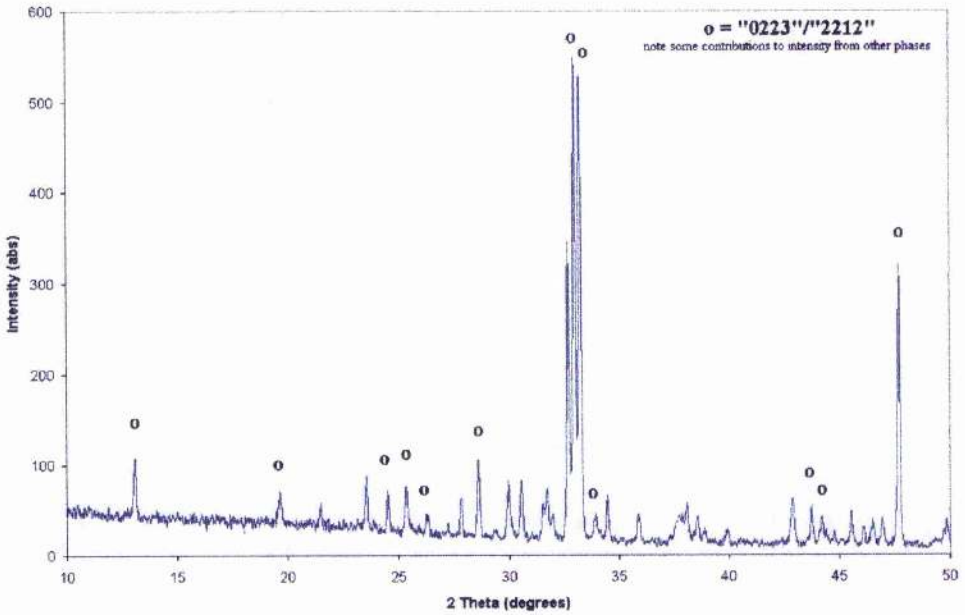

Figure 6.31. Presence of Pb based 2212 phase in decomposed 1212 phase.

It is quite likely that the longest spacing observed from electron diffraction relates to a 002 reflection and so the ~27Å structure, figure 6.30, is the best option. The literature reports[8-12], however, deal with samples containing Ba and do not show any indication that Ba free samples can be synthesised. Synthesis of the Ba free phase is discussed in section 6.32.

6.24. Decomposition mechanism

Taking into consideration the results presented in the previous sections, there appears to be a possible pathway in which the decomposition proceeds. The decomposition of the 1212 phase may be considered as follows in steps 1-5 as a function of temperature in a low pO_2 environment. Temperatures shown below are used as a guide and are of course dependent on the actual pO_2 during an experiment.

❶ 1212 - $(Pb,Cu)Sr_2(Y,Ca)Cu_2O_y$ (Room Temperature)

↓

❷ "1212" + $(Ca,Sr)CuO_y$ (~600°C)

↓

❸ Decomposed unknown phase(s) + "SrCuO" impurities (~750°C)

↓

❹ 3212 phase + "2212" phase + "SrCuO" impurities (~800-900°C)

↓

❺ Sample destruction (~975°C)

6.3. Synthesis and characterisation of 3212 and 2212 phases

The previous sections suggest that 3212 and 2212 type phases result from the decomposition of 1212. In this section the synthesis of cation deficient 3212 and Ba free 2212 samples has been attempted and the possibility of inducing superconductivity investigated.

6.31. The 3212 phase.

The 3212 phase, figures 6.32 and 6.33, deviates slightly from tetragonal symmetry and the simplest cell consistent with the X-ray pattern is C-centred, with lattice parameters $\underline{a} \approx 5.40$Å, $\underline{b} \approx 5.43$Å, and $\underline{c} \approx 15.74$Å. Cava et al[6] showed that systematic absences were consistent with C-centring.

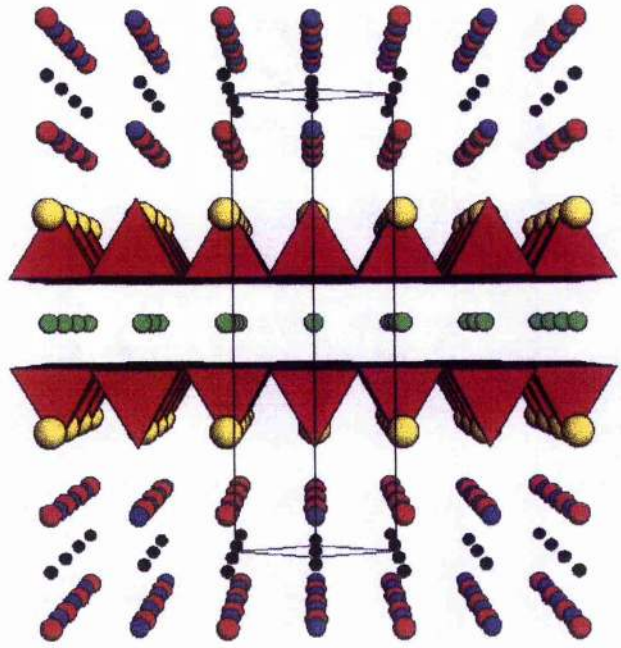

Figure 6.32. Structure of the 3212 phase in ac projection (Pb = blue, O = red, Y = green, Sr = yellow).

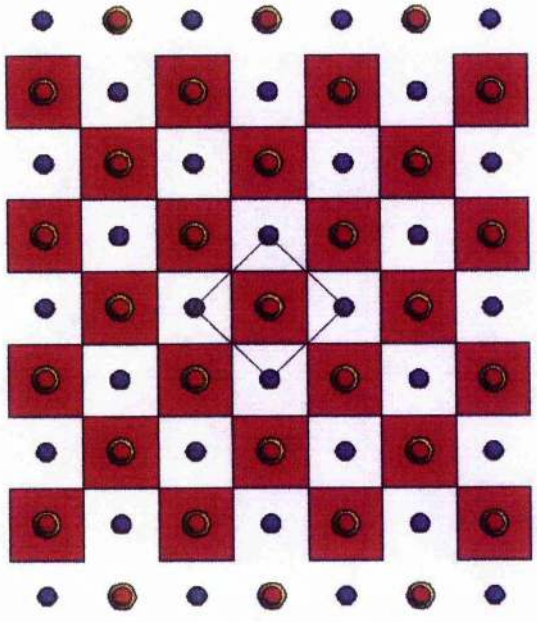

Figure 6.33. Structure of the 3212 phase shown in **ab** projection

The 3212 phase has a stacking sequence:

$$-(Y,Ca) - CuO_2 - SrO - PbO - CuO_\delta - PbO - SrO - CuO_2 - (Y,Ca) -$$

In the PbO - CuO_δ - PbO rocksalt intergrowth, where $\delta = 0$, the Pb is present as Pb^{2+} and has a distorted flattened square pyramid co-ordination (sharing edges with adjacent pyramids), with the lone pair probably pointing towards the vacant sixth site of the co-ordination octahedron. The PbO_5 pyramids are separated by a single copper layer, which for $\delta = 0$ is oxygen free and displays linear O - Cu - O co-ordination characteristic of Cu^{1+}. The 3212 phase can accommodate a δ value up to 1.5[13]; however, $\delta \approx 0$ is the only value of interest in this study. Superconductivity has not been induced in $(Pb_2Cu_1)Sr_2YCu_2O_8$ and only by doping Ca^{2+} for Y^{3+} can onset temperatures approaching 80K be achieved.

Initially, before the TEM work, it was thought that the decomposition product might

be some sort of 1212-3212 intergrowth. Subsequently a sample of nominal composition $Pb_1Sr_2Y_1Cu_2O_y$ - $Pb_2Cu_1Sr_2Y_1Cu_2O_y$ was synthesised in a low pO_2 environment. The resulting product was found to be that of the 3212 phase was formed along with a small amount of "SrCuO" type impurity. This phase was indexed with a unit cell size of 5.39 x 5.42 x 15.74Å and consistent with the Cmmm space group. TEM investigations showed this sample to have a level of disorder from variable brightness of spots within layers and the presence of extra or missing layers, section 6.22 shows examples on these types of materials. It is better to look at the nominal composition of this phase not as $Pb_3Cu_1Sr_4Y_2Cu_4O_y$ but rather $(Pb_{1.5}Cu_{0.5})Sr_2Y_1Cu_2O_y$ which would appear to have a cation deficient rocksalt layer. Rietveld refinement results from such a sample using XRD and neutron diffraction are summarised in tables 6-1, 6-2 and figures 6.34 and 6.35.

R_{wp} (%)	R_p (%)	Chi^2	a (Å)	b (Å)	c (Å)
10.95	7.32	5.151	5.39126(13)	5.42568(13)	15.7427(5)

Atom	x	y	z	Frac*	Ui/Ue*100 (Å^2)
Pb	0.5	0	0.38786(12)	0.95	0.35(8)
Sr	0	0	0.22036(23)	1.00	0.81(17)
Y	0	0	0	1.00	0.54(20)
Cu(1)	0	0	0.5	0.89	0.95(34)
Cu(2)	0.5	0	0.1069(4)	1.00	1.56(20)
O(1)	0.5	0	0.2608(16)	1.00	1.5
O(2)	0	0	0.3879(15)	1.00	1.5
O(3)	0.25	0.25	0.0938(10)	1.00	1.5

* = Errors smaller than 0.01.

Table 6-1. Summary of Rietveld refinement from XRD data.

R_{wp} (%)	R_p (%)	Chi^2	a (Å)	b (Å)	c (Å)
10.38	7.92	8.743	5.39596(17)	5.42157(17)	15.7300(5)

Atom	x	y	z	Frac*	Ui/Ue*100 ($Å^2$)
Pb	0.5	0	0.38721(19)	1.00	0.68(8)
Sr	0	0	0.22142(23)	1.00	0.89(11)
Y	0	0	0	1.00	0.54(13)
Cu(1)	0	0	0.5	0.91	0.51(14)
Cu(2)	0.5	0	0.10604(22)	1.00	0.84(10)
O(1)	0.5	0	0.2512(16)	1.00	0.78(11)
O(2)	0.0503(19)	0.0702(14)	0.38520(50)	0.25(x4)	1.77(34)
O(3)	0.25	0.25	0.09294(10)	1.00	1.53(11)

* = Errors smaller than 0.01.

Table 6-2. Summary of Rietveld refinement from neutron diffraction data.

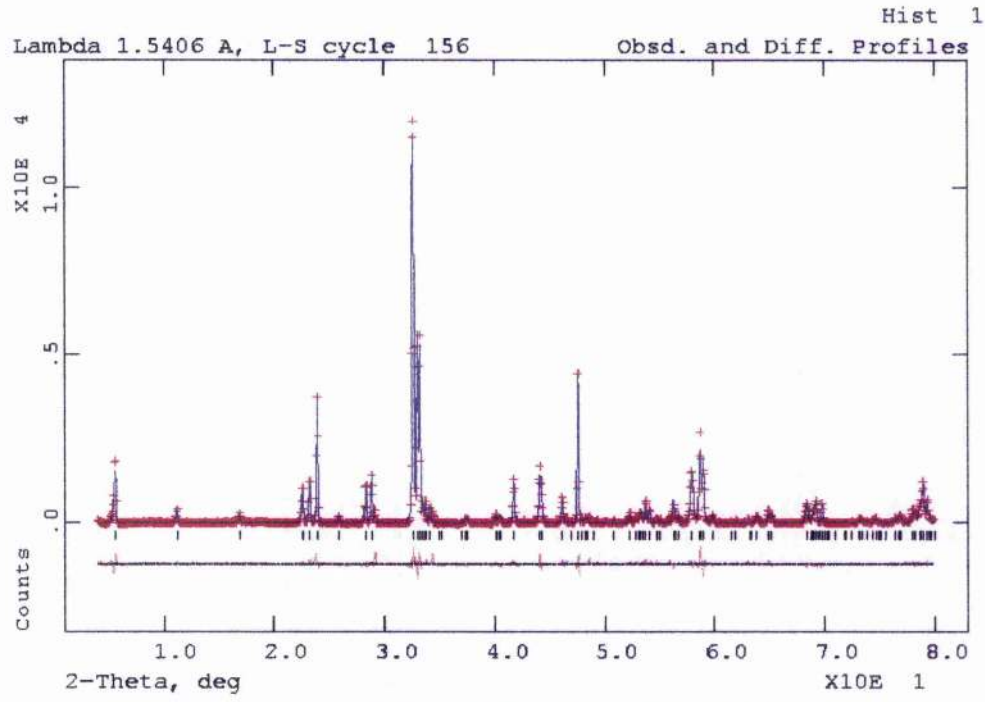

Figure 6.34. Rietveld fit to XRD data. Impurity peaks removed in analysis shown.

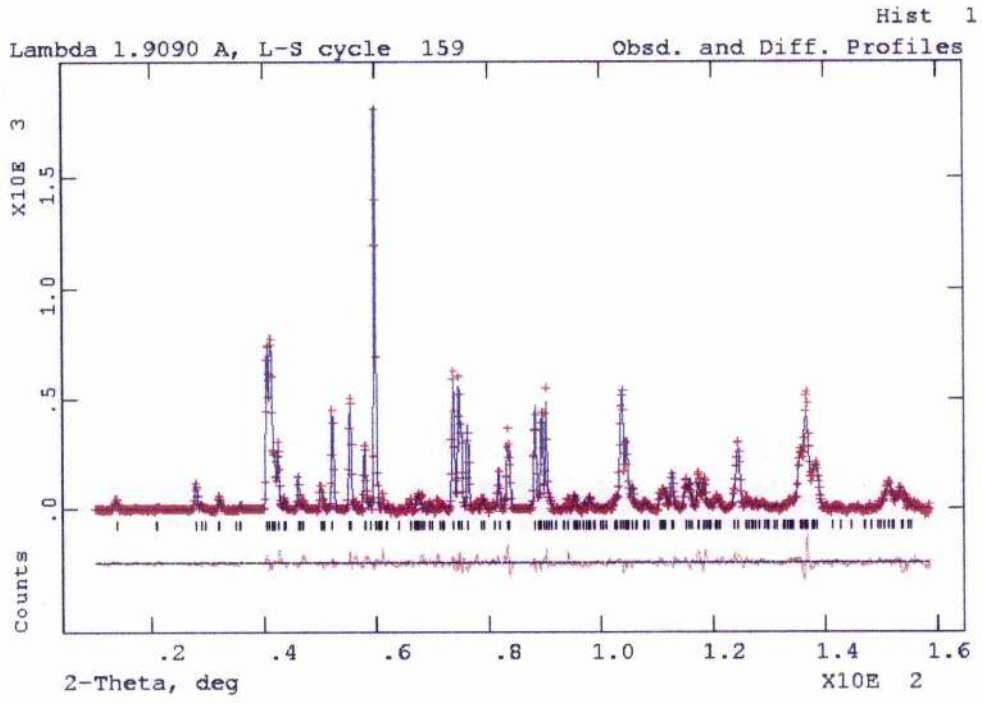

Figure 6.35. Rietveld fit to neutron data. Impurity peaks removed in analysis shown.

In terms of unit cell dimensions and volume, the two results match each other. However, it is the difference between site occupancies using the different techniques that is more interesting. The Pb scattering dominates using XRD and it might appear that this site is not fully occupied, but the particularly low ITF would suggest that an element(s) with lowering scattering power is present on this site. Using neutron diffraction the scattering factors of Pb,Cu, Sr and Y are similar and the full fractional occupancy of the Pb site would appear to confirm that a mixture of atoms are present on this site. The Cu(1) site is deficient, but occupancy is greater than the value of 0.5 expected from the ideal composition. There does not appear to be any indication that any other element than Cu is on this site. A more complete study of the cation disorder is discussed from a resonant X-ray diffraction study below.

The magnetic behaviour of this sample proves quite interesting, and susceptibility measurements show that the sample has an onset of 67K, figure 6.36. As mentioned previously the standard $(Pb_2Cu_1)Sr_2Y_1Cu_2O_8$ end member itself is not superconducting from literature[4,6,13] reports, and it is only through Ca doping that this may be achieved. Magnetic measurements on samples of nominal composition

$(Pb_{1.5}Cu_{0.5})Sr_2(Y_{0.5}Ca_{0.5})Cu_2O_y$ show a T_c = 76K, figure 6.37. Clearly to observe superconductivity in this cation deficient sample shows that superconductivity occurring in the decomposition products of reduced 1212 is indeed quite possible.

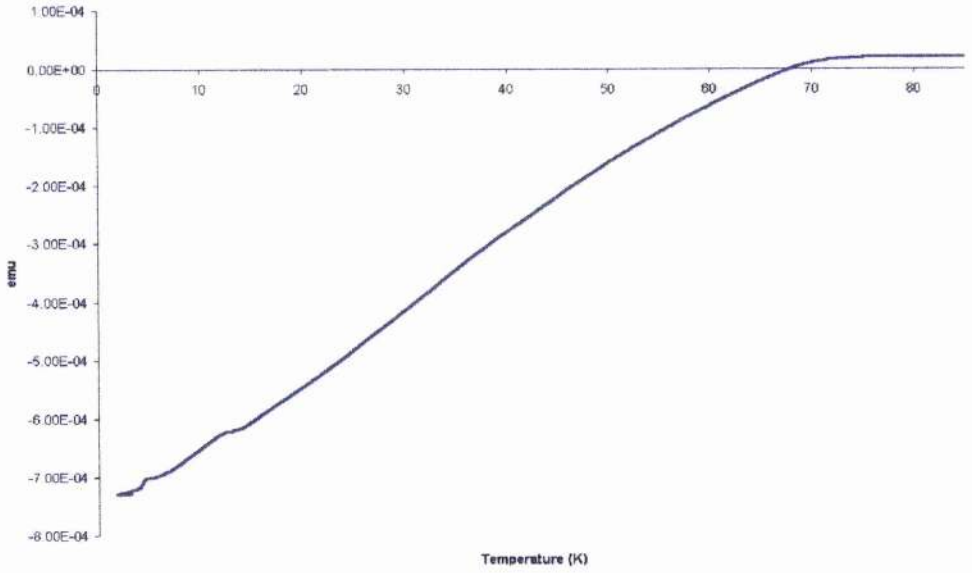

Figure 6.36. Magnetic susceptibility of 3212 Ca free phase.

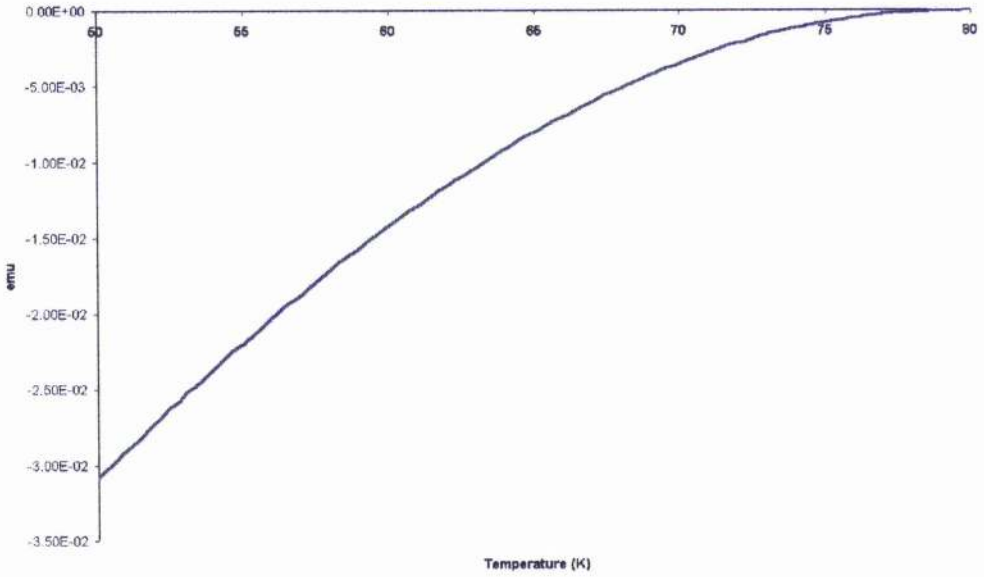

Figure 6.37. Magnetic susceptibility of Ca doped 3212 phase.

Two samples were studied having nominal compositions of $(Pb_{1.5}Cu_{0.5})Sr_2Y_1Cu_2O_y$ and $(Pb_{1.5}Cu_{0.5})Sr_2(Y_{0.5}Ca_{0.5})Cu_2O_y$. The Ca free sample showed lesser levels of impurity and certainly seemed to give better counting statistics, although it was

possible to collect good data at all edges selected. The diffraction pattern for the Ca free 3212 sample is shown in figures 6.38 and 6.39. The main pattern as presented shows nothing interesting, but from figure 6.39 it is evident that peaks can still be clearly resolved out to 50° 2θ when ~0.5Å (25keV) is the selected wavelength. For all other edges selected, diffraction peaks could still be clearly resolved above the background noise at the highest 2θ angle. Certainly one or two groups[6,7] have questioned whether or not this 3212 phase is actually monoclinic and they have been by no means certain. In figure 6.40 part of the laboratory diffraction pattern for the 3212 phase is shown. Over the range 32-34° 2θ the three largest peaks are present in the spectrum and each peak is assigned one marked reflection using the Cmmm spacegroup, these being from left to right 114, 020, 200). The FWHM for each peak, black line on figure, is essentially the same by a rough calculation. On BM16 at ESRF Grenoble, the resolution of the instrument is such, that instrumental broadening contributions have effectively been eliminated. Thus, in all samples it is quite clear in figures 6.41 and 6.42 that the "114" peak is broadened compared to the "020" and "200". This broadening is not due to the sample being monoclinic, but instead is associated with anisotropic particle broadening which is common in such layered materials. There does not appear to be any evidence from the BM16 data that this material is monoclinic, either by inspection of the powder pattern or from the results of Rietveld refinements. Using the GSAS routine, all attempts to fit a monoclinic spacegroup to the data were unstable. If the sample is actually monoclinic then β must be very close to 90°.

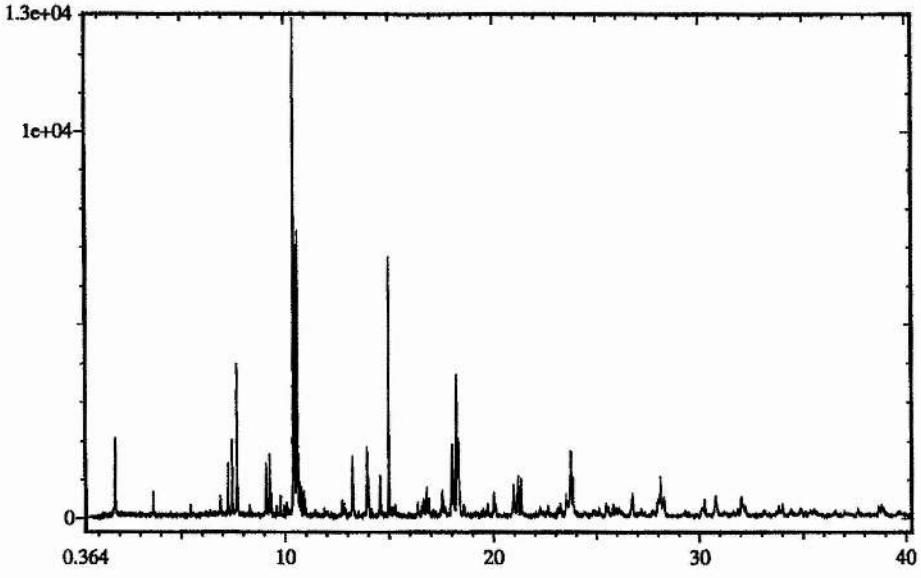

Figure 6.38. Diffractogram at 25 keV, $(Pb_{1.5}Cu_{0.5})Sr_2Y_1Cu_2O_y$ sample.

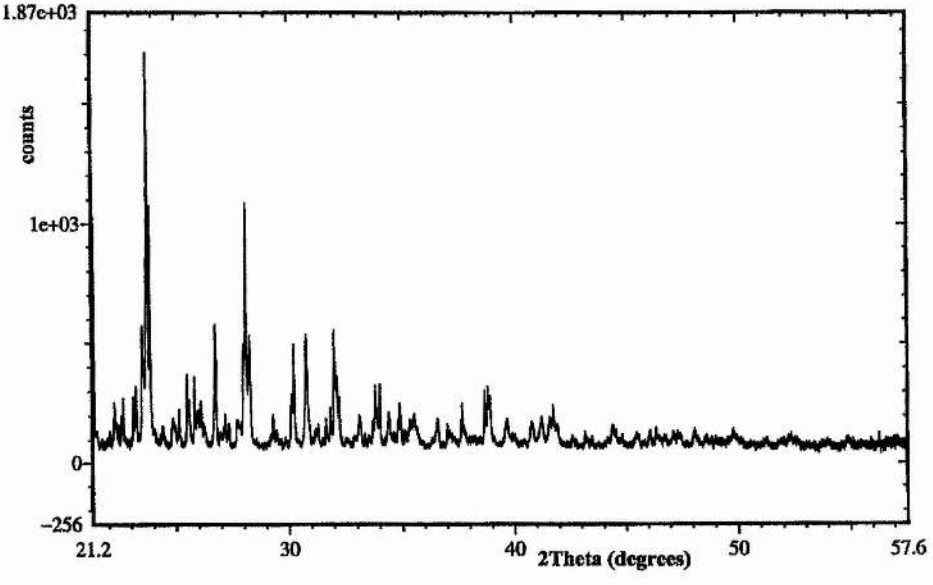

Figure 6.39. Peaks resolved above background noise in $(Pb_{1.5}Cu_{0.5})Sr_2Y_1Cu_2O_y$ sample at 50° 2θ.

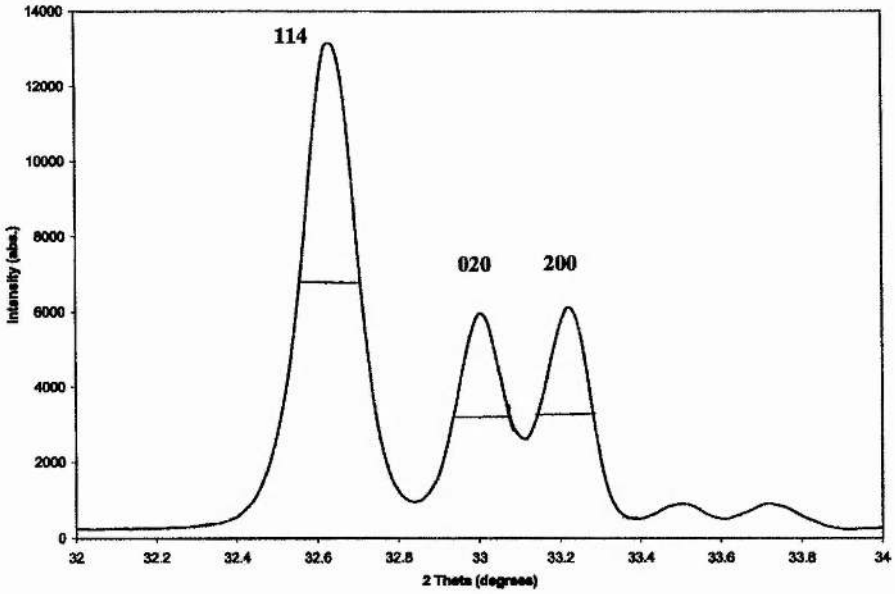

Figure 6.40. FWHM of three largest peaks in Ca free 3212 sample, taken using Stoe Stadi P.

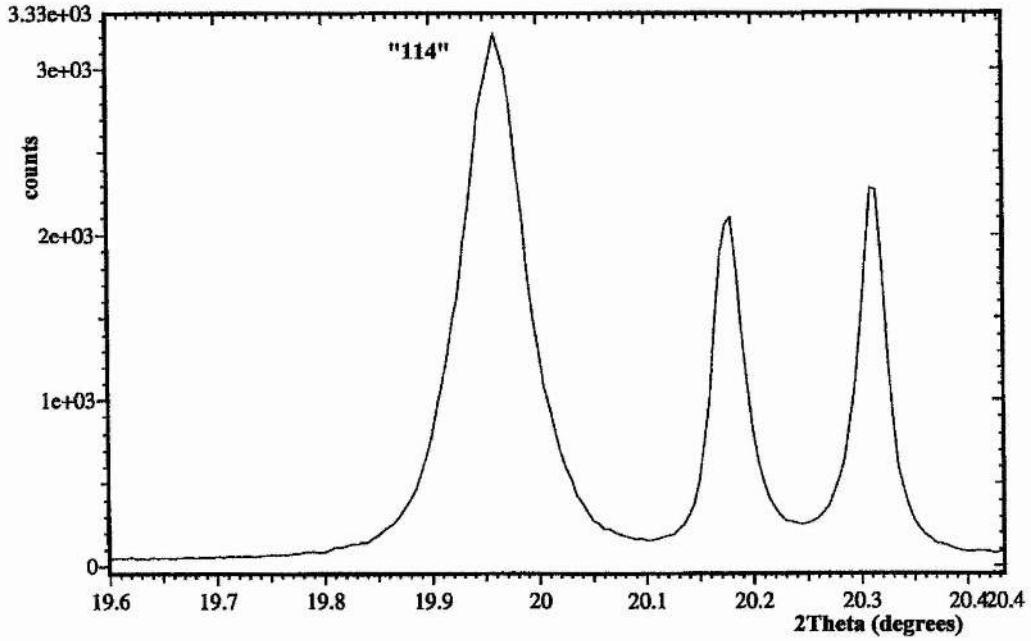

Figure 6.41. Anisotropic broadening of "114" reflection, Pb edge data shown here from BM16 instrument.

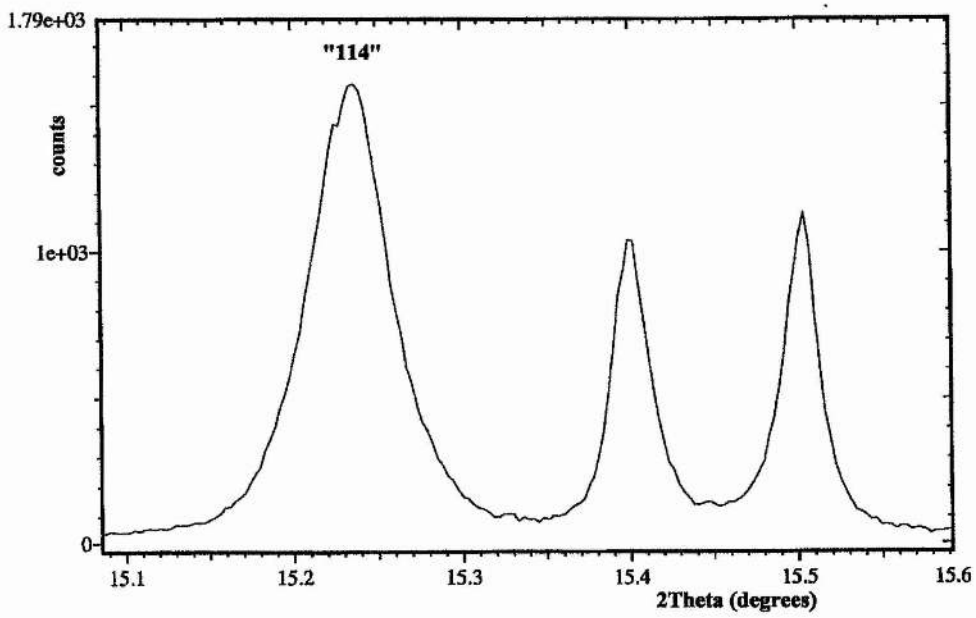

Figure 6.42. Anisotropic broadening of "114" reflection, Y edge data shown here from BM16 instrument.

The sample used for the resonance calculation was $(Pb_{1.5}Cu_{0.5})Sr_2Y_1Cu_2O_y$. The best fit obtained using all sets of compressed data are summarised below in table 6-3 and the fit to the 25keV data set is shown in figure 6.43.

R_{wp} (%)	R_p (%)	Chi^2	a (Å)	b (Å)	c (Å)
16.63	13.38	5.24	5.39185(6)	5.42666(6)	15.74353

Atom	x	y	z	Frac	Ui/Ue*100 (Å^2)
Pb#	0.5	0	0.38748(7)	0.943(4)	0.72(2)
Sr#	0.5	0	0.38748(7)	0.040(8)	0.72(2)
Sr	0	0	0.22038(13)	1.00	0.83(5)
Y	0	0	0	1.00	0.78(7)
Cu(1)*	0	0	0.5	0.877(7)	0.36(9)
Y(2)*	0	0	0.5	0.0355(7)	0.36(9)
Cu(2)	0.5	0	0.10313(13)	1.00	0.91(7)
O(1)	0.5	0	0.2541(12)	1.00	1.5
O(2)	0	0	0.3888(10)	1.00	1.5
O(3)	0.25	0.25	0.0912(7)	1.00	1.5

= ITF and positional parameters constrained to move together. * = ITF constrained.

Table 6-3. Resonant diffraction results for $(Pb_{1.5}Cu_{0.5})Sr_2Y_1Cu_2O_y$.

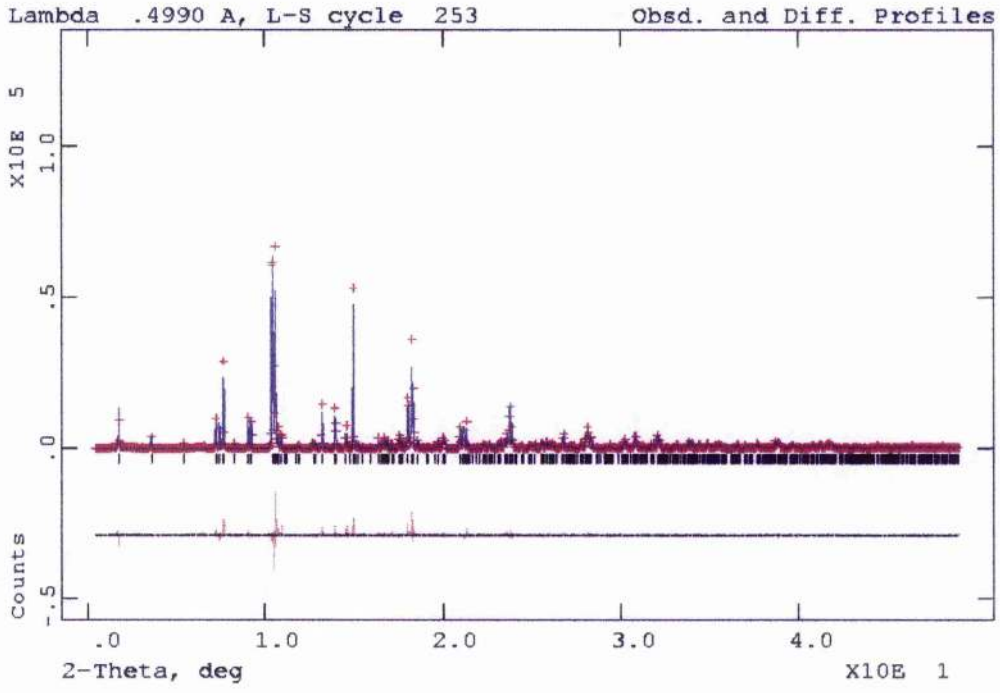

Figure 6.43. Rietveld fit to 25 keV data, impurity peaks removed in analysis shown.

The resonant diffraction data once again gives relatively poor R_{wp} values, although there does not seem to be much wrong with the fit to the data. The reasons are discussed fully in section 5.43.

On the CuO_2 planes i.e. Cu(2), Sr and Y sites there is no indication that any significant amount of cation disorder is present on these sites. At the Pb site it was possible to detect ~4% of Sr present. It was also possible to detect small amounts of Y and Cu, but these results were too small to say in a quantitative manner that these elements are present. The amount of Sr is small, and 4% is probably as small an amount as one would want to present quantitatively. Probably 5% and above would be better. Some Y was found on the Cu(1) site; however, the result should really only be taken as a guide and not accepted as being a quantitative value.

Although there are certainly indications that cation disorder exists in this material, there seems to be problems with the stacking sequences of the PbO-Cu(1)-PbO rocksalt sandwich. Certainly the PbO layer oxygen is displaced from its ideal site and this in turn could well affect the Cu(1) layer. The disordered nature of these samples with stacking faults and other problems is actually distorting the results. Thus, they should be treated cautiously because the Rietveld method is only fitting a model.

6.32. The "2212"/"0223" phase.

Tokiwa et al[12] assign a sample of nominal composition $PbBaSrYCu_3O_{7+\delta}$ as 2212, while Rouillon et al[9] assign the same nominal composition as 0223. Under low pO_2 synthesis conditions both samples have identical diffraction patterns. The structure of this material is rather complicated as shown in figure 6.44. The symmetry is tetragonal with space group I4mm, $\underline{a} \approx 3.84$Å and $\underline{c} \approx 27.4$Å. Rietveld analysis reveals that the Ba preferentially occupies one of the Ba/Sr sites, while the Sr preferentially occupies the other.

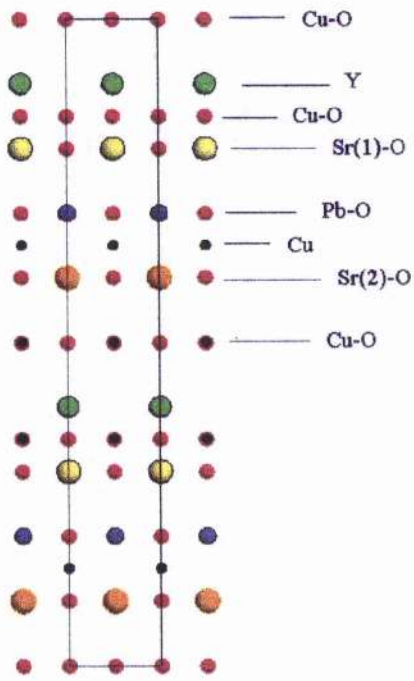

Figure 6.44. The 2212 structure presented in an **ac** projection.

A Ba free sample of nominal composition $(Pb_1Cu_1)Sr_2YCu_2O_{7+\delta}$ was synthesised under reducing conditions and the XRD pattern is shown in figure 6.45. There is evidence that two phases are present in the above figure, the two peaks at low 2θ angles confirm this. It is possible, figure 6.46 to match the 3212 and 2212 phases to those present in figure 6.45. Evidently the Ba free 2212 phase is not stable with the stoichiometric composition.

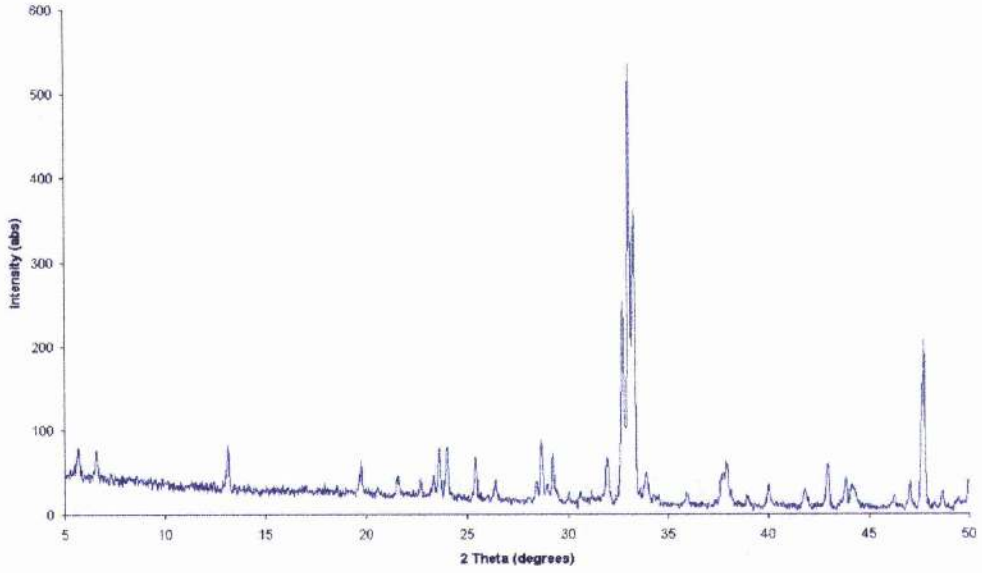

Figure 6.45. XRD pattern of synthesis product(s) derived from a mixture of nominal composition $(Pb_1Cu_1)Sr_2YCu_2O_y$.

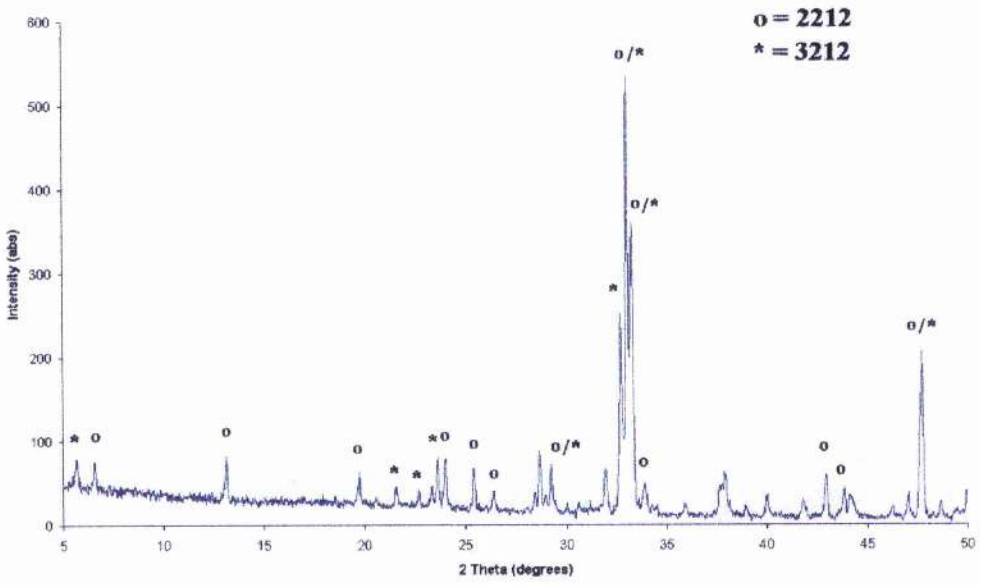

Figure 6.46. Pb based 3212 and 2212 phases identified as being present as synthesis products from a mixture of nominal composition of. $(Pb_1Cu_1)Sr_2YCu_2O_y$.

Magnetic measurements, figure 6.47, on the "apparent" two phase mixture shows a rather complicated behaviour. It could be speculated that at least one superconducting phase is present below 40K and the rising susceptibility at 15K due to the presence of

some paramagnetic phase in the mixture. The drop in susceptibility below 10K might indicate some other phase in the material becomes superconducting; however, such a complex pattern should be treated with caution.

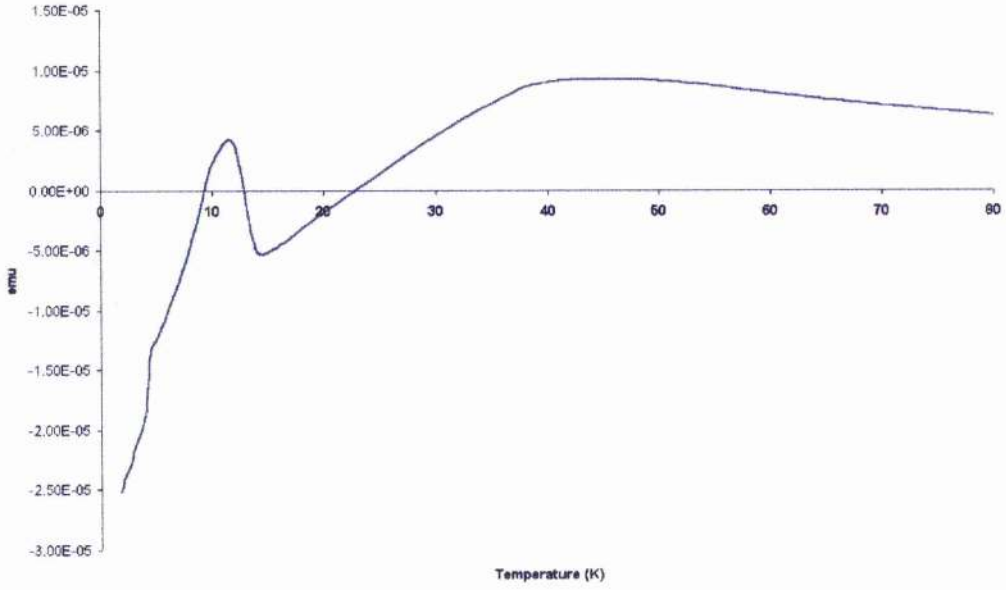

Figure 6.47. Mixed superconductivity in "$Pb_1Sr_2Y_1Cu_3O_y$" sample?

This "two phase" sample shows a complex oxidation behaviour under flowing O_2, figure 6.48-6.50. The resulting product is that of 1212, the 5.9Å peak at 15° 2θ confirms this, plus some type of impurity phase(s). Magnetic measurements reveal this fully oxidised sample to be non-superconducting. This result is probably not surprising, since it is most probable that the formation of Pb^{4+} and Cu^{2+} shall lead to the existence of a single rocksalt layer due to size consideration discussed in chapter 5.

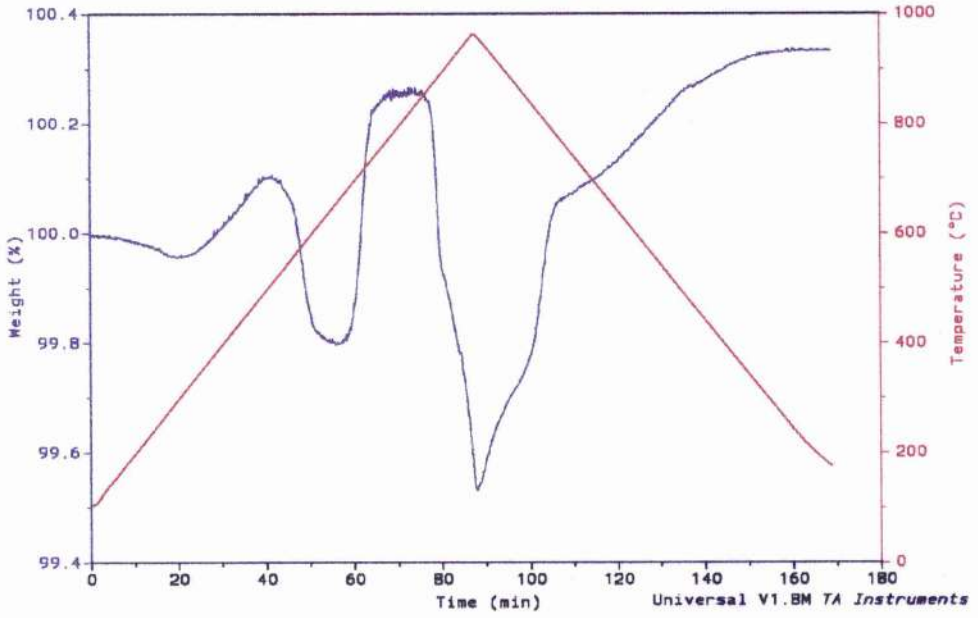

Figure 6.48. 2212 sample undergoing thermal analysis under oxygen

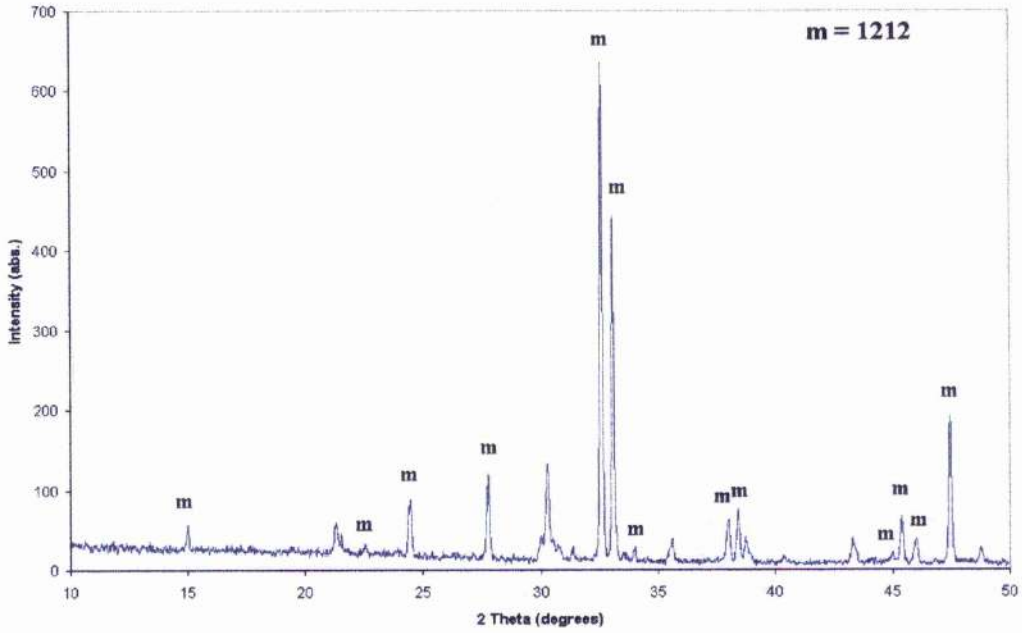

Figure 6.49. 2212 sample XRD pattern taken after thermal analysis under oxygen.

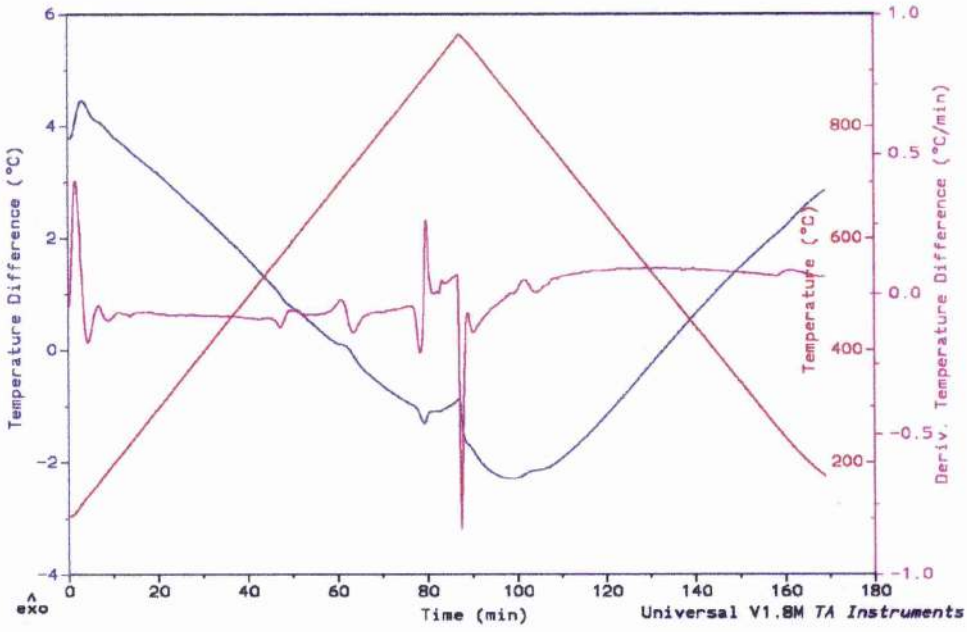

Figure 6.50. 2212 sample XRD pattern taken after thermal analysis under oxygen, DTA plot shown.

6.4. Summary

It is possible using low pO_2 annealing conditions to effectively remove the excess oxygen δ in $(Pb_{[1+x]/2}Cu_{[1-x]/2})Sr_2(Y_{1-x}Ca_x)Cu_2O_{7+\delta}$, but there are a number of problems. The optimal superconducting properties exist when the oxygen content of the sample is 7.0, but there is no clear temperature window over which this oxygen content exists. To further add to this problem, variations in the pO_2 can dramatically alter the oxygen content at a particular temperature. There was no evidence to suggest from this removal of the excess oxygen that superconducting onset temperatures were any better than those achieved by annealing in high pO_2 atmospheres.

As the oxygen removal proceeds within the sample, at a critical point exsolution of the $(Ca,Sr)CuO_y$ impurity occurs and at higher temperatures the 1212 phase itself undergoes complete decomposition. This decomposition leads to the formation of new phases, particularly 3212 and 2212. HREM studies revealed these phases to be quite

disordered and possibly containing cation disorder. Synthesis of the 2212 phase and a cation deficient 3212 phase was attempted. The 2212 was not single phase, rather a mixture of 2212 and 3212 and superconductivity induced around 40K. Referring to steps 3 and 4 in the decomposition mechanism, section 6.24, it is not possible to say whether or not the 2212 phase is formed first and then undergoes decomposition. This might well be the case, but a full in situ study would be required to answer the question. In the 3212 system, samples of nominal compositions $(Pb_{1.5}Cu_{0.5})Sr_2Y_1Cu_2O_y$ and $(Pb_{1.5}Cu_{0.5})Sr_2(Y_{0.5}Ca_{0.5})Cu_2O_y$ were synthesised nearly single phase and superconducting onset temperatures of 67K and 76K were achieved respectively. These results would strongly suggest that the reports[1,2] of >70K onset temperatures in PbCu:1212 samples were due to the 3212 phase.

6.5. Bibliography and references for chapter 6

[1] H. Zhang, G.S. Chen, S.Q. Feng, X. Zhu and Q.R. Feng, *Solid State Comm.*, 1992, **83**, 601.

[2] S.H.H. Naqvi and I.W. Boyd, *Physica C*, 1993, **213**, 161.

[3] S. Adachi, H. Adachi, K. Setsune and K. Wasa, *Jpn. J. Appl. Phys.*,1991, **30**, L690.

[4] S.H.H. Naqvi and I.W. Boyd, *Mat. Sci. and Eng*, 1995, **B33**, 67.

[5] T. Rouillon, R. Retoux, D. Groult, C. Michel, M. Hervieu, J. Provost and B. Raveau, *J. Solid State. Chem.*, 1989, **78**, 322.

[6] R.J. Cava, B. Batlogg, J.J. Krajewski, L.W. Krupp, L.F. Schneemeyer, T. Siegrist, R.B. vanDover, P. Marsh, W.F. Peck, P.K. Gallagher, S.H. Glarum, J.H. Marshall, R.C. Farrow, J.V. Waszczak, R. Hull and P. Trevor, *Nature*, 1988, **336**, 211.

[7] H. Fujishita, M. Sato, Y. Morii and S. Funahashi, *Physica C*, 1993, **210**, 529.

[8] T. Rouillon, V. Caignaert, M. Hervieu, C. Michel, D. Groult and B. Raveau, *J. Solid State Chem.*, 1992, **97**, 56.

[9] T. Rouillon, R. Retoux, D. Groult, C. michel, M. Hervieu, J. Provost and B. Raveau, *J. Solid State Chem.*, 1989, **78**, 322.

[10] A. Tokiwa, T. Oku, M. Nagoshi, M. Kikuchi, K. Hiraga and Y. Syono, *Physica C*, 1989, **161**, 459.

[11] A. Tokiwa, N. Nagoshi, T. Oku, N. Kobayashi, M. Kikuchi, K. Hiraga and Y. Syono, *Physica C*, 1990,**168**, 285.

[12] A. Tokiwa, F. Izumi, T. Oku and Y Syono, *Physica C*, 1993, **215**, 243.

[13] V.V. Nemoshkalenko, V.N. Uvarov, A.G. Popov, L.V. Timoshevskaja, N.V. Dan'ko and V.S. Melnikov, *Physica C*, 1995, **252**, 313.

Chapter 7. CONCLUSIONS

This research aimed to study the PbCu:1212 system and attempt to develop its potential. In particular the areas of synthesis, post annealing and structural determination required detailed study in order to understand the system and hence attempt to optimise sample stability and superconducting properties.

Formation of the 1212 phase does not proceed directly from sample precursors to product, but rather proceeds through a hexagonal intermediate phase. These findings disagree with a number of groups[1,2,3] who describe this phase as being an impurity. In $(Pb_{[1+x]/2}Cu_{[1-x]/2})Sr_2(Y_{1-x}Ca_x)Cu_2O_{7\pm\delta}$ the stability of the intermediate phase is such at higher Ca levels that it begins to dominate the XRD pattern and indeed at the Ca end member $Pb_1Sr_2Ca_1Cu_2O_y$ the 1212 phase cannot be formed at ambient pressure. Only through the applications of very high pressures in the 5GPa region have attempts been made to overcome[4,5] this problem. It is possible though to synthesise single-phase samples in this series up to x=0.3 at ambient pressure. The sol-gel method produces better quality samples than by conventional solid-state methods, although the final reaction temperatures essentially are the same as those used in a conventional solid-state synthesis.

TGA analysis of samples under normal reaction conditions reveals the 1212 phase to be unstable. Irreversible formation of the $(Ca,Sr)CuO_y$ impurity occurs when the sample oxygen content drops below a critical level. With increasing Ca content, the temperature at which the phase instability occurs is lowered.

Using standard oxidising environments for post annealing treatment in $(Pb_{[1+x]/2}Cu_{[1-x]/2})Sr_2(Y_{1-x}Ca_x)Cu_2O_{7\pm\delta}$, superconductivity is only achieved in quenched samples where the Ca content (x) is >0.2. The onset temperature reaches a maximum of 43K in the x=0.4 sample and drops to 25K in the x=0.5 and 0.6 samples. However, the samples are not phase pure when $x > 0.3$ and the increasing level of impurity above x=0.4 means it is not at all certain what the proper composition of the 1212 phase is. Therefore, it is not clear what onset temperatures might be achieved if phases with nominal stoichiometry could be prepared.

The annealing temperature can greatly affect both the superconducting fraction and onset temperature. It is possible to calculate the actual oxygen content within the sample at any particular temperature, and the results show that the optimal T_c and superconducting volume fraction are obtained over a very narrow oxygen content range of 6.99-7.00.

Application of low pO_2 annealing conditions to effectively remove the excess oxygen in $(Pb_{[1+x]/2}Cu_{[1-x]/2})Sr_2(Y_{1-x}Ca_x)Cu_2O_{7+\delta}$ is possible; however there are a number of problems. The optimal superconducting properties exist when the oxygen content of the sample is 7.00, but there is no clear temperature window over which this oxygen content exists. To further add to this problem, variations in the pO_2 can dramatically alter the oxygen content at a particular annealing temperature. There is no evidence to suggest that low pO_2 environments produce better superconducting properties than those achieved by annealing in high pO_2 atmospheres. While the oxygen removal proceeds within the sample, at a critical point exsolution of the $(Ca,Sr)CuO_y$ impurity occurs and then the 1212 phase itself undergoes complete decomposition to a series of new phases. This questions the validity of claims[6,7] of >70K transitions in samples having undergone low pO_2 annealing treatments.

Rietveld refinements on samples of nominal composition $(Pb_{0.7}Cu_{0.3})Sr_2(Y_{0.6}Ca_{0.4})Cu_2O_{7.0}$ and $(Pb_{0.7}Cu_{0.3})Sr_2(Y_{0.6}Ca_{0.4})Cu_2O_{7.1}$ using X-ray diffraction suggest that these samples are Y rich and Ca deficient on the (½,½,½) site as well as being Pb deficient/Cu rich on the rocksalt layer. Neutron diffraction results on the other hand show that the sample does not appear to be particularly Ca deficient/Y rich and they also show no indication of any oxygen deficiency in quenched samples. With neutron diffraction it is possible to detect the excess oxygen on the rocksalt layer, but the value for this excess is not reliable. Resonant X-ray diffraction studies on $(Pb_{0.5}Cu_{0.5})Sr_2Y_1Cu_2O_{7.0}$ and $(Pb_{0.7}Cu_{0.3})Sr_2(Y_{0.6}Ca_{0.4})Cu_2O_{7.0}$ show that no cation substitution is present on the Sr and CuO_2 plane Cu in any of the samples. The Ca free Y end member shows within experimental error no indication of any cation deficiency/substitution. The Ca containing sample shows presence of ~5% Pb on the Y/Ca site, with only a small excess of yttrium (0.65 compared to nominal

0.60). The sample is certainly Ca deficient on this site. There is evidence for a small Pb deficiency on the rocksalt layer, but the Cu content remains at its nominal level. There may well be Ca and vacancies in the rocksalt layer. It seems fairly clear that disorder within the sample increases as Ca content does so, but whether or not the system could still be described as self-doping is not totally clear since the experimental composition of $Pb_{0.7}Cu_{2.3}Sr_2Y_{0.65}Ca_{0.35}O_{6.975}$ is virtually the same as the nominal composition of $Pb_{0.7}Cu_{2.3}Sr_2Y_{0.6}Ca_{0.4}O_{7.0}$.

EXAFS experiments studying the local environment reveal clear differences between the local structure and the model produced from diffraction data. In fully oxygenated samples as room temperature the Pb is surrounded by ~4.5 oxygens at ~2.12Å and this decreases to a stable value of 4.0 upon heating. This change in the Pb-O co-ordination number reduction follows the loss of oxygen from a TGA experiment under similar low pO_2 conditions. The Pb is co-ordinated by 4 oxygens, when the excess is not present, two in the plane O(3) and two out of plane i.e. O(2) above and below the plane of the Pb. It is the excess oxygen that accounts for the extra 0.5. The local environment would appear to be best described as being PbO_4 molecular in type, rather than as PbO_6 octahedra.

NMR measurements on PbCu:1212 samples generate interesting results, in particular the fact that the Pb resonance in this system does not sense the CuO_2 planes magnetisation unlike in the PbTl:1212 system. There is evidence of Y dimerisation in some of the PbCu:1212 samples, as shown by Meiboom-Gill spin-echo measurements. Its origin is not at all certain; perhaps the Pb that was shown to substitute on this site plays some effect.

References

[1] R.S. Liu, S.F. Hu, I. Gameson and P.P. Edwards, *J. Solid State Chem.*, 1991, **93**, 276.

[2] T. Maeda, K. Sakuyama, F. Izumi, H. Yamauchi, H. Asano and S. Tanaka, *Physica C*, 1991, **175**, 393.

[3] S. Adachi, H. Adachi, K. Setsune and K. Wasa, *Jpn. J. Appl. Phys.*, 1991, **30**, L690.

[4] T. Tamura, S. Adachi, X.J. Wu, C.Q. Jin, T. Tatsuki and H. Yamauchi, *Physica C*, 1995, **249**, 111.

[5] X.J. Wu, T. Tamura, S. Adachi, C.Q. Jin, T. Tatsuki and H. Yamauchi, *Physica C*, 1995, **247**, 96.

[6] H. Zhang, G.S. Chen, S.Q. Feng, X. Zhu and Q.R. Feng, *Solid State Comm.*, 1992, **83**, 601.

[7] S.H.H. Naqvi and I.W. Boyd, *Physica C*, 1993, **213**, 161.